

**Gas-Phase Cryogenic Vibrational Spectroscopy
of Metal Oxide Cluster Ions:**

Structure-Reactivity Relationship

Der Fakultät für Chemie und Mineralogie
der Universität Leipzig

vorgelegte

D I S S E R T A T I O N

zur Erlangung des akademischen Grades

Doctor Rerum Naturalium

(Dr. rer. nat.)

von M.Sc. Sreekanta Debnath

geboren am 19. June 1991 in Kolkata, Indien

Leipzig, den 23. June 2020

The studies reported in this thesis have been conducted between
January 2015 and June 2020
at the
Fritz Haber Institute of the Max Planck Society in Berlin
Faradayweg 4, 14195 Berlin
and at the
Wilhelm-Ostwald-Institut für Physikalische und Theoretische Chemie
of the Universität Leipzig
Linnéstr. 3
D-04103, Leipzig

under the
supervision of Prof. Dr. Knut R. Asmis.



UNIVERSITÄT
LEIPZIG



FRITZ-HABER-INSTITUT
MAX-PLANCK-GESELLSCHAFT

This thesis is written in the format of a publication-based dissertation and parts of it have already been published. The chapter 4 of this thesis comprise unpublished work and prepared in the format of the prospective journal. Chapters 5 & 6 contain published articles. Respective manuscript and supporting information of the published articles are presented in their corresponding sections. The supporting information of the unpublished article can be found in the appendix.

Bibliographische Daten

Gas-Phase Cryogenic Vibrational Spectroscopy of Metal Oxide Cluster Ions: Structure-Reactivity Relationship

Sreekanta Debnath, Universität Leipzig, Dissertationsschrift, 23.06.2020
161 Seiten, 73 Abbildungen, 14 Tabellen, 25 Schemata, 356 Literaturzitate

Selbstständigkeitserklärung gemäß § 9 (2) der Promotionsordnung

Ich versichere, dass die vorliegende Arbeit ohne unzulässige Hilfe und ohne Benutzung anderer als der angegebenen Hilfsmittel angefertigt wurde und dass die aus fremden Quellen direkt oder indirekt übernommenen Gedanken in der Arbeit als solche kenntlich gemacht worden sind.

Alle Personen, von denen ich bei der Erstellung, Auswahl und Auswertung des Materials Unterstützungsleistungen erhalten habe, sind in der Dissertationsschrift angegeben.

Ich versichere, dass außer den genannten keine weiteren Personen bei der geistigen Herstellung der vorliegenden Arbeit beteiligt waren, insbesondere auch nicht die Hilfe eines Promotionsberaters in Anspruch genommen wurde, und dass Dritte von mir weder unmittelbar noch mittelbar geldwerte Leistungen für Arbeiten erhalten haben, die im Zusammenhang mit dem Inhalt der vorgelegten Dissertation stehen.

Außerdem versichere ich, dass die vorgelegte Arbeit weder im Inland noch im Ausland in gleicher oder in ähnlicher Form einer anderen Prüfungsbehörde zum Zwecke einer Promotion oder eines anderen Prüfungsverfahrens vorgelegt wurde.

Es haben keine früheren, erfolglosen Promotionsversuche stattgefunden.

Ort, Datum

Sreekanta Debnath

Summary

Gas phase cryogenic ion trap vibrational spectroscopy in combination with high level quantum chemical calculations provides an ideal arena to investigate structure-reactivity relationships of pure- and bi- metallic oxide clusters as a function of size, charge-state and coordination environment. In the last decades, characterization of binary metal oxide nanomaterials has received special attention, mainly because catalytically inactive materials can be activated by doping with a second metal. Precisely controlled conditions and the absence of perturbing interactions with an environment allow the gas phase clusters to serve as powerful model systems for nanomaterials. Moreover, the active site(s) of these reactive intermediates can be unambiguously identified by their characteristic vibrational signatures. Such insights ultimately allow for a molecular level understanding of the reaction mechanisms at play at reactive surfaces in heterogeneous catalysis.

Iron is the most common impurity in naturally occurring zeolites. Atomic Fe-substituted small Al-oxide clusters $[(\text{Al}_2\text{O}_3)_n\text{FeO}]^+$ function as model system for Fe-doped zeolites. The influence of an Fe-atom in an Al-oxide network is investigated in terms of structural change and preferred coordination site in Chapter 4. The results demonstrate that the Fe-atom prefers to occupy a position in the outer ring of the cluster and induces substantial change in the cluster structure for the smallest cluster studied ($n=1$), but not for the larger ones. Furthermore, a structural evolution from planar ($n=1$) over quasi-2D ($n=2$) to cage type ($n\geq 3$) structures is observed with increasing cluster size. The insights correlate with reported results of Fe-doped nanoparticles and nanocrystals, where the dopant Fe-atom is mostly found to replace the under-coordinated surface Al-atoms of the Al_2O_3 network.

In Chapter 5 the active site(s) of heteronuclear metal oxide clusters towards oxygen atom transfer (OAT) reactions is identified. $[\text{AlVO}_{x=3,4}]^{\bullet+}$ and $[\text{VPO}_{x=3,4}]^{\bullet+}$ radical cations are studied in the context of CO to CO_2 conversion (chapter 5.1) and ethylene to formaldehyde oxidation (chapter 5.2), respectively. In both cases, the oxygen atom bound to the main group atom, either Al or P, in contrast to the transition metal atom (V) takes part in the OAT cycle.

The results presented in Chapter 6 reveal that the oxygen-deficient Ti^{3+} centre, which represents a model system for an oxygen vacancy at a titania surface, is the active site for CO_2 adsorption. The first two CO_2 molecules adsorb chemically on $[\text{Ti}_3\text{O}_6]^-$, forming asymmetric bidentate-bridged and symmetric tridentate-bridged binding motifs. The tridentate-bridged binding motif, which is reported here for the first time, plays a central role in the oxygen exchange mechanism on a defective anatase surface and activation of CO_2 on wet titania surfaces.

Zusammenfassung

Die Schwingungsspektroskopie von Gasphasenclustern in kryogenen Ionenfallen in Kombination mit quantenchemischen Berechnungen bietet eine ideale Methodik zur Untersuchung der Struktur-Reaktivitäts-Beziehungen von reinen wie auch bimetallic Oxidclustern als Funktion der Größe, des Ladungszustands und der Koordinationsumgebung. In den letzten Jahrzehnten hat die Charakterisierung von binären Metalloxid-nanomaterialien besondere Aufmerksamkeit erhalten, vor allem weil katalytisch inaktive Materialien durch Dotierung mit einem zweiten Metall aktiviert werden können. Durch genau kontrollierte Bedingungen und das Fehlen störender Wechselwirkungen mit der Umgebung können Gasphasencluster als perfekte Modellsysteme für Nanomaterialien dienen. Darüber hinaus können die aktiven Stellen dieser reaktiven Zwischenprodukte anhand ihrer charakteristischen Schwingungsmoden eindeutig identifiziert werden. Solche Erkenntnisse ermöglichen es letztlich, die Reaktionsmechanismen, die an reaktiven Oberflächen in der heterogenen Katalyse ablaufen, auf molekularer Ebene zu verstehen.

Eisen ist die häufigste Verunreinigung in natürlich vorkommenden Zeolithen. Kleine atomar Fe-substituierte kleine Aluminiumoxid-cluster $[(Al_2O_3)_nFeO]^+$ dienen als Modellsystem für Fe-dotierte Zeolithe. Der Einfluss eines Fe-Atoms in einem Aluminiumoxid-netzwerk wird im Hinblick auf Strukturänderung und bevorzugte Koordinationsstellen in Kapitel 4 untersucht. Die Ergebnisse zeigen, dass das Fe-Atom bevorzugt eine Position im äußeren Ring des Clusters einnimmt und für den kleinsten untersuchten Cluster ($n=1$) eine wesentliche Änderung der Clusterstruktur induziert, was für die größeren Cluster nicht der Fall ist. Darüber hinaus ist mit zunehmender Clustergröße eine strukturelle Entwicklung von planar ($n=1$) über quasi-2D ($n=2$) zu Käfigstrukturen ($n \geq 3$) zu beobachten. Die Erkenntnisse korrelieren mit Ergebnissen, die für Fe-dotierte Nanopartikel und Nanokristalle berichtet wurden, nach denen Fe-Atome meist als Ersatz für unterkoordinierte Oberflächen-Al-Atome des Al_2O_3 -Netzwerks gefunden wurden.

In Kapitel 5 wird die aktiv Stelle, an der die Sauerstoffatomtransferreaktion (oxygen atom transfer - OAT) an heteronuklearen Metalloxid-clustern abläuft, identifiziert. Die radikalischen Kationen $[AlVO_{x=3,4}]^{\bullet+}$ und $[VPO_{x=3,4}]^{\bullet+}$ werden im Zusammenhang mit der Umwandlung von CO zu CO_2 (Kapitel 5.1) bzw. der Oxidation von Ethylen zu Formaldehyd (Kapitel 5.2) untersucht. In beiden Fällen nimmt das an das Hauptgruppenatom (Al oder P) gebundene Sauerstoffatom am OAT-Zyklus teil, wohingegen der am Übergangsmetallatom (V) gebundene Sauerstoff unbeteiligt bleibt.

Die in Kapitel 6 vorgestellten Ergebnisse zeigen, dass das sauerstoffarme Ti^{3+} -Zentrum, das ein Modellsystem für eine Sauerstofffehlstelle einer Titanoxidoberfläche darstellt, das aktive Zentrum für die CO_2 -Adsorption ist. Die ersten beiden CO_2 -Moleküle adsorbieren chemisch an $[Ti_3O_6]^-$ und bilden dabei asymmetrische zweizählig verbrückte und symmetrische dreizählig verbrückte Bindungsmotive.

Das hier erstmals berichtete dreizählig verbrückte Bindungsmotiv spielt eine zentrale Rolle beim Sauerstoffaustauschmechanismus auf einer defekthaltigen Anatasoberfläche sowie bei der Aktivierung von CO_2 auf feuchter Titandioxidoberfläche.

Contents

0. Abbreviations	xiii
1. Introduction	1
1.1. Metal Oxides.....	1
1.2. Gas Phase Clusters.....	3
1.3. Action Spectroscopy.....	4
1.4. Al/Fe- Mixed Metal Oxide.....	5
1.5. Active Site Characterization of $\text{VMO}_4^{\bullet+}$ (M=Al, P) Model Clusters.....	7
1.6. CO_2 Adsorption on Ti_3O_6^-	9
2. Infrared Spectroscopy	15
2.1. Theoretical Background.....	15
2.1.1. Infrared Spectra.....	17
2.1.2. Anharmonicity.....	18
2.2. Gas Phase IR Spectroscopy.....	20
2.3. Infrared Photodissociation Spectroscopy.....	20
3. Experimental Setup	25
3.1. Laser Vaporization Source.....	25
3.1.1. Laser Vaporization Source Used for This Thesis Work.....	26
3.2. Electrospray Ionisation Source.....	29
3.2.1. ESI Source Used for This Thesis Work.....	30
3.3. Tandem Mass Spectrometer.....	32
3.4. Detection Scheme and Data Acquisition.....	34
3.5. Infrared Light Sources.....	37
3.5.1. The FHI FEL.....	37
4. Al/Fe- Mixed Metal Oxide Clusters	41
4.1. Infrared Photodissociation Spectroscopy of $[(\text{Al}_2\text{O}_3)_n(\text{FeO})]^+$ with $n=2-5$: Influence of Fe-Impurities on Structure and Other Properties.....	41
5. Catalytic Active Site Characterization of Heteronuclear Metal Oxide Clusters	61
5.1. Experimental Identification of the Active Site in the Heteronuclear $[\text{AlVO}_x]^{\bullet+}/\text{CO}/\text{N}_2\text{O}$ ($x = 3, 4$) Redox Couples by Gas-Phase IR Spectroscopy.....	61
Supporting Information.....	69
5.2. Direct Identification of Acetaldehyde Formation and Characterization of the Active Site in the $[\text{VPO}_4]^{\bullet+}/\text{C}_2\text{H}_4$ Couple By Gas-Phase Vibrational Spectroscopy.....	77

Supporting Information.....	83
6. CO₂ Adsorption on Ti₃O₆⁻	89
6.1. CO ₂ Adsorption on Ti ₃ O ₆ ⁻ : A Novel Carbonate Binding Motif.....	89
Supporting Information.....	101
7. Conclusion and Outlook	117
7.1. Conclusion.....	117
7.2. Outlook.....	119
Appendix A	123
A.1. Supporting Information- Infrared Photodissociation Spectroscopy of [(Al ₂ O ₃) _n (FeO)] ⁺ with n=2-5: Influence of Fe-Impurities on Structure and Other Properties.....	123
Appendix B: Fe-Oxides	143
B.1. Structure and Reactivity of Mixed Valence Fe-Oxides, Fe ₃ O ₃ ⁺ and Fe ₄ O ₅ ⁺ : Towards Water.....	144
B.2. [Fe ₃ O ₄ (H ₂ O) _{n=0-4}] ⁺	146
Appendix C: Microhydration of Salts	149
C.1. Infrared Spectroscopic Snapshots of MgNO ₃ Solvation in Water: [MgNO ₃ •(H ₂ O) _n] ⁺	150
C.2. [Fe(OH)(Cl)•(H ₂ O) _n] ⁺	151
Acknowledgements	153
List of Publications	157
Talks and Conference Contributions	159
Curriculum Vitae	161

Abbreviations:

FHI-FEL	Fritz-Haber-Institute free electron laser
IRPD	Infrared single photon dissociation
IRMPD	Infrared multiple photon dissociation
MOF	Metal organic framework
DFT	Density functional theory
HR-TEM	High-resolution transmission electron microscopy
EXAFS	Extended X-Ray absorption fine structure
HAT	Hydrogen atom transfer
OAT	Oxygen atom transfer
ODH	Oxidative dehydrogenation
IVR	Intramolecular vibrational energy relaxation
FWHM	Full width at half maxima
OPO	Optical parametric oscillator
RF	Radio frequency
LAS	Laser ablation/vaporization source
ESI	Electrospray ionization
IS	Ion spray
EL	Einzel lense
RET	Ring electrode ion trap
TOF	Time-of-flight
QMS	Quadrupole mass spectra
TOF-MS	Time-of-flight mass spectra
HV	High voltage
CID	Collision induced dissociation
IR FEL	Infrared free electron laser
Linac	Linear accelerator
MIR	Mid infrared

Chapter 1

Introduction

Experimental gas phase studies on isolated metal oxide clusters with well-defined composition provide an ideal arena to explore their intrinsic physical and chemical properties. Precisely controlled experimental conditions and absence of perturbing interactions from the background allow gas phase cluster studies to achieve a high level of selectivity and sensitivity. Hence, metal oxide clusters in the gas phase can serve as potential model systems¹⁻⁴ to gain molecular level understanding of underlying reaction mechanism in heterogeneous catalysis⁵⁻⁷ together with active site characterization of the catalyst model. The central goal of the work presented in this thesis is the structure and reactivity characterization of pure- and mixed- metal oxide clusters, together with the identification of the clusters' active site, with the arsenal of modern spectroscopic and spectrometric techniques.

The experiments were performed using the free electron laser FHI-FEL (see section 3.5) at the Fritz-Haber-Institute of the Max-Planck-Society (Berlin, Germany). Most of the studies presented in this thesis were performed as part of the project D01 "Microhydrated metal oxide clusters in the gas phase: structure, stability, reactivity" within the framework of DFG funded Collaborative Research Center CRC1109, "Understanding of Metal Oxide/Water Systems at the Molecular Scale: Structural Evolution, Interfaces, and Dissolution" (2014 to 2018). The general goal of the CRC 1109 was to develop a detailed molecular level understanding of the structural evolution, aging and dissolution of metal oxides as a function of oxide complexity and water content.

The following sections describe why metal oxides are intriguing candidates to be studied, followed by a description of special aspects of gas phase cluster studies and action spectroscopy, and finally the motivation and open questions to be addressed by the particular studies presented in this thesis is discussed.

1.1. Metal Oxides

Modern technological development and advancement in material science is complementary to each other. Use of metal oxide based materials dates back as early as 1500 BC when the Egyptians used iron oxide (hematite)⁸ as pigment to produce red and yellow ink to write on papyrus.⁹ In modern days, metal oxide nanomaterials are of importance due to their versatile use in our everyday life, as heterogeneous catalysts,¹⁰ coatings,¹¹ catalyst support,^{12, 13} nano-sensors,¹⁴ biomedical applications,^{15, 16} magnetic materials,¹⁷ fuel cells¹⁸ and advanced energy materials.^{19, 20} Among the metal oxides iron, aluminium and titanium oxides are among the most abundant materials of the earth crust, and thus it is of great interest

to characterize their diverse properties such as redox activity, electrical, and thermal resistivity and chemical activity. A band gap of ~ 3.1 eV of TiO_2 makes it a suitable semiconductor to be used as photocatalyst, gas sensor, water splitting catalyst, photovoltaics or pigment. The use of these metal oxide nanostructures, perhaps in combination with doping, such as Fe-doped zeolites or transition metal doped TiO_2 , enhances the photoelectric properties and increases surface area for reaction.^{21, 22} In fact, mixed-metal organic-framework (MOF) or catalysts composed of multiple components (different metal centres), such as aluminosilicate MOFs,²³ VPO catalysts,^{24, 25} V/Ce mixed oxides²⁶ and so on, are used in contemporary heterogeneous catalysis.²⁷ As a result, despite of the low abundance of vanadium on earth, VPO catalysts are extensively used in chemical industries for large scale transformation of small hydrocarbons into value added products e.g. *n*-butane to maleic anhydride.²⁸⁻³⁰ It is also seen that VPO catalysts are more reactive towards oxidative dehydration (ODH) or oxygen atom transfer (OAT) reactions, with respect to pure vanadium oxides or phosphates.³¹

To understand the reactions occurring at metal oxide interfaces, to design functional building blocks for nanostructured materials or to enhance catalytic properties at the molecular surface, a fundamental insight into the structure and reactivity of the corresponding material is important. Although metal oxides have been investigated intensively in the past decades, the molecular level understanding of its structure and functionality is still incomplete. Moreover, despite of the vast use in industrial applications, a comprehensive mechanistic understanding of the elementary steps and an atomic scale understanding of the reactive sites of e.g. solid-state catalysts are still rather scarce. Thus, there remain many unanswered questions, e.g. what are the structural and electronic properties of the metal oxide nanoparticles? How do these properties influenced by increasing size of the nanocrystals? What are the active sites for the catalytic reaction? Which structural motif leads to a particularly high reactivity? What are the reactive intermediates? Therefore, highly selective and sensitive experimental techniques are needed, to characterize the particular surface structure and active sites.

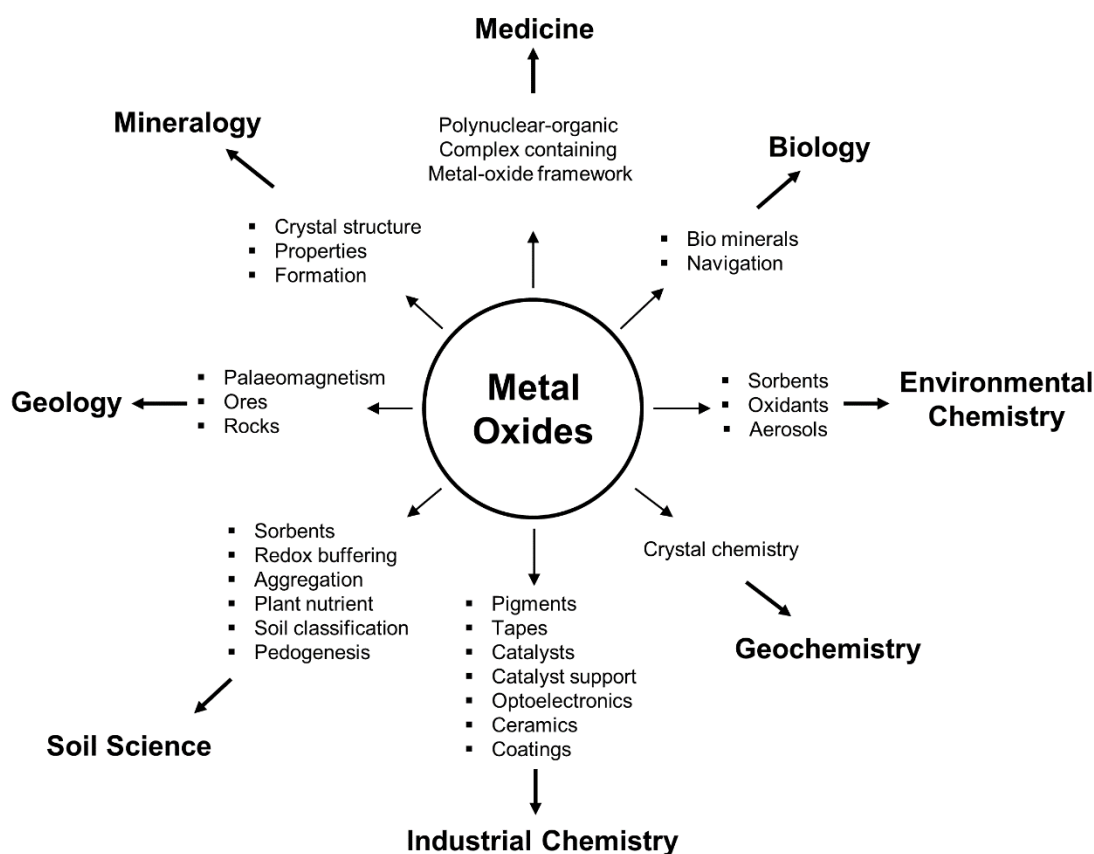


Figure 1.1: Versatile uses of metal oxides. Figure adapted from Ref.³²

1.2. Gas Phase Clusters

The term “cluster” has different meanings, depending on the discipline, i.e. in astronomy it represents a gravitationally bound group of stars, in computer science it stands for a set of computers which are connected with each other to work together and in the field of music and medicine cluster has yet another meaning. In the field of physics or chemistry (the topic of this thesis), “cluster” refers to an aggregate comprised of a countable number of atoms or molecules. Smaller clusters, with less than 100 atoms, are of particular interest because their properties typically lie in the *non-scalable* regime, i.e., they cannot be derived from the properties of bulk material by extrapolation.³³ For small gas phase clusters, at the size regime of a few tens of atoms, every single atom or molecule can have a significant effect on the cluster properties.³⁴⁻³⁶ Moreover, the structure and reactivity of the clusters can also change with the charge state. For example, $[(\text{Al}_2\text{O}_3)_4]^+$ is assigned to have an “arrowhead” shaped structure with a terminal Al-O bond, whereas its neutral analogue $[(\text{Al}_2\text{O}_3)_4]$ possess a complete different structure with 8m, 6m and 4m rings and more interestingly they both are different from the bulk structural motif of most stable polymorph of solid alumina i.e. $\alpha\text{-Al}_2\text{O}_3$ (corundum).³⁷ Another example can be given for Boron clusters i.e. for small cationic boron clusters, B_n^+ , 2D to 3D geometric transition occurs at $n=16$,³⁸ whereas for anionic clusters B_{38}^- and B_{40}^- are predicted

to be planar while B_{39}^- exhibit 3D structure which is proved by both theory and experiment.^{39, 40}

The combination of computational chemistry with experimental spectroscopic techniques brought gas phase cluster research to an elevated importance, because, they serve as an excellent model system to bridge the gap between atomic, molecular and condensed phase matter. With state-of-art experimental techniques it is difficult to directly probe the morphology of thin film or nanomaterial surfaces. Also, understanding of a detailed mechanism regarding the elementary steps of a catalytic reaction occurring at the surface remain unsolved due to, for example, surface reconstruction in presence of reactant molecules and difficulties in preparing reproducible surface. Here, gas phase cluster model systems play a crucial role for elucidating atomic level understanding of structure, dynamics and electronic properties of this intermediate form of matter. These valuable insights may help in deriving the properties of nanoclusters or nanoparticles.

The absence of perturbing interaction with an environment and control over solvation, aggregation, counter-ion and reactant ligand, allows a systematic characterization of cluster size, shape and structure together with understanding energetics, kinetics and dynamics of a chemical reaction at a molecular level.^{41, 42} Moreover, a systematic investigation of gas phase model clusters can shed new light on the understanding of structural evolution of clusters from atoms to bulk, O_2 transport and proton transfer reaction in biological systems,⁴³ different heterogeneous processes occurring at the atmosphere,⁴⁴ mechanism of catalytic reactions,⁴⁵ and even bond making-breaking type ultrafast processes.⁴⁶

High level quantum chemical calculations using density functional theory (DFT) or wave function based theory (MP2 or CCSD(T)) are capable of providing nearly accurate and often quantitative information on physical and chemical properties such as ionization potentials, electron affinities, HOMO – LUMO gaps, dissociation energies, solvation energies, and vibrational frequencies of the studied clusters. Comparison of these predicted properties with the experimental results allow for testing of different computational models and benchmarking these methods in the context of e.g. electron localization at defect sites, energetic ordering of various isomers and spin states, or understanding larger and more complex systems.

1.3. Action Spectroscopy

Various mass spectrometric approaches can be used to study gas phase cluster's composition and its structure/reactivity relationship. However, to gain unambiguous insight concerning structure, shape and reactive center of a particular cluster, a spectroscopic approach is necessary. High resolution experimental techniques used for the characterization of condensed phase materials often cannot be adopted for gas phase studies simply because the sample lacks the needed degree of structural order and required number density. Moreover, direct IR absorption spectroscopy relies on the attenuation of light intensity upon interaction with the molecules and a

minimum $\sim 10^{10}$ molecules/cm³ number density is prerequisite to acquire a absorption spectrum.⁴⁷ Whereas, for the experimental scenarios presented in this thesis, the maximum attainable ion densities are on the order of $< 10^8$ ions/cm³ limited by the space charge effect,⁴⁷⁻⁴⁹ restricting application of the direct absorption technique. An alternative experimental approach, so-called action spectroscopy⁵⁰ has been developed to overcome these limitations. Here, the absorption of photons is indirectly measured by the response of the ions upon interaction with light, i.e. change in charge state, quantum state or change in mass.^{51, 52}

A number of action spectroscopy techniques, for example, laser-induced fluorescence spectroscopy, anion photoelectron spectroscopy have been used for the systematic characterization of structure and other properties of isolated metal oxide clusters. However, Infrared photodissociation (IRPD) spectroscopy (see section 2.3 for details) of cryogenically cooled mass and charge selected ions is arguably the most powerful and widely applied action spectroscopic technique in present days and was used for the characterization of gas phase clusters in this thesis. This technique works with measuring the extent of photodissociation yield of the ions as a function of photon energy. An intense and widely tunable free electron laser, the FHI-FEL (see chapter 3.5), was used here as the light source. Cryogenic ion trapping under multiple collision conditions ensures that the molecules reach their vibrational ground state and facilitates messenger complex formation.⁵³⁻⁵⁷ Moreover, the possibility of appearance of anharmonic effects such as hot bands, combination bands, and spectral congestions due to high internal energy are reduced by cryogenic cooling of the ions of interest.

As the experimentally measured IRPD spectrum is in general linear to the number of absorbed photons (see section 2.3 for more details), thus the linear vibrational spectra derived from quantum chemical calculations are often in quite good agreement with it. Hence, interpretation of the experimental spectra usually carried out by comparing them with the theoretical spectra, which facilitates unambiguous assignment of the geometric structure. Although, combination of experiment and theory has proven extremely powerful over the last two decades in explicit identification of structural properties of small ionic clusters,⁴¹ the unambiguous identification of the global minimum energy structure of a complex potential energy surface remains challenging and the difficulty increases by many fold with the inclusion of transition metal atoms. Open d-shell of the d-block elements results in a shallow potential energy surface and brings the possibility of energetically close lying isomer formation with different spins, making the structural assignment arduous. Choice of smaller clusters is advantageous where high level quantum chemical calculations need to be performed.

1.4. Al/Fe- Mixed Metal Oxide

Oxides of Al, Fe and Si are ubiquitous in nature. They are present with highest weight percentage on earth crust (46.6% oxygen, 27.7% silicon, 8.1% aluminium and 5% iron). Zeolites, microporous crystalline solid aluminosilicates, have attracted

attention as nanomaterials for catalytic studies and other technological applications. They contain cavities and channels in their framework thus often they are called molecular sieves. Furthermore, the presence of these cavities makes them nearly perfect adsorbents and prone to catalytic activity. Iron is eventually the most common impurity in naturally occurring zeolites. Atomic Fe- impurities into small Al- oxide clusters represent a perfect model system for Fe- doped zeolite molecular sieve. The influence of Fe- atom on small Al-oxides, regarding structure and other properties is studied as a part of this thesis and presented in chapter 4 (a manuscript under preparation). The project is performed in close-collaboration with the group of Prof. Joachim Sauer (Humboldt University Berlin). They apply genetic algorithm method and state-of-the-art quantum chemical techniques to explore complex potential energy surfaces in order to find global and local minimum energy structures and compute their vibrational spectra.

Zeolites appear naturally with 40 different types,⁵⁸ however, a large number of synthetic zeolites are also produced industrially. Research on zeolites is of particular interest because they are cheap, non-hazardous and can afford higher selectivity. Their multidisciplinary applications are briefly described as follows: a) the cation exchange property is used in water softening, heavy metal containing waste water cleaning, detergent production, filter for odor control, toxin removal and drug delivery,⁵⁹ b) the specific cavity size is used in designing site selective catalyst in acid or metal-catalysed reaction; also they are used in production of Caprolactam and NO_x removal agent for diesel vehicles,^{60, 61} c) zeolite crystals are used in chromatographic separation process considering varied interaction of the adsorbent with the surface; the shape-selective property is executed for their use in molecular adsorption processes,⁶⁰ d) hydrophobic silica zeolites absorb organic solvents, whereas cation-containing zeolites used as desiccants owing to high water affinity.

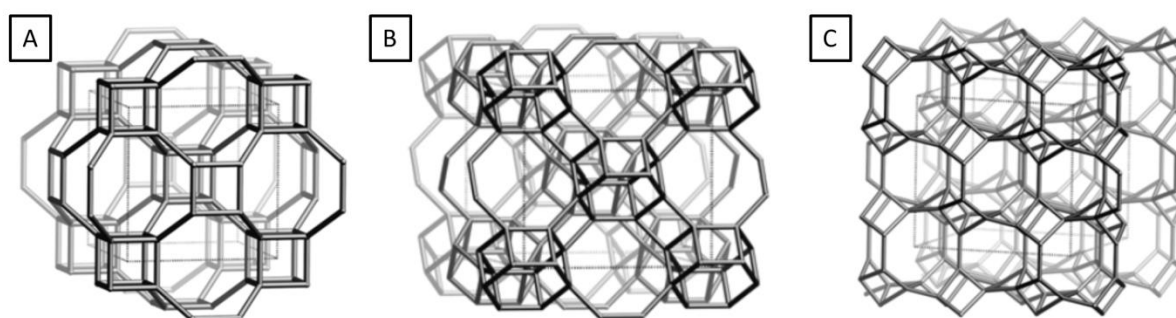


Figure 1.2: Different crystal structures of zeolites, A) Cubic B) Orthorhombic C) Monoclinic. All of them contain three- and four- fold coordinated Al- atom, similar to the studied clusters. (figures taken from Ref.⁵²)

Interestingly, it is now experimentally proved that not the Al-O units but the transition metal impurities present in zeolites are actually the active sites for the photochemical reactions²². Moreover, $[\text{Fe}^{2+}\text{-O}]^*$ moiety present in the zeolite network is characterized as the charge transfer excited state, which promotes the reactivity, in particular,

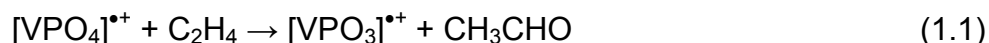
photocatalytic reduction of CO₂ with H₂O;⁶² photocatalytic oxidation of organic molecules like ethylene, bromomethane and methyl orange,⁶³ and oxidation of benzene to phenol.⁶⁴ Despite of these experimental advancements, a molecular level understanding about the nature of the charge transfer excited state or the active site is still missing.

IRPD spectroscopy of gas phase metal oxide clusters in combination with quantum chemical calculations can provide significant insight into the structure – reactivity correlation. Here, within the scope of this thesis I studied Al/Fe –mixed metal oxide clusters as a function of cluster size; and tried to answer the following questions: How does the structure and geometry of the binary metal oxide clusters evolve with increasing cluster size? How does the structural motif of the binary metal oxides compare with the pure (mono metallic) metal oxide clusters? What is the preferential coordination site for the Fe-atom? What is the preferred oxidation state and coordination environment of the dopant Fe-atom? How does the nature of active site (oxygen deficient Fe-atom) correlate with the cluster size?

1.5. Active Site Characterization of VMO₄^{•+} (M=Al, P) Model Clusters

Chapter 5.1 presents the experimental identification of the active site in the [AlVO_x]^{•+}/CO/N₂O (x=3,4) heteronuclear redox couple. The reduction of [AlVO₄]^{•+} to [AlVO₃]^{•+} in presence of CO (reaction efficiency 59%) and re-oxidation process in presence of N₂O (reaction efficiency 65%) was studied with mass spectrometry by Schwarz *et al.*⁶⁵ DFT calculations on the reaction mechanism predicted not the V-O_t unit but the Al-O_t is involved in the OAT reaction cycle. However, the experimental verification for this prediction was missing. To this end, in collaboration with the group of Prof. H. Schwarz (TU Berlin, Germany), the active site of the above mentioned catalytic cycle is experimentally verified. The experiments are performed at the FHI Berlin using the FHI-FEL. Theoretical support is provided by the Schwarz group. This study is published in the *Angewandte Chemie International Edition* and selected as a very important article (top 5%).^{66, 67}

In a similar experimental fashion, the active site of the [VPO₄]^{•+} model catalyst involved in reaction (i) is identified, and presented in Chapter 5.2.



The structural characterization of gas phase [VPO₄]^{•+} and reactivity towards small hydrocarbons was previously reported by Schwarz *et al.*³¹ Collision induced dissociation (CID) studies show that the [VPO₄]^{•+} can undergo OAT reaction with ethylene to form [VPO₃]^{•+} and acetaldehyde. DFT calculations predict that the phosphate atom favours to attain lower oxidation state (P^{+III} over P^{+V}), thus the OAT reaction proceeds via breaking of the/a P-O_t unit not via the/a V-O_t unit. What was missing so far is the experimental verification of the theoretical prediction and unambiguous assignment of reaction products and intermediates. In a collaborative work with the group of Prof. Helmut Schwarz (TU Berlin, Germany), the theoretical

prediction of the active site is verified and more interestingly, the neutral CH_3CHO formed by the OAT reaction is spectroscopically identified. This study is published in the *Angewandte Chemie International Edition*.⁶⁸

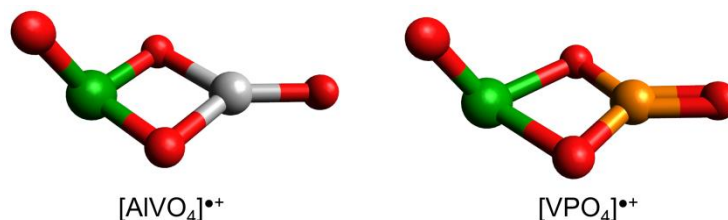


Figure 1.3: Structure of $[\text{AlVO}_4]^{\bullet+}$ and $[\text{VPO}_4]^{\bullet+}$ from B3LYP /def2TZVP calculations. V= green, Al= grey, P= yellow, O= red. (Structures are taken from Ref.^{66,31} respectively).

Catalytic conversion of environmentally noxious gases, produced from fossil fuel combustion, into value added chemicals using cost effective and environmentally benign pathways are one of the major focuses of contemporary natural sciences to solve global problems such as climate change. Development of metal-based catalysts started in the early 70s and has undergone a significant evolution over the past three decades. However, more research conducted on monometallic-oxides than that of mixed metal oxides, due to increased complexity induced by addition of a second metal atom.⁶⁹ Recent advancements in surface science techniques such as HR-TEM and EXAFS have enabled access to bulk and surface properties of mixed metal oxide catalysts. These studies are intriguing in particular because of the multiscale nature of the catalysts. Their oxidation state, structure termination and composition of surface are different than that of bulk lattice. These properties are dependent on their local environments and more interestingly, chemical and physical properties of mixed metal-oxides differ significantly than that of monometallic-oxides.⁷⁰⁻⁷³ Nonetheless, variable local coordination, different surface termination functionalities, coexisting bulk and surface phases make it difficult to get a molecular level understanding of structure, growth and active sites of the catalysts in condensed phase. Moreover, few predictions from surface studies were questioned by gas phase experiments. For example, in the catalytic conversion of *n*-butane to maleic acid with VPO-catalyst, the phosphate center was said to be catalytically inert,⁷⁴ however, it was showed with gas phase experiments that $[\text{P}_4\text{O}_{10}]^{\bullet+}$ is efficient to activate methane at ambient condition.⁷⁵ These limitations and conflicts calls for model system studies to get unambiguous insight about the intrinsic chemical and physical properties of catalytic active sites involved in selective oxidation process of heterogeneous catalysis.

Looking at the underlying mechanisms, the selective oxidation with metal oxides can be categorized in three general terms: 1) hydrogen-atom transfer (HAT), 2) oxygen-atom transfer (OAT) and 3) oxidative dehydrogenation (ODH).³¹ A number of gas phase spectrometric and spectroscopic studies have been reported in last decades

to investigate heteronuclear metal oxide catalysts such as $[Al_xV_yO_z]^{+/-}$ ($x + y=2, 3, 4$; $z= 3-10$),^{76, 77} $[Ce_xV_yO_z]^{+/-}$ ($x + y=2, 3$; $z=4, 5, 6$),⁷⁸ $[(V_2O_5)_x(SiO_2)_y]^{+/-}$ ($x=1, 2$; $y= 1-4$),^{79, 80} $[V_xP_{4-x}O_{10}]^{*+}$ ($x=1-3$),^{81, 82} and other VPO-catalysts.³¹ VPO-catalysts are of particular interest because despite of being electronically and structurally similar and having analogous terminal oxygen centered radical, $[V_4O_{10}]^{*+}$ facilitates OAT & ODH reactions, whereas, $[P_4O_{10}]^{*+}$ promotes HAT reaction with ethane, propane and ethylene, even interestingly both of the monometallic oxides gives rise to thermal H-atom abstraction from methane in a similar way.⁸³ The above mentioned exciting oxidation reactivity of the heteronuclear metal-oxides suggests a more systematic investigation to uncover the underlying mechanisms at atomistic level, also to identify the explicit active site in the metal oxide clusters.

I used gas phase cryogenic infrared spectroscopy in combination with quantum chemical calculations, to unambiguously characterize the structure and active site of VMO_4^+ ($M=Al, P$) catalytic model systems. The results give significant insight for the understanding of the associated reaction mechanism as a part of a more complex catalytic cycle.

1.6. CO_2 Adsorption on $Ti_3O_6^-$

Increasing concentration of CO_2 in the atmosphere is a colossal threat to humanity in the 20th century, because the released CO_2 acts like a blanket, preventing heat to escape and the evident impact is climate change. CO_2 causes about 20% of earth's greenhouse effect; however, it has other indirect effects leading to increase in average global temperature. On the other hand, a large amount of CO_2 released by humans get dissolved into the ocean, reflected in increased acidity of sea water and sets the life of marine animals and plants in danger. Hence, it is important to find efficient methods for the conversion of atmospheric CO_2 into value-added products.^{84, 85} Ti-oxide based materials have been undoubtedly accepted as environmentally benign, cost effective and most promising candidates for CO_2 capture and conversion. CO_2 adsorption on titania-surfaces have been mainly studied on the basis of chemi- vs physisorption, i.e. formation of carbonate and bicarbonate vs binding of CO_2 to a metal center, and the binding efficiency is mainly characterized with the Lewis acidity and basicity of the active sites.⁸⁶⁻⁸⁹

$(TiO_2)_n^-$ ($n=3-8$) has been studied earlier in our group. There, structural evolution of the studied clusters is discussed with increasing cluster size and the effect of an excess negative charge on the clusters is characterized.⁹⁰ This is important in particular because the photocatalytic reduction of CO_2 on bulk-titania proceeds via the transfer of a photoexcited electron first to the surface followed by transfer to the adsorbate.⁹¹ So, negatively charged TiO_2 clusters can in principle be considered as model systems to understand the photocatalytic behaviour at titania-surface and to unambiguously characterize the underlying reaction mechanism at atomic resolution. Moreover, the afore mentioned study on $(TiO_2)_n^-$ ($n=3-8$) revealed that the studied Ti-oxide clusters mainly consists of four-fold coordinated Ti^{4+} and three-fold coordinated Ti^{3+} centres, and the later carries the excess negative charge which represents the

oxygen vacancy defect site on surface. Many surface studies showed that the water- or CO_2 - adsorption reaction on titania-surface is initiated at these defect sites.⁹² Water adsorption on $[(\text{TiO}_2)_n(\text{D}_2\text{O})_m]^-$ ($n=2-4$ and $m=1-3$) clusters was also investigated by our group as a follow-up of the previous experiment, and dissociative adsorption of water molecule is seen in every case.⁹²

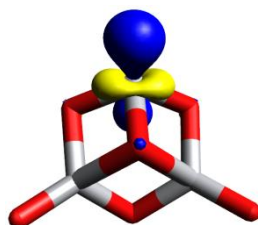


Figure 1.4: Spin density plot of the singly occupied molecular orbital in the Ti_3O_6^- anion from $\omega\text{B97XD}/\text{aug-cc-pVTZ}$ calculations. The unpaired electron is localized at the under coordinated Ti^{3+} center. Al= grey, O= red.

The main goals of the experimental study presented in chapter 6 is: a) to gain a molecular level understanding of the CO_2 adsorption mechanism on negatively charged titania surface, b) identifying different CO_2 binding motif on TiO_2 , c) elucidation of vibrational signatures of characteristic binding motifs in the vicinity of oxygen-vacancy defect sites. This study is published in the *Journal of Physical Chemistry C*.^{93, 94} Ti_3O_6^- cluster was carefully chosen for the study as it is the smallest model system in the $(\text{TiO}_2)_n^-$ group which consists of two Ti^{4+} and one Ti^{3+} centre, and the latter contains the excess electron, which in principle can be donated to a π -acceptor ligand, such as CO_2 .

References:

1. K. Asmis, M. Brümmer, C. Kaposta, G. Santambrogio, G. Von Helden, G. Meijer, K. Rademann and L. Wöste, *Physical Chemistry Chemical Physics*, 2002, **4**, 1101-1104.
2. K. R. Asmis and J. Sauer, *Mass spectrometry reviews*, 2007, **26**, 542-562.
3. K. R. Asmis, A. Fielicke, G. von Helden and G. Meijer, *The Chemical Physics of Solid Surfaces*, 2007, **12**, 327-375.
4. M. Brümmer, C. Kaposta, G. Santambrogio and K. R. Asmis, *The Journal of chemical physics*, 2003, **119**, 12700-12703.
5. A. W. Castleman, *Catalysis letters*, 2011, **141**, 1243.
6. D. Schröder and H. Schwarz, *Angewandte Chemie International Edition in English*, 1995, **34**, 1973-1995.
7. J. Roithova and D. Schroder, *Chemical reviews*, 2010, **110**, 1170-1211.
8. T. Christiansen, D. Buti, K. N. Dalby, P. E. Lindelof, K. Ryholt and A. Vila, *Journal of Archaeological Science: Reports*, 2017, **14**, 208-219.
9. *Journal*, 2010.
10. N. R. Shiju and V. V. Guliants, *Applied Catalysis A: General*, 2009, **356**, 1-17.
11. E. E. Chain, *Appl. Opt.*, 1991, **30**, 2782-2787.
12. I. E. Wachs, *Catalysis Today*, 2005, **100**, 79-94.
13. M. A. Bañares, *Catalysis Today*, 1999, **51**, 319-348.
14. R. Bogue, *Sensor Review*, 2009, **29**, 310-315.

15. J. Gao, H. Gu and B. Xu, *Accounts of Chemical Research*, 2009, **42**, 1097-1107.
16. S.-H. Huang and R.-S. Juang, *Journal of Nanoparticle Research*, 2011, **13**, 4411.
17. R. Kodama, *Journal of magnetism and magnetic materials*, 1999, **200**, 359-372.
18. J. Garcia-Barriocanal, A. Rivera-Calzada, M. Varela, Z. Sefrioui, M. R. Díaz-Guillén, K. J. Moreno, J. A. Díaz-Guillén, E. Iborra, A. F. Fuentes, S. J. Pennycook, C. Leon and J. Santamaria, *ChemPhysChem*, 2009, **10**, 1003-1011.
19. A. Weidenkaff, R. Robert, M. H. Aguirre, L. Bocher and L. Schlapbach, *physica status solidi (RRL) – Rapid Research Letters*, 2007, **1**, 247-249.
20. M. Zäch, C. Häggglund, D. Chakarov and B. Kasemo, *Current Opinion in Solid State and Materials Science*, 2006, **10**, 132-143.
21. S. A. Shevlin and S. M. Woodley, *The Journal of Physical Chemistry C*, 2010, **114**, 17333-17343.
22. M. Matsuoka and M. Anpo, *Journal of Photochemistry and Photobiology C: Photochemistry Reviews*, 2003, **3**, 225-252.
23. R. A. Van Santen and M. Neurock, *Molecular heterogeneous catalysis: a conceptual and computational approach*, John Wiley & Sons, 2009.
24. P. Borah, A. Datta, K. T. Nguyen and Y. Zhao, *Green Chemistry*, 2016, **18**, 397-401.
25. M. a. J. Lorences, G. S. Patience, F. V. Díez and J. Coca, *Applied Catalysis A: General*, 2004, **263**, 193-202.
26. J. Lu, M. Luo, H. Lei, X. Bao and C. Li, *Journal of Catalysis*, 2002, **211**, 552-555.
27. R. Schlögl, *Topics in Catalysis*, 2011, **54**, 627.
28. G. J. Hutchings, *Journal of Materials Chemistry*, 2004, **14**, 3385-3395.
29. J.-M. M. Millet, *Topics in Catalysis*, 2006, **38**, 83-92.
30. Y. H. Taufiq-Yap, C. K. Goh, G. J. Hutchings, N. Dummer and J. Bartley, *Catalysis Letters*, 2009, **130**, 327-334.
31. N. Dietl, T. Wende, K. Chen, L. Jiang, M. Schlangen, X. Zhang, K. R. Asmis and H. Schwarz, *Journal of the American Chemical Society*, 2013, **135**, 3711-3721.
32. R. M. Cornell and U. Schwertmann, *The iron oxides: structure, properties, reactions, occurrences and uses*, John Wiley & Sons, 2003.
33. W. A. de Heer, *Reviews of Modern Physics*, 1993, **65**, 611-676.
34. B. K. R. P. Jena, S. N. Khanna, *Physics and Chemistry of Small Clusters* Springer, Boston, MA, 1987.
35. H. Haberland, *Clusters of Atoms and Molecules*, Springer, Berlin, Heidelberg, 1994.
36. A. W. CASTLEMAN and R. G. KEESEE, *Science*, 1988, **241**, 36-42.
37. M. Sierka, J. Döbler, J. Sauer, G. Santambrogio, M. Brümmer, L. Wöste, E. Janssens, G. Meijer and K. R. Asmis, *Angewandte Chemie International Edition*, 2007, **46**, 3372-3375.
38. E. Oger, N. R. M. Crawford, R. Kelting, P. Weis, M. M. Kappes and R. Ahlrichs, *Angewandte Chemie International Edition*, 2007, **46**, 8503-8506.
39. S. Li, Z. Zhang, Z. Long, G. Sun and S. Qin, *Scientific Reports*, 2016, **6**, 25020.
40. Q. Chen, W.-L. Li, Y.-F. Zhao, S.-Y. Zhang, H.-S. Hu, H. Bai, H.-R. Li, W.-J. Tian, H.-G. Lu, H.-J. Zhai, S.-D. Li, J. Li and L.-S. Wang, *ACS Nano*, 2015, **9**, 754-760.
41. H. Schwarz and K. R. Asmis, *Chemistry – A European Journal*, 2019, **25**, 2112-2126.
42. K. R. Asmis, *Physical Chemistry Chemical Physics*, 2012, **14**, 9270-9281.
43. P.-Y. Cheng, J. S. Baskin and A. H. Zewail, *Proceedings of the National Academy of Sciences*, 2006, **103**, 10570-10576.
44. W. Klemperer and V. Vaida, *Proceedings of the National Academy of Sciences*, 2006, **103**, 10584-10588.
45. G. A. Somorjai, A. M. Contreras, M. Montano and R. M. Rioux, *Proceedings of the National Academy of Sciences*, 2006, **103**, 10577-10583.
46. V. Bonačić-Koutecký, R. Mitrić, U. Werner, L. Wöste and R. S. Berry, *Proceedings of the National Academy of Sciences*, 2006, **103**, 10594-10599.
47. M. R. Fagiani, PhD Thesis, Freie Universität Berlin, 2017.

48. D. Gerlich, *State-Selected and State-to-State Ion-Molecule Reaction Dynamics. Part 1: Experiment*, 1992, **82**.
49. D. J. Goebbert, G. Meijer and K. R. Asmis, *AIP Conference Proceedings*, 2009, **1104**, 22-29.
50. R. Setlow, *Adv. Biol. Med. Phys.*, 1957, **5**, 37-74.
51. M. A. Duncan, *International Journal of Mass Spectrometry*, 2000, **200**, 545-569.
52. E. J. Bieske and J. P. Maier, *Chemical Reviews*, 1993, **93**, 2603-2621.
53. N. Heine and K. R. Asmis, *International Reviews in Physical Chemistry*, 2015, **34**, 1-34.
54. N. Heine and K. R. Asmis, *International Reviews in Physical Chemistry*, 2016, **35**, 507-507.
55. M. Brümmer, C. Kaposta, G. Santambrogio and K. R. Asmis, *The Journal of Chemical Physics*, 2003, **119**, 12700-12703.
56. K. R. Asmis, M. Brümmer, C. Kaposta, G. Santambrogio, G. von Helden, G. Meijer, K. Rademann and L. Wöste, *Physical Chemistry Chemical Physics*, 2002, **4**, 1101-1104.
57. Y. S. Wang, C. H. Tsai, Y. T. Lee, H. C. Chang, J. C. Jiang, O. Asvany, S. Schlemmer and D. Gerlich, *The Journal of Physical Chemistry A*, 2003, **107**, 4217-4225.
58. C. Baerlocher, L. B. McCusker and D. H. Olson, *Atlas of zeolite framework types*, Elsevier, 2007.
59. R. P. Townsend and E. N. Coker, in *Studies in Surface Science and Catalysis*, eds. H. van Bekkum, E. M. Flanigen, P. A. Jacobs and J. C. Jansen, Elsevier, 2001, vol. 137, pp. 467-524.
60. M. Guisnet and J.-P. Gilson, *Zeolites for cleaner technologies*, Imperial College Press London, 2002.
61. J. Weitkamp and L. Puppe, *Catalysis and zeolites: fundamentals and applications*, Springer Science & Business Media, 2013.
62. Y. Tong, Y. Zhang, N. Tong, Z. Zhang, Y. Wang, X. Zhang, S. Zhu, F. Li and X. Wang, *Catalysis Science & Technology*, 2016, **6**, 7579-7585.
63. G. Yan, X. Wang, X. Fu and D. Li, *Catalysis Today*, 2004, **93-95**, 851-856.
64. G. I. Panov, G. A. Sheveleva, A. S. Kharitonov, V. N. Romannikov and L. A. Vostrikova, *Applied Catalysis A: General*, 1992, **82**, 31-36.
65. Z.-C. Wang, N. Dietl, R. Kretschmer, T. Weiske, M. Schlangen and H. Schwarz, *Angewandte Chemie International Edition*, 2011, **50**, 12351-12354.
66. S. Debnath, H. Knorke, W. Schöllkopf, S. Zhou, K. R. Asmis and H. Schwarz, *Angewandte Chemie International Edition*, 2018, **57**, 7448-7452.
67. S. Debnath, H. Knorke, W. Schöllkopf, S. Zhou, K. R. Asmis and H. Schwarz, *Angewandte Chemie*, 2018, **130**, 7570-7574.
68. Y.-K. Li, S. Debnath, M. Schlangen, W. Schöllkopf, K. R. Asmis and H. Schwarz, *Angewandte Chemie International Edition*, 2019, **58**, 18868-18872.
69. I. E. Wachs, *Catalysis Today*, 2005, **100**, 79-94.
70. V. V. Guliyants, J. B. Benziger, S. Sundaresan, N. Yao and I. E. Wachs, *Catalysis Letters*, 1995, **32**, 379-386.
71. H. Bluhm, D. F. Ogletree, C. S. Fadley, Z. Hussain and M. Salmeron, *Journal of Physics: Condensed Matter*, 2002, **14**, L227-L233.
72. A. Knop-Gericke, F. de Groot, J. van Bokhoven and T. Ressler, *In Situ Spectroscopy of Catalysts*, American Scientific Publishers, California, 2004, 145-160.
73. B. M. Weckhuysen, 2004.
74. T. Blasco and J. M. L. Nieto, *Applied Catalysis A: General*, 1997, **157**, 117-142.
75. N. Dietl, M. Engeser and H. Schwarz, *Angewandte Chemie*, 2009, **121**, 4955-4957.
76. Z.-C. Wang, X.-N. Wu, Y.-X. Zhao, J.-B. Ma, X.-L. Ding and S.-G. He, *Chemical Physics Letters*, 2010, **489**, 25-29.
77. Z. C. Wang, X. N. Wu, Y. X. Zhao, J. B. Ma, X. L. Ding and S. G. He, *Chemistry—A European Journal*, 2011, **17**, 3449-3457.
78. L. Jiang, T. Wende, P. Claes, S. Bhattacharyya, M. Sierka, G. Meijer, P. Lievens, J. Sauer and K. R. Asmis, *The Journal of Physical Chemistry A*, 2011, **115**, 11187-11192.
79. X. L. Ding, Y. X. Zhao, X. N. Wu, Z. C. Wang, J. B. Ma and S. G. He, *Chemistry—A European Journal*, 2010, **16**, 11463-11470.

80. Y.-X. Zhao, X.-N. Wu, J.-B. Ma, S.-G. He and X.-L. Ding, *The Journal of Physical Chemistry C*, 2010, **114**, 12271-12279.
81. J.-B. Ma, X.-N. Wu, X.-X. Zhao, X.-L. Ding and S.-G. He, *Physical Chemistry Chemical Physics*, 2010, **12**, 12223-12228.
82. N. Dietl, R. F. Höckendorf, M. Schlangen, M. Lerch, M. K. Beyer and H. Schwarz, *Angewandte Chemie*, 2011, **123**, 1466-1470.
83. N. P. R. Dietl, *Journal*, 2013.
84. S. N. Habisreutinger, L. Schmidt-Mende and J. K. Stolarczyk, *Angewandte Chemie International Edition*, 2013, **52**, 7372-7408.
85. S. Civiš, M. Ferus, A. Knížek, P. Kubelík, L. Kavan and M. Zukalová, *Optical Materials*, 2016, **56**, 80-83.
86. G. Martra, *Applied Catalysis A: General*, 2000, **200**, 275-285.
87. L.-F. Liao, C.-F. Lien, D.-L. Shieh, M.-T. Chen and J.-L. Lin, *The Journal of Physical Chemistry B*, 2002, **106**, 11240-11245.
88. L. Mino, G. Spoto and A. M. Ferrari, *The Journal of Physical Chemistry C*, 2014, **118**, 25016-25026.
89. H. He, P. Zapol and L. A. Curtiss, *The Journal of Physical Chemistry C*, 2010, **114**, 21474-21481.
90. M. L. Weichman, X. Song, M. R. Fagiani, S. Debnath, S. Gewinner, W. Schöllkopf, D. M. Neumark and K. R. Asmis, *The Journal of Chemical Physics*, 2016, **144**, 124308.
91. S. N. Habisreutinger, L. Schmidt-Mende and J. K. Stolarczyk, *Angewandte Chemie International Edition*, 2013, **52**, 7372-7408.
92. M. L. Weichman, S. Debnath, J. T. Kelly, S. Gewinner, W. Schöllkopf, D. M. Neumark and K. R. Asmis, *Topics in Catalysis*, 2018, **61**, 92-105.
93. S. Debnath, X. Song, M. R. Fagiani, M. L. Weichman, M. Gao, S. Maeda, T. Taketsugu, W. Schöllkopf, A. Lyalin, D. M. Neumark and K. R. Asmis, *The Journal of Physical Chemistry C*, 2019, **123**, 8439-8446.
94. S. Debnath, X. Song, M. R. Fagiani, M. L. Weichman, M. Gao, S. Maeda, T. Taketsugu, W. Schöllkopf, A. Lyalin, D. M. Neumark and K. R. Asmis, *The Journal of Physical Chemistry C*, 2020, **124**, 6952-6953.

Chapter 2

Infrared Spectroscopy

Infrared (IR) spectroscopy is the analysis of IR radiation, interacting with matter in the gas, liquid or solid phase. In absorption IR spectroscopy, an IR photon excites a vibrational mode of the sample when energy of the photon is in resonance with the frequency of the mode. Typically, an IR spectrum is generated by plotting absorbance (or transmittance) of the IR light as a function of its wavenumber and the IR signatures are commonly called as IR bands. Intensity of the IR band of an IR-active transition is directly proportional to the dipole moment difference between the initial and final state of the functional group upon IR excitation (see section 2.1.1). The electric dipole moment of a chemical bond is typically a measure of the bond's polarity within a molecule and higher the electronegativity difference of the connected atoms, higher is the polarity, consequently higher dipole moment. For homonuclear diatomic molecules like D_2 , N_2 , O_2 etc., there is no electronegativity difference of the connected atoms. As a result, transition to a higher vibrationally excited state is forbidden and they are called as IR inactive molecules.

In this chapter, first the theoretical background of gas phase vibrational spectroscopy will be summarized, followed by general description of gas phase action spectroscopy with particular focus on infrared multiple photon dissociation (IRMPD) and infrared vibrational predissociation (IRVPD) spectroscopy.

2.1. Theoretical Background

A molecular vibration is defined as a periodic oscillation of atoms of the molecule about their equilibrium position.¹ Generally, molecular vibrations can be categorized into two major types, stretching and bending, besides, there are also deformation and ring breathing modes. Non-linear polyatomic molecules with N number of atoms have $(3N - 6)$ and linear molecules have $(3N - 5)$ vibrational degrees of freedom or vibrational modes. To understand these vibrational modes, we will first look into an example of a diatomic molecule and then extend the insights to the context of polyatomic ones. The vibrational motion of a chemical bond within a molecule can be approximated as a harmonic oscillator and treated with the ball-and-spring model (Fig. 2.1).

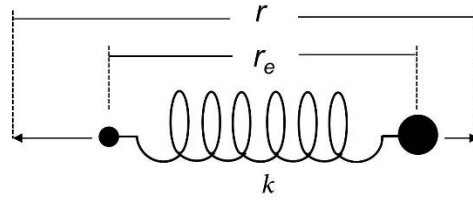


Figure 2.1: Vibration of a heteronuclear diatomic molecule depicted with ball-and-spring model. Here, r_e is the equilibrium length of the spring, $(r-r_e)$ the displacement along the axis and k the force constant of the spring. Figure adapted from Ref.²

From classical mechanics, the restoring force F of the spring follows Hooke's law:

$$F = -\frac{dV(x)}{dx} = -kx \quad , \quad (2.01)$$

where, V is the potential energy, k the force constant of the spring, and x equal to $(r-r_e)$ i.e. the displacement from the equilibrium bond length r_e . Integration of equation 2.01 gives:

$$V(x) = \frac{1}{2}kx^2 \quad , \quad (2.02)$$

The quantum mechanical Hamiltonian (\hat{H}) for a 1D-harmonic oscillator is given by

$$\hat{H} = \mathbf{T} + \mathbf{V}$$

i.e.

$$\hat{H} = -\frac{\hbar}{2\mu} \frac{d^2}{dx^2} + \frac{1}{2}kx^2 \quad , \quad (2.03)$$

where, \mathbf{T} and \mathbf{V} are kinetic and potential energy operators, respectively and μ is the reduced mass ($\frac{m_1m_2}{m_1+m_2}$) of the oscillator. Accordingly, the Schrödinger equation $\hat{H}\Psi_v = E_v\Psi_v$ can be written as:

$$-\frac{\hbar}{2\mu} \frac{d^2\Psi_v}{dx^2} + \frac{1}{2}kx^2\Psi_v = E_v\Psi_v \quad , \quad (2.04)$$

By solving this differential equation we obtain the value of E_v :

$$E_v = hv \left(v + \frac{1}{2} \right) \quad , \quad (2.05)$$

here, ν is the vibrational frequency of the oscillator and the vibrational quantum number $v = 0, 1, 2, 3 \dots$ ν is related to the force constant (k) and reduced mass (μ) of the oscillator by:

$$\nu = \frac{1}{2\pi} \left(\frac{k}{\mu} \right)^{1/2} \quad (2.06)$$

Generally, transition energies in IR spectroscopy are given in wavenumbers (and not in kJ/mol or Hz). From equation 2.05 we can derive:

$$\frac{E_v}{hc} = G(v) = \omega \left(v + \frac{1}{2} \right) \quad (2.07)$$

where, ω is the wavenumber, and $G(v)$ represents the vibrational term value expressed in wavenumbers.

2.1.1. Infrared Spectra

The **selection rule** for a vibrational mode to be IR active is, during the oscillation there should be non-zero dipole moment change in the molecule. In the following part the selection rule for a vibrational transition is derived mathematically (adapted from Ref.²:

Let's consider Ψ'_v as the vibrational wave function for the lower energy state with vibrational quantum number v' and Ψ''_v for the higher energy state v'' and μ as the dipole moment operator, then, the transition moment matrix element $R_v(v'', v')$ is defined as

$$R_v = \int \Psi''_v{}^* \mu \Psi'_v dx \quad (2.08)$$

For a homonuclear diatomic molecule, as μ is zero, R_v also becomes zero, means the vibrational transitions are forbidden. For a heteronuclear diatomic molecule, generally μ is non-zero and the dipole moment operator μ varies with x following Taylor series expansion:

$$\mu = \mu_e + \left(\frac{d\mu}{dx} \right)_e x + \frac{1}{2!} \left(\frac{d^2\mu}{dx^2} \right)_e x^2 + \dots \quad (2.09)$$

here, $x = r - r_e$ and subscript "e" refers to the equilibrium configuration. Substituting μ from equation 2.09 into equation 2.08, we get:

$$R_v = \mu_e \int \Psi''_v{}^* \Psi'_v dx + \left(\frac{d\mu}{dx} \right)_e \int \Psi''_v{}^* x \Psi'_v dx + \dots \quad (2.10)$$

Since, Ψ_v' and Ψ_v'' are eigenfunctions of the same Hamiltonian and they are orthogonal, i.e. $\int \Psi_v''^* \Psi_v' dx = 0$ for $v' \neq v''$, equation 2.10 then becomes:

$$R_v = \left(\frac{d\mu}{dx}\right)_e \int \Psi_v''^* x \Psi_v' dx + \dots \quad (2.11)$$

The integral $\int \Psi_v''^* x \Psi_v' dx$ is positive only when $v'' = v' \pm 1$. For all other values of Δv the integral vanishes, as in harmonic oscillator approximation it becomes an odd function and the limit goes from $-\infty$ to $+\infty$.³ In case of absorption of photons, Δv mainly refers to $v(\text{upper}) - v(\text{lower})$, so the effectively allowed vibrational transitions are possible for $\Delta v = +1$. Additionally, the term $\left(\frac{d\mu}{dx}\right)_e$ in front of the integral must be non-zero, i.e. the dipole moment of the molecule must change upon excitation. Thus, the selection rule for vibrational transition are derived as $\left(\frac{d\mu}{dx}\right)_e \neq 0$ and $\Delta v = +1$.

From the Boltzmann factor $\frac{N_v}{N_0} = e^{\left(\frac{-E_v}{kT}\right)}$ (where, N_v and N_0 are the population at the v^{th} and zeroth level respectively), we know at normal temperature the population at higher energy levels drops rapidly. Thus, in case of absorption IR spectroscopy, the intensity of the vibrational transitions drops rapidly with increasing v' .² Transitions with $v' \neq 0$ are called **vibrational hot bands**, because they are typically only observed when the molecule is hot.

2.1.2. Anharmonicity

The dipole moment operator can be considered to vary harmonically with x , only when equation 2.10 & 2.11 are expressed up to the 1st power of “ x ” i.e. linearly dependent on x . The effect of the higher terms is referred to as anharmonicity and as this particular anharmonic effect is caused by the electronic properties of the molecule, it is referred to as electronic anharmonicity. This relaxes the vibrational selection rule ($\Delta v = \pm 1$) to be modified to $\Delta v = \pm 2, \pm 3, \dots$, and the associated transitions are called as **overtones**. However, contribution of the higher order terms drops rapidly with increasing power of x . Thus, the so-called overtone excitations ($\Delta v = \pm 2, \pm 3 \dots$) typically carry very small intensities.

The dashed line in Fig 2.2 represents the vibrational potential of a 1D-harmonic oscillator which obeys Hook's law and the energy levels are the solution of nuclear Schrödinger equation. However, for diatomic molecules this hypothesis is only valid when x is small i.e. r is not very different from r_e . At a large value of $r-r_e$, the diatomic molecule approaches the dissociation limit D_e and eventually dissociates, forming isolated atoms. On the other hand, when the atoms come closer i.e. for $r < r_e$, Pauli repulsion comes into play, which makes the potential energy curve steeper than the harmonic oscillator. This anharmonicity is known as mechanical anharmonicity and also relaxes the vibrational selection rule to $\Delta v = \pm 1, \pm 2, \pm 3 \dots$

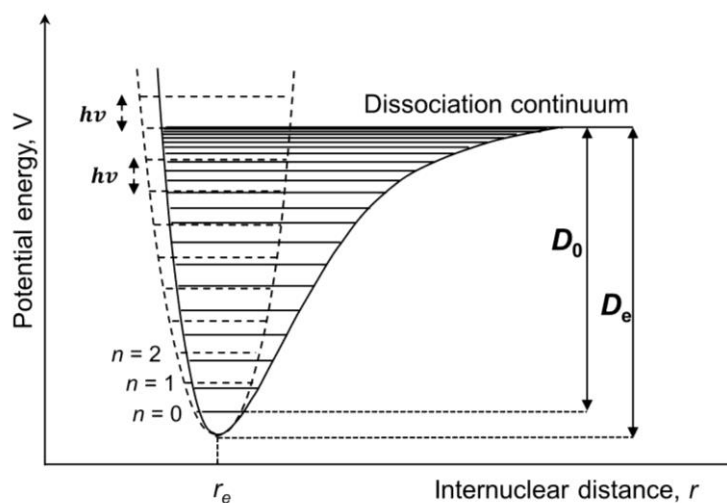


Figure 2.2: Internuclear potential energy curve of a diatomic molecule. Dashed line curve represents harmonic potential (ball-and-spring model). The Morse function (solid line) approximates the anharmonic nature of molecules.

Thus, both electrical and mechanical anharmonicity can contribute to overtone excitation and combination band intensities. However, only the mechanical anharmonicity affects the vibrational term values and equation 2.07 changes to a power series in $\left(v + \frac{1}{2}\right)$, as follows:

$$G(v) = \omega_e \left(v + \frac{1}{2}\right) - \omega_e x_e \left(v + \frac{1}{2}\right)^2 + \dots \quad (2.12)$$

where, ω_e is the vibrational wavenumber and x_e is the **anharmonicity constant**. The higher order terms of equation 2.12 are typically negligibly small w.r.t the harmonic term and are thus not shown. The corresponding energy levels are compared with those of the harmonic oscillators in Fig 2.2 and the anharmonic oscillator levels converge to the dissociation limit D_e .

The expressions for D_e and D_0 are approximated as follows:

$$D_e \cong \frac{\omega_e^2}{4\omega_e x_e} \quad \text{and} \quad D_0 = \sum_v \Delta G_{v+1/2}$$

Experimentally only D_0 can be measured. The simplest mathematical equation to explain the molecular dissociation associated with anharmonic potential energy curve of a diatomic molecule is known as Morse potential, given by the formula:

$$V(x) = D_e (1 - e^{-ax})^2 \quad , \quad (2.13)$$

with $a = \sqrt{\frac{k_e}{2D_e}}$ and $x = r - r_e$.

2.2. Gas Phase IR Spectroscopy

Generally, IR spectra are typically measured by direct absorption spectroscopy. The intensity difference of the incident and transmitted light is measured and the frequency-dependent absorption cross section $\sigma(\nu)$ is calculated using *Lambert-Beer's law*:

$$\frac{I_\nu}{I_0} = e^{-\sigma(\nu) \cdot n \cdot l} \quad , \quad (2.14)$$

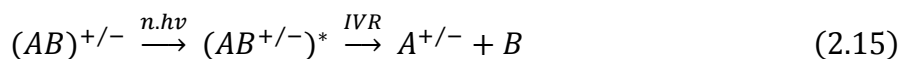
where, I_ν and I_0 are the transmitted and incident light intensities respectively, n the concentration of the solution and l the optical path length.

As mentioned earlier (section 1.3), absorption IR experiment in gas phase requires a minimum of $\sim 10^{10}$ molecules/cm³ to detect the attenuation of light intensity,⁴ which is not achievable with the state-of-art gas phase experiments. The sensitivity can be enhanced by increasing the interaction time of the molecular beam with the incoming light, with an elongated optical beam path. This technique is applied in cavity ring-down spectroscopy, where the absorption cell is placed inside an optical cavity and the light beam passes the cell multiple times leading to an increased path length on the order of kilometres, thus enhancing the sensitivity.^{5, 6}

For the work presented in this thesis, the number density ($\sim < 10^8$ ions/cm³) is limited⁷ by space charge effect,⁸ which is too low regarding sensitivity of the direct absorption spectroscopy to be applied. So, the vibrational spectra of isolated ions are investigated using an alternative method known as **action spectroscopy**, where, photo-absorption is studied by detecting either fluorescence, ionization, fragmentation or a change in quantum state.^{9, 10}

2.3. Infrared Photodissociation Spectroscopy

Infrared photodissociation spectroscopy (IRPD) is probably the most commonly used action spectroscopic technique as of today.^{9, 11-13} Here, the photodissociation yield is monitored as a function of laser wavenumber. The ion of interest $(AB)^{+/-}$, interacts with an intense laser pulse, either from a FEL or OPO laser system (see section 3.5). When the laser frequency is in resonance with the frequency of an IR-active vibrational transition of the molecule, resonant absorption of a photon can occur. The dissociation energy (D_0) for covalently bound charged clusters are generally high, so, to reach the dissociation threshold the molecule needs to absorb a multiple number of IR photons, thus it is called IRMPD process:

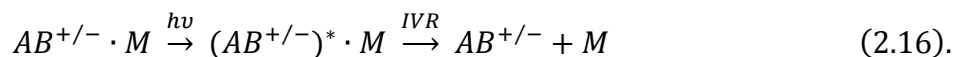


IRMPD is most commonly assumed to be a non-coherent sequential absorption process involving three overlapping regions: the resonant region, the quasi-continuum region and the dissociation region.^{14, 15} In the first region, vibrational excitation between discrete energy levels of a vibrational mode occurs with sequential absorption of multiple photons. With increasing vibrational quantum number the energy spacing between consecutive vibrational levels drops owing to the mechanical anharmonicity of the molecule. Thus, for higher energy levels, typically already starting at $v = 2,3..$, the excitation source runs out of resonance for transitions between higher levels of the system and further resonant absorption is not possible. This situation is referred to as reaching the **anharmonic bottleneck**. In some cases it is compensated with the bandwidth of the laser or excitation of the ro-vibrational states.

Absorption of many photons increases the internal energy of the system, leading to a rapid increase in the density of rovibrational states $\rho(E_i)$, which roughly scales with E_i^N , where, N is the number of vibrational degrees of freedom.¹⁶ Consequently, even small molecules can reach the quasi-continuum region upon absorption of a few photons. Unlike a vibrational ladder climbing process, the absorbed photon energy is quickly dissipated throughout the molecule due to coupling of the excited vibrational mode with other vibrational degrees of freedom (anharmonic coupling). This phenomenon is called **intramolecular vibrational energy relaxation** (IVR). A fast IVR rate allows absorption of more photons by depopulating the excited energy levels. However, this leads to spectral broadening by reducing the lifetime of excited vibrational levels. For large polyatomic molecules, the IVR timescale is on the order of $10^{-11} - 10^{-12}$ s,^{17, 18} from Heisenberg's energy-time uncertainty principle $\Delta E \Delta t \geq \frac{\hbar}{2}$, the corresponding linewidth can be calculated as $\Delta E \approx 5.3 \text{ cm}^{-1}$. Typically the bandwidth of the FHI-FEL is $\leq 10 \text{ cm}^{-1}$ (FWHM), so the spectral broadening in the experimental spectra mainly comes from the light source. When the internal energy of the system exceeds the dissociation limit, the molecule reaches the true continuum region and fragmentation becomes energetically allowed. Typically, the dissociation takes place through breaking of the weakest bond in the system, however if sufficient energy is absorbed other dissociation channel become accessible.

The above discussed anharmonic effects (shifting fundamental vibrational modes, peak broadening) induce spectral congestion and thus the assignment of IRMPD spectra is typically more difficult than that of IRPD spectra. Moreover, the unavoidable anharmonic bottleneck and a change in transition dipole moment upon heating can result in IRMPD **transparent bands** (IR-active transitions which do not show up in the corresponding IRMPD spectra).^{19, 20} The *messenger* tagging technique was introduced to overcome the limitations of multiphoton absorption measurements. Here, unlike IRMPD, a weakly bound ion-messenger complex is irradiated with IR light to induce photo-fragmentation. This technique is called IRPD or IRVPD spectroscopy.²¹⁻²³ Rare gas atoms like He and Ne or inert molecules such

as H₂ and D₂ are generally used as messengers. Use of a messenger substantially reduces the dissociation threshold, as now the weakest bond in the system is the ion-messenger bond and energy of a single photon is typically enough to induce fragmentation according to:



Ideally, the messenger atom/molecule remains innocent upon complexation. This means that the geometry or electronic structure of the bare cluster ion remains unperturbed. Moreover, the experimental IRPD spectrum can be directly compared to the computed linear absorption spectra. The IVR process is relatively slow in case of IRPD ($\sim 10^{-9} - 10^{-10}$ s),²³ due to weak coupling between the excited modes and other low energy states in the ion-messenger complex. This sufficiently reduces the lifetime broadening of the spectral bands ($\sim 10^{-2} - 10^{-3}$ cm⁻¹). In the presented experiments here in the context of this thesis, width of the IRPD bands is typically limited by the laser band width.

The studies presented in this thesis rely on mainly He or D₂ as messenger. He is often considered as an ideal messenger, but it is difficult to form He-complexes, especially for anionic clusters. D₂ is probably the second best choice as messenger, but particular care should be taken that it does not chemically react with the system of interest.

References:

1. A. Barth, in *Encyclopedia of Biophysics*, ed. G. C. K. Roberts, Springer Berlin Heidelberg, Berlin, Heidelberg, 2013, DOI: 10.1007/978-3-642-16712-6_301, pp. 1593-1596.
2. J. M. Hollas, *Modern spectroscopy*, John Wiley & Sons, 2004.
3. D. A. McQuarrie and J. D. Simon, *Physical chemistry: a molecular approach*, University science books Sausalito, CA, 1997.
4. M. R. Fagiani, PhD Thesis, Freie Universität Berlin, 2017.
5. G. W. Drake, *Springer handbook of atomic, molecular, and optical physics*, Springer Science & Business Media, 2006.
6. M. D. Wheeler, S. M. Newman, A. J. Orr-Ewing and M. N. Ashfold, *Journal of the Chemical Society, Faraday Transactions*, 1998, **94**, 337-351.
7. D. J. Goebbert, G. Meijer and K. R. Asmis, *AIP Conference Proceedings*, 2009, **1104**, 22-29.
8. D. Gerlich, *State-Selected and State-to-State Ion-Molecule Reaction Dynamics. Part 1: Experiment*, 1992, **82**.
9. M. A. Duncan, *International Journal of Mass Spectrometry*, 2000, **200**, 545-569.
10. E. Bieske and J. Maier, *Chemical reviews*, 1993, **93**, 2603-2621.
11. A. S. Sudbø, P. A. Schulz, Y. R. Shen and Y. T. Lee, in *Multiple-Photon Excitation and Dissociation of Polyatomic Molecules*, ed. C. D. Cantrell, Springer Berlin Heidelberg, Berlin, Heidelberg, 1986, DOI: 10.1007/978-3-642-82292-6_3, pp. 95-122.
12. E. J. Bieske and O. Dopfer, *Chemical Reviews*, 2000, **100**, 3963-3998.
13. T. Ebata, A. Fujii and N. Mikami, *International Reviews in Physical Chemistry*, 1998, **17**, 331-361.

14. J. G. Black, E. Yablonovitch, N. Bloembergen and S. Mukamel, *Physical Review Letters*, 1977, **38**, 1131.
15. A. Makarov, I. Y. Petrova, E. Ryabov and V. Letokhov, *The Journal of Physical Chemistry A*, 1998, **102**, 1438-1449.
16. K. R. Asmis and J. Sauer, *Mass spectrometry reviews*, 2007, **26**, 542-562.
17. J. Oomens, B. G. Sartakov, G. Meijer and G. Von Helden, *International Journal of Mass Spectrometry*, 2006, **254**, 1-19.
18. K. R. Asmis, A. Fielicke, G. von Helden and G. Meijer, *The Chemical Physics of Solid Surfaces*, 2007, **12**, 327-375.
19. T. I. Yacovitch, N. Heine, C. Brieger, T. Wende, C. Hock, D. M. Neumark and K. R. Asmis, *The Journal of Physical Chemistry A*, 2013, **117**, 7081-7090.
20. N. Heine and K. R. Asmis, *International Reviews in Physical Chemistry*, 2015, **34**, 1-34.
21. M. Okumura, L. Yeh, J. Myers and Y.-T. Lee, *The Journal of chemical physics*, 1986, **85**, 2328-2329.
22. M. Okumura, L. Yeh, J. Myers and Y. T. Lee, *Journal of Physical Chemistry*, 1990, **94**, 3416-3427.
23. M. Johnson, *The Encyclopedia of Mass Spectrometry: Theory and Ion Chemistry*, 2003, **1**.

Chapter 3

Experimental Setup

This chapter describes the experimental setup, which is used to perform all the experiments reported in this thesis. A tandem mass spectrometer is combined with a radio frequency (RF) ring electrode ion trap to study the ions generated with either laser ablation or electrospray ionisation technique. In the following, a detailed description of the ion sources and the tandem mass spectrometer is given, followed by the ion detection scheme and a description of used IR light sources.

3.1. Laser Vaporization Source

The Laser vaporization is the most commonly used ion source for the production of metal and metal-containing neutral and ionic clusters in mass spectrometry. It was developed in 1981, independently by the groups of R. E. Smalley at Rice University and Dr. V. Bondybey at Bell laboratories.¹⁻³ The initial idea for the application of this source was to study transition and main group metal clusters,⁴ but its proficiency extended the use to effectively produce metal oxides, metal carbides and even mixed-metal clusters. The schematic of the original “Smalley” source is shown below in Fig. 3.1.

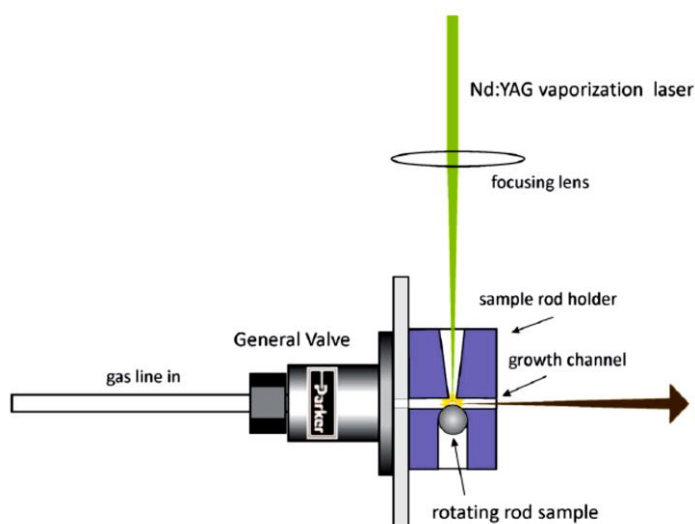


Figure 3.1: The schematic of standard “Smalley” source. Fig. adapted from Ref.⁴

Although it is based on a simple operating principle, subtle design features have considerable influence on composition, number, size, charge state, temperature and stability of the clusters produced. Detailed studies on cluster formation have shown that vaporization yield depends on the laser pulse energy, reflectivity of the metal surface, laser pulse duration, thermal conductivity of the material and composition of

the plasma produced above the material.⁵ Different types of sample targets, such as metal rods,⁶ pellets, disks, powders and liquid metals⁷ have been used by different groups in the last 40 years. Dense metal plasma is produced by focusing a laser pulse on the surface of the sample, which is then cooled by collisions with inert gas atoms in a confined channel. This is followed by supersonic expansion at the end of the channel, which allows for adiabatic cooling. The choice of laser pulse length and energy has dramatic effect on the size distribution of the clusters produced. Lasers with longer pulses, such as are more effective in penetrating metal surfaces and vaporize more material than short pulse lasers.⁴ However, vaporization occurs within the first few picoseconds of the laser pulse and the plasma formed on the surface of the sample then interacts with the light for the remaining time to form a super-heated plasma.⁵ After threshold energy is reached, vaporization process begins and laser pulse beyond this energy actually results in excessive heating of the plasma, making it more difficult to condense thus inhibits efficient formation of clusters. Nanosecond lasers are most commonly used with typical pulse energies of 1-30 mJ. The choice of carrier gas is also crucial owing to their different cooling capacity. He- or Ar- is the best suited carrier gas, but molecular gases or gas mixtures are also used in particular cases.⁴

3.1.1. Laser Vaporization Source Used for This Thesis Work

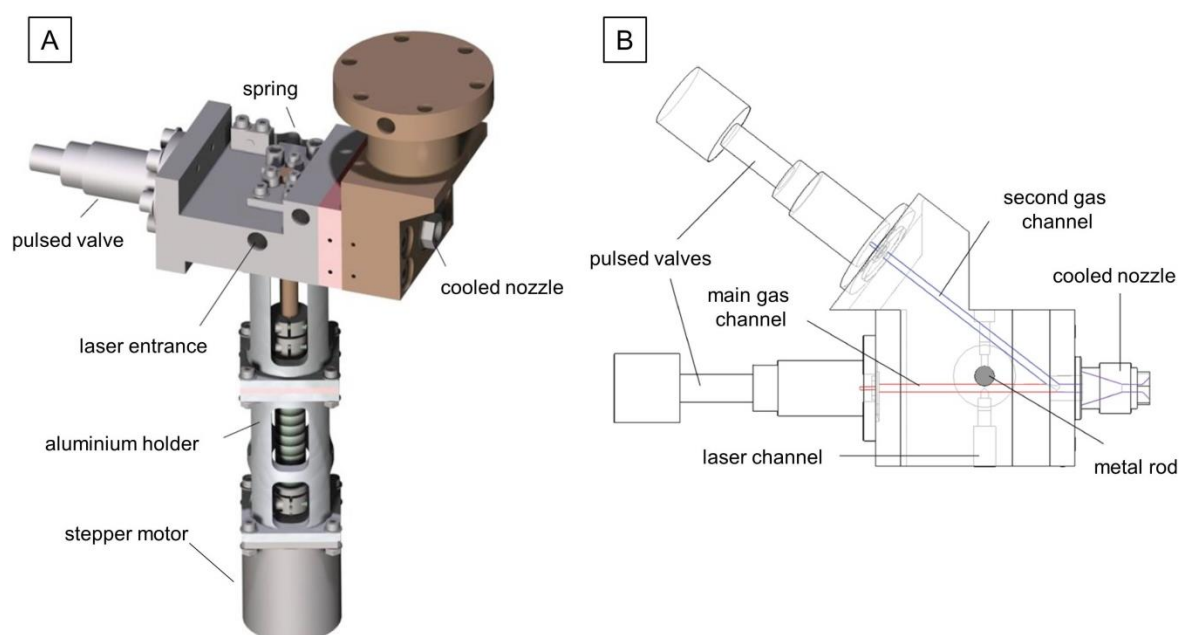


Figure 3.2: Schematic of the laser vaporization source used for the works presented in this thesis. A) Single channel source block connected to a stepper motor and cryostat. B) Schematic of dual channel source block. Figures adapted from Ref.^{8,9}

For the IRPD experiments on Al/V- and Al/Fe-mixed metal oxide clusters a single channel laser vaporization source (Fig. 3.2-A) was used. Whereas, a dual channel source block (Fig. 3.2-B) was used for the formation of Ti-oxide – CO₂ clusters.

Schematics of the single and dual channel source block are shown in Fig. 3.2A and 3.2B respectively.

A stepper motor is mounted below the source block with an aluminium holder. A screw thread system, which holds the target rod, is attached to the stepper motor, allowing for translational rotation of the rod. A solenoid pulse valve (Parker, Series 99), which is orthogonally mounted to the target rod, provides the gas pulse ensuring thermalization and clustering. The gas channel diameter is 5 mm and extends 30 mm past the position of the sample rod. The channel ends with a cooled nozzle mounted on a copper block, which serves as the cooling unit. The copper block is attached to the second stage of a 4K cold head close-cycle helium cryostat. The cryostat allows temperature control over the range of 20-350 K, but in practice lowest operational temperature is limited by the minimum working temperature of the stepper motor, which is ~200 K. An 8 mm thick polyimide block (Vespel SP-21) is used as a thermal insulator between the copper and the source block. Two heating cartridges are installed, one at the source block and another at the copper block. In this way, continuous temperature control of both the source block and cooling unit is attained. The second harmonic (532 nm) of a Q-switched Nd:YAG laser with 50 Hz repetition rate is used to induce vaporization of the metal target. When necessary (in most of the cases), the laser pulse energy is attenuated with a commercial beam attenuator equipped with Brewster type polarizers. The laser beam then passes through a focusing lens (focal length = 40 cm, which is mounted onto a translation stage for fine adjustment) and hits the sample rod going through the laser channel. Typically, in the present experiments the opening of the gas pulse valve is triggered 300 to 600 μs before the Q-switch of the laser, so that, the buffer gas is already present when the laser hits the target rod. The temporal delay between the gas pulse and laser pulse is adjusted with microsecond precision to optimize the ion signal.

The dual channel source block, which is shown in Fig. 3.2B, was designed to allow the formed clusters from the main gas channel to react with reactant gases. The second gas channel intersects the main one under a 38 degree angle and at 24 mm distance from the laser channel. This design ensures that the vaporization process and subsequent clustering along the main gas channel remain unperturbed upon addition of a second gas pulse. A detailed description of the source blocks are given in Ref.^{8,9}

After the ion yield of the (bare) metal oxide clusters of interest is optimized, the second pulsed valve is activated, requiring little or no changes to the rest of the source parameters. The timing of opening of the second pulse valve can also be adjusted with μs precision. Generally, a 10 – 300 μs delay is used between openings of the two valves. A comparison of quadrupole mass spectra of Ti-oxide cluster anions with and without reaction with CO_2 molecules is shown in Fig. 3.3. Bare Ti_mO_n^- clusters are produced using a pure Ti-rod target and 0.75% O_2/He gas mixture from the main gas channel. A pure CO_2 gas pulse was provided from the second gas channel to form the CO_2 reaction product. A delay of 180 μs and 5 bar backing pressure was used for the efficient formation of multiple CO_2 reacted clusters.

3. Experimental Setup

Addition of the CO₂ reactant gas to the main gas channel would expose it to the hot plasma and would have led to formation of side products; which was avoided by using the second gas channel. From the mass spectra in Fig. 3.3 it is seen that Ti-oxide/CO₂ complexes are predominantly formed without formation of any undesirable side products.

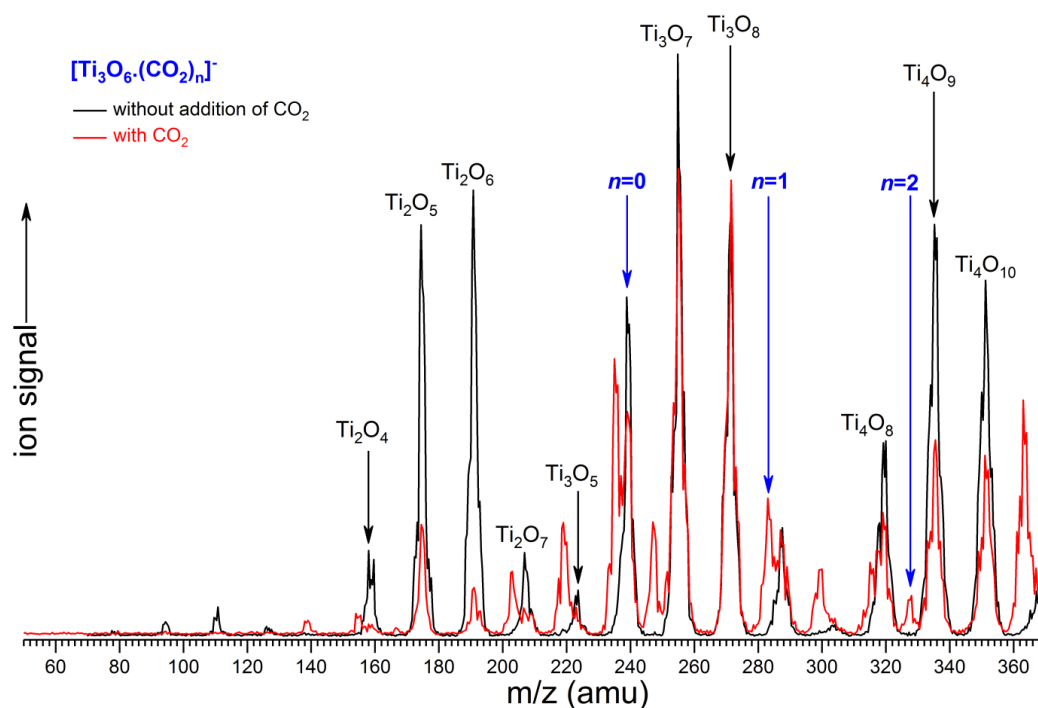


Figure 3.3: Quadrupole mass spectrum of the ions produced by pulsed laser vaporization of a pure Ti-metal rod and quenching in a gas pulse of 0.75 % O₂ seeded in He. Pure CO₂ was added from the second gas channel of the source block to get CO₂ reaction product.¹⁰ Best signal was observed with the source block temperature of 270 K.

For projects involving the production of mixed metal-oxide clusters, a bimetallic metal rod target (Plasmaterials, Inc.) was used. The rod composition was chosen depending on the system of interest. The studied Al/Fe- oxide systems are aluminium rich, so, a 70/30 wt% Al/Fe rod was used. Whereas, for AlVO_x (x=3, 4) project the clusters of interest contain a single atom of each metal. So, a 50/50 wt% Al/V rod target was used. Fig 3.4 represents a mass spectrum obtained by ablating the Al/Fe mixed metal rod followed by quenching with 0.5% O₂ seeded in He gas. Formation of pure and mixed metal oxide clusters is seen from the mass spectrum and this makes the proper assignment of the mass peaks challenging. Each pure- and mixed- oxide cluster series is indicated with green, black, blue and red lines. The most intense mass peaks are assigned to the [(Al₂O₃)_m(AlO)]⁺ clusters. The closed-shell electronic configuration of these clusters results in their relative high abundance. The systems of interest for this particular project are [(Al₂O₃)_m(FeO)]⁺ (m=1-5) cations and the corresponding mass peaks are shown with the blue line.

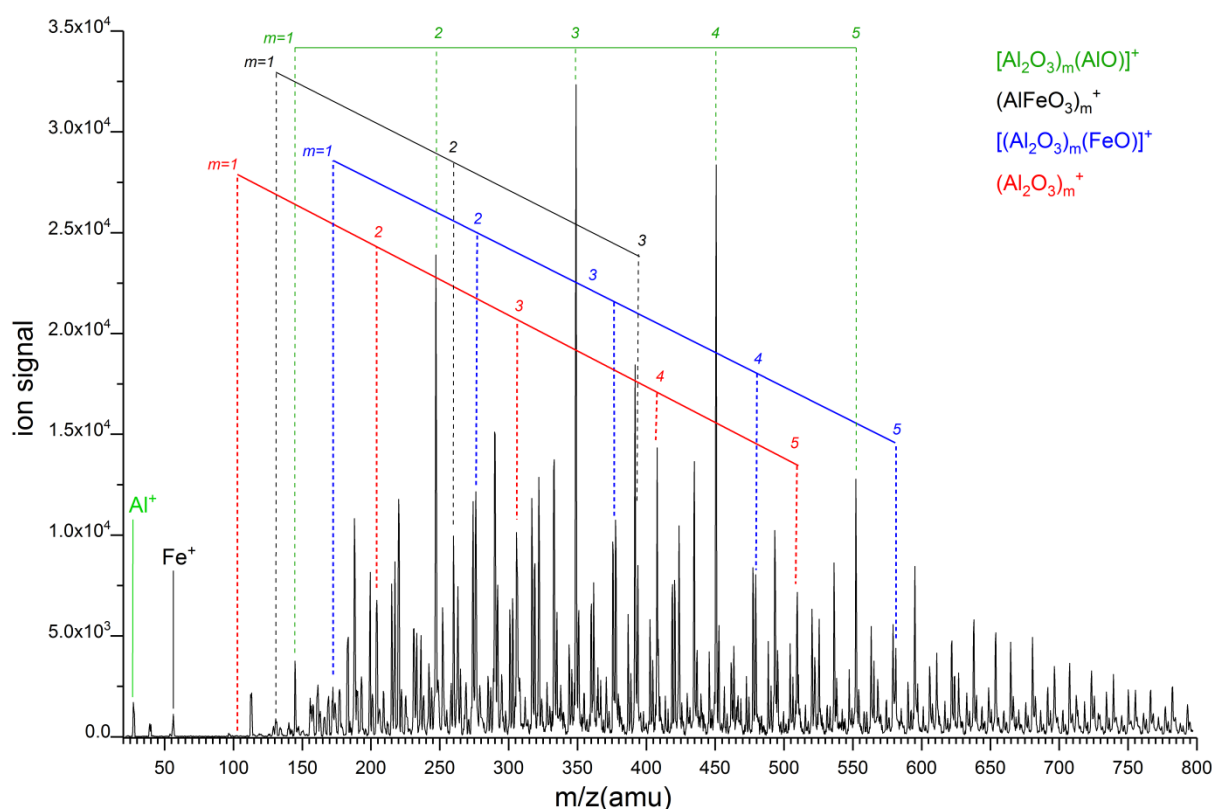


Figure 3.4: Quadrupole mass spectrum of the ions produced by pulsed laser vaporization of a Fe/Al (30/70 wt%) metal rod and quenching in a gas pulse of 0.5 % O₂ seeded in He, at a source block temperature of 270 K.

3.2. Electrospray Ionization Source

Electrospray ionization (ESI) has emerged to be a powerful technique in mass spectrometry to transfer intact analyte molecules from solution to the gas phase. By varying spray conditions it can be used to produce small salts to large in size macromolecular ions. Being a soft ionization technique, it is capable of transferring weakly bound complexes having low vapour pressure into the gas phase without decomposition, as in case of other desorption methods.¹¹ Malcolm Dole (Northwestern University) first used this method in 1968 to look into polymeric macromolecules.¹² 20 years later, John B. Fenn (Yale University) combined mass spectrometry technique with this ionization method and revolutionized the field of quantitative analysis of biologically important macromolecules;¹¹ later, he also worked with smaller solute species to establish the applicability of this method over a wide size range.¹³ Henion et al. modified the ESI technique to a pneumatically assisted method (with N₂ gas)^{14, 15} which they called as ion spray (IS) technique,¹⁶ is used here in the context of the thesis to investigate VPO₄⁺/C₂H₄ system.

3.2.1. ESI Source Used for This Thesis Work

The IS source used for the experiments presented in this thesis is a modified commercial (Waters, Quattro Ultima) Z-spray source. A schematic of the source is shown in figure 3.5^{8, 17} and the general working principle is described in the following.

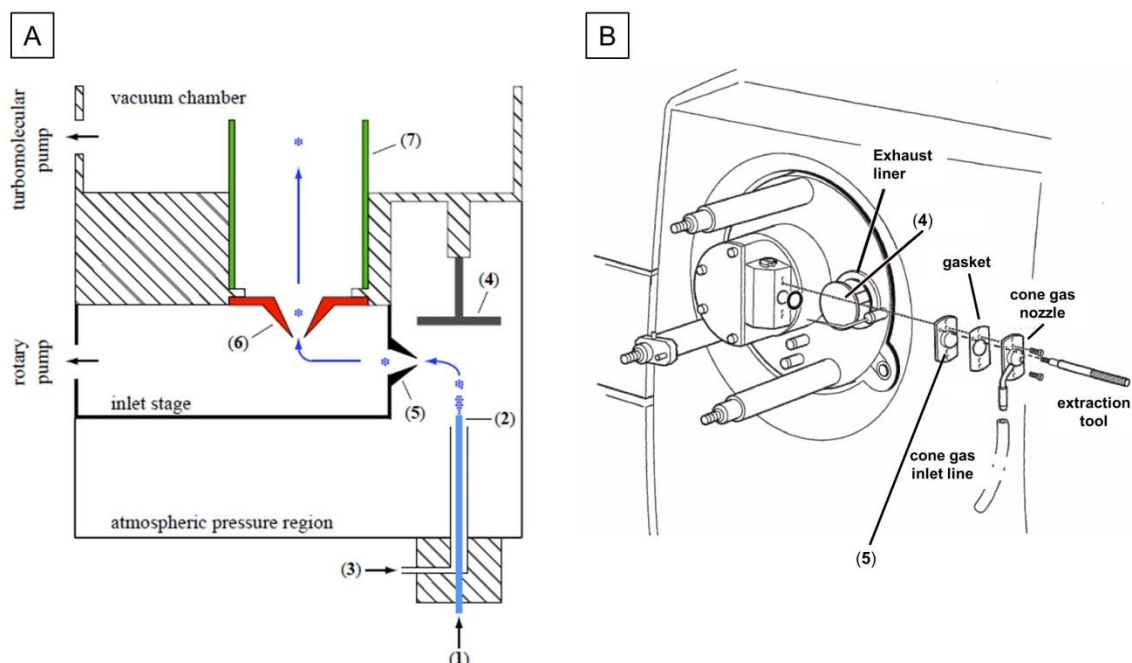


Figure 3.5: A. Schematic illustration of the Z-spray source taken from Ref. ⁸. The indicated numbers refer to: (1) sample solution inlet, (2) stainless steel capillary, (3) nebulizer gas inlet, (4) grounded baffle, (5) skimmer 1 attached to the source block, (6) skimmer 2, (7) cylindrical lens. B. 3D front view of the ESI source block taken from Ref. ¹⁷. The operating principles and typical voltages used are given in the text.

The sample solution is pumped with a syringe pump and enters a stainless steel capillary (2 in Fig. 3.5.A), which is kept at high voltage. The flowrate of the solution is generally maintained at 10-20 $\mu\text{l}/\text{min}$ and is optimized with the signal stability. The applied electric field at the tip of the needle charges the meniscus of the flowing liquid, resulting in the formation of a Taylor cone and thus leads to a fine spray of charged droplets. Typically the applied voltage on the capillary is 2-4 kV depending on the used solvent. Equation 3.01, derived by David P. H. Smith,¹⁸ represents the dependence of the required onset potential (V_0) on the surface tension of the used solvent to begin electrospray. Solvents with lower surface tension thus facilitate electrospraying at a lower voltage. Typically, a solvent mixture water/acetonitrile or water/methanol is used to achieve a stable spray condition with lower voltages.

$$V_0 \propto \sqrt{\frac{2r_c \gamma \cos \theta}{\epsilon_0}} \ln \left(\frac{4d}{r_c} \right) \quad (3.01)$$

where, r_c is the capillary radius, γ the surface tension of the used solvent, θ (49.3°) the half angle of the Taylor cone, ϵ_0 permittivity of the vacuum and d the capillary-to-

counter electrode distance. Electric field difference between the capillary and the ground drives the formed droplets to migrate towards the grounded baffle (4 in Fig. 3.5). The atmospheric pressure region of the source facilitates evaporation of solvent from each droplet as it drifts forward. As a result, the charge density on its surface increases until the *Rayleigh limit* ($q = \sqrt{8\pi\epsilon_0\gamma D^3}$, q being the total charge and D diameter of the droplet) is reached. When the Coulomb repulsion exceeds the surface tension of the droplet, the resulting instability causes fission of the droplets, called “Coulomb explosion”. The formed daughter charged droplets also evaporate in multiple cycles. When the radius of the droplet becomes small enough, the high surface charge density desorb the sample ions from the droplets into the gas phase.¹¹ A flow of nebulizer gas (3 in Fig. 3.5.A) surrounding the capillary helps in the evaporation process. The choice of nebulizer gas is also important. A relatively high dielectric strength of the gas is needed to avoid fragmentation and discharge with the applied high voltage at the needle tip. Moreover, it should be inert to not undergoing reaction with the analyte and inexpensive in order to run the experiment for long time. N₂ is generally used as the nebulizer gas with satisfactory results.

The first skimmer (skimmer 1 in Fig. 3.5) with 700 μm diameter, which is also the opening to the first pumping stage, is installed on the source block perpendicular to the direction of the spray. The first pumping stage is referred to as the inlet stage in Fig. 3.5.A. The second skimmer (skimmer 2 in Fig. 3.5, 1mm diameter opening) is mounted perpendicular to the inlet stage. This Z-shape arrangement blocks the neutral analyte and solvent particles to enter the inlet region. Generally, skimmer 1 and the source block are held at a potential of (V_1) 30 –100 V and skimmer 2 at (V_2) 20 – 60 V. To maintain this voltage difference, skimmer 2 is electrically isolated from the source block. Passing through skimmer 2, the ion beam enters the vacuum chamber. Here, either a cylindrical lens (7 in Fig. 3.5.A), held at a third voltage (V_3) of 0–60 V, or a RF guide (0-30 V DC, 400-500 V RF) is installed. This choice depends on the system of interest. It is seen that the RF guide helps in guiding highly solvated clusters without fragmentation. After this stage, the ion beam is focused into a tandem mass spectrometer, which is discussed in the following section (section 3.3). Applied voltages to the aforementioned skimmer and lenses are optimized (typically $V_1 > V_2 > V_3$) to ensure smooth transmission of the ions to the mass spectrometer.

The signal intensity, extent of solvation, charge state and the degree of fragmentation of the formed gas phase clusters can be varied by changing the source parameters, such as, the inlet pressure, flow rate of the nebulizer gas, flow rate of the sample solution, temperature of the source block, temperature of the nebulizer gas and the skimmer voltages. Fig. 3.6 shows how the distribution of bare and solvated acetate anions [CH₃COO][−] can be influenced with the skimmer voltages. For the generation of bare acetate anions a high skimmer voltage is needed (skimmer 1: 81 V, skimmer 2: 37 V) and generation of hydrated clusters is favoured by lower skimmer voltages (corresponding voltages are mentioned in Fig. 3.6). Note, the potential difference between the skimmers plays a significant role on the extent of hydration. Higher

potential difference will induce breaking of the weakly bounded solvation shell and vice versa.

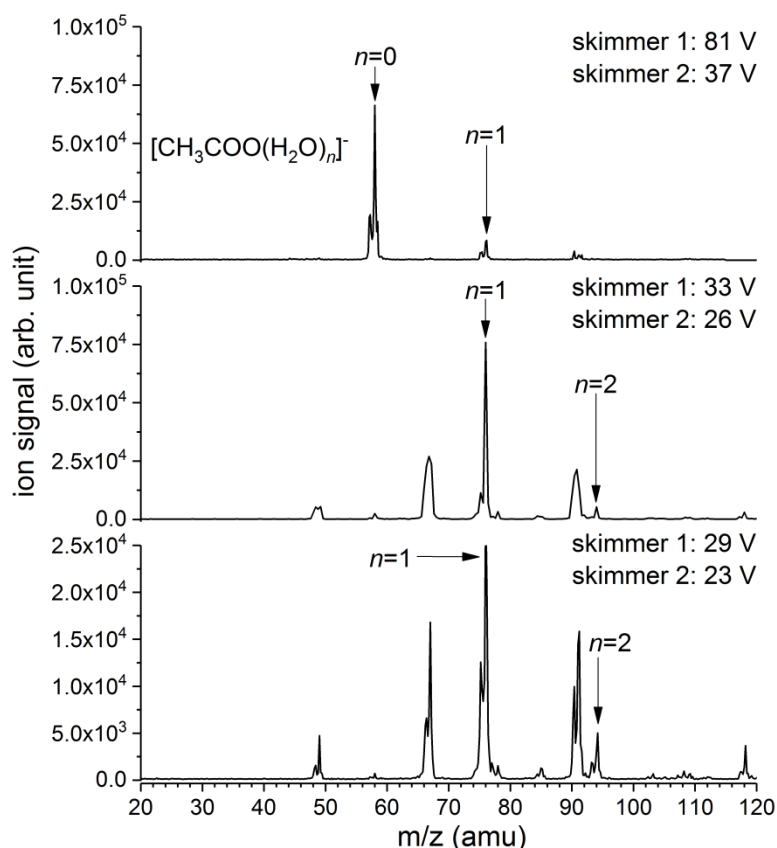


Figure 3.6: Mass spectra of microhydrated acetate anions $[\text{CH}_3\text{COO}(\text{H}_2\text{O})_n]^-$, measured with different sets of skimmer voltages. Higher voltages on the skimmers result in less hydrated anions.

3.3. Tandem Mass Spectrometer

A schematic overview of the experimental setup, i.e. the cryogenic ion trap-tandem mass spectrometer, used to perform the experiments presented in this thesis is shown in Fig. 3.7. The complete setup is housed in a vacuum chamber, which is divided into five interconnected stages: (a) Source, (b) Guide, (c) Quadrupole mass filter, (d) Ion trap and (e) Time-of-flight (TOF) mass spectrometer. Gas phase cluster ions are formed either by laser ablation (section 3.1) or ion spray (section 3.2) in the source region. The beam of ions then passes through a 4 mm diameter skimmer and is focused into a radio frequency (RF) decapole ion guide. The focusing is performed by the einzel lens (EL 1) placed before the ion guide. The guide is generally continuously filled with He-buffer gas, which helps in thermalization of the ions to room temperature and collimates the ion beam into a cylindrical shape. The collimated ion beam then passes through a second einzel lens (EL 2) and is mass-selected (m/z) using a quadrupole mass filter (Extrel CMS, 4-2000 amu). The mass-selected ion beam is then deflected into 90° using an electrostatic quadrupole deflector and enters the RF ring-electrode ion trap (RET) passing through another set of einzel lens (EL 3) used for focusing of the ion beam. The deflector is used to select

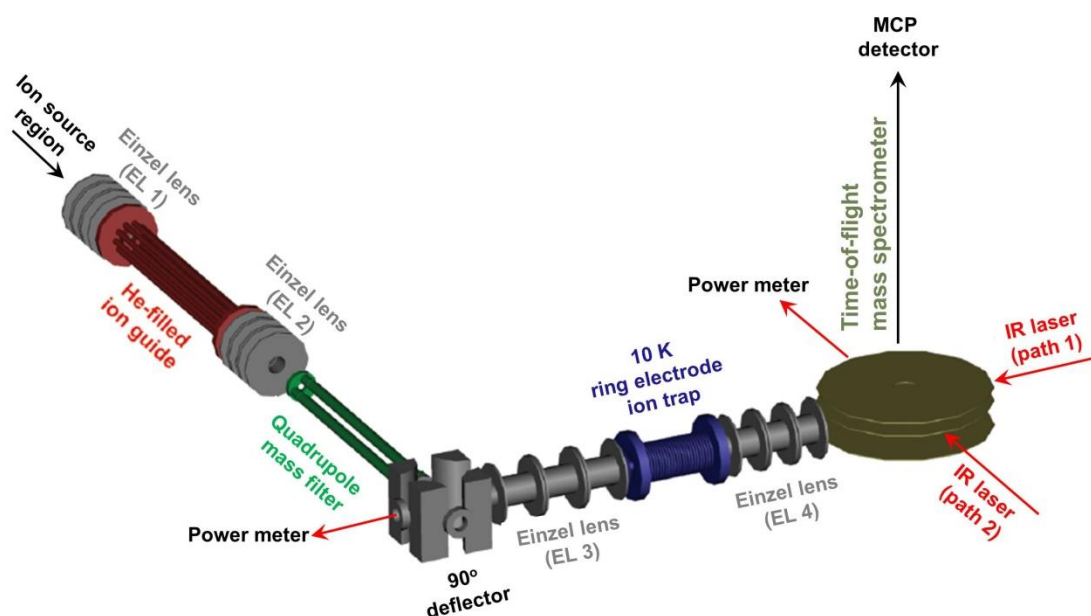


Figure 3.7: Schematic 3D-view of the cryogenic ion trap-tandem mass spectrometer used to perform the experiments presented in this thesis. The figure is adapted from Ref.¹⁹

the electrical charge (cation or anion) of the ions; also, the neutral particles generated at the source get separated at this point. The trap is mounted on the cold-head of a close-cycle helium cryostat and the temperature can be controlled within the range of 10 K to 350 K. The trap is continuously filled with buffer gas allowing accumulation and thermalization of the mass- and charge-selected ions to the ambient temperature through multiple collisions with the buffer gas atoms. When required, messenger tagging is also performed inside the trap at sufficiently low temperature and *via* three-body collisions.²⁰ Collisional thermalization of the ions down to cryogenic temperature typically brings them to their global minimum energy structure. After the accumulation and thermalization, all ions are extracted from the ion trap and focused both temporally and spatially into the center of the extraction region of an orthogonally-mounted linear time-of-flight (TOF) mass spectrometer. An einzel lens (EL 4), which is placed after the RET and an ion beam deflector (placed between EL 4 and TOF, not shown in Fig. 3.7), is used for this focusing. Ion trapping and extraction is performed by a set of DC voltages applied to the trap electrodes. Typically, the ion cloud is irradiated with a counter propagating IR light pulse (path 1 in Fig. 3.7) when they are in-between the center of the TOF plates. All parent and photodissociated (fragment) ions are accelerated towards the microchannel plate (MCP) detector by applying two properly timed high voltage pulses (extraction: $\sim \pm 3000$ V, acceleration: $\sim \pm 2500$ V, '+' for cations and '-' for anions) to the TOF electrodes. A TOF mass spectrum is recorded by simultaneously monitoring the intensity of all the ions and an IRPD spectrum is obtained as a function of the scanning wavelength of the laser. In special cases, the IR laser can also be aligned from the perpendicular direction of the molecular beam axis (IR laser path 2 in fig. 3.7). The vacuum chamber is terminated with IR windows (3-5 mm thick with 25 mm diameter) along both the laser beam paths. They allow entering the laser beam

inside the instrument. Depending on the wavelength region, different IR windows (KBr, KRS-5, CaF₂ etc.) are used. Typically, a power meter is placed at the indicated place in fig. 3.7, to measure and record the shot-to-shot laser pulse energy.

The five stages of the vacuum chamber of the machine are differentially pumped using turbomolecular pumps. Achieving the right pressure at every stage is critical in terms of signal intensity. Compact pressure gauges (combination of pirani and cold cathode sensors), which typically can read pressures from 10³ down to 10⁻⁹ mbar, are connected to every chamber. Approximate background and operating pressure at every stage is listed in Table 3.1. When using the ESI source, due to high gas ballast, the background pressure is generally high in the source and the guide region. A More detailed description of the ion optics and multipole RF devices used in this experimental setup can be found in Ref.⁸

Table 3.1: Approximate background and operating pressure (in mbar) at different stages of the vacuum chamber is listed.

Chambers	Source	Guide	Quadrupole	Trap	TOF
Background pressure	10 ⁻⁴ (ESI)	10 ⁻⁶ (ESI)	10 ⁻⁸	10 ⁻⁸	10 ⁻⁸ -10 ⁻⁹
	10 ⁻⁸ (Laser ablation)	10 ⁻⁸ (Laser ablation)			
Operating pressure	10 ⁻⁴ (ESI)	10 ⁻⁵ (ESI)	10 ⁻⁷	10 ⁻⁵	10 ⁻⁷ -10 ⁻⁸
	10 ⁻⁴ (Laser ablation)	10 ⁻⁴ (Laser ablation)			

3.4. Detection Scheme and Data Acquisition

The experimental setup discussed above can be operated either in the quadrupole mass spectra (QMS) or in the TOF mass spectra (TOF-MS) mode. In case of the QMS mode, the ions are detected with a channeltron electron multiplier (Burle), which is placed behind the extraction plates of the TOF mass spectrometer, in an off-axis configuration along the trap axis. A preamplifier (Advanced Instrument Research Corporation, MTS-100) amplifies the channeltron signal and the output signal is sent to a counter-timer card (National Instruments) for processing. In this mode the TOF plates remain grounded and the trap is used in RF-only mode to guide the mass-selected ion beam towards the channeltron detector. A quadrupole mass spectrum, where signal intensity is plotted as a function of mass-to-charge ratio, is measured using the quadrupole mass filter. Typically, source parameters and ion optics voltages are optimized by monitoring the total counts of a mass-selected signal using a channeltron detector and then the TOF-MS mode is activated for further experiments. Mostly, the ion optics voltages are first optimized manually and then fine tuning is done using a genetic algorithm.²¹

In the TOF-MS mode, the ion of interest is trapped in the RET after mass selection with the quadrupole mass filter. The ion trap is comprised of six different DC voltage stages. For trapping of the ions, a set of mixed RF-DC voltage is applied to the ion trap electrodes forming a potential well along the trap axis. The entrance lens potential is chosen in a way that the ions can barely overcome the barrier with their kinetic energy. Whereas, the potential of the exit lens is set so high, such that the ions are reflected back towards the entrance lens. A continuous flow of buffer gas (typically Helium) inside the trap is maintained ensuring thermalization of the ions. This arrangement results in reducing sufficient kinetic energy of the ions that they cannot leave the trap and get accumulated.

Internal cooling of the ions is achieved by means of multiple collisions with the buffer gas atoms, and at sufficiently low temperature ion-messenger complex are formed. After accumulation for typically 100 or 200 ms, the ions are extracted from the trap by quickly switching the trap electrode potentials to a second set of DC voltages. This set of voltages is set in a way to form an axial declining voltage ramp from entrance to the exit lens and applied for around 1 ms. All trapped ions are then temporally and spatially focused at the center of the extraction region of a linear Wiley-McLaren TOF mass spectrometer²² using a set of four deflectors. The time that the ions take to travel from the trap to the center of the extraction region is called the **TOF delay**, which typically is within 50-200 μ s. The TOF delay for particular ions depends on their kinetic energy, which is determined by the extraction DC voltage ramp of the ion trap and the buffer gas pressure in the ion trap. During the TOF delay time the extraction plates remain grounded. Once the ions reach the center in-between the plates, short high voltage (HV) pulses are applied to the TOF extraction and acceleration plates. Switching of these voltages is controlled by two fast push-pull *Behlke* switches (Behlke Power Electronics GmbH, HTS 61-03-GSM). These high voltage pulses accelerate the ions through the orthogonally mounted \sim 1 m long field free TOF tube. During their flight the ions separate according to their mass-to-charge ratio and their arrival time distribution is detected using a MCP detector. A fast preamplifier amplifies the signal from the MCP detector and this signal is ultimately evaluated by an *Acquiris* card (DP130) installed in the computer. The trapping conditions and messenger tagging efficiencies are generally optimized by tuning the applied DC and RF voltages on the trap electrodes, buffer gas flow and trap temperature. A TOF mass spectrum can be recorded by scanning the TOF delay of the ions.

An IRPD spectrum is recorded in the TOF-MS mode, typically in three subsequent steps. The first step is extraction of the ions from the trap, followed by irradiation with the IR light and then recording of the TOF MS. The triggering scheme of the IRPD experiments is illustrated in Fig. 3.8. The fill and extraction cycle of the ion trap is synchronized with the repetition rate of the IR radiation source (5 or 10 Hz, see section 3.5). The extracted ion cloud (parent) from the trap is irradiated with an IR light pulse prior to or at the same time with the application of the HV pulses discussed above. The trigger timing of the IR laser and HV pulses is critical.

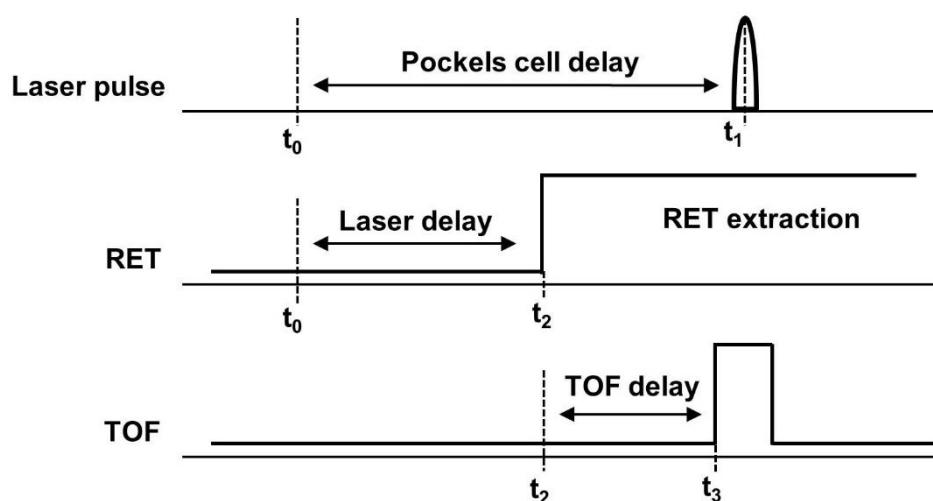


Figure 3.8: Trigger scheme for IRPD experiments.

Three possible cases are:

1. $t_3 = t_1$: The TOF HV pulses are triggered at the same time with the irradiation by the IR laser pulse. This is the standard way of measurement. Here, the ions are irradiated when they are in the center of the extraction plates and at the very beginning of the acceleration process.
2. $t_2 > t_1$: The IR laser pulse is emitted prior to ion extraction from the trap. The ion packet is irradiated inside the trap. This should be avoided in normal operation.
3. $t_3 < t_1$: The IR laser pulse is triggered after TOF high voltage pulses have been applied, i.e. the ion packet is irradiated during the acceleration process. This mode is advantageous in case of an unavoidable collision induced dissociation (CID) process occurring at the trap. Here, with the pre-acceleration, the CID fragments get separated from the parent ions according to their mass-to-charge ratio prior to the irradiation with laser light. So, photofragmented and CID ions get separated in time, which allows measuring the photofragmented ion yield background free i.e. without any contribution from the CID fragments.

When the frequency of the IR radiation is in resonance with a vibrational transition of the irradiated cluster ion, resonant absorption of one or multiple photons occurs followed by photodissociation (for details, see chapter 2.3) forming fragment ions. As a result, a decrease in the parent ion signal $I_P(\nu)$ and an increase in the fragment ion signal $I_F(\nu)$ are observed. The fluctuations in ion signal due to instabilities at the ion source are cancelled out by normalizing the parent and fragment ion intensities to the total ion signal. Generally, the IRPD process assumes photodissociation with the absorption of a single photon. The photon fluence, $F(\nu)$, which is defined as the number of photons passing through an area A , is used to normalize the logarithm of the relative parent ion abundance to obtain the IRPD cross section $\sigma_{IRPD}(\nu)$.^{23, 24}

$$\sigma_{IRPD}(\nu) = -\ln \left[\frac{I_P(\nu)}{I_P(\nu) + I_F(\nu)} \right] / F(\nu) \quad 3.02$$

as, $I_P(\nu) + \Sigma I_F(\nu) = 1$, $\sigma_{IRPD}(\nu)$ effectively becomes:

$$\sigma_{IRPD}(\nu) = -\ln[I_P(\nu)] / F(\nu) \quad 3.03$$

However, determination of the laser and ion beam interaction volume is difficult, due to the fact of a) the laser beam diameter changes with changing wavenumber and b) the exact dimension of the ion packets is unknown. If we assume that the laser beam diameter is smaller than the diameter of the irradiated ion beam, thus all the ions along the laser beam are irradiated. Then, $F(\nu)$ can be approximated by measuring the laser pulse energy $P(\nu)$, where, $F(\nu) = P(\nu)/h\nu$.^{8, 9} This approximation holds fairly well for the messenger tagging or IRPD process. For IRMPD measurements considering $P(\nu)$ instead of $F(\nu)$ is seen to give better results in terms of relative peak intensities.²⁵ The effect of the laser diameter change probably compensated by the IRMPD photodissociation efficiency and that can be the reason for improved results.^{8, 9}

3.5 Infrared Light Sources

It is already discussed in Chapter 2 of this thesis, that action spectroscopy demands intense and tunable laser light sources. However, the availability of powerful and tunable light sources in the mid and far IR spectral range is very limited. Development of optical parametric oscillator/amplifier (OPO/OPA) laser systems started in the early 90's,²⁶ but wide range accessibility was achieved much later. Nowadays the OPO/OPA system combined with AgGaSe₂ crystal can produce IR light in the range of ~ 770 -7400 cm⁻¹. The IR free electron laser (IR FEL) remains the only source to produce tunable IR light with high output power over a wide IR spectral range, but there are only a few them around the world. The Fritz Haber Institute Free Electron Laser (FHI FEL) became operational from the year 2013. It provides powerful pulsed laser radiation in the 200 – 3400 cm⁻¹ wavenumber range.²⁷ This section provides the operating principles of the FHI FEL,²⁷ which was used to perform all the experiments presented in this thesis. The detailed description and operating principles of a table top OPO/OPA laser system, which is also available in our group, are summarized in ref.^{8, 9} and not shown here.

3.5.1. The FHI FEL

A schematic overview of the FHI FEL is shown in Fig. 3.9. Electron bunches are produced with a gridded electron gun running at a bunch repetition rate of 1 GHz. A buncher cavity is used to compress the electron bunches before entering the first RF linear accelerator (linac 1 in fig. 3.9) where the electrons are accelerated to a constant 20 MeV energy. The second linac (linac 2 in fig. 3.9) is used for further acceleration or deceleration of the electrons to a final energy within the range 15-50

3. Experimental Setup

MeV. The electron micro bunches are as short as ~ 3 to 5 ps. The chicane, placed in between the two linacs, can be used to further shorten the micro bunch length, but it was not in operation when running the experiments presented in this thesis. The micro bunches form bunch trains (macro bunches), which are usually 10-12 μs long and come at a repetition rate of 5 Hz (10 Hz repetition rate is also possible). A set of dipole and quadrupole magnets guide the electron beam into the Mid-IR (MIR) undulator.

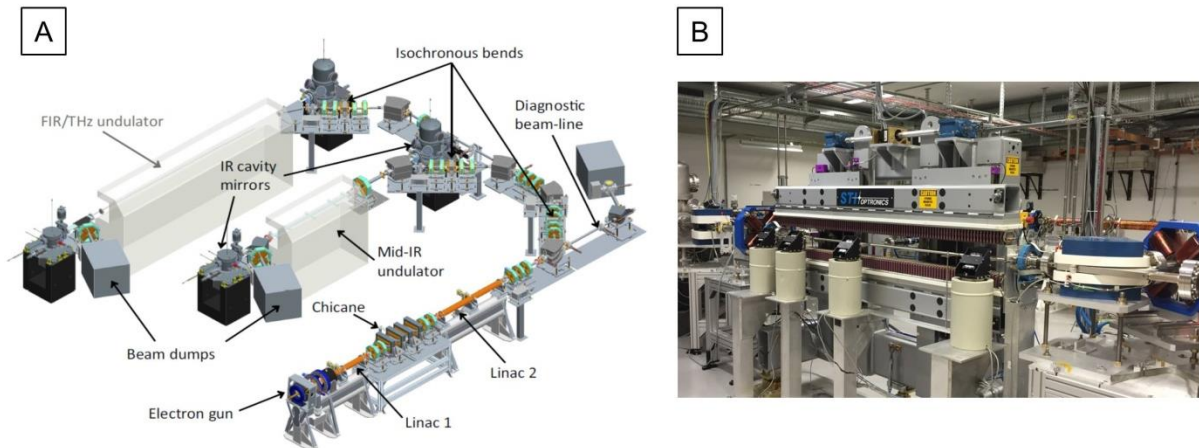


Fig. 3.9: A. Schematic overview of the FHI FEL, the figure is taken from Ref.²⁷. B. MIR FEL undulator.

The 2 m long hybrid-magnet undulator, located within a 5.4 m long IR cavity (fig. 3.8B) is built with strong NdFeB magnets. The undulator contains 50 periods with an undulator period $\lambda_u = 40$ mm. When operating, the alternating orientation of the magnetic field forces the electrons onto a “wiggling” motion by the effect of the Lorentz force. The MIR FEL cavity is formed by two gold plated concave copper mirrors named as end- and out-coupling mirror. A motorized in vacuum mirror changer is used for precise positioning of the out-coupling mirrors. Different hole diameters are used to achieve optimized out-coupling efficiency at different wavelengths: five different mirrors with hole diameter of 0.75, 1.0, 1.5, 2.5 and 3.5 mm are available. The out-coupled light is guided through a vacuum system (IR beamline) to the user stations.

While travelling with the “wiggling” motion, radiation is emitted tangentially in the forward direction at every turn of the electron trajectory. The wavelength of the radiation corresponds to the slippage (per undulator period) between the photons (straight path) and the electrons (wiggling path). Due to the transverse motion, the effective longitudinal path length travelled by the electrons is shortened w.r.t the path travelled by the photons by a factor of $(1+K^2)$. Here, K denotes the dimensionless undulator parameter which is directly proportional to the magnetic field strength. The emitted wavelength is further influenced by a strong Doppler shift which shifts it by a factor of $2\gamma^2$ (γ being the relativistic Lorentz factor that gives the electron's total energy in terms of its rest energy) and the resulting wavelength is given by:

$$\lambda_{FEL} = \frac{\lambda_u}{2\gamma^2} (1 + K^2) \quad 3.04$$

The accessible spectral range is limited by electron energy and minimum undulator gap. At the minimum undulator gap of ~ 17 mm with the minimum possible electron energy of 15 MeV, the smallest wavenumber that can be reached is 200 cm^{-1} . Presently, lasing is possible up to a maximum wavenumber of $\sim 3400 \text{ cm}^{-1}$. The full width at half maximum (FWHM) bandwidth ranges between 0.3 to 1% of the central wavelength. The typical micro pulse energy is 5-10 μJ . This corresponds to 50-100 mJ macro pulse energy as can be seen in detail in fig. 3.10.

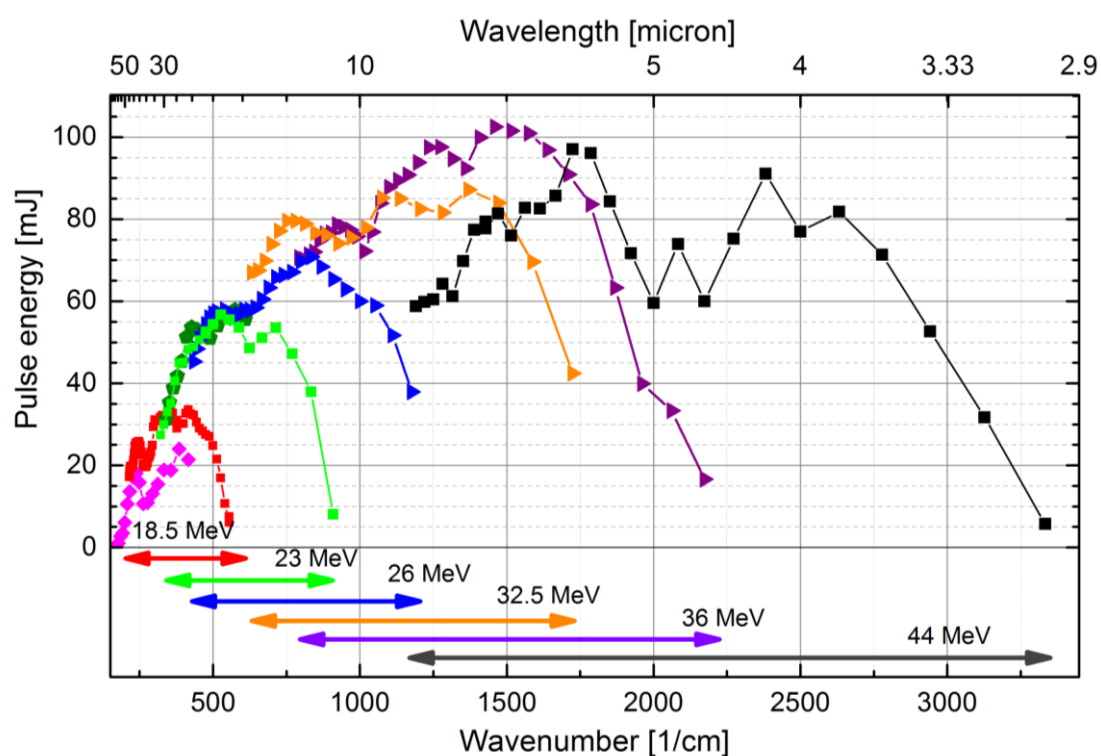


Fig. 3.10: Macro-pulse energies of the FHI FEL for narrow bandwidth conditions ($< 1\%$ relative full width at half maximum) at various electron energies. The Figure adapted from Ref.²⁸

References:

1. T. G. Dietz, M. A. Duncan, D. E. Powers and R. E. Smalley, *The Journal of Chemical Physics*, 1981, **74**, 6511-6512.
2. D. E. Powers, S. G. Hansen, M. Geusic, A. Puiu, J. Hopkins, T. Dietz, M. Duncan, P. Langridge-Smith and R. Smalley, *The Journal of Physical Chemistry*, 1982, **86**, 2556-2560.
3. V. Bondybey and J. English, *The Journal of Chemical Physics*, 1981, **74**, 6978-6979.
4. M. A. Duncan, *Review of Scientific Instruments*, 2012, **83**, 041101.
5. J. Ready, *Effects of high-power laser radiation*, Elsevier, 2012.
6. P. Milani and W. A. deHeer, *Review of scientific instruments*, 1990, **61**, 1835-1838.
7. C. M. Neal, G. A. Breaux, B. Cao, A. K. Starace and M. F. Jarrold, *Review of Scientific Instruments*, 2007, **78**, 075108.

3. Experimental Setup

8. T. Wende, PhD Thesis, Freie Universität Berlin, 2012.
9. M. R. Fagiani, PhD Thesis, Freie Universität Berlin, 2017.
10. S. Debnath, X. Song, M. R. Fagiani, M. L. Weichman, M. Gao, S. Maeda, T. Taketsugu, W. Schöllkopf, A. Lyalin, D. M. Neumark and K. R. Asmis, *The Journal of Physical Chemistry C*, 2019, **123**, 8439-8446.
11. J. B. Fenn, M. Mann, C. K. Meng, S. F. Wong and C. M. Whitehouse, *Science*, 1989, **246**, 64-71.
12. M. Dole, L. L. Mack, R. L. Hines, R. C. Mobley, L. D. Ferguson and M. B. Alice, *The Journal of chemical physics*, 1968, **49**, 2240-2249.
13. J. B. Fenn, M. Mann, C. K. Meng, S. F. Wong and C. M. Whitehouse, *Mass Spectrometry Reviews*, 1990, **9**, 37-70.
14. A. P. Bruins, T. R. Covey and J. D. Henion, *Analytical Chemistry*, 1987, **59**, 2642-2646.
15. T. R. Covey, R. F. Bonner, B. I. Shushan and J. Henion, *Rapid communications in mass spectrometry : RCM*, 1988, **2**, 249-256.
16. M. G. Ikonomidou, A. T. Blades and P. Kebarle, *Analytical Chemistry*, 1991, **63**, 1989-1998.
17. Micromass Quattro Ultima PtMass Spectrometer, https://www.waters.com/webassets/cms/support/docs/quattro_ultima_pt_guide_reva.pdf.
18. D. P. Smith, *IEEE transactions on industry applications*, 1986, 527-535.
19. D. J. Goebbert, T. Wende, R. Bergmann, G. Meijer and K. R. Asmis, *The Journal of Physical Chemistry A*, 2009, **113**, 5874-5880.
20. M. Brümmer, C. Kaposta, G. Santambrogio and K. R. Asmis, *The Journal of chemical physics*, 2003, **119**, 12700-12703.
21. T. Esser, Msters Thesis, Freie Universität Berlin, 2013.
22. W. Wiley and I. H. McLaren, *Review of scientific instruments*, 1955, **26**, 1150-1157.
23. N. Heine and K. R. Asmis, *International Reviews in Physical Chemistry*, 2015, **34**, 1-34.
24. N. Heine and K. R. Asmis, *International Reviews in Physical Chemistry*, 2016, **35**, 507-507.
25. J. Oomens, A. Tielens, B. G. Sartakov, G. von Helden and G. Meijer, *The Astrophysical Journal*, 2003, **591**, 968.
26. W. Bosenberg and D. R. Guyer, *JOSA B*, 1993, **10**, 1716-1722.
27. W. Schöllkopf, S. Gewinner, H. Junkes, A. Paarmann, G. von Helden, H. Bluem and A. M. Todd, *The new IR and THz FEL facility at the Fritz Haber Institute in Berlin*, SPIE, 2015.
28. The FHI free-electron laser (FEL) facility <http://fel.fhi-berlin.mpg.de/Main/Specs>.

Chapter 4

Al/Fe- Mixed Metal Oxide Clusters

The main goal of this chapter is characterization of structure-reactivity relationship of mixed-metal oxide clusters. In 2008, Santambrogio et al. published a study on identifying global minimum structures of electronically closed shell small aluminium oxide clusters.¹ The same Al-oxide clusters are chosen and one Al- atom is substituted with an Fe- atom into each cluster. The binary metal oxide clusters are studied using gas phase cryogenic vibrational spectroscopy in combination with high level quantum chemical calculations. Insights are gained regarding structural evolution of the mixed-metal oxide clusters compared to the pure Al-oxide ones together with understanding of charge state and preferred coordination site of the substituted Fe-atom.

4.1. Infrared Photodissociation Spectroscopy of $[(\text{Al}_2\text{O}_3)_n\text{FeO}]^+$ with $n = 2-5$: Influence of Fe-Impurities on Structure and Other Properties

The ready to submit manuscript “Infrared Photodissociation Spectroscopy of $[(\text{Al}_2\text{O}_3)_n\text{FeO}]^+$ with $n = 2-5$: Influence of Fe-Impurities on Structure and Other Properties” demonstrates the influence of an Fe-atom on structure and other properties of small Al-oxide clusters. The $[(\text{Al}_2\text{O}_3)_{2-5}(\text{FeO})]^+$ clusters are produced in a pulsed laser vaporization source using an Fe/Al (30/70 wt%) mixed metal rod. Experimental IRPD spectra are compared with high level theoretical calculations and the structures are assigned based on energetic preference together with spectral match. The unambiguous structural assignment allows identification of characteristic vibrational modes of the studied clusters. Moreover, for smaller clusters ($n=2-3$) the Fe-O signature vibrations were identified. These insights allow testing the theoretical methods to be applied to more complex systems or even investigation of chemical reactions involving small molecular clusters.

*supporting info of this manuscript can be found in Appendix A.

1. Santambrogio, G., et al., *Journal of the American Chemical Society*, 2008, **130(45)**, 15143-15149.

Declaration of Contribution:

I planned and performed the experimental work, including the measurement of all IRPD spectra, evaluated the data using the cosine similarity score and interpreted the results. The electronic structure calculations were done by Fabian Müller. I made all the figures and wrote the first version of the manuscript. Other contributions of the co-authors are listed below:

Marcel Jorewitz	Assisted during the beam-time measurements.
Julius B. Stückerath	Contributed in part to the calculations with Fabian Müller.
Florian Bischoff	Supervised Fabian Müller.
Joachim Sauer, Knut. R. Asmis	Coordinated the project, framed the principal idea, supervised the research, helped in the data interpretation and revised the manuscript.

Infrared Photodissociation Spectroscopy of $[(\text{Al}_2\text{O}_3)_n\text{FeO}]^+$ with $n = 2-5$: Influence of Fe-Impurities on Structure and Other Properties

Sreekanta Debnath,^{a,b} Marcel Jorewitz,^a Fabian Müller,^c Julius B. Stückrath^c, Florian Bischoff,^c Knut R. Asmis,^{a*} Joachim Sauer^{c*}

^aWilhelm-Ostwald-Institut für Physikalische und Theoretische Chemie, Universität Leipzig, Linnéstrasse 2, 04103 Leipzig, Germany

^bFritz-Haber-Institut der Max-Planck-Gesellschaft, Faradayweg 4-6, 14195 Berlin, Germany

^cInstitut für Chemie, Humboldt-Universität zu Berlin, Unter den Linden 6, D-10099 Berlin, Germany

*knut.asmis@uni-leipzig.de, js@chemie.hu-berlin.de

Abstract

Atomic Fe-impurities in small aluminium oxide clusters are studied by cryogenic ion trap vibrational spectroscopy combined with density functional theory (DFT) calculations. The infrared photodissociation spectra of He-tagged $[(\text{Al}_2\text{O}_3)_n\text{FeO}]^+$ ($n=2-5$) are reported in the Al-O and Fe-O stretching and bending spectral region ($430-1200\text{ cm}^{-1}$), and assigned based on a comparison to harmonic IR spectra from DFT calculations. The exchange of an Al- for a Fe-center occurs preferentially at 3-fold oxygen coordination sites located at the cluster rim, leaving the Al-O network structure nearly unperturbed. The results are discussed in the context of Fe-doped zeolites and in how far isolated clusters can serve as model systems for these.

Introduction

Research on metal oxides has attracted considerable attention because of their versatile use, for example as photocatalysts, catalyst supports,¹ coatings,² abrasives and nanosensors.³ Microporous aluminosilicates, which are commonly known as zeolites, are one of the most studied metal oxides in last decades because of their increasing applications in chemical industry. Pure aluminosilicates cannot be photoexcited, even with UV radiation, because they are insulators with a band gap of about 7 eV. However, transition metal (TM) doping of the zeolite molecular sieve can activate them towards photocatalysis⁴ by generating electron-hole pairs as in semiconductors. Moreover, several studies have shown that the photocatalytic efficiency increases with increasing dopant concentration, i.e. the TM-impurities present in zeolites, and not the Al-O units, are responsible for the light-induced activity. It is known that for example, the charge transfer excited state $[\text{Fe}^{2+}-\text{O}]^*$ can promote photocatalytic reduction of CO_2 with H_2O ,⁵ photocatalytic oxidation of organic molecules like ethylene, bromomethane and methyl orange,⁶ and oxidation of benzene to phenol.⁷ In order to obtain better insight into the elementary steps of heterogeneous photocatalysis⁸ and to ultimately design functional building blocks in nanostructured materials, gas phase studies on isolated metal oxide clusters of well-defined compositions have proven to be an ideal arena. The reduced complexity due to the absence of a perturbing environment or support, combined with the highly selective and sensitive arsenal

of experimental techniques allows for a systematic characterization of a cluster's intrinsic physical and chemical properties at the molecular level.

Cryogenic ion trap vibrational spectroscopy⁹⁻¹⁰ in combination with quantum chemical calculations is a useful tool to investigate structure-reactivity correlations in isolated polynuclear metal oxide clusters.^{9, 11-12} While a number of studies has been reported to address the reactivity and structural characterization of pure aluminium oxide cluster ions,¹³⁻²³ experimental studies on the mixed metal oxides²⁴⁻³¹ are more scarce. Mafuné et al. have studied the influence of substitution with a transition metal on the cluster reactivity.³²⁻³⁵ Lievens et al. have addressed the nature of the optical properties of clusters confined inside zeolite frameworks.³⁶⁻³⁸

In the present study we characterize how a Fe-impurity influences the structure and other properties of Al-oxide clusters. Therefore, we chose the $[(\text{Al}_2\text{O}_3)_{2-5}\text{FeO}]^+$ clusters as a model system for Fe-impurities in zeolites and our goal is to understand the preferred doping site of the Fe-atom in an innocent metal oxide network. The structural property of $\text{FeAl}_2\text{O}_4^+$ ($n = 1$) is also studied and reported elsewhere³⁹ where the nature of the $[\text{Fe}^{2+}\text{-O}]^*$ photocatalytic active site is also summarized.

Experimental Methods:

The infrared photodissociation (IRPD) experiments are carried out on a 10 K ion trap-tandem mass spectrometer⁴⁰ using the widely tunable, intense IR radiation from the Fritz-Haber-Institute Free-Electron Laser (FHI FEL).⁴¹ In brief, $[(\text{Al}_2\text{O}_3)_n\text{FeO}]^+$ ions ($n = 2 - 5$) are produced in a pulsed laser vaporization source by focusing a frequency-doubled Nd:YAG laser (50 Hz, 10–15 mJ) onto a rotating Fe/Al (30/70 wt%) metal rod (Plasmaterials). The resulting plasma is quenched with a gas pulse of 0.5% O_2 seeded in He. Cluster ions are formed during expansion through a clustering channel downstream from the rod and pass through a skimmer. The beam of ions is then collimated and thermalized close to room temperature in a He-gas filled radio frequency (RF) ion guide, mass-selected using a quadrupole mass-filter, and focused into a cryogenically cooled RF ring-electrode ion-trap. The trap is continuously filled with He-buffer gas and held at a temperature of 12 K. Many collisions of the trapped ions with the buffer gas provide gentle cooling of the internal degrees of freedom close to the ambient temperature. At sufficiently low ion-trap temperatures, ion-He complexes are formed via three-body collisions.⁴² All ions are extracted from the ion trap and focused both temporally and spatially into the center of the extraction region of an orthogonally mounted reflectron time-of-flight (TOF) tandem mass-spectrometer. Here, the ions are irradiated with a counter-propagating IR laser pulse produced by the FHI-FEL ($430\text{--}1200\text{ cm}^{-1}$, 5Hz), with a bandwidth of $\sim 0.5\%$ fwhm and pulse energy of 0.7-2.5 mJ. Parent as well as photofragment ion yields are monitored simultaneously as a function of the irradiation wavelength. IRPD scans are recorded by averaging over 100 TOF mass spectra per wavelength step (3 cm^{-1}). Typically, at least three scans are summed to obtain the final IRPD spectrum. The photodissociation cross section σ_{IRPD} is determined as described previously.⁴³⁻⁴⁴

Computational Methods:

A global energy minimization for the clusters of the compositions $[(Al_2O_3)_nFeO]^+$ ($n = 2 - 5$) is carried out employing a genetic algorithm (GA)^{13, 45} to create reasonable isomer structures. Splitting and recombination of the produced structures is stopped when the energy of the most stable isomer as well as the averaged energy of all unique structures per generation did not change any more. Thereby, 1200 structures are created in the case of $[(Al_2O_3)_2FeO]^+$ and 1700 for each of the $[(Al_2O_3)_{3-5}FeO]^+$ systems.

In the genetic algorithm optimizations the BP86⁴⁶⁻⁴⁷ exchange correlation density functional is used together with a split valence basis set (def2-SVP⁴⁸) for the sake of computational efficiency. The total electronic spin of all investigated systems in this step was fixed at $S = 5/2$, i.e. the high spin state of the iron atom. Thus, the orbital unrestricted Kohn-Sham (UKS) formalism is required to handle the open shell electronic structure. The resolution of the identity (RI) approximation is used to accelerate the Coulomb fitting in the global structure search of the biggest cluster ($n = 5$). The most stable unique isomers of each composition are re-optimized employing both the TPSSh⁴⁹ and the B3LYP⁵⁰⁻⁵² exchange correlation functional in conjunction with the triple zeta basis set def2-TZVP⁵³. Vibrational frequencies are calculated within the double harmonic approximation. The resulting stick spectra are convoluted with Gaussian functions of 10 cm^{-1} full width at half maximum (FWHM) to account for the broadening of the measured features.

Additionally, PBE0/def2-TZVP is used to optimize the structure of the two lowest energy isomers of $[(Al_2O_3)_2FeO]^+$ and anharmonic frequencies are calculated with the algorithms implemented in Gaussian 16. Molecular dynamics simulations of about 40 ps length (step size 100 a.u.) starting from the most stable isomer are carried out at a pseudo-temperature of 400 K to provide a compensation for the missing zero point vibration energy. PBE0 was chosen for all anharmonic calculations since it provides properties of iron oxygen systems that are in excellent agreement with experimental data and is only slightly worse in predicting correct energetics than TPSSh.

The influence of the He tagging atoms was investigated recently³⁹ for the cluster $[(Al_2O_3)FeO]^+$ and found to be of negligible extent. It is, therefore, not further considered in this work.

All calculations except the anharmonic frequency estimation are performed with the Turbomole program package V7.0.2.⁵⁴⁻⁵⁶ The isomers are labelled with $^y n \mathbf{x}_{Fe/Al}$, where n is the number of (Al_2O_3) unit present in the cluster, $\mathbf{x} = a, b, c..$ indicates the energetic ordering, superscript y represents the spin state, subscript **Fe** stands for the doped clusters whereas **Al** represents pure Al-oxide systems. Isomers with similar geometry but having the Fe-atom at different positions are marked off with i, ii, iii, etc. together with the general labelling.

To obtain a quantitative measure for the agreement of experimental and theoretical spectra, the cosine similarity score⁵⁷ is used. The score S expresses the similarity between two

spectra. The intensity of the experimental and predicted absorptions is represented by, say, the vectors **A** and **B**, and the score is calculated using eq. 1. i.e. by their normalized dot product.

$$S = \cos(\theta) = \frac{\mathbf{A} \cdot \mathbf{B}}{\|\mathbf{A}\| \|\mathbf{B}\|} = \frac{\sum_{i=1}^n A_i B_i}{\sqrt{\sum_{i=1}^n A_i^2} \sqrt{\sum_{i=1}^n B_i^2}} \quad (1)$$

The score can vary from zero to unity, and a *S* value closer to 1 indicates greater similarity. A uniform protocol was followed to obtain the cosine score between the experimental spectrum and the scaled computed spectra for all the cluster sizes reported here. The experimental spectrum of $n = 1$ is well reproduced by isomer ${}^6\mathbf{1b}_{Fe}$ whereas ${}^6\mathbf{1a}_{Fe}$ can barely explain it (Fig. S1).³⁹ The cosine score was calculated for both the isomers following eq.1; the best result was obtained ${}^6\mathbf{1b}_{Fe}$ ($S=0.88$), ${}^6\mathbf{1a}_{Fe}$ ($S=0.20$) with a scaling factor of 1.0166, 15 cm^{-1} FWHM and within 440 – 1080 cm^{-1} measured range. The same parameters are used to calculate the cosine scores throughout the paper.

Result and Discussion:

The IRPD spectra of He-tagged $[(\text{Al}_2\text{O}_3)_n\text{FeO}]^+$ with $n = 2$ to 5 are compared to those previously reported¹⁴ for the He-tagged *all*-aluminium analogues $[(\text{Al}_2\text{O}_3)_n\text{AlO}]^+$ in the spectral region from 430 cm^{-1} to 1200 cm^{-1} in Fig. 1 (see Table S2 for experimental band positions and assignments). Based on our previous studies of monometallic Al- and Fe-oxide clusters, we group the observed IR absorptions into three characteristic spectral regions: (i) 1200-900 cm^{-1} , (ii) 900-600 cm^{-1} and (iii) 600-430 cm^{-1} .^{15-16, 26, 58-59} These regions cover (i) Al-O stretching modes involving the shortest (≤ 1.73 Å) Al-O bonds, (ii) Fe-O stretching modes together with medium-length (1.74-1.78 Å) Al-O bond stretches and (iii) ring breathing modes as well as stretching and bending modes involving the longest (>1.8 Å) Al-O bonds.

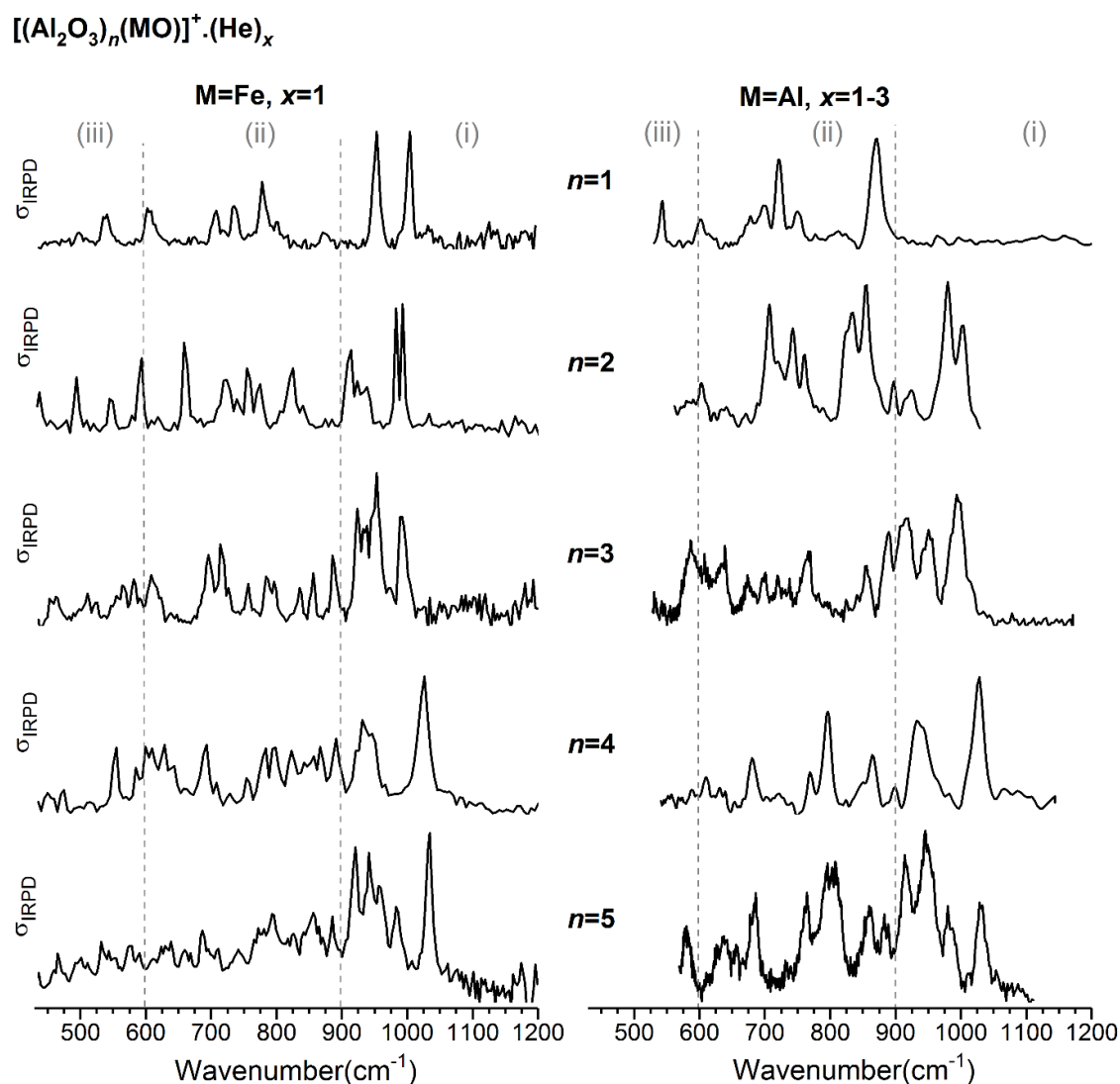


Figure 1. Experimental IRPD spectra of He-tagged $[(\text{Al}_2\text{O}_3)_n(\text{MO})]^+$ with $n = 1-5$. Spectra for $\text{M}=\text{Fe}$ are shown on the left hand side and those for $\text{M}=\text{Al}$ on the right hand side panel. See Table S2 for band positions and assignments. Three characteristic spectral regions are indicated by the dashed lines and cover (i) Al-O stretching modes involving the shortest (1.70 -1.73 Å) Al-O bonds (1200-900 cm^{-1}), (ii) Fe-O stretching and lower-energy Al-O stretching modes involving medium (1.74 -1.78 Å) bond lengths (900-600 cm^{-1}), and (iii) ring deformation modes (<600 cm^{-1}).

Fig. 1 reveals that the spectra for $[(\text{Al}_2\text{O}_3)_n\text{FeO}]^+$ and $[(\text{Al}_2\text{O}_3)_n\text{AlO}]^+$ do not agree well for $n = 1$, but the degree of agreement is higher for $n > 2$, in particular in region (i), suggesting that the structures differ significantly for the smallest cluster, but become more alike with increasing n . This observation is confirmed by applying the cosine similarity score to each pair of experimental spectra with same n , which yields S values of 0.31, 0.49, 0.68, 0.85 and 0.86 for $n = 1$ to 5, respectively. The most intense absorption bands for $[(\text{Al}_2\text{O}_3)_n\text{FeO}]^+$ are seen in region (i), and the highest energy transition is found in the spectrum of the largest cluster, $n = 5$, at 1034 cm^{-1} . Region (ii) is rich with IR signatures and the spectral congestion

increases with increasing cluster size. Spectra of the *all*-Al species also show most intense absorption in region (i), except for Al_3O_4^+ , which does not absorb significantly in this region.

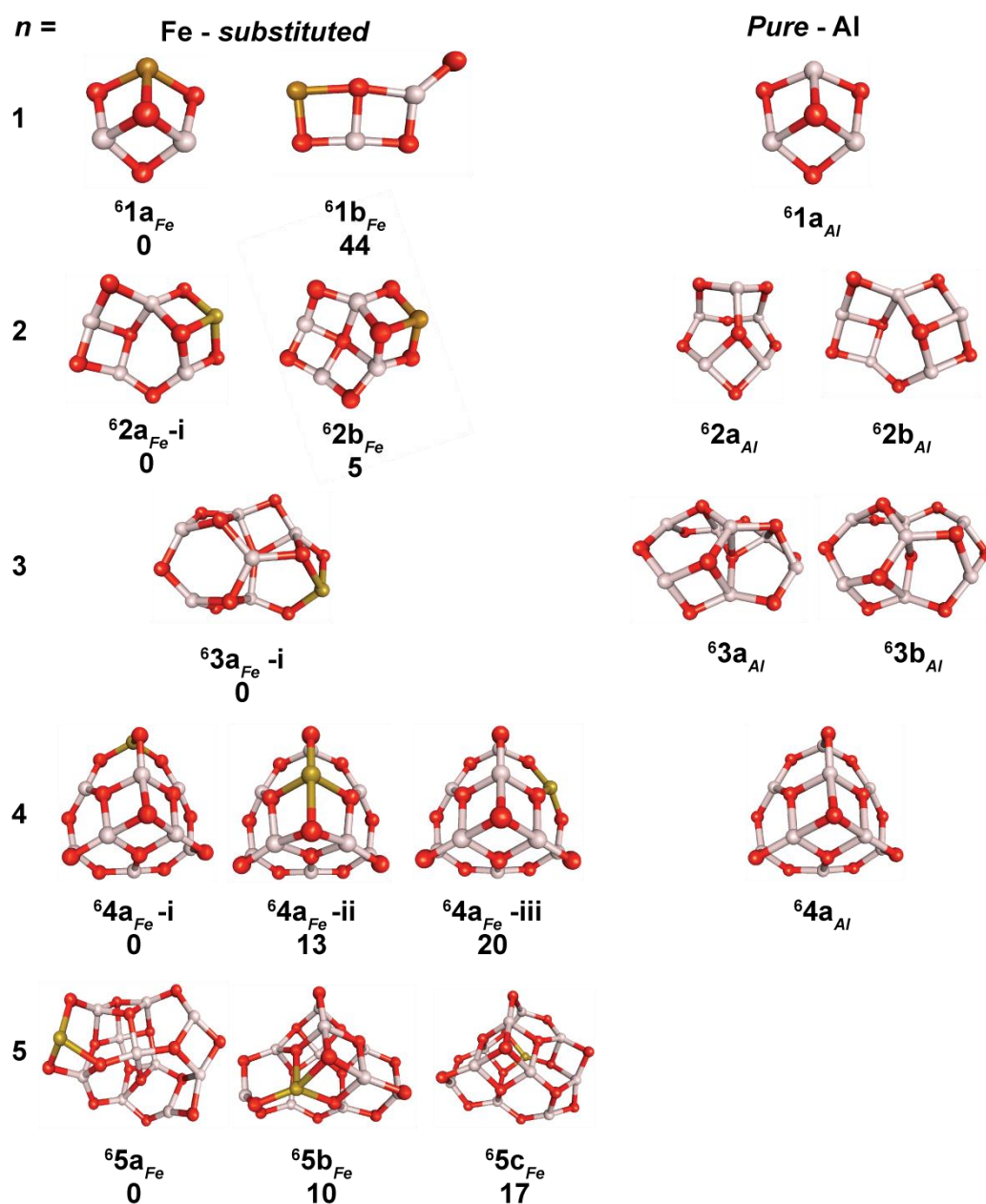


Figure 2. Comparison of the TPSSH/def2-TZVP low-energy isomers (left side) that are found to contribute to the IRPD spectra of $[(\text{Al}_2\text{O}_3)_n(\text{FeO})]^+$ ($n = 1-5$)³⁹ and the B3LYP/def2-TZVP structures (right side) assigned to the corresponding IRPD spectra of the *all*-Al-analogue¹⁴ for each cluster size. The isomers are labelled with ${}^y n x_{\text{Fe/Al}}$, where n is the number of (Al_2O_3) unit, $x = \text{a, b, c, ...}$, which indicates the energetic ordering, superscript y indicates the spin state and subscript *Fe/Al* corresponds to the Fe-substituted and *all*-Al clusters, respectively. The ZPE-corrected DFT energies (in $\text{kJ}\cdot\text{mol}^{-1}$) are given below to each structure. Atoms in white = Al, yellow = Fe, and red = O.

The calculated minimum-energy structures for the pure and iron-doped aluminium oxide cations of each size are compared in Fig. 2. The structure of $\text{Al}_2\text{FeO}_4^+$ ($n = 1$) has been

assigned previously.³⁹ Briefly, it is a planar bicyclic structure with a terminal Al-O bond (${}^6\mathbf{1b}_{Fe}$ in Fig 2.), which is considerably different from the structure assigned for the all-Al analogue (${}^6\mathbf{1a}_{Al}$, first row Fig. 2). Isomer ${}^6\mathbf{1b}_{Fe}$ is considered to contain an unpaired electron on the terminal oxygen atom and accordingly six electrons in d-states of iron. This implies that iron is formally reduced to Fe^{+II} while a radical is formed on the terminal oxygen. Hence, $Al_2FeO_4^+$ can be written as $[Fe^{+II}Al_2O_3(O\cdot)]^+$ and represents the charge transfer excited state $[Fe^{2+}-O]^*$ in Fe-doped zeolites.

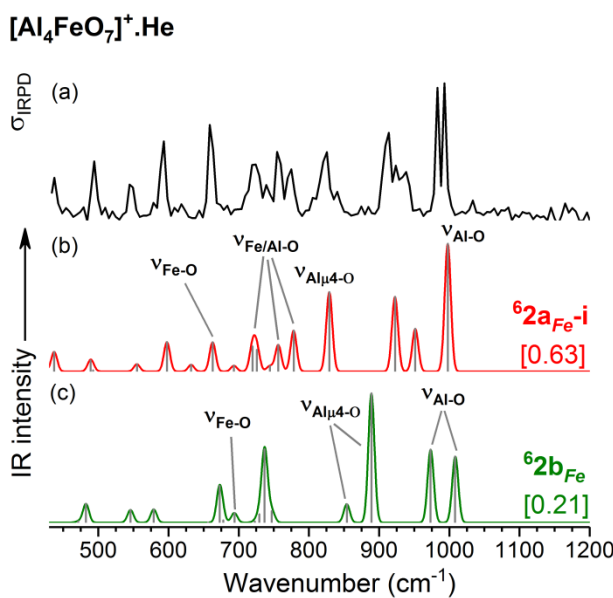


Figure 3A. Experimental IRPD spectra of He-tagged $Al_4FeO_7^+$ (top trace) compared with computed un-tagged IR spectra (lower traces) of the lowest-energy isomers [${}^6\mathbf{2a}_{Fe-i}$ and ${}^6\mathbf{2b}_{Fe}$]. The calculated IR spectra, derived from TPSSh/def2-TZVP harmonic frequencies (scaled by 1.0166) and intensities, are plotted with sticks (gray) and a 10 cm^{-1} FWHM Gaussian line shape convolution. Individual spectrum is colour coded using red and green. The cosine similarity score (see eq. 1) is shown in square brackets. See Fig. 2 for the structures and relative energies of the contributing isomers, SI for the relative energies of the low energy isomers (Table S1) and the individual spectra of the isomers and IR band assignments (Table S2).

The global minimum-energy structure predicted for $Al_4FeO_7^+$ ($n = 2$) is the sheet-like structure ${}^6\mathbf{2a}_{Fe-i}$ of C_1 symmetry (see Fig. 2). It is a bicyclic compound with two 6-membered rings which are fused together with a 4-fold coordinated Al-atom on one side and a bridging 2-fold coordinated oxygen atom on another side. This structure has 3- and 4-fold coordinated Al-atoms with 2- and 3-fold coordinated O-atoms in alternating positions, and a 3-fold coordinated Fe atom. Isomer ${}^6\mathbf{2b}_{Fe}$ ($5\text{ kJ}\cdot\text{mol}^{-1}$) is a C_s symmetric cage type structure, where, one of the 3-fold oxygen atom ($\mu_3\text{-O}$) from ${}^6\mathbf{2a}_{Fe-i}$ is linked with the 3-fold coordinated Al-atom from the Fe-atom containing ring, i.e. generating a 4-fold coordinated O-atom. Thus, an Al_2FeO_4 conical part (similar to ${}^6\mathbf{1a}_{Fe}$) is formed which is fused together with three other 4-membered rings next to each other. Other calculated low energy isomers are shown in Fig. S7 and comparison of their corresponding calculated IR spectra with the

experiment is presented in Fig. S2. Isomers ${}^6\mathbf{2a}_{Fe}$ -ii (52 kJ·mol⁻¹) and ${}^6\mathbf{2a}_{Fe}$ -iii (95 kJ·mol⁻¹) have similar geometries and the same spin as ${}^6\mathbf{2a}_{Fe}$ -i, but the Fe-atom is located at a different position (see Fig. S7).

The simulated spectrum of ${}^6\mathbf{2a}_{Fe}$ -i (see Fig. 3A-b) accounts for most of the observed peaks in the IRPD spectrum of Al₄FeO₇⁺·He. However, the doublet observed at 983/993 cm⁻¹ and the shoulder of 825 cm⁻¹ peak at 840 cm⁻¹ call for a closer investigation. Unfortunately, the simple combination of the harmonic spectra of ${}^6\mathbf{2a}_{Fe}$ -i (S=0.63) and the energetically close lying ${}^6\mathbf{2b}_{Fe}$ (S=0.21) does not satisfactorily reproduce the experimental finding. This is mainly caused by the improper ratios of the peak intensities. Based on the DFT relative energies, the contribution of ${}^6\mathbf{2b}_{Fe}$ to the experimental spectrum should be minor and the characteristic doublet could not be reproduced. Hence, anharmonicity of the vibrational modes are taken into account. The calculated anharmonic vibrational frequencies of ${}^6\mathbf{2a}_{Fe}$ -i and ${}^6\mathbf{2b}_{Fe}$ derived on the PBE0 level (Fig. S3-a) are identical but blue shifted wrt. TPSSh harmonic frequencies; inherently, the doublet feature is not reproduced. However, the intensity difference of the highest energy absorption of the two isomers is reduced. In a molecular dynamic (MD) simulation starting from the ${}^6\mathbf{2a}_{Fe}$ -i isomer, infrequent isomerization to ${}^6\mathbf{2b}_{Fe}$ was observed. The MD result (Fig. S3-c) shows an emerging small peak at 11 cm⁻¹ lower (calc. at 994 cm⁻¹) than the major one (calc. at 1005 cm⁻¹). The Fe/Al – O vibration predicted at 777 cm⁻¹ (anharm. 781 cm⁻¹) and similar type of vibration at 236 cm⁻¹ of ${}^6\mathbf{2a}_{Fe}$ -i contributes one quantum each to generate a combination band at 1000 cm⁻¹, which is assumed to be responsible for the 994 cm⁻¹ signal in the MD spectra and provides a possible explanation for the highest energy doublet peak seen in the experimental spectrum. The rather low intensity of the new peak in the MD can be explained by the pure classic coupling between the motions. Incorporation of quantum effects via a quantum dynamic would result in an approaching of the features' strengths. The above mentioned doublet absorption band is assigned to the Al-μ₂-O-Al stretching modes (harmonic: 998 cm⁻¹) involving the shortest Al-O bonds (1.69 - 1.73 Å). The μ₄-Al – O stretching mode (calc. 829 cm⁻¹ for ${}^6\mathbf{2a}_{Fe}$ -i) is assigned to the 825 cm⁻¹ absorption and the shoulder 840 cm⁻¹ peak is a combination bands predicted at 830 cm⁻¹ and 832 cm⁻¹ in the anharmonic spectra of ${}^6\mathbf{2a}_{Fe}$ -i. The peak at 593 cm⁻¹ (calc. 597 cm⁻¹), results from the excitation of the 3-fold coordinated oxygen – aluminium (Al – μ₃-O) stretching. Fe-O stretching modes exclusively appear in region (ii) coupled with the medium length (>1.73 – 1.78 Å) Al-O stretches, almost decoupled Fe – μ₂-O stretching mode is assigned to the transition predicted at 663 cm⁻¹ (experiment 659 cm⁻¹).

The IRPD spectrum of the *all*-Al analogue Al₅O₇⁺·He (see Fig. 1) contains a contribution of the two isomers ${}^6\mathbf{2a}_{Al}$ and ${}^6\mathbf{2b}_{Al}$ (3:1 ratio), also shown in Fig. 2. While ${}^6\mathbf{2b}_{Al}$ is similar in structure to ${}^6\mathbf{2a}_{Fe}$ -i, the analogue of the cage-like structure ${}^6\mathbf{2a}_{Al}$ is ${}^6\mathbf{2c}_{Fe}$, which we do not observe here. As a fact, indeed, the experimental spectra of Al₄FeO₇⁺·He and Al₅O₇⁺·He show considerable differences in region (i) and (ii). Summarizing, substitution of an Al-atom by a Fe-atom in Al₅O₇⁺ stabilizes the sheet-like quasi 2D-structure over the 3D cage-like structure.

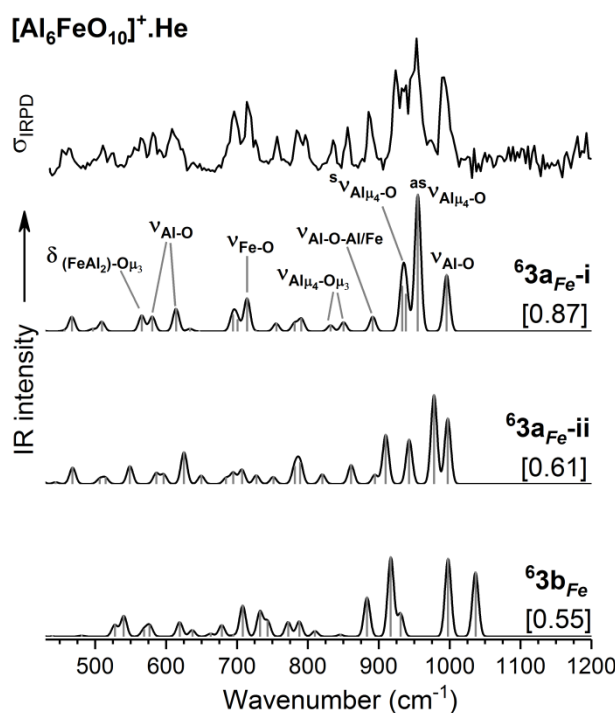


Figure 4. Experimental IRPD spectra of He-tagged $\text{Al}_6\text{FeO}_{10}^+$ (top trace) compared with computed IR spectra (lower traces) of the lowest-energy isomers [${}^6\mathbf{3a}_{\text{Fe-i}}$, ${}^6\mathbf{3a}_{\text{Fe-ii}}$ and ${}^6\mathbf{3b}_{\text{Fe}}$]. The calculated IR spectra, derived from TPSSH/def2-TZVP harmonic frequencies (scaled by 1.0166) and intensities, are plotted with sticks (gray) and a 10 cm^{-1} FWHM Gaussian line shape convolution. The cosine similarity score (see eqs. 1) is shown in square brackets. See Fig. 2 for the structures and relative energies of the contributing isomers and SI for the relative energies of the low energy isomers (Table S1), the individual spectra of the isomers and IR band assignments (Table S2).

The global minimum-energy isomer predicted for $\text{Al}_6\text{FeO}_{10}^+$, i.e. $n = 3$, is a cage-like structure ${}^6\mathbf{3a}_{\text{Fe-i}}$ (see Fig. 2) of C_1 symmetry, consisting of 6- and 4-membered rings, similar to the assigned ${}^6\mathbf{3a}_{\text{Al}}$ structure of $\text{Al}_7\text{O}_{10}^+$. Possible contributing structures are obtained by substituting an Al-atom in one of seven different positions of ${}^6\mathbf{3a}_{\text{Al}}$ with a Fe atom. This leads to structures ${}^6\mathbf{3a}_{\text{Fe-i}}$ to ${}^6\mathbf{3a}_{\text{Fe-vii}}$ (${}^6\mathbf{3a}_{\text{Fe-ii}}$ and ${}^6\mathbf{3a}_{\text{Fe-iii}}$ are identical structures with small distortion), which are listed in Fig. S7. They all are 20 - 75 $\text{kJ}\cdot\text{mol}^{-1}$ higher in energy than ${}^6\mathbf{3a}_{\text{Fe-i}}$. Isomers ${}^6\mathbf{3c}_{\text{Fe}}$ (24 $\text{kJ}\cdot\text{mol}^{-1}$), ${}^6\mathbf{3d}_{\text{Fe}}$ (24 $\text{kJ}\cdot\text{mol}^{-1}$) and ${}^6\mathbf{3f}_{\text{Fe}}$ (77 $\text{kJ}\cdot\text{mol}^{-1}$) are more symmetric variants of ${}^6\mathbf{3a}_{\text{Fe-i}}$, whereas ${}^6\mathbf{3b}_{\text{Fe}}$ (16 $\text{kJ}\cdot\text{mol}^{-1}$) and ${}^6\mathbf{3e}_{\text{Fe}}$ (35 $\text{kJ}\cdot\text{mol}^{-1}$) are distorted cage type structure (C_1 symmetry).

The identical structural motif of $\text{Al}_6\text{FeO}_{10}^+$ and $\text{Al}_7\text{O}_{10}^+$ is reflected in their similar He-tagged IRPD spectra. Most of the peaks observed in the experimental spectra of $\text{Al}_6\text{FeO}_{10}^+\cdot\text{He}$ can be explained with the simulated IR spectrum of ${}^6\mathbf{3a}_{\text{Fe-i}}$ (see Fig. 4), which also yields the highest cosine similarity score (0.87) among the lowest energy isomers (see Table S3). Unlike the IRPD spectra of all the other cluster sizes, the highest energy bands for $n = 3$ is not the most intense one. This band (992 cm^{-1}) is assigned to the stretching mode involving the shortest (1.70-1.73 Å) Al-O bonds comprising the outer rim of the cluster. The $\mu_4\text{-Al} - \text{O}$ bonds are

slightly longer (1.74-1.75 Å) and the corresponding stretching mode is blue-shifted from the $n = 2$ and lies in region (i). Region (ii) is rich with IR signatures from multiple Al-O and Fe-O stretching modes. The Fe – μ_2 -O stretching mode is observed at 714 cm^{-1} (calc.: 714 cm^{-1}). For $\text{Al}_7\text{O}_{10}^+$ the largest contribution is also from the corresponding structure ${}^6\mathbf{3a}_{\text{Al}}$ with a minor contribution (3:1 ratio) from the higher symmetric ${}^6\mathbf{3b}_{\text{Al}}$ isomer (3rd row, Fig. 2), even though ${}^6\mathbf{3b}_{\text{Al}}$ is predicted to be more stable than ${}^6\mathbf{3a}_{\text{Al}}$ using DFT or MP2.

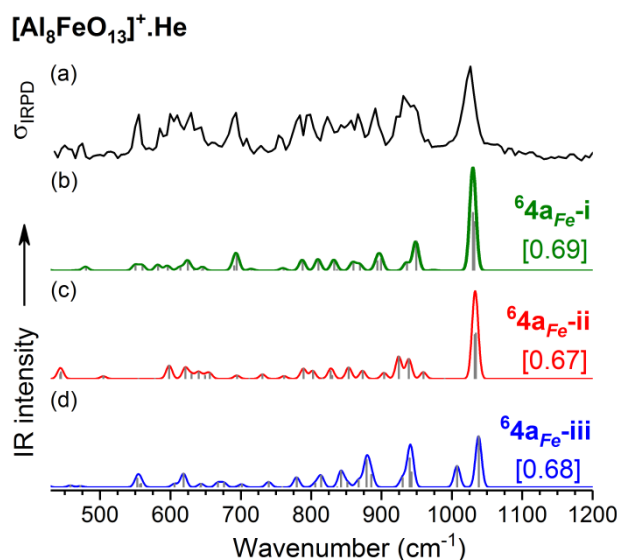


Figure 5. Experimental IRPD spectra of He-tagged $\text{Al}_8\text{FeO}_{13}^+$ (top trace) compared with computed IR spectra (lower traces) of the lowest-energy isomers ${}^6\mathbf{4a}_{\text{Fe}}\text{-i}$, ${}^6\mathbf{4a}_{\text{Fe}}\text{-ii}$ and ${}^6\mathbf{4a}_{\text{Fe}}\text{-iii}$. The calculated IR spectra, derived from TPSSh/def2-TZVP harmonic frequencies (scaled by 1.0166) and intensities, are plotted with sticks (gray) and a 10 cm^{-1} FWHM Gaussian line shape convolution. Each spectrum is colour coded with green, red and blue for individual isomers. The cosine similarity score (see eqs. 1) is shown in square brackets. See Fig. 2 for the structures and relative energies of the contributing isomers and the SI for the relative energies of the low energy isomers (Table S1), the individual spectra of the isomers and IR band assignments (Table S2).

The global minimum-energy structure for $\text{Al}_8\text{FeO}_{13}^+$ is the conical structure ${}^6\mathbf{4a}_{\text{Fe}}\text{-i}$ (see Fig. 2) in a sextet spin state and a symmetry, which is reduced from C_{3v} to C_s upon substitution of an Al with a Fe atom in the outer rim with $\mu_3\text{Fe} - \mu_2\text{O}$ coordination. The structure consists of a tip that is similar to ${}^6\mathbf{1a}_{\text{Al}}$, which is linked to a 12-membered Al_5FeO_6 ring by three additional O-atoms in Al-O-Al/Fe-O-Al bridges. Al/Fe-atom substitution can also occur at two other positions and leads to the analogous ${}^6\mathbf{4a}_{\text{Fe}}\text{-ii}$ and ${}^6\mathbf{4a}_{\text{Fe}}\text{-iii}$ structures. In ${}^6\mathbf{4a}_{\text{Fe}}\text{-ii}$ ($13\text{ kJ}\cdot\text{mol}^{-1}$) the Fe-atom is part of the $\text{Al}_2\text{FeO}_4^+$ unit (the tip of the structure) whereas ${}^6\mathbf{4a}_{\text{Fe}}\text{-iii}$ ($20\text{ kJ}\cdot\text{mol}^{-1}$) is identical to the lowest energy isomer, but the Fe atom is substituted at the $\mu_3\text{-Fe} - \mu_3\text{-O}$ coordination center. Other calculated structures ${}^6\mathbf{4b}_{\text{Fe}}$ to ${}^6\mathbf{4p}_{\text{Fe}}$ have cage like structural motifs, and are lying at least $45\text{ kJ}\cdot\text{mol}^{-1}$ higher in energy than the global minimum isomer, reported in Fig. S10.

Assuming the presence of a single isomer, all simulated spectra yield similarly low S values. The best agreement with the IRPD spectrum of $Al_8FeO_{13}^+ \cdot He$ is found for the simulated IR spectrum of ${}^64a_{Fe}$ -i ($S=0.69$), which has slightly higher scores than ${}^64a_{Fe}$ -ii ($S=0.67$) and ${}^64a_{Fe}$ -iii ($S=0.68$). ${}^64a_{Fe}$ -i and ${}^64a_{Fe}$ -ii has nearly similar simulated IR signatures with a high intense peak at 1030 cm^{-1} and 1033 cm^{-1} respectively, but the relative intensity of the low energy absorptions are fairly low with respect to the experimental peaks. Interestingly, the simulated spectra of ${}^64a_{Fe}$ -iii shows better agreement considering relative intensity of the peaks. Moreover, two closely lying bands at 1008 cm^{-1} and 1038 cm^{-1} can account for the broadness of the experimental absorption at 1026 cm^{-1} . An improved agreement is achieved with a combination of 50/50 ratio of ${}^64a_{Fe}$ -i/ ${}^64a_{Fe}$ -iii ($S=0.77$), which has the highest cosine similarity value among all the possible combinations of ${}^64a_{Fe}$ -i, ${}^64a_{Fe}$ -ii and ${}^64a_{Fe}$ -iii (see Table S3).

Similar to the smaller clusters, the shortest Al-O bonds ($1.69\text{-}1.72\text{ \AA}$) form the 12-membered ring comprising the outer rim. The associated Al-O stretching mode is observed with the highest intensity at the highest energy (1026 cm^{-1}). Different Fe atom coordination environments in the various isomers results in varying Fe-O bond lengths ($1.74 - 1.97\text{ \AA}$) and this is reflected in the complex pattern of Fe-O stretching modes, which spreads over region (ii) and (iii). Multiple bands attributed to the various $\mu_4Al - O$ stretching modes are also observed and attributed to the large distribution in $\mu_4Al - O$ bond lengths ($1.70\text{-}1.87\text{ \AA}$). In comparison to the spectrum of $Al_8FeO_{13}^+ \cdot He$ the $Al_9O_{13}^+ \cdot He$ spectrum is much simpler and shows fewer features, in line with its higher symmetry (C_{3v} vs C_s). However, the features in region (i) remain similar due to the similar outer ring structure of these isomers. The influence of the Fe atom on the IRPD spectrum and hence the isomer-specific features can be best seen in the region $550\text{-}900\text{ cm}^{-1}$, where coupled Fe-O/Al-O stretching and bending modes are predicted. Summarizing, for $n = 4$ the substitution is isomorphous.

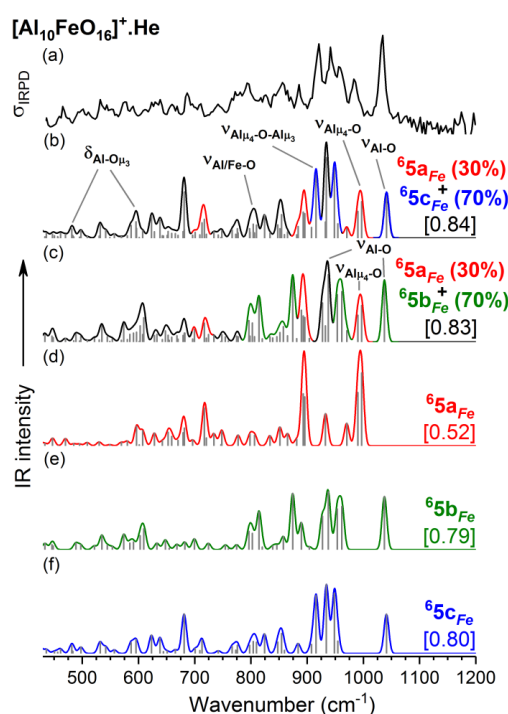


Figure 6. Experimental IRPD spectra of He-tagged $\text{Al}_{10}\text{FeO}_{16}^+$ (top trace) compared with computed IR spectra (lower traces) of the lowest-energy isomers ${}^6\mathbf{5a}_{\text{Fe}}$, ${}^6\mathbf{5b}_{\text{Fe}}$ and ${}^6\mathbf{5c}_{\text{Fe}}$. The calculated IR spectra, derived from TPSSh/def2-TZVP harmonic frequencies (scaled by 1.0166) and intensities, are plotted with sticks (gray) and a 10 cm^{-1} FWHM Gaussian line shape convolution. Each sum spectrum is colour coded using red, green and blue for individual and black for common contributions. The cosine similarity score (see Eqs. 1) is shown in square brackets. See Fig. 2 for the structures and relative energies of the contributing isomers and the SI for the relative energies of the low energy isomers (Tab. S1), the individual spectra of the isomers and IR band assignments (Tab. S2).

The predicted global minimum-energy isomer for $\text{Al}_{10}\text{FeO}_{16}^+$ is the high spin cage like irregular 3D structure ${}^6\mathbf{5a}_{\text{Fe}}$ (Fig. 2). Isomers ${}^6\mathbf{5b}_{\text{Fe}}$ ($10\text{ kJ}\cdot\text{mol}^{-1}$) and ${}^6\mathbf{5c}_{\text{Fe}}$ ($17\text{ kJ}\cdot\text{mol}^{-1}$) are higher in energy with similarly irregular cage structures (see Fig. 2) consisting of 6- and 4-membered rings. Isomers ${}^6\mathbf{5a}_{\text{Fe}}$ to ${}^6\mathbf{5c}_{\text{Fe}}$ have 3- and 4-fold coordinated Al-atom with 2- and 3-fold coordinated O-atoms in alternating positions. Moreover, ${}^6\mathbf{5b}_{\text{Fe}}$ and ${}^6\mathbf{5c}_{\text{Fe}}$ exhibit a conical Al_2MO_4^+ (M=Fe for **5b** and Al for **5c**) unit, similar to that found in $n = 1$ (${}^6\mathbf{1a}_{\text{Fe}}$) and $n = 4$ (${}^6\mathbf{4a}_{\text{Fe}}$) clusters. The Fe-atom in ${}^6\mathbf{5a}_{\text{Fe}}$ and ${}^6\mathbf{5c}_{\text{Fe}}$ is 3-fold coordinated, whereas it is 4-fold coordinated in ${}^6\mathbf{5b}_{\text{Fe}}$. Higher energy isomers (${}^6\mathbf{5d}_{\text{Fe}}$ to ${}^6\mathbf{5o}_{\text{Fe}}$) were also calculated and are shown in Fig. S7.

The IRPD spectrum of $\text{Al}_{10}\text{FeO}_{16}^+$ is rich with IR features over the complete spectral region studied here. The distinctive features in region (i) are most useful for assigning the contributing isomers. The most intense IRPD band at 1034 cm^{-1} together with three other intense bands at 921 cm^{-1} , 941 cm^{-1} and 959 cm^{-1} do not agree satisfactorily with the simulated IR spectra of the lowest energy isomer ${}^6\mathbf{5a}_{\text{Fe}}$ ($S=0.52$). Interestingly, theoretical spectra of isomer ${}^6\mathbf{5b}_{\text{Fe}}$ ($S=0.79$) and ${}^6\mathbf{5c}_{\text{Fe}}$ ($S=0.80$) better reproduce the experimental spectrum. However, the remaining feature at 983 cm^{-1} is characteristic of ${}^6\mathbf{5a}_{\text{Fe}}$ (see Fig. 6b). A higher cosine similarity score is obtained by assuming the presence of multiple isomers. Note, both the 70/30 ratio of ${}^6\mathbf{5c}_{\text{Fe}}/{}^6\mathbf{5a}_{\text{Fe}}$ ($S=0.84$, Fig. 6b) as well as of ${}^6\mathbf{5b}_{\text{Fe}}/{}^6\mathbf{5a}_{\text{Fe}}$ ($S=0.83$, Fig. 6c) yield nearly the same value. The 1034 cm^{-1} band is assigned to the stretching mode involving the shortest Al-O bonds ($1.67 - 1.74\text{ \AA}$) whereas the band at 983 cm^{-1} is attributed to $\mu_4\text{Al}-\text{O}$ stretches. $\mu_4\text{Al}-\text{O}-\mu_3\text{Al}$ stretches are observed in the range $850 - 950\text{ cm}^{-1}$. At this cluster size it becomes difficult to identify the IR-signature of the Fe-center, because the associated modes strongly couple with other modes. Similar infrared features regarding position and intensity in the experimental spectra of $\text{Al}_{10}\text{MO}_{16}^+\cdot\text{He}$ (M=Al, Fe) suggest similar structural motifs. Summarizing, cage like structures predominate for the largest cluster and the Fe atom prefers 3-fold coordination sites over 4-fold.

The presented results allow exploring the influence of doping a small aluminium oxide network with a Fe-atom. In general, the IRPD spectra of the Fe-doped clusters are richer in features due to symmetry-lowering upon doping. For $n = 2$, the highest energy doublet absorption arises due to the structural rearrangement of lowest energy isomers, and this feature establishes the characteristic of sheet-like structural motif. For all cluster sizes, only

high spin species are found. Analysis of the structures of $[(Al_2O_3)_nFeO]^+$ ($n = 2-5$) reveals that the Fe-atom prefers to acquire a relaxed geometry i.e. the site with longer bond length and wider bond angle. This preference is reflected in attaining ${}^61b_{Fe}$ structural motif over ${}^61a_{Fe}$ for $n=1$, ${}^62a_{Fe}$ over ${}^62c_{Fe}$ for $n = 2$, ${}^63a_{Fe}$ over ${}^63c_{Fe}$ for $n = 3$ and ${}^64a_{Fe}$ -i over ${}^64a_{Fe}$ -ii & ${}^64a_{Fe}$ -iii for $n = 4$. The reason for such selectivity is the larger size of the Fe-atom over Al, correspondingly, Fe prefers to be in 3-fold coordinated geometry rather than 4-fold coordination. Moreover, the d-type valence orbitals of Fe help in adopting a more flexible geometry, whereas Al is limited to either trigonal planar or tetrahedral oxygen coordination. This observation is in line with results for Fe-doped nanocrystals or nanoparticles, in which dopant Fe-atoms replace Al-atoms of the Al_2O_3 network, mostly in the surface, inducing only minor distortions of the network rather than structural changes.⁶⁰

The present results confirm that the cosine similarity score is a useful and objective method to verify the contribution of isomers for metal oxide clusters. Previously it had only been applied to hydrocarbon systems.⁶¹⁻⁶² Moreover, it can be used as an alternative method to identify the best fit sum-spectrum in a quantitative way in case of multiple isomer contribution, which is challenging to achieve either with the DFT energetics or by visual inspection.

For $n=5$, TPSSh or B3LYP energies are not adequate to explain the contribution of the isomers (see table S1 for relative energies). This is mainly because of the shallow potential energy surface of the species, which results many close lying low energy isomers within the DFT error bar (~ 30 kJ.mol⁻¹). In case of sufficiently large clusters, wave function based theory with local correlation treatment such as LMP2 or LCCSD(T) should be considered for better accuracy.

Conclusions and Outlook:

In conclusion, the study of the cluster ions with increasing size permits us to identify the structural motif change from quasi 2D sheet type for $n = 2$ to 3D cage structure at $n = 3$. A highly symmetric conical structure is present for $n = 1, 2$ (${}^62b_{Fe}$) and 4.

The Fe-atom is found to preferentially acquire the outer ring of the cluster as a common doping site, implying the higher probability of populating the surface of a catalyst with increasing dopant molecules, and hence increased number of accessible active sites (under-coordinated Fe-atoms). Consequently, the elevated photocatalytic efficiency of zeolites upon transition metal doping⁵ can be explained.

In this unique study, the satisfactory agreement between experimental and theoretical results established the high potential of TPSSh and B3LYP quantum chemical calculation methods for the structural investigation of molecular clusters with Al and Fe atoms, which can be extended towards calculations of more complex systems and investigation on chemical reactions of small molecular clusters.

References:

1. Trueba, M.; Trasatti, S. P. γ -Alumina as a Support for Catalysts: A Review of Fundamental Aspects. *European Journal of Inorganic Chemistry* **2005**, 2005 (17), 3393-3403.
2. Franks, G. V.; Gan, Y. Charging Behavior at the Alumina–Water Interface and Implications for Ceramic Processing. *Journal of the American Ceramic Society* **2007**, 90 (11), 3373-3388.
3. Álvarez, J.; Serrano, C.; Hill, D.; Martínez-Pastor, J. Real-time polarimetric optical sensor using macroporous alumina membranes. *Optics Letters* **2013**, 38 (7), 1058-1060.
4. Matsuoka, M.; Anpo, M. Local structures, excited states, and photocatalytic reactivities of highly dispersed catalysts constructed within zeolites. *Journal of Photochemistry and Photobiology C: Photochemistry Reviews* **2003**, 3 (3), 225-252.
5. Tong, Y.; Zhang, Y.; Tong, N.; Zhang, Z.; Wang, Y.; Zhang, X.; Zhu, S.; Li, F.; Wang, X. HZSM-5 zeolites containing impurity iron species for the photocatalytic reduction of CO₂ with H₂O. *Catalysis Science & Technology* **2016**, 6 (20), 7579-7585.
6. Yan, G.; Wang, X.; Fu, X.; Li, D. A primary study on the photocatalytic properties of HZSM-5 zeolite. *Catalysis Today* **2004**, 93-95, 851-856.
7. Panov, G. I.; Sheveleva, G. A.; Kharitonov, A. S.; Romannikov, V. N.; Vostrikova, L. A. Oxidation of benzene to phenol by nitrous oxide over Fe-ZSM-5 zeolites. *Applied Catalysis A: General* **1992**, 82 (1), 31-36.
8. Böhme, D. K.; Schwarz, H. Gas-Phase Catalysis by Atomic and Cluster Metal Ions: The Ultimate Single-Site Catalysts. *Angewandte Chemie International Edition* **2005**, 44 (16), 2336-2354.
9. Asmis, K. R. Structure characterization of metal oxide clusters by vibrational spectroscopy: possibilities and prospects. *Physical Chemistry Chemical Physics* **2012**, 14 (26), 9270-9281.
10. Asmis, K. R.; Brümmer, M.; Kaposta, C.; Santambrogio, G.; von Helden, G.; Meijer, G.; Rademann, K.; Wöste, L. Mass-Selected Infrared Photodissociation Spectroscopy of V₄O₁₀⁺. *Physical Chemistry Chemical Physics* **2002**, 4, 1101-4.
11. Asmis, K. R.; Sauer, J. Mass-selective Vibrational Spectroscopy of Vanadium Oxide Cluster Ions. *Mass Spectrometry Reviews* **2007**, 26, 542-62.
12. Asmis, K. R.; Sauer, J. Erratum to: Mass-selective Vibrational Spectroscopy of Vanadium Oxide Cluster Ions. *Mass Spectrometry Reviews* **2008**, 27 (2), 205.
13. Sierka, M.; Döbler, J.; Sauer, J.; Santambrogio, G.; Brümmer, M.; Wöste, L.; Janssens, E.; Meijer, G.; Asmis, K. R. Unexpected Structures of Aluminum Oxide Clusters in the Gas Phase. *Angewandte Chemie International Edition* **2007**, 46 (18), 3372-3375.
14. Santambrogio, G.; Janssens, E.; Li, S.; Siebert, T.; Meijer, G.; Asmis, K. R.; Döbler, J.; Sierka, M.; Sauer, J. Identification of Conical Structures in Small Aluminum Oxide Clusters: Infrared Spectroscopy of (Al₂O₃)₁–4(AlO)⁺. *Journal of the American Chemical Society* **2008**, 130 (45), 15143-15149.
15. Song, X.; Fagiani, M. R.; Gewinner, S.; Schöllkopf, W.; Asmis, K. R.; Bischoff, F. A.; Berger, F.; Sauer, J. Gas phase structures and charge localization in small aluminum oxide anions: Infrared photodissociation spectroscopy and electronic structure calculations. *The Journal of Chemical Physics* **2016**, 144 (24), 244305.
16. Song, X.; Fagiani, M. R.; Gewinner, S.; Schöllkopf, W.; Asmis, K. R.; Bischoff, F. A.; Berger, F.; Sauer, J. Gas-Phase Vibrational Spectroscopy of the Aluminum Oxide Anions (Al₂O₃)₁–6AlO₂[–]. *ChemPhysChem* **2017**, 18 (8), 868-872.
17. Feyel, S.; Döbler, J.; Höckendorf, R.; Beyer, M. K.; Sauer, J.; Schwarz, H. Activation of Methane by Oligomeric (Al₂O₃)_x (x=3,4,5): The Role of Oxygen-Centered Radicals in Thermal Hydrogen-Atom Abstraction. *Angewandte Chemie International Edition* **2008**, 47 (10), 1946-1950.
18. Wang, Z.-C.; Weiske, T.; Kretschmer, R.; Schlangen, M.; Kaupp, M.; Schwarz, H. Structure of the Oxygen-Rich Cluster Cation Al₂O₇⁺ and its Reactivity toward Methane and Water. *Journal of the American Chemical Society* **2011**, 133 (42), 16930-16937.
19. Sierka, M.; Döbler, J.; Sauer, J.; Zhai, H.-J.; Wang, L.-S. The [(Al₂O₃)₂][–] Anion Cluster: Electron Localization–Delocalization Isomerism. *ChemPhysChem* **2009**, 10 (14), 2410-2413.
20. Mascariolo, K. J.; Gardner, A. M.; Heaven, M. C. Autodetachment spectroscopy of the aluminum oxide anion dipole bound state. *The Journal of Chemical Physics* **2015**, 143 (11), 114311.

21. Stößer, G.; Schnöckel, H. The Molecules AlO_2 , $\text{Al}(\text{O}_2)_2$, and $\text{Al}(\text{O}_2)_3$: Experimental and Quantum-Chemical Investigations on the Oxidation of Aluminum Atoms. *Angewandte Chemie International Edition* **2005**, *44* (27), 4261-4264.
22. van Heijnsbergen, D.; Demyk, K.; Duncan, M. A.; Meijer, G.; von Helden, G. Structure determination of gas phase aluminum oxide clusters. *Physical Chemistry Chemical Physics* **2003**, *5* (12), 2515-2519.
23. Demyk, K.; van Heijnsbergen, D.; von Helden, G.; Meijer, G. Experimental study of gas phase titanium and aluminum oxide clusters. *A&A* **2004**, *420* (2), 547-552.
24. Jiang, L.; Wende, T.; Claes, P.; Bhattacharyya, S.; Sierka, M.; Meijer, G.; Lievens, P.; Sauer, J.; Asmis, K. R. Electron Distribution in Partially Reduced Mixed Metal Oxide Systems: Infrared Spectroscopy of $\text{Ce}_m\text{V}_n\text{O}_o^+$ Gas-Phase Clusters. *The Journal of Physical Chemistry A* **2011**, *115* (41), 11187-11192.
25. Jan Vanbuel, E. M. F., Mei-ye Jia, Piero Ferrari, Wieland Schöllkopf, Luis C. Balbás, Minh Tho Nguyen, André Fielicke and Ewald Janssens. Hydrogen Chemisorption on Doubly Vanadium Doped Aluminum Clusters. In *Z. Phys. Chem*, 2019; Vol. 6, pp 799-812.
26. New Tools for Structure Elucidation in the Gas Phase: IR Spectroscopy of Bare and Doped Silicon Nanoparticles. In *Ideas in Chemistry and Molecular Sciences*, pp 183-206.
27. Li Y., F. A., Lievens P., Janssens E. Structural Identification of Doped Silicon Clusters. In *Nguyen M., Kiran B. (eds) Clusters. Challenges and Advances in Computational Chemistry and Physics*, Springer, Cham: 2017; Vol. 23.
28. Janssens, E.; Lang, S. M.; Brümmer, M.; Niedziela, A.; Santambrogio, G.; Asmis, K. R.; Sauer, J. Kinetic study of the reaction of vanadium and vanadium–titanium oxide cluster anions with SO_2 . *Physical Chemistry Chemical Physics* **2012**, *14* (41), 14344-14353.
29. Li, Y.-K.; Debnath, S.; Schlangen, M.; Schöllkopf, W.; Asmis, K.; Schwarz, H. Direct Identification of Acetaldehyde Formation and Characterization of the Active Site in the $[\text{VPO}_4] \cdot + / \text{C}_2\text{H}_4$ Couple By Gas-Phase Vibrational Spectroscopy. *Angewandte Chemie International Edition* *0* (ja).
30. Debnath, S.; Knorke, H.; Schöllkopf, W.; Zhou, S.; Asmis, K. R.; Schwarz, H. Experimental Identification of the Active Site in the Heteronuclear Redox Couples $[\text{AlVO}_x]^+ / \text{CO}/\text{N}_2\text{O}$ ($x=3, 4$) by Gas-Phase IR Spectroscopy. *Angewandte Chemie International Edition* **2018**, *57* (25), 7448-7452.
31. Dietl, N.; Wende, T.; Chen, K.; Jiang, L.; Schlangen, M.; Zhang, X.; Asmis, K. R.; Schwarz, H. Structure and chemistry of the heteronuclear oxo-cluster $[\text{VPO}_4]^{n+}$: a model system for the gas-phase oxidation of small hydrocarbons. *Journal of the American Chemical Society* **2013**, *135* (9), 3711-3721.
32. Miyajima, K.; Fukushima, N.; Mafuné, F. Reactivity of Group 5 Bielement Clusters with H_2 . *The Journal of Physical Chemistry A* **2009**, *113* (17), 4858-4861.
33. Miyajima, K.; Fukushima, N.; Himeno, H.; Yamada, A.; Mafuné, F. Breakdown of the Hume–Rothery Rules in Sub-Nanometer-Sized Ta-Containing Bimetallic Small Clusters. *The Journal of Physical Chemistry A* **2009**, *113* (48), 13448-13450.
34. Himeno, H.; Miyajima, K.; Yasuike, T.; Mafuné, F. Gas Phase Synthesis of Au Clusters Deposited on Titanium Oxide Clusters and Their Reactivity with CO Molecules. *The Journal of Physical Chemistry A* **2011**, *115* (42), 11479-11485.
35. Yamaguchi, M.; Kudoh, S.; Miyajima, K.; Lushchikova, O. V.; Bakker, J. M.; Mafuné, F. Tuning the Dissociative Action of Cationic Rh Clusters Toward NO by Substituting a Single Ta Atom. *The Journal of Physical Chemistry C* **2019**, *123* (6), 3476-3481.
36. Baekelant, W.; Aghakhani, S.; Coutino-Gonzalez, E.; Grandjean, D.; Kennes, K.; Jonckheere, D.; Fron, E.; d’Acapito, F.; Longo, A.; Lievens, P.; Roeffaers, M. B. J.; Hofkens, J. Confinement of Highly Luminescent Lead Clusters in Zeolite A. *The Journal of Physical Chemistry C* **2018**, *122* (25), 13953-13961.
37. Grandjean, D.; Coutiño-Gonzalez, E.; Cuong, N. T.; Fron, E.; Baekelant, W.; Aghakhani, S.; Schlexer, P.; D’Acapito, F.; Banerjee, D.; Roeffaers, M. B. J.; Nguyen, M. T.; Hofkens, J.; Lievens, P. Origin of the bright photoluminescence of few-atom silver clusters confined in LTA zeolites. *Science* **2018**, *361* (6403), 686-690.

38. Baekelant, W.; Aghakhani, S.; Coutino-Gonzalez, E.; Kennes, K.; D'Acapito, F.; Grandjean, D.; Van der Auweraer, M.; Lievens, P.; Roefsaers, M. B. J.; Hofkens, J.; Steele, J. A. Shaping the Optical Properties of Silver Clusters Inside Zeolite A via Guest–Host–Guest Interactions. *The Journal of Physical Chemistry Letters* **2018**, *9* (18), 5344-5350.
39. Fabian Müller, J. B. S., Florian A. Bischoff, Laura Gagliardi, Joachim Sauer, Sreekanta Debnath, Marcel Jorewitz, Knut R. Asmis,. The [FeAl₂O₄]⁺ radical cation and its ability to activate C-H bonds.
40. Goebbert, D. J.; Meijer, G.; Asmis, K. R. 10 K Ring Electrode Trap—Tandem Mass Spectrometer for Infrared Spectroscopy of Mass Selected Ions. *AIP Conference Proceedings* **2009**, *1104* (1), 22-29.
41. Schöllkopf, W.; Gewinner, S.; Junkes, H.; Paarmann, A.; Helden, G. v.; Bluem, H. P.; Todd, A. M. M. *The new IR and THz FEL facility at the Fritz Haber Institute in Berlin*. SPIE: 2015; Vol. 9512.
42. Brümmer, M.; Kaposta, C.; Santambrogio, G.; Asmis, K. R. Formation and photodepletion of cluster ion–messenger atom complexes in a cold ion trap: Infrared spectroscopy of VO⁺, VO₂⁺, and VO₃⁺. *The Journal of Chemical Physics* **2003**, *119* (24), 12700-12703.
43. Heine, N.; Asmis, K. R. Cryogenic ion trap vibrational spectroscopy of hydrogen-bonded clusters relevant to atmospheric chemistry. *International Reviews in Physical Chemistry* **2015**, *34* (1), 1-34.
44. Heine, N.; Asmis, K. R. Cryogenic Ion Trap Vibrational Spectroscopy of Hydrogen-Bonded Clusters Relevant to Atmospheric Chemistry (International Reviews in Physical Chemistry, 2015, Vol. 34, No. 1, 1–34). *International Reviews in Physical Chemistry* **2016**, *35* (3), 507-507.
45. Deaven, D. M.; Ho, K. M. Molecular-Geometry Optimization with a Genetic Algorithm. *Physical Review Letters* **1995**, *75* (2), 288-291.
46. Perdew, J. P. BP86. *Physical Review B: Condensed Matter and Materials Physics* **1986**, *33*, 8822-8824.
47. Becke, A. D. Phys. Rev. A. *Physical Review A* **1988**, *38*, 3098.
48. Schäfer, A.; Horn, H.; Ahlrichs, R. Fully optimized contracted Gaussian basis sets for atoms Li to Kr. *Journal of Chemical Physics* **1992**, *97*, 2571-2577.
49. Staroverov, V. N.; Scuseria, G. E.; Tao, J.; Perdew, J. P. Comparative assessment of a new nonempirical density functional: Molecules and hydrogen-bonded complexes. *The Journal of Chemical Physics* **2003**, *119* (23), 12129-12137.
50. Vosko, S. H.; Wilk, L.; Nusair, M. *Canadian Journal of Physics* **1980**, *58*, 1200.
51. Lee, C.; Yang, W.; Parr, R. G. ((LYP)) Development of the Colle-Salvetti correlation-energy formula into a functional of the electron density. *Physical Review B* **1988**, *37*, 785-789.
52. Becke, A. D. "B3LYP"Density-functional thermochemistry. III. The role of exact exchange. *Journal of Chemical Physics* **1993**, *98*, 5648-5652.
53. Weigend, F.; Ahlrichs, R. Balanced basis sets of split valence, triple zeta valence and quadruple zeta valence quality for H to Rn: Design and assessment of accuracy. *Physical Chemistry Chemical Physics* **2005**, *7*, 3297-3305.
54. *TURBOMOLE V7.0; a development of the University of Karlsruhe and Forschungszentrum Karlsruhe GmbH, 1989-2007, Turbomole GmbH since 2007; available from <http://www.turbomole.com>, 2015.*
55. Treutler, O.; Ahlrichs, R. Efficient Molecular Numerical Integration Schemes. *Journal of Chemical Physics* **1995**, *102* (1), 346-354.
56. Eichkorn, K.; Weigend, F.; Treutler, O.; Ahlrichs, R. Auxiliary basis sets for main row atoms and transition metals and their use to approximate Coulomb potentials. *Theoretical Chemistry Accounts* **1997**, *97* (1-4), 119-124.
57. Kempkes, L. J. M.; Martens, J.; Berden, G.; Houthuijs, K. J.; Oomens, J. Investigation of the position of the radical in z₃-ions resulting from electron transfer dissociation using infrared ion spectroscopy. *Faraday Discussions* **2019**, *217* (0), 434-452.
58. Fagiani, M. R.; Song, X.; Debnath, S.; Gewinner, S.; Schollkopf, W.; Asmis, K. R.; Bischoff, F. A.; Müller, F.; Sauer, J. Dissociative Water Adsorption by Al₃O₄⁺ in the Gas Phase. *Journal of Physical Chemistry Letters* **2017**, *8* (6), 1272-1277.

-
59. Maier, T. M.; Boese, A. D.; Sauer, J.; Wende, T.; Fagiani, M.; Asmis, K. R. The vibrational spectrum of FeO₂⁺ isomers-Theoretical benchmark and experiment. *Journal of Chemical Physics* **2014**, *140* (20), 204315.
60. Khodadadi, A.; Farahmandjou, M.; Yaghoubi, M.; Amani, A. R. Structural and optical study of Fe³⁺-doped Al₂O₃ nanocrystals prepared by new sol gel precursors. *International Journal of Applied Ceramic Technology* **2019**, *16* (2), 718-726.
61. van Outersterp, R. E.; Houthuijs, K. J.; Berden, G.; Engelke, U. F.; Kluijtmans, L. A. J.; Wevers, R. A.; Coene, K. L. M.; Oomens, J.; Martens, J. Reference-standard free metabolite identification using infrared ion spectroscopy. *International Journal of Mass Spectrometry* **2019**, *443*, 77-85.
62. Mayer, M.; Pahl, M.; Spanka, M.; Grellmann, M.; Sickert, M.; Schneider, C.; Asmis, K. R.; Belder, D. Unravelling the configuration of transient ortho-quinone methides by combining microfluidics with gas phase vibrational spectroscopy. *Physical Chemistry Chemical Physics* **2020**, *22* (8), 4610-4616.

Chapter 5

Catalytic active site characterization of heteronuclear metal oxide clusters

This chapter focuses on unambiguous structural characterization of heteronuclear metal oxide clusters in one side, and on the other hand, identification of their active site is performed. The following sections present, study of $[\text{AlVO}_x]^{*+}$ ($x=3, 4$) clusters in the context of CO to CO_2 conversion (section 5.1) followed by investigation of $[\text{VPO}_4]^{*+}$ cluster model for the formation of acetaldehyde from ethylene (section 5.2). Both the studies are published in the *Angewandte Chemie International Edition*^{1,2} and the former one is selected as a very important article (top 5%). IRPD spectra are compared with that of the theoretically calculated linear spectra for the structural assignment of the studied clusters and identification of their characteristic vibrational signatures. These heteronuclear clusters are used as model system to gain insights about the underlying reaction mechanism in the context of heterogeneous catalysis.

5.1. Experimental Identification of the Active Site in the Heteronuclear $[\text{AlVO}_x]^{*+}/\text{CO}/\text{N}_2\text{O}$ ($x = 3, 4$) Redox Couples by Gas-Phase IR Spectroscopy

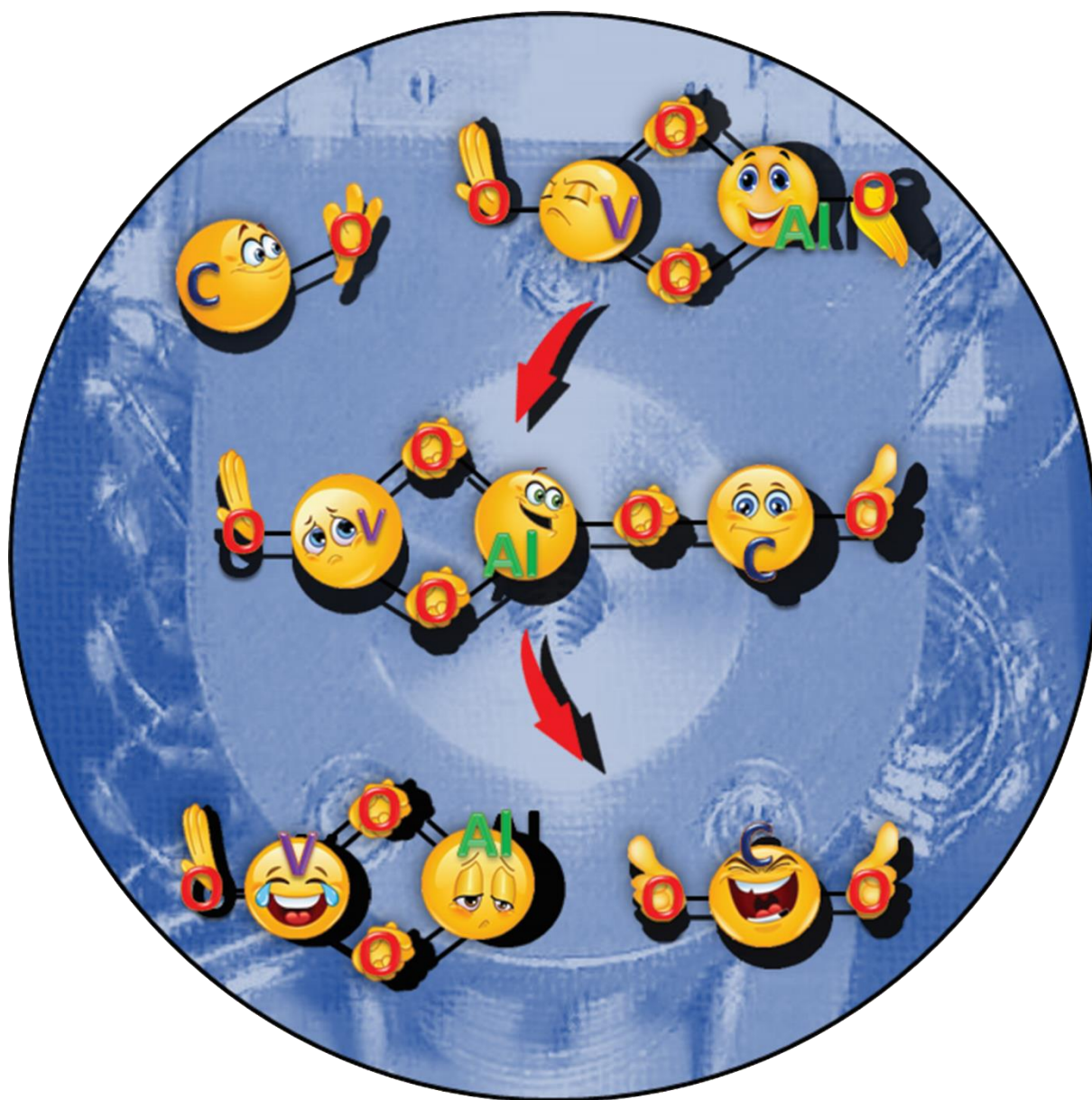
In the published article “Experimental Identification of the Active Site in the Heteronuclear $[\text{AlVO}_x]^{*+}/\text{CO}/\text{N}_2\text{O}$ ($x = 3, 4$) Redox Couples by Gas-Phase IR Spectroscopy”,¹ gas phase cryogenic infrared spectroscopy is used for the structural characterization of $[\text{AlVO}_x]^{*+}$ ($x=3, 4$) clusters. The clusters are produced in a pulsed laser vaporization source using a mixed Al/V (50/50 wt%) metal rod. Comparison of the experimental IRPD spectral signatures to the computed spectra demonstrate that in contrast to $[\text{AlVO}_4]^{*+}$, $[\text{AlVO}_3]^{*+}$ is devoid of a terminal Al-O_t unit while the terminal V-O_t group remains intact. When mass selected $[\text{AlVO}_4]^{*+}$ was reacted with CO molecules in the trap at 60K (CO started to condense below this trap temperature), almost 98% conversion of $[\text{AlVO}_4]^{*+}$ into $[\text{AlVO}_3]^{*+}$ was observed. The multiple collision condition of the present experimental technique lead to the solvation of $[\text{AlVO}_3]^{*+}$ cluster and formation of $[\text{AlVO}_3]^{*+}\cdot(\text{CO})_{0-7}$ type complex. IRPD spectrum of $[\text{AlVO}_3]^{*+}\cdot(\text{CO})_6$ was obtained looking at the CO loss channel and comparison to the DFT calculated spectrum confirmed that the $[\text{AlVO}_3]^{*+}$, which was formed by the reaction of $[\text{AlVO}_4]^{*+}$ and CO lacks the terminal Al-O_t unit. This finding supports that not the transition metal V-O_t centre but the main group Al-O_t centre is the active site.

1. Debnath, S., et al., *Angewandte Chemie International Edition*, 2018, **57**, 7448-7452
2. Li, Y.-K., et al., *Angewandte Chemie International Edition*, 2019, **58**, 18868-18872

Declaration of Contribution:

I planned and performed the experimental work, including the measurement of all IRPD spectra, data evaluation and interpretation. All the theoretical calculations were done by Shadong Zhou. Harald Knorke and I made the figures. I wrote the first version of experimental results part of the manuscript. Other contributions of the co-authors are listed below:

Harald Knorke	Assisted during the beam time measurements, made part of the figures, also contributed to data evaluation.
Wieland Schöllkopf	Evening operator of the FHI-FEL.
Helmut Schwarz, Knut. R. Asmis	Coordinated the project, framed the principal idea, supervised the research, helped in data interpretation and wrote the manuscript.



This study was nominated for the cover of that particular issue of *Angewandte Chemie International Edition* and here is the figure which we proposed.

VIP Heteronuclear Cluster Oxides Very Important Paper

International Edition: DOI: 10.1002/anie.201804056
German Edition: DOI: 10.1002/ange.201804056Experimental Identification of the Active Site in the Heteronuclear Redox Couples $[AlVO_x]^{+}/CO/N_2O$ ($x = 3, 4$) by Gas-Phase IR Spectroscopy

Sreekanta Debnath, Harald Knorke, Wieland Schöllkopf, Shaodong Zhou,* Knut R. Asmis,* and Helmut Schwarz*

Dedicated to Professor Hans-Joachim Freund and Professor Joachim Sauer

Abstract: Cryogenic ion vibrational spectroscopy was used in combination with electronic structure calculations to identify the active site in the oxygen atom transfer reaction $[AlVO_4]^{+} + CO \rightarrow [AlVO_3]^{+} + CO_2$. Infrared photodissociation spectra of messenger-tagged heteronuclear clusters demonstrate that in contrast to $[AlVO_4]^{+}$, $[AlVO_3]^{+}$ is devoid of a terminal Al–O_t unit while the terminal V=O_t group remains intact. Thus it is the Al–O_t moiety that forms the active site in the $[AlVO_x]^{+}/CO/N_2O$ ($x = 3, 4$) redox couples, which is in line with theoretical predictions.

Arguably, the metal-mediated conversion of CO into CO₂ constitutes one of the best-studied oxidation processes, both at surfaces^[1] and in the gas phase.^[2] Catalytic conversions of harmful gases that are produced in fossil-fuel combustions, such as CO or the oxides of nitrogen, into N₂ and CO₂ are of particular importance, both environmentally as well as economically. While these redox reactions are quite exothermic, for example, $\Delta_r H = -365 \text{ kJ mol}^{-1}$ for the reaction $N_2O + CO \rightarrow N_2 + CO_2$, they do not occur directly to any measurable extent at either room or elevated temperature. This impediment is due to the high activation barriers, which exceed 197 kJ mol^{-1} for the N₂O/CO system. Catalysts are

required to bypass the barrier by opening up new, energetically less demanding pathways. The combination of computational studies with gas-phase experiments has proven helpful in this endeavor, shedding new light on the catalytic mechanisms that operate at a strictly atomistic level.^[2] For example, in a landmark experiment, Kappes and Staley^[3] demonstrated that a single Fe⁺ atom can superbly mediate the coupled redox processes described in Equations (1) and



(2) under ambient conditions. Theoretical work, comple-



mented by experimental studies over an extended temperature regime, revealed fascinating details concerning the electronic structure requirements and dynamic aspects of oxygen atom transfers (OATs) in this system,^[4] which involve a two-state reactivity scenario.^[5]

Subsequently, numerous other atomic main-group and transition-metal cations have been tested, mostly by the Böhme group^[6] and others.^[2g,7] More recently, the focus of activity has shifted to the investigation of metal oxide clusters, in particular heteronuclear ones, to uncover the underlying mechanisms.^[2fg] Here, one of the pertinent challenges concerns the identification of the active site^[8] in the metal oxide cluster, the so-called aristocratic atom.^[9]

The redox couple $[AlVO_x]^{+}/CO/N_2O$ ($x = 3, 4$) may serve as a good example.^[10] At room temperature and under single-collision conditions, the heteronuclear oxide cluster $[AlVO_4]^{+}$ is reduced to $[AlVO_3]^{+}$ in the presence of CO, and if N₂O is added, re-oxidation occurs. Both OATs proceeded cleanly and with reaction efficiencies of 59% and 65%, relative to the collision rate, respectively. In principle, the turnover number (TON) of this ideal catalytic cycle (Scheme 1) is infinite; however, in reality, the TON is limited by side reactions with background impurities, for example, hydrogen atom abstraction from hydrocarbons.^[10]

DFT calculations have provided insight into parts of the mechanism responsible for these redox processes. Furthermore, theory predicted that in the course of the OAT (Scheme 1), the active site should involve exclusively the terminal Al–O_t unit of $[AlVO_4]^{+}$. In contrast, the V=O_t moiety of $[AlVO_4]^{+}$ cannot provide an oxygen atom in the

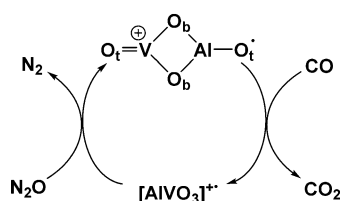
[*] Prof. Dr. S. Zhou, Prof. Dr. H. Schwarz
Institut für Chemie
Technische Universität Berlin
Straße des 17. Juni 135, 10623 Berlin (Germany)
E-mail: Helmut.Schwarz@tu-berlin.de

Prof. Dr. S. Zhou
Zhejiang Provincial Key Laboratory of Advanced Chemical Engineering
Manufacture Technology
College of Chemical and Biological Engineering
Zhejiang University
310027 Hangzhou (P. R. China)
E-mail: szhou@zju.edu.cn

M. Sc. S. Debnath, Dipl.-Phys. H. Knorke, Prof. Dr. K. R. Asmis
Wilhelm-Ostwald-Institut für Physikalische und Theoretische Chemie
Universität Leipzig
Linnéstr. 2, 04103 Leipzig (Germany)
E-mail: knut.asmis@uni-leipzig.de

M. Sc. S. Debnath, Dr. W. Schöllkopf
Fritz-Haber-Institut der Max-Planck-Gesellschaft
Faradayweg 4–6, 14195 Berlin (Germany)

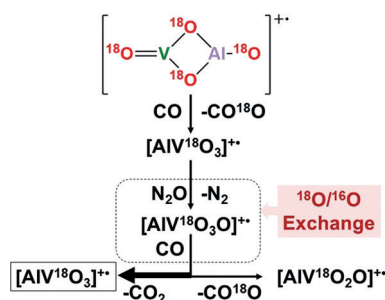
Supporting information and the ORCID identification number(s) for the author(s) of this article can be found under:
<https://doi.org/10.1002/anie.201804056>.



Scheme 1. Oxygen atom transfer in the redox couple $[AlVO_3]^+ / CO / N_2O$.

oxidation of CO on both kinetic and thermodynamic grounds.^[10]

By definition, the active site of the cluster cannot be identified in a labeling experiment with, for example, $[AlV^{18}O_4]^+ / CO / N_2O$. Nevertheless, inspection of the branching ratio for the final product pairs $CO_2 / [AlV^{18}O_3]^+$ versus $C^{18}OO / [AlV^{18}O_2O]^+$ reveals some interesting details (Scheme 2). The first step, that is, the reduction of



Scheme 2. ^{18}O labeling experiments.

$[AlV^{18}O_4]^+$ to $[AlV^{18}O_3]^+$ by CO, occurs without any measurable $^{18}O / ^{16}O$ exchange, and the trioxide is cleanly generated. Similarly, re-oxidation of the latter with N_2O gives rise to $[AlV^{18}O_3O]^+$ exclusively. Based on CCSD(T, full)/CBS//B3LYP-D3(BJ)/cc-pVTZ calculations, this re-oxidation step of the cluster is extremely exothermic (-219 kJ mol^{-1}); thus, while part of the liberated energy is carried off as kinetic energy, the product ion generated is rovibrationally quite hot, and in the absence of (or prior to) efficient collisional cooling, it may undergo degenerate intramolecular isomerization processes in the course of which the $Al-O_t$ unit is converted to some extent into an $Al-^{18}O_t$ group.^[11] Consequently, in the final reaction of $[AlV^{18}O_3O]^+$ with CO, both unlabeled and labeled carbon dioxide molecules are liberated with a branching ratio of approximately 2.8:1. Variation of the delay time between the individual reaction steps or changing the thermalization conditions, which is limited in our experimental FT-ICR set-up, did not bring about any substantial changes in this branching ratio. Therefore, the question then still remains open as to which of the two terminal MO bonds ($M = V, Al$) of the metal oxide cluster is involved in the redox process.

Herein, we verify this theoretical prediction^[10] by recording gas-phase infrared photodissociation (IRPD) spectra of messenger-tagged $[AlVO_x]^+$ ($x = 3, 4$) using the intense and widely tunable radiation from an IR free electron laser

(FEL)^[12] and comparing them with simulated IR spectra of various isomers.^[13] The result is unambiguous and confirms the theoretical analysis.

Figure 1 shows the computed harmonic IR spectra of four stable $[AlVO_4]^+$ isomers (**1–4**) as well as that of isomer **1** “tagged” with He as a messenger atom (**1-He**; for technical details and references, see the Supporting Information). The global ground state of $[AlVO_4]^+$ is a doublet electronic state. Its structure is characterized by a four-membered $V-(\mu-O)_2-Al$ ring containing terminal VO and AlO units (Figure 1, **1**); similar bonding patterns have previously been reported for $[Zr_2O_4]^+$,^[14] $[V_2O_4]^+$,^[15] $[CeVO_4]^+$,^[16] $[VPO_4]^+$,^[17] $[Al_2O_4]^+$,^[18] and $[Ti_2O_4]^+$.^[19] The other isomers considered were predicted to be $> 100 \text{ kJ mol}^{-1}$ higher in energy, ruling them out as possible candidates purely on energetic grounds. These isomers include the chain-like structure **4** (121 kJ mol^{-1}) and the two cyclic variants containing a terminal $Al(O_2)$ group (**2**; 140 kJ mol^{-1}) and a terminal VO_2 unit (**3**;

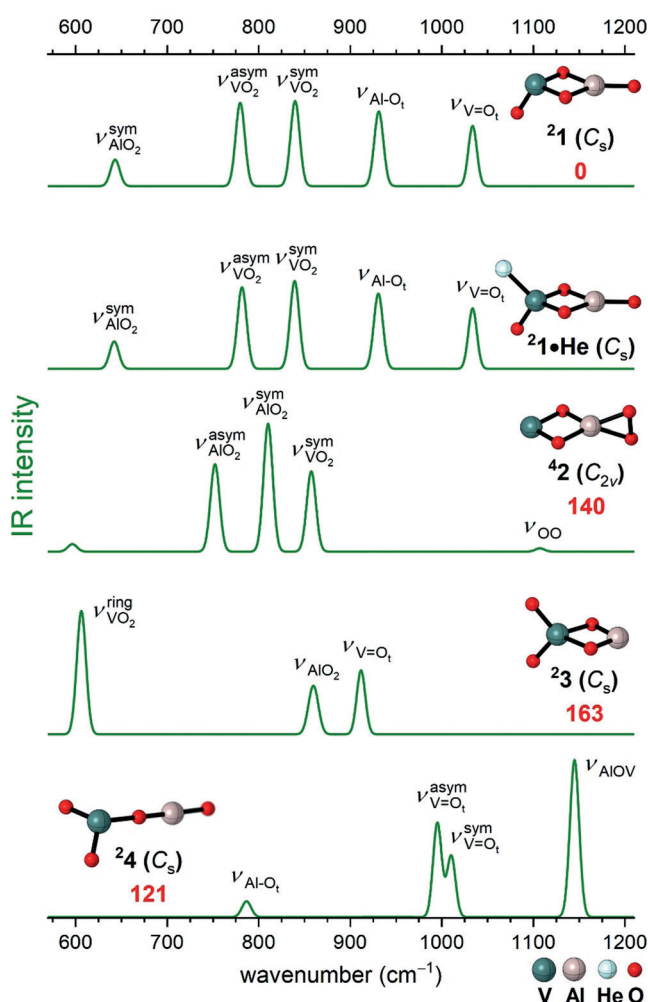


Figure 1. Simulated IR spectra of **2**¹, **2**^{1-He}, **4**², **3**, and **4**⁴ as calculated at the B3LYP-D3(BJ)/cc-pVTZ level of theory. The numbers in red give the relative energies (in kJ mol^{-1}) of different isomers of the $[AlVO_4]^+$ species as calculated at the CCSD(T,full)/CBS(cc-pV[D:T]Z)//B3LYP-D3(BJ)/cc-pVTZ level of theory. Harmonic frequencies of the $V=O$ modes are scaled by 0.9167, and all other modes by 0.9832. For further details, see Table 1 as well as Table S1 and Figure S1.

163 kJ mol⁻¹). Note that tagging cluster **1** with a helium atom does not perturb the IR spectrum significantly.

A comparison of the computed IR spectra of the [AlVO₄]⁺ isomers **1** to **4** (Figure 1) with the experimental IRPD spectrum of He-tagged [AlVO₄]⁺ (panel I in Figure 2) leaves no doubt that the global-minimum-energy structure **1** is formed exclusively upon laser ablation (see the Supporting Information, Figure S2) and subsequent helium tagging in the cold ion trap. Comparing the relevant frequencies

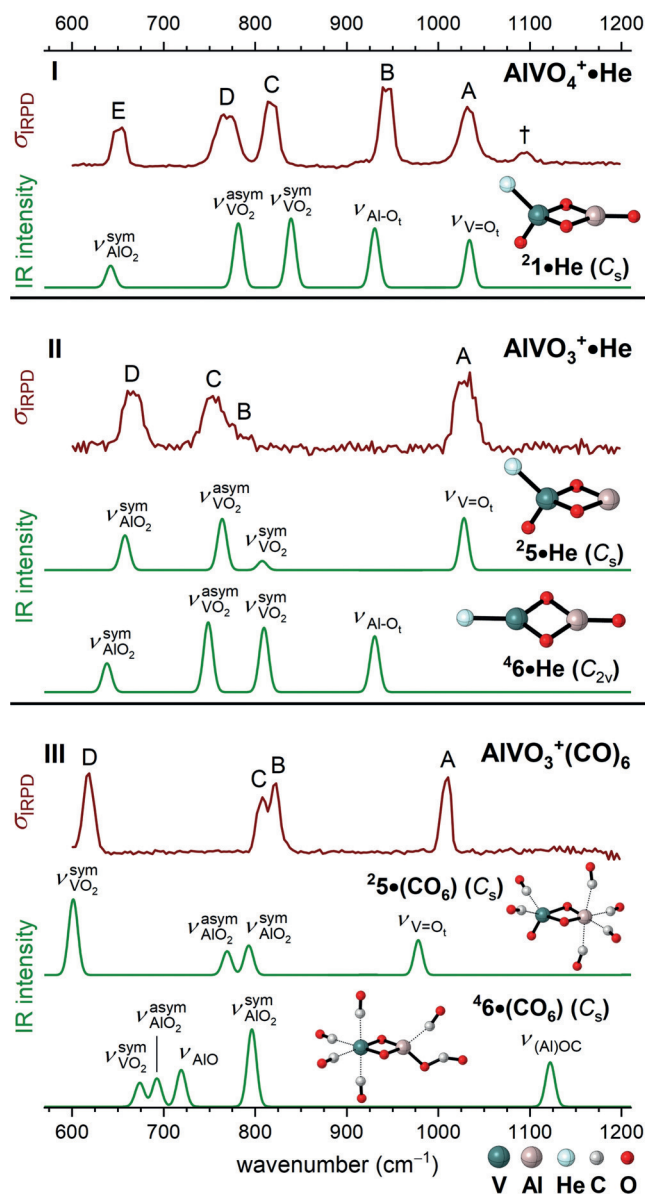


Figure 2. The experimental IRPD spectra (dark red) and the harmonic IR spectra (green) of I) [AlVO₄]⁺•He, II) [AlVO₃]⁺•He, and III) [AlVO₃]⁺•(CO)₆. The messenger-tagged clusters were produced either by mass-selecting the corresponding bare cations and subsequently tagging them with He in the ion trap at 12 K (I and II) or by trapping [AlVO₄]⁺ in a CO/He gas mixture at 60 K (III). The simulated IR spectra were determined from scaled B3LYP-D3(BJ)/cc-pVTZ harmonic frequencies and intensities and convoluted with a 10 cm⁻¹ full width at half maximum (FWHM) Gaussian line shape function. See Table 1 for the band positions and assignments.

(Table 1) shows satisfying to excellent agreement given the limitations of the harmonic approximation used in the simulation.

Table 1: Experimental band labels and positions, scaled harmonic B3LYP-D3(BJ)/cc-pVTZ vibrational wavenumbers, and band assignments. Values in parentheses indicate the FWHM of the observed bands.

System/band	Experiment [cm ⁻¹]	Scaled harmonic wavenumber [cm ⁻¹]	Assignment
[AlVO ₄ He] ⁺			
†	1094 (17)	n.a.	overtone antisymmetric AlO ₂ stretch
A	1032 (19)	1034 ^[a]	VO stretch
B	943 (16)	930 ^[b]	AlO stretch
C	817 (18)	839 ^[b]	symmetric VO ₂ stretch
D	769 (28)	781 ^[b]	antisymmetric VO ₂ stretch
E	651 (16)	641 ^[b]	symmetric AlO ₂ stretch
[AlVO ₃ He] ⁺			
A	1029 (21)	1028 ^[a]	VO stretch
B	783 (20)	808 ^[b]	symmetric VO ₂ stretch
C	754 (24)	764 ^[b]	antisymmetric VO ₂ stretch
D	666 (20)	658 ^[b]	symmetric AlO ₂ stretch
[AlVO ₃ (CO) ₆] ⁺			
A	1008 (10)	978 ^[a]	VO stretch
B	822 (10)	793 ^[b]	symmetric AlO ₂ stretch
C	807 (11)	769 ^[b]	antisymmetric AlO ₂ stretch
D	618 (12)	601 ^[b]	symmetric VO ₂ stretch

[a] Scaling factor: 0.9167 (VO stretches). [b] Scaling factor: 0.9832 (all other modes).

The three intense IRPD bands A–C proved to be particularly diagnostic for the discussion from which site of the heteronuclear cluster [AlVO₄]⁺ the oxygen atom is abstracted in the reduction. Band A at 1032 cm⁻¹ was assigned to the terminal V=O_t stretching mode of **1**, which is in line with the IRPD data reported previously for [V₂O₄]⁺^[15] and [VPO₄]⁺^[17]. Bands B (943 cm⁻¹) and C (817 cm⁻¹) correspond to the stretching of the terminal Al–O_t group and the symmetric OVO ring stretching mode, respectively.

When [AlVO₃]⁺ was generated directly by laser ablation (Figure S2) and subsequently tagged with He, its IRPD spectrum (spectrum II in Figure 2) was in excellent agreement with the one simulated for **5**•He, confirming that also in this case, the global-minimum-energy isomer is formed exclusively. This species is devoid of an Al–O_t unit but contains a V=O_t bond. In contrast, isomer **6**, in which the Al–O_t unit is preserved, is 106 kJ mol⁻¹ higher in energy than **5**, and, more importantly, the predicted IR spectrum of **6**•He does not match the experimental one (Figure 2).

Before moving on, a brief comment on the origin of the weaker IR band B (783 cm⁻¹) in panel II, which was assigned to the symmetric OVO ring stretching mode, might be helpful. This mode gives rise to the strong absorption band C in [AlVO₄]⁺•He (panel I), and the substantial drop in intensity is

due to the rather small change in the dipole moments associated with this vibration for the $[AlVO_3]^{+}$ cluster (for details, see Figure S1).

Next, we will address the central question as to whether isomer **5** is also and solely generated from the redox couple $[AlVO_4]^{+}/CO$. This experiment was performed with CO seeded in He gas at slightly higher temperatures (60 K) to avoid CO condensation on the ion trap walls. The obtained time-of-flight mass spectrum (see Figure S3) shows that also under multiple collision conditions, $[AlVO_4]^{+}$ is very efficiently (>98%, see Figure S3) converted into $[AlVO_3]^{+}$. Additional collisions with CO molecules cannot be avoided under the present conditions, but exclusively lead to “solvated” $[AlVO_3]^{+}$ clusters of the type $[AlVO_3]^{+} \cdot (CO)_{0-7}$, of which the $[AlVO_3]^{+} \cdot (CO)_6$ complex is formed predominantly (Figure S2). Its IRPD spectrum, obtained by monitoring the CO loss channels, is shown in Figure 2 (panel III). Comparison with the simulated IR spectra of isomers **5**·(CO)₆ and **6**·(CO)₆ clearly demonstrates that it is indeed the main-group aluminum oxide that delivers its oxygen atom in the redox process.^[20] This observation, namely that main-group oxides rather than transition-metal oxides serve as the active site in various catalytic transformations, seems to be a rather general structural feature of quite a few metal oxide clusters;^[21] moreover, as shown in a different context, these centers also play a decisive role in the thermal activation of strong C–H bonds by metal-attached oxyl groups.^[22]

In summary, we have used IRPD spectroscopy to unambiguously identify the active site of the heterogeneous metal oxide cluster $[AlVO_4]^{+}$, which serves as a computationally tractable gas-phase model system for studying OAT reactions as part of more complex catalytic cycles.^[23] The strategy employed here, which is based on using highly sensitive mass spectrometry for screening potentially interesting reactions and then applying the more complex methodology of cryogenic ion vibrational spectroscopy, in combination with electronic structure calculations, to resolve structural issues involving isobaric and isomeric species, is generally applicable and will prove helpful in future experiments, for example, in the context of coupling methane with carbon dioxide in the presence of metal-based heterogeneous catalysis.^[24]

Acknowledgements

Generous financial support of the work at TU Berlin by the Fonds der Chemischen Industrie and the Deutsche Forschungsgemeinschaft (“UniCat”) is appreciated. The research of the Asmis group was funded by the Deutsche Forschungsgemeinschaft within the Collaborative Research Center 1109, “Metal Oxide/Water Systems”. The work at Zhejiang University has been supported by the Fundamental Research Funds for the Central Universities of China (2018QNA4040). We thank Dr. Thomas Weiske, Dr. Maria Schlangen-Ahl, Dr. Xiaoyan Sun, and Sandy Gewinner for technical and computational assistance and Andrea Beck for her support in the preparation of the manuscript.

Conflict of interest

The authors declare no conflict of interest.

Keywords: active-site characterization · heteronuclear cluster oxides · infrared photodissociation spectroscopy · redox catalysis

How to cite: *Angew. Chem. Int. Ed.* **2018**, *57*, 7448–7452
Angew. Chem. **2018**, *130*, 7570–7574

- [1] a) H.-J. Freund, G. Meijer, M. Scheffler, R. Schlögl, M. Wolf, *Angew. Chem. Int. Ed.* **2011**, *50*, 10064–10094; *Angew. Chem.* **2011**, *123*, 10242–10275; b) B. Qiao, A. Wang, X. Yang, L. F. Allard, Z. Jiang, Y. Cui, J. Liu, J. Li, T. Zhang, *Nat. Chem.* **2011**, *3*, 634–641; c) A. Nilsson, J. LaRue, H. Öberg, H. Ogasawara, M. Dell’Angela, M. Beye, H. Öström, J. Gladh, J. K. Nørskov, W. Wurt, F. Abild-Pedersen, L.-G. M. Pettersson, *Chem. Phys. Lett.* **2017**, *675*, 145–173.
- [2] For a selected reviews, see: a) D. K. Böhme, H. Schwarz, *Angew. Chem. Int. Ed.* **2005**, *44*, 2336–2354; *Angew. Chem.* **2005**, *117*, 2388–2406; b) M. L. Kimble, A. W. Castleman, C. Bürgel, V. Bonačić-Koutecký, *Int. J. Mass Spectrom.* **2006**, *254*, 163–167; c) Z.-C. Wang, S. Yin, E. R. Bernstein, *J. Phys. Chem. Lett.* **2012**, *3*, 2415–2419; d) Q.-Y. Liu, S.-G. He, *Chem. J. Chin. Univ.* **2014**, *35*, 665–688; e) S. M. Lang, I. Fleischer, T. M. Bernhardt, R. N. Barnett, U. Landman, *ACS Catal.* **2015**, *5*, 2275–2289; f) H. Schwarz, *Catal. Sci. Technol.* **2017**, *7*, 4302–4314; g) see also the many references in: L.-N. Wang, X.-N. Li, L.-X. Jiang, B. Yang, Q.-Y. Liu, H.-G. Xu, W.-J. Zheng, S.-G. He, *Angew. Chem. Int. Ed.* **2018**, *57*, 3349–3353; *Angew. Chem.* **2018**, *130*, 3407–3411.
- [3] M. M. Kappes, R. H. Staley, *J. Am. Chem. Soc.* **1981**, *103*, 1286–1287.
- [4] a) J. J. Melko, S. G. Ard, J. A. Fournier, J. Li, N. S. Shuman, H. Guo, J. Troe, A. A. Viggiano, *Phys. Chem. Chem. Phys.* **2013**, *15*, 11257–11267; b) V. G. Ushakov, J. Troe, R. S. Johnson, H. Guo, S. G. Ard, J. J. Melko, N. S. Shuman, A. A. Viggiano, *Phys. Chem. Chem. Phys.* **2015**, *17*, 19700–19708.
- [5] a) H. Schwarz, *Int. J. Mass Spectrom.* **2004**, *237*, 75–105; b) D. Schröder, S. Shaik, H. Schwarz, *Acc. Chem. Res.* **2000**, *33*, 139–145; c) J. N. Harvey, *Phys. Chem. Chem. Phys.* **2007**, *9*, 331–343; d) S. Shaik, *Int. J. Mass Spectrom.* **2013**, *354/355*, 5–14; e) J. N. Harvey, *WIREs Comput. Mol. Sci.* **2014**, *4*, 1–14.
- [6] a) G. Koyanagi, D. K. Böhme, *J. Phys. Chem. A* **2001**, *105*, 8964–8968; b) V. V. Lavrov, V. Blagojevic, G. K. Koyanagi, G. Orlova, D. K. Böhme, *J. Phys. Chem. A* **2004**, *108*, 5610–5624; c) V. Blagojevic, G. Orlova, D. K. Böhme, *J. Am. Chem. Soc.* **2005**, *127*, 3545–3555.
- [7] M. Brönstrup, D. Schröder, I. Kretzschmar, H. Schwarz, J. N. Harvey, *J. Am. Chem. Soc.* **2001**, *123*, 142–147.
- [8] J. Sauer, H.-J. Freund, *Catal. Lett.* **2015**, *145*, 109–125.
- [9] H. S. Taylor, *J. Phys. Chem.* **1926**, *30*, 145–171.
- [10] Z.-C. Wang, N. Dietl, R. Kretzschmar, T. Weiske, M. Schlangen, H. Schwarz, *Angew. Chem. Int. Ed.* **2011**, *50*, 12351–12354; *Angew. Chem.* **2011**, *123*, 12559–12562.
- [11] A reviewer has surmised that in the oxidation of $^2[AlVO_3]^{+}$ with N_2O , electronically excited $^4[AlVO_4]^{+}$ may have been co-generated. While this process is spin-forbidden and part of the liberated 219 kJ mol^{-1} energy is carried away as kinetic energy, from an energetic point of view, this possibility cannot be ruled out as $^4[AlVO_4]^{+}$ is “only” 130 kJ mol^{-1} higher in energy than ground-state $^2[AlVO_4]^{+}$.
- [12] For selected reviews on FEL-IRPD, see: a) K. R. Asmis, J. Sauer, *Mass Spectrom. Rev.* **2007**, *26*, 542–562; b) K. R. Asmis, *Phys. Chem. Chem. Phys.* **2012**, *14*, 9270–9281; c) L. Jašíková, J. Roithová, *Chem. Eur. J.* **2018**, *24*, 3374–3390.

- [13] For an excellent essay on this approach entitled “High-Level Spectroscopy, Quantum Chemistry, and Catalysis: Not just a Passing Fad”, see: F. Neese, *Angew. Chem. Int. Ed.* **2017**, *56*, 11003–11010; *Angew. Chem.* **2017**, *129*, 11147–11154.
- [14] G. von Helden, A. Kirilyuk, D. van Heijnsbergen, B. Sartakov, M. A. Duncan, G. Meijer, *Chem. Phys.* **2000**, *262*, 31–39.
- [15] K. R. Asmis, G. Meijer, M. Brümmer, C. Kaposta, G. Santambrogio, L. H. Wöste, J. Sauer, *J. Chem. Phys.* **2004**, *120*, 6461–6470.
- [16] L. Jiang, T. Wende, P. Claes, S. Bhattacharyya, M. Sierka, G. Meijer, P. Lievens, J. Sauer, K. R. Asmis, *J. Phys. Chem. A* **2011**, *115*, 11187–11192.
- [17] N. Dietl, T. Wende, K. Chen, L. Jiang, M. Schlangen, X. Zhang, K. R. Asmis, H. Schwarz, *J. Am. Chem. Soc.* **2013**, *135*, 3711–3721.
- [18] X. Song, M. R. Fagiani, S. Gewinner, W. Schöllkopf, K. R. Asmis, F. A. Bischoff, F. Berger, J. Sauer, *J. Chem. Phys.* **2016**, *144*, 244305.
- [19] X. Song, M. R. Fagiani, S. Debnath, M. Gao, S. Maeda, T. Taketsugu, S. Gewinner, W. Schöllkopf, K. R. Asmis, A. Lyalin, *Phys. Chem. Chem. Phys.* **2017**, *19*, 23154–23161.
- [20] Actually, structure $6\cdot(\text{CO})_6$ should be better viewed as a complex of $[\text{AlVO}_2]^+$ tagged with five CO and one CO_2 ligands. Thus, if this species was generated at all in the redox reaction, one would expect loss of n CO and CO_2 molecules upon photon absorption. However, this is not the case.
- [21] a) G. E. Johnson, R. Mitrić, E. C. Tyo, V. Bonačić-Koutecký, A. W. Castleman, Jr., *J. Am. Chem. Soc.* **2008**, *130*, 13912–13920; b) G. E. Johnson, R. Mitrić, M. Nöbler, E. C. Tyo, V. Bonačić-Koutecký, A. W. Castleman, Jr., *J. Am. Chem. Soc.* **2009**, *131*, 5460–5470; c) J.-B. Ma, Z.-C. Wang, M. Schlangen, S.-G. He, H. Schwarz, *Angew. Chem. Int. Ed.* **2013**, *52*, 1226–1230; *Angew. Chem.* **2013**, *125*, 1264–1268; d) J.-B. Ma, B. Xu, J.-H. Meng, X.-N. Wu, X.-L. Ding, X.-N. Li, S.-G. He, *J. Am. Chem. Soc.* **2013**, *135*, 2991–2998; e) X. Sun, S. Zhou, L. Yue, M. Schlangen, H. Schwarz, *Angew. Chem. Int. Ed.* **2017**, *56*, 9990–9993; *Angew. Chem.* **2017**, *129*, 10122–10126.
- [22] For reviews, see: a) X.-L. Ding, X.-N. Wu, Y.-X. Zhao, S.-G. He, *Acc. Chem. Res.* **2012**, *45*, 382–390; b) N. Dietl, M. Schlangen, H. Schwarz, *Angew. Chem. Int. Ed.* **2012**, *51*, 5544–5555; *Angew. Chem.* **2012**, *124*, 5638–5650; c) W. Lai, C. Li, H. Chen, S. Shaik, *Angew. Chem. Int. Ed.* **2012**, *51*, 5556–5578; *Angew. Chem.* **2012**, *124*, 5652–5676; d) H. Schwarz, *Isr. J. Chem.* **2014**, *54*, 1413–1431; e) H. Schwarz, S. Shaik, J. Li, *J. Am. Chem. Soc.* **2017**, *139*, 17201–17212.
- [23] Note added in proof (16 May 2018): Dr. A. Viggiano has informed us (15 May 2018) about his experimental/computational studies on the role of non-reactive binding sites in the $[\text{AlVO}_x]^+/\text{CO}/\text{N}_2\text{O}$ ($x=3, 4$) redox systems. In line with our findings, the Al–O_i site constitutes the active center, and (unproductive) complexation of the vanadium site by N_2O is the root cause for the reduced efficiency of the redox process.
- [24] For many references, see: J. Li, P. González-Navarrete, M. Schlangen, H. Schwarz, *Chem. Eur. J.* **2015**, *21*, 7780–7789.

Manuscript received: April 5, 2018

Accepted manuscript online: April 26, 2018

Version of record online: May 23, 2018



Supporting Information

Experimental Identification of the Active Site in the Heteronuclear Redox Couples [AlVO_x]⁺/CO/N₂O (x = 3, 4) by Gas-Phase IR Spectroscopy

Sreekanta Debnath, Harald Knorke, Wieland Schöllkopf, Shaodong Zhou, Knut R. Asmis,* and Helmut Schwarz**

anie_201804056_sm_miscellaneous_information.pdf

Supporting Information

Experimental and Computational Section

The infrared photodissociation (IRPD) experiments are carried out on a 10 K ion trap-tandem mass spectrometer^[1] using the widely tunable, intense IR radiation from the Fritz Haber Institute Free-Electron Laser (FHI FEL).^[2] In brief, $[\text{AlVO}_x]^{+*}$ ($x = 3, 4$) ions are produced in a pulsed laser vaporization source by focusing a frequency-doubled Nd:YAG laser operated at 50 Hz with a pulse energy of 15–20 mJ onto a rotating Al/V (50-50 wt %) metal rod. The resulting plasma is quenched with a gas pulse of 0.75 % O_2 seeded in He. Cluster ions are formed during expansion through a clustering channel downstream from the rod and pass through a skimmer with a diameter of 4 mm. The beam of ions is collimated and thermalized close to room temperature in a He-gas filled radio frequency (RF) decapole ion-guide, mass-selected using a quadrupole mass-filter, and focused into a cryogenically cooled RF ring-electrode ion-trap. The trap is continuously filled with He buffer gas and held at a temperature of 12 K. Many collisions of the trapped ions with the buffer gas provide gentle cooling of the internal degrees of freedom close to the ambient temperature. At sufficiently low ion-trap temperatures, ion-messenger complexes are formed via three-body collisions.^[3] All ions are extracted from the ion trap at 5 Hz and focused both temporally and spatially into the center of the extraction region of an orthogonally mounted reflectron time-of-flight (TOF) tandem photofragmentation mass-spectrometer. Here, the ions are irradiated with a counter-propagating IR laser pulse produced by the FHI FEL ($600\text{--}1300\text{ cm}^{-1}$, bandwidth: $\sim 0.5\%$ fwhm, pulse energy: 5-15 mJ). All parent and photofragment ions are then accelerated toward an MCP detector and monitored simultaneously. IRPD scans are recorded by averaging over 100 TOF mass spectra per wavelength step (3 cm^{-1}) and scanning the wavelength. Typically, at least three scans are summed to obtain the final IRPD spectrum. The photodissociation cross section σ_{IRPD} is determined as described previously.^[4]

For the reaction with CO, mass-selected $[\text{AlVO}_4]^{+*}$ ions interact with a $< \sim 0.01\%$ CO, seeded in He, gas mixture inside the ion trap held at 60 K. $[\text{AlVO}_3 \cdot n(\text{CO})]^{+*}$ is the most abundant reaction product under these conditions and its IRPD spectrum is measured monitoring the n -CO loss channels ($n = 1, 2$).

The labeling experiments were carried out using a Spectrospin-CMS-47X Fourier-transform ion cyclotron resonance (FT-ICR) mass spectrometer as described elsewhere.^[5] $[\text{AlV}^{18}\text{O}_4]^{+*}$ ions

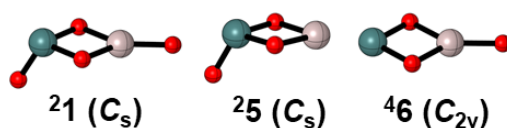
were generated by laser ablation of an Al-V target using a Nd:YAG laser ($\lambda=532$ nm); helium, mixed with ¹⁸O-oxygen, served as a carrier gas. The ions were transferred from the external ion source into the cylindrical ICR-cell, which is located in a superconducting magnetic field (7.05 T), by using a system of electrostatic potentials and lenses. Thermalization of the ions of interest has been achieved by collisions with repeatedly pulsed-in argon.

The theoretical work was performed using the Gaussian 09 program.^[6] The cc-pVTZ basis set^[7] was employed for all atoms to perform structural optimization and frequency analysis. More accurate single-point energies were obtained at the CCSD(T,full)^[8]/CBS(cc-pV[D:T]Z) level of theory. Stationary points were optimized without symmetry constraint, and their nature was confirmed by vibrational frequency analysis. Unscaled vibrational frequencies were used to correct the relative energies for zero-point vibrational energy (ZPVE) contributions.

In order to select a reliable method for the IR calculations, the structural parameters of the ground-state [AIVO₄]⁺ (**21**),^[9] [Al(μ -O)₂VO]⁺ (**25**), and [O₄Al(μ -O)₂V]⁺ (**46**) calculated using B3LYP^[10]-D3(BJ),^[11] PBE0^[10]-D3(BJ), TPSS^[12]-D3(BJ), B2PLYP^[13]-D3(BJ), B2GP-PLYP^[14]-D3(BJ), DSD-PBEP86^[15]-D3(BJ), B97-1,^[16] M06,^[17] M06L,^[18] SCS-MP2^[19] and TPSSh,^[12] were compared with those given by CCSD. More details are given in Table S1.

5. Catalytic Active Site Characterization of Heteronuclear Metal Oxide Clusters

Table S1. Bond lengths of ${}^2\mathbf{1}$, ${}^2\mathbf{5}$ and ${}^4\mathbf{6}$ as calculated with different methods. The standard deviations (STDs) from the CCSD results are included. Bond lengths are given in Å.^a



Bond	CCSD	B3LYP-D3(BJ)	PBE0-D3(BJ)	TPSS-D3(BJ)	B2PLYP-D3(BJ)	B2GP-PLYP-D3(BJ)	DSD-PBEP86-D3(BJ)	B97-1	M06	M06L	SCS-MP2	TPSSh
${}^2\mathbf{1}$ (Al-O _t)	1.715	1.718	1.713	1.73	1.717	1.713	1.716	1.72	1.707	1.713	1.718	1.722
${}^2\mathbf{1}$ (Al-O _b)	1.779	1.783	1.777	1.792	1.785	1.781	1.784	1.784	1.769	1.772	1.793	1.785
${}^2\mathbf{1}$ (V-O _t)	1.536	1.553	1.539	1.571	1.611	1.6	1.602	1.549	1.543	1.562	1.578	1.558
${}^2\mathbf{1}$ (V-O _b)	1.728	1.734	1.721	1.745	1.762	1.756	1.759	1.731	1.725	1.74	1.766	1.735
${}^2\mathbf{1}$ (Al-V)	2.524	2.526	2.507	2.528	2.535	2.526	2.527	2.521	2.502	2.513	2.537	2.521
${}^2\mathbf{5}$ (V-O _t)	1.54	1.556	1.542	1.573	1.579	1.552	1.606	1.551	1.546	1.564	1.586	1.56
${}^2\mathbf{5}$ (V-O _b)	1.722	1.739	1.723	1.755	1.765	1.75	1.761	1.738	1.731	1.751	1.749	1.742
${}^2\mathbf{5}$ (Al-O _b)	1.806	1.799	1.795	1.801	1.802	1.804	1.806	1.798	1.782	1.781	1.82	1.798
${}^2\mathbf{5}$ (Al-V)	2.535	2.536	2.516	2.536	2.545	2.542	2.534	2.529	2.51	2.52	2.525	2.528
${}^4\mathbf{6}$ (Al-O _t)	1.718	1.721	1.716	1.732	1.719	1.716	1.719	1.724	1.709	1.715	1.721	1.713
${}^4\mathbf{6}$ (Al-O _b)	1.766	1.772	1.766	1.784	1.775	1.77	1.773	1.779	1.769	1.766	1.775	1.762
${}^4\mathbf{6}$ (V-O _b)	1.754	1.749	1.736	1.753	1.757	1.754	1.752	1.755	1.73	1.748	1.758	1.747
${}^4\mathbf{6}$ (Al-V)	2.532	2.526	2.507	2.526	2.532	2.529	2.524	2.532	2.466	2.5	2.54	2.519
STD	0	0.009	0.012	0.019	0.028	0.021	0.030	0.008	0.023	0.018	0.023	0.012

^aO_t: terminal oxygen atom; O_b: bridging oxygen atom

As shown in Table S1, the B3LYP-D3(BJ) and B97-1 exhibit the smallest STD as compared with CCSD. Considering the reliability of the B3LYP functional in calculating frequencies of vanadium-containing metal-oxide clusters,^[20] the IR calculations are thus performed with B3LYP-D3(BJ). We use the scaling factors that were determined for small vanadium oxide cluster cations;^[21] thus, harmonic frequencies of the V=O stretching modes are scaled by 0.9167 and all the other modes by 0.9832.

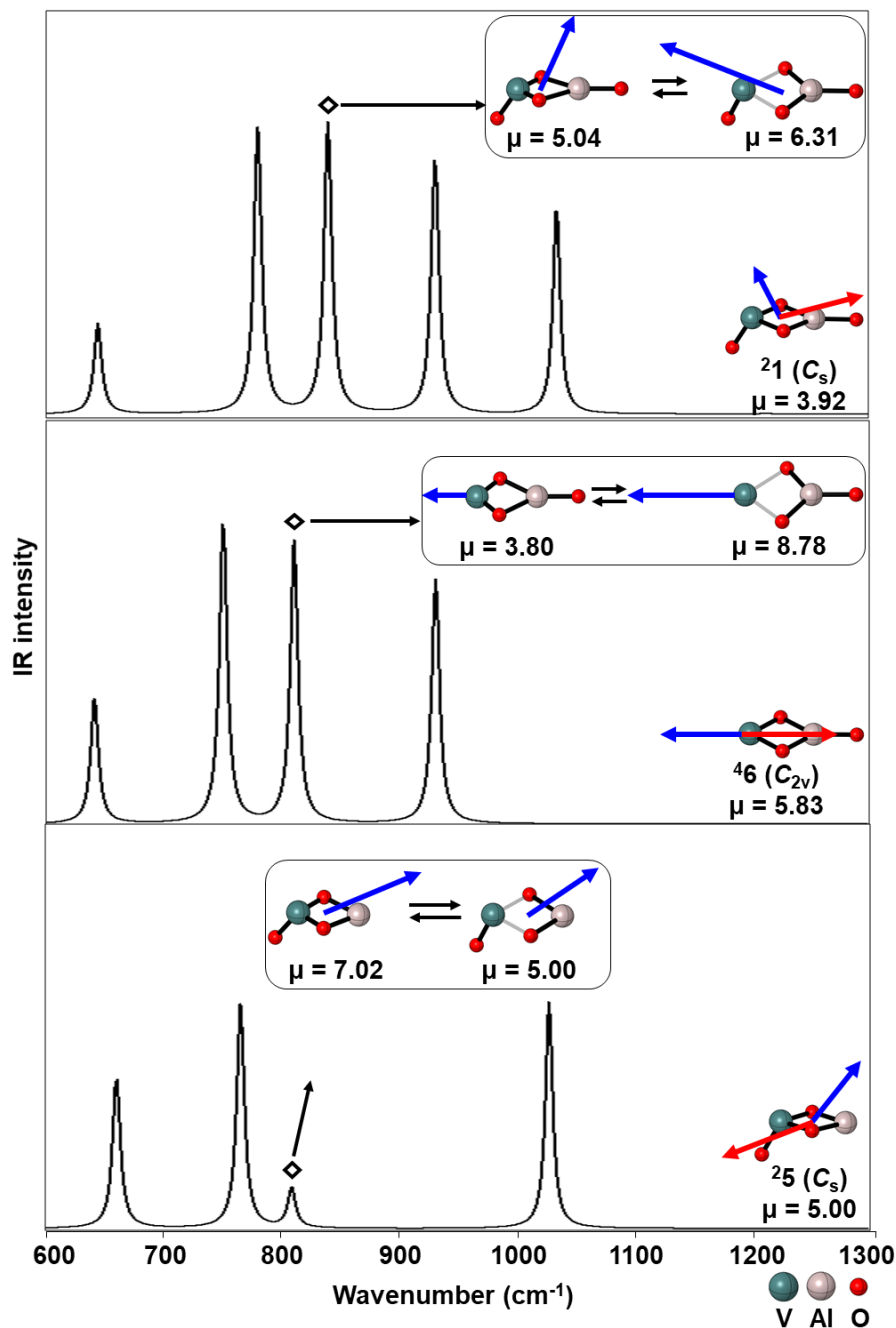


Figure S1. Simulated IR spectra of 21 , 45 and 26 as calculated at the B3LYP-D3(BJ)/cc-pVTZ level of theory. The signal for the symmetric O_b-V-O_b stretch is marked with rhombs; dipole moments of the structures are given in Debye, and the corresponding vectors are shown as blue arrows; as red arrows, the dipole derivative unit vectors concerning the O_b-V-O_b mode are given. The displacements of vibrating structures from the associated stable points are with a scale ± 0.5 . Harmonic frequencies of the $V=O$ modes are scaled by 0.9167 and all other modes by 0.9832.

As shown in Figure S1, the O_b-V-O_b vibration is associated with significant changes of the dipole moments of ${}^2\mathbf{1}$ and ${}^4\mathbf{6}$ either in orientation or in magnitude; in contrast, this vibration does not bring too much change of the dipole moment to ${}^2\mathbf{5}$. Thus, for ${}^2\mathbf{1}$ and ${}^4\mathbf{6}$ high IR intensities result regarding this vibration while a rather low intensity is expected for ${}^2\mathbf{5}$.

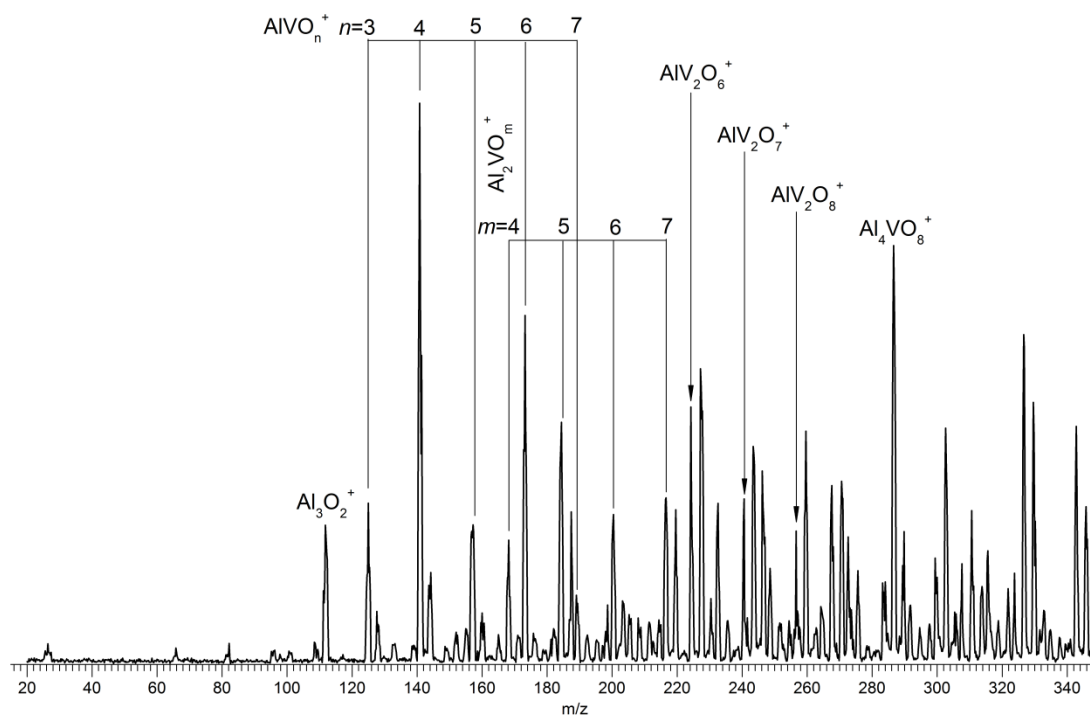


Figure S2: Quadrupole mass spectrum of the ions produced by pulsed laser vaporization of an Al/V (50-50 wt %) metal rod and quenching in a gas pulse of 0.75 % O₂ seeded in He.

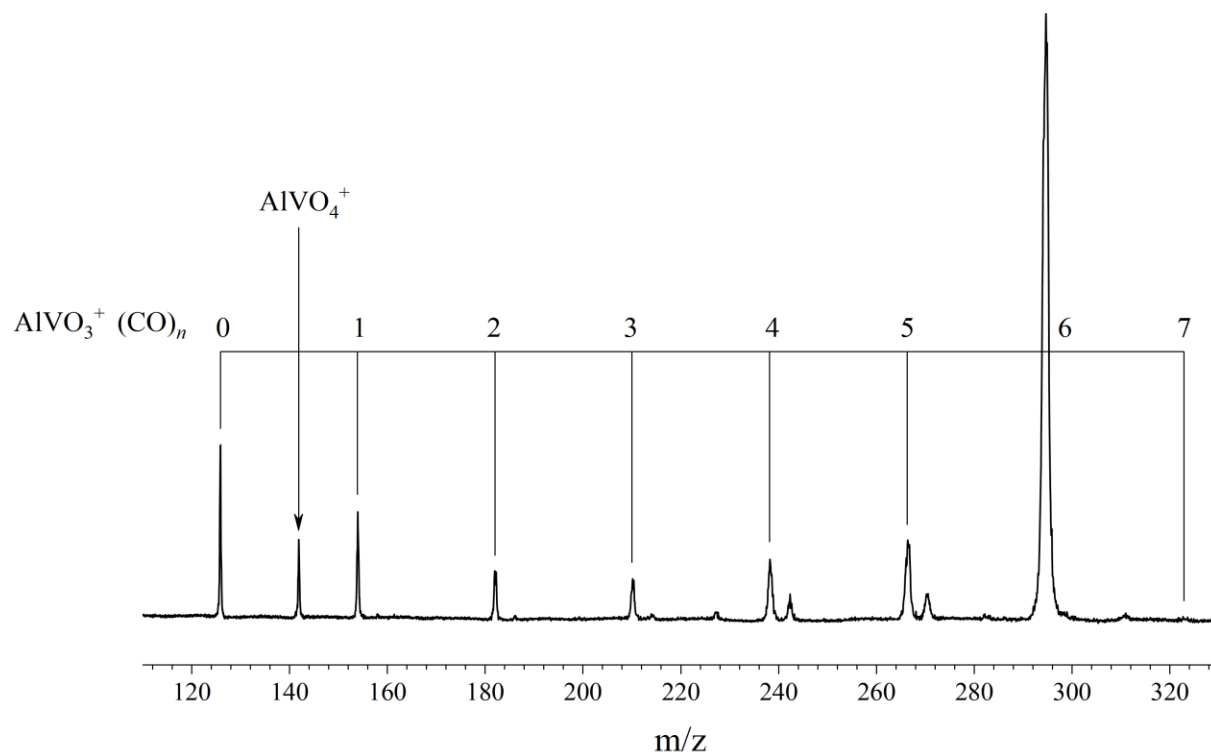


Figure S3: Time-of-flight mass spectrum (converted to a m/z scale) of the reaction products obtained after trapping mass-selected $AiVO_4^+$ ions for up to 200 ms in the gas-filled (CO seeded in He) ion trap held at 60 K.

References

- [1] D. J. Goebbert, A. J. Meijer, K. R. Asmis, *AIP Conf. Proc.* **2009**, 1104, 22-29.
- [2] W. Schöllkopf, S. Gewinner, H. Junkes, A. Paarmann, G. von Helden, H. Bluem, A. M. M. Todd, *Proc. SPIE* **2015**, 9512, 95121L1-13.
- [3] M. Brummer, C. Kaposta, G. Santambrogio, K. R. Asmis, *J. Chem. Phys.* **2003**, 119, 12700-12703.
- [4] a) N. Heine, K. R. Asmis, *Int. Rev. Phys. Chem.* **2016**, 35, 507-507; b) N. Heine, K. R. Asmis, *Int. Rev. Phys. Chem.* **2015**, 34, 1-34.
- [5] a) M. Engeser, T. Weiske, D. Schröder, H. Schwarz, *J. Phys. Chem. A* **2003**, 107, 2855-2859; b) K. Eller, W. Zummack, H. Schwarz, *J. Am. Chem. Soc.* **1990**, 112, 621-627; c) K. Eller, H. Schwarz, *Int. J. Mass Spectrom. Ion Processes* **1989**, 93, 243-257.
- [6] M. J. Frisch, G. W. Trucks, H. B. Schlegel, G. E. Scuseria, M. A. Robb, J. R. Cheeseman, G. Scalmani, V. Barone, B. Mennucci, G. A. Petersson, H. Nakatsuji, M.

- Caricato, X. Li, H. P. Hratchian, A. F. Izmaylov, J. Bloino, G. Zheng, J. L. Sonnenberg, M. Hada, M. Ehara, K. Toyota, R. Fukuda, J. Hasegawa, M. Ishida, T. Nakajima, Y. Honda, O. Kitao, H. Nakai, T. Vreven, J. A. Montgomery, Jr., J. E. Peralta, F. Ogliaro, M. Bearpark, J. J. Heyd, E. Brothers, K. N. Kudin, V. N. Staroverov, R. Kobayashi, J. Normand, K. Raghavachari, A. Rendell, J. C. Burant, S. S. Iyengar, J. Tomasi, M. Cossi, N. Rega, J. M. Millam, M. Klene, J. E. Knox, J. B. Cross, V. Bakken, C. Adamo, J. Jaramillo, R. Gomperts, R. E. Stratmann, O. Yazyev, A. J. Austin, R. Cammi, C. Pomelli, J. W. Ochterski, R. L. Martin, K. Morokuma, V. G. Zakrzewski, G. A. Voth, P. Salvador, J. J. Dannenberg, S. Dapprich, A. D. Daniels, O. Farkas, J. B. Foresman, J. V. Ortiz, J. Cioslowski, D. J. Fox, Gaussian 09, Revision D.01, Gaussian, Inc., Wallingford CT, 2009.
- [7] a) N. B. Balabanov, K. A. Peterson, *J. Chem. Phys.* **2005**, *123*; b) D. E. Woon, T. H. Dunning, *J. Chem. Phys.* **1993**, *98*, 1358-1371; c) T. H. Dunning, *J. Chem. Phys.* **1989**, *90*, 1007-1023.
- [8] a) G. E. Scuseria, H. F. Schaefer, *J. Chem. Phys.* **1989**, *90*, 3700-3703; b) G. E. Scuseria, C. L. Janssen, H. F. Schaefer, *J. Chem. Phys.* **1988**, *89*, 7382-7387; c) J. A. Pople, M. Headgordon, K. Raghavachari, *J. Chem. Phys.* **1987**, *87*, 5968-5975; d) G. D. Purvis, R. J. Bartlett, *J. Chem. Phys.* **1982**, *76*, 1910-1918.
- [9] Z. C. Wang, N. Dietl, R. Kretschmer, T. Weiske, M. Schlangen, H. Schwarz, *Angew. Chem. Int. Ed.* **2011**, *50*, 12351-12354.
- [10] a) C. T. Lee, W. T. Yang, R. G. Parr, *Phys. Rev. B* **1988**, *37*, 785-789; b) B. Miehlich, A. Savin, H. Stoll, H. Preuss, *Chem. Phys. Lett.* **1989**, *157*, 200-206; c) A. D. Becke, *J. Chem. Phys.* **1993**, *98*, 1372-1377; d) A. D. Becke, *J. Chem. Phys.* **1993**, *98*, 5648-5652.
- [11] a) S. Grimme, S. Ehrlich, L. Goerigk, *J. Comput. Chem.* **2011**, *32*, 1456-1465; b) S. Grimme, J. Antony, S. Ehrlich, H. Krieg, *J. Chem. Phys.* **2010**, *132*, 154104.
- [12] J. M. Tao, J. P. Perdew, V. N. Staroverov, G. E. Scuseria, *Phys. Rev. Lett.* **2003**, *91*.
- [13] S. Grimme, *J. Chem. Phys.* **2006**, *124*.
- [14] A. Karton, A. Tarnopolsky, J.-F. Lamère, G. C. Schatz, J. M. L. Martin, *J. Phys. Chem. A* **2008**, *112*, 12868-12886.
- [15] S. Kozuch, J. M. L. Martin, *Phys. Chem. Chem. Phys.* **2011**, *13*, 20104-20107.
- [16] F. A. Hamprecht, A. J. Cohen, D. J. Tozer, N. C. Handy, *J. Chem. Phys.* **1998**, *109*, 6264-6271.
- [17] Y. Zhao, D. G. Truhlar, *Theor. Chem. Acc.* **2008**, *120*, 215-241.
- [18] Y. Zhao, D. G. Truhlar, *J. Chem. Phys.* **2006**, *125*.
- [19] S. Grimme, *J. Chem. Phys.* **2003**, *118*, 9095-9102.
- [20] N. Dietl, T. Wende, K. Chen, L. Jiang, M. Schlangen, X. H. Zhang, K. R. Asmis, H. Schwarz, *J. Am. Chem. Soc.* **2013**, *135*, 3711-3721.
- [21] K. R. Asmis, G. Meijer, M. Brümmer, C. Kaposta, G. Santambrogio, L. Wöste, J. Sauer, *J. Chem. Phys.* **2004**, *120*, 6461-6470.

5.2. Direct Identification of Acetaldehyde Formation and Characterization of the Active Site in the $[\text{VPO}_4]^{*+}/\text{C}_2\text{H}_4$ Couple By Gas-Phase Vibrational Spectroscopy

In the publication “Direct Identification of Acetaldehyde Formation and Characterization of the Active Site in the $[\text{VPO}_4]^{*+}/\text{C}_2\text{H}_4$ Couple By Gas-Phase Vibrational Spectroscopy”,¹ cryogenic ion trap vibrational spectroscopy is used to identify the active site in $[\text{VPO}_4]^{*+}$ cluster. To this end, $[\text{VPO}_4]^{*+}$ is generated by electro spraying a mM solution of VOCl_3 and $\text{PO}(\text{OEt})_3$ in methanol. IRPD spectra of He-tagged $[\text{VPO}_4]^{*+}$ is measured which reproduced previous experimental finding.² In the next step mass selected $[\text{VPO}_4]^{*+}$ clusters are trapped and brought in contact with C_2H_4 (0.025% C_2H_4 in He) at 150K. Even under this multiple collision condition a small amount of $[\text{VPO}_3]^{*+}$ is formed and the main reaction channel is C_2H_4 -tagged $[\text{VPO}_4]^{*+}$ clusters. This result is consistent with the previous mass spectrometric study by Schwarz *et al.*² IRPD spectrum of $[\text{VPO}_4]^{*+}\cdot(\text{C}_2\text{H}_4)_2$ is recorded monitoring the dissociation channel of the second ethylene tag (I didn't see any dissociation of the first tag). Comparison of spectral signatures of $[\text{VPO}_4]^{*+}\cdot\text{He}$ and $[\text{VPO}_4]^{*+}\cdot(\text{C}_2\text{H}_4)_2$ reveals that the $\text{P}-\text{O}_t$ stretching band at 1445 cm^{-1} is missing in case of the later species, inferring that the $\text{P}-\text{O}_t$ species is the active site and was involved in the OAT reaction. More interestingly, the new peak which appeared in the carbonyl stretching region at 1653 cm^{-1} in the IRPD spectrum of the latter species, was assigned to the $\text{C}=\text{O}$ stretching of the formed CH_3CHO . This is how the neutral product of the OAT reaction was spectroscopically identified.

Declaration of Contribution:

Ya-Ke Li and I planned and performed the experimental work, including the measurement of all IRPD spectra, data evaluation and interpretation. All the theoretical calculations were done by Maria Schlangen. Other contributions of the co-authors are listed below:

Ya-Ke Li	Made most of the figures, wrote first version of experimental results part of the manuscript.
Maria Schlangen	Made part of the figures.
Wieland Schöllkopf	Evening operator of the FHI-FEL.
Helmut Schwarz, Knut. R. Asmis	Coordinated the project, framed the principal idea, supervised the research, helped in data interpretation and wrote the manuscript.

1. Li, Y.-K., et al., *Angewandte Chemie International Edition*, 2019. **58**, 18868-18872
2. Dietl, N., et al., *Journal of the American Chemical Society*, 2013. **135**, 3711-3721

IR Spectroscopy

International Edition: DOI: 10.1002/anie.201911040
German Edition: DOI: 10.1002/ange.201911040Direct Identification of Acetaldehyde Formation and Characterization of the Active Site in the $[\text{VPO}_4]^{+}/\text{C}_2\text{H}_4$ Couple by Gas-Phase Vibrational Spectroscopy

Ya-Ke Li, Sreekanta Debnath, Maria Schlangen, Wieland Schöllkopf, Knut R. Asmis,* and Helmut Schwarz*

Dedicated to Professor Wolfram Koch on the occasion of his 60th birthday

Abstract: The gas-phase reaction of the heteronuclear oxide cluster $[\text{VPO}_4]^{+}$ with C_2H_4 is studied under multiple collision conditions at 150 K using cryogenic ion-trap vibrational spectroscopy combined with electronic structure calculations. The exclusive formation of acetaldehyde is directly identified spectroscopically and discussed in the context of the underlying reaction mechanism. In line with computational predictions it is the terminal P=O and not the V=O unit that provides the oxygen atom in the barrier-free thermal $\text{C}_2\text{H}_4 \rightarrow \text{CH}_3\text{CHO}$ conversion. Interestingly, in the course of the reaction, the emerging CH_3CHO product undergoes a rather complex intramolecular migration, coordinating eventually to the vanadium center prior to its liberation. Moreover, the spectroscopic structural characterization of neutral $\text{C}_2\text{H}_4\text{O}$ deserves special mentioning as in most, if not all, ion/molecule reactions, the neutral product is usually only indirectly identified.

The identification of the active site(s) of single-site catalysts—the so-called “aristocratic atoms”^[1]—constitutes one of the intellectual cornerstones in contemporary catalysis research.^[2] This holds true in particular for heteronuclear cluster oxides whose judicious “doping” allows for an unprecedented control of their gas-phase ion chemistry.^[3] In this respect, the redox couple $[\text{AlVO}_x]^{+}/\text{CO}/\text{N}_2\text{O}$ ($x=3, 4$) may serve as a good example.^[4] At room temperature,

$[\text{AlVO}_4]^{+}$ is reduced to $[\text{AlVO}_3]^{+}$ in the presence of CO, and if N_2O is added, re-oxidation occurs; both oxygen atom transfers (OATs) are clean and proceed with reaction efficiencies of 59 and 65 %, respectively. DFT calculations have provided insight into the mechanism of this OAT catalytic cycle and predicted the terminal Al–O and not the expected V–O unit as the active site of the catalyst.^[4] Experimental confirmation of these predictions for both the structure of the $[\text{AlVO}_4]^{+}$ cluster oxide as well as its active site was only obtained much later by cryogenic ion-trap vibrational spectroscopy of messenger-tagged cluster ions.^[5,6]

Herein, we describe the spectroscopic characterization of the reaction of the $[\text{VPO}_4]^{+}/\text{C}_2\text{H}_4$ couple. This heteronuclear oxo cluster has served as a model system of industrially important VPO catalysts^[7] in the gas-phase oxidation of small hydrocarbons.^[8] At room temperature, $[\text{VPO}_4]^{+}$ brings about the selective conversion of C_2H_4 to form $\text{C}_2\text{H}_4\text{O}$.^[8] In line with DFT calculations, IR photodissociation spectroscopy permitted an unambiguous structural assignment of $[\text{VPO}_4]^{+}$ (**1**). Other isomers considered were not only predicted to lie $> 100 \text{ kJ mol}^{-1}$ higher in energy than **1**, also their calculated IR spectra did not match the experimentally recorded one.^[8] DFT calculations further predicted that it is only the terminal P=O unit that serves as the active site in the course of the $\text{C}_2\text{H}_4 \rightarrow \text{C}_2\text{H}_4\text{O}$ conversion. The alternative OAT process involving the terminal V=O group of **1** was calculated to require too much energy to play a role at ambient temperature.^[8]

What has been missing thus far is an unambiguous experimental characterization of relevant reaction intermediates and the products, for example, the structural assignment of the $[\text{VPO}_3]^{+}$ ion and in particular the neutral OAT $\text{C}_2\text{H}_4\text{O}$ (Scheme 1). In fact, to the best of our knowledge, in none of the numerous gas-phase ion/molecule reactions, the neutral product has ever been spectroscopically characterized. Furthermore, and as suggested by a reviewer, in addition to the previous DFT calculations,^[8] a more detailed discussion of the actual mechanism of the $\text{C}_2\text{H}_4 \rightarrow \text{CH}_3\text{CHO}$ conversion is indicated. This will be provided further below.

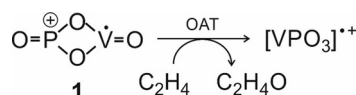
[*] Dr. M. Schlangen, Prof. Dr. H. Schwarz
Institut für Chemie, Technische Universität Berlin
Straße des 17. Juni 135, 10623 Berlin (Germany)
E-mail: Helmut.Schwarz@tu-Berlin.de

Dr. Y.-K. Li, M. Sc. S. Debnath, Prof. Dr. K. R. Asmis
Wilhelm-Ostwald Institut für Physikalische und Theoretische
Chemie, Universität Leipzig
Linnéstr. 2, 04103 Leipzig (Germany)
E-mail: knut.asmis@uni-leipzig.de

Dr. Y.-K. Li, M. Sc. S. Debnath, Dr. W. Schöllkopf
Fritz-Haber-Institut der Max-Planck-Gesellschaft
Faradayweg 4–6, 14195 Berlin (Germany)

Supporting information and the ORCID identification number(s) for the author(s) of this article can be found under:
<https://doi.org/10.1002/anie.201911040>

© 2019 The Authors. Published by Wiley-VCH Verlag GmbH & Co. KGaA. This is an open access article under the terms of the Creative Commons Attribution License, which permits use, distribution and reproduction in any medium, provided the original work is properly cited.



Scheme 1. Oxygen atom transfer in the reaction of $[\text{VPO}_4]^{+}$ with C_2H_4 .

To this end, we revisited the OAT reaction of **1** with C_2H_4 and studied it by ion-trap mass spectrometry in combination with cryogenic ion vibrational spectroscopy (see the Supporting Information for experimental details).^[6,9] Species **1** is produced as previously described,^[8] mass-selected, and interacts with 0.025% C_2H_4 in He ($p_{\text{He}} \approx 0.022$ mbar) under multiple collision conditions in a linear radiofrequency ion trap. The reaction products obtained after 100 ms are shown in Figure 1. Two series of mass peaks are observed. The dominant product channel corresponds to the formation of $[\text{VPO}_4, (\text{C}_2\text{H}_4)_n]^{+}$ adducts with $n=0-3$. Formation of $[\text{VPO}_3]^{+}$ and its adducts with C_2H_4 is roughly 100 times less efficient. The present results are in qualitative agreement with the previous results obtained under single-collision conditions, which also found that adduct formation is favored over O-atom loss; however, adduct formation was less efficient, and obviously no adducts with $n > 1$ were observed under single-collision conditions.^[8] The adduct ion yields are also expected to be higher in the present case as the reaction under scrutiny is predicted to be barrier-free with respect to the energy of the entrance channel (energy of **1** and C_2H_4 in Figure 2), and hence shows a negative temperature dependence.

As to the mechanism of OAT in the $[\text{VPO}_4]^{+}/\text{C}_2\text{H}_4$ couple, the new DFT calculations (Figure 2) provide some unexpected findings:

- 1) Coordination of the incoming C_2H_4 ligand can occur at both the phosphorus (**1**→**2**) and the vanadium sites of the cluster (**1**→**6**), with the latter path being energetically clearly favored.
- 2) In the course of the multistep OAT reaction, the global minimum corresponds to a complex in which the newly formed CH_3CHO ligand (containing the oxygen atom of the P=O unit) is coordinated to the vanadium center (**1**→**5**). The isomeric cluster **9**, generated from **6**, is approximately 115 kJ mol^{-1} less stable than **5**. However, as the transition states leading to both **5** and **9** are located below the entrance channel **1** + C_2H_4 , both routes are energetically accessible. Interestingly, **5** and **9** are connected via transition state **TS9/4** and **TS4/5**.

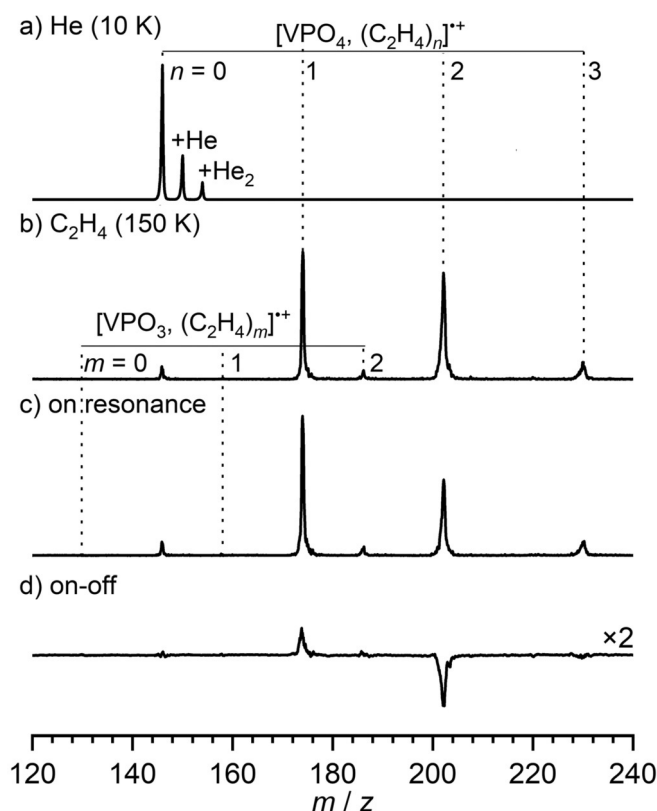


Figure 1. Time-of-flight (TOF) mass spectra obtained after storing mass-selected $[\text{VPO}_4]^{+}$ ions for 100 ms in the ion trap filled with a) He at 10 K and b) $\text{C}_2\text{H}_4/\text{He}$ and held at 150 K. c) Upon resonant excitation ($\bar{\nu} = 1655 \text{ cm}^{-1}$; see Figure 3), fragmentation of the weaker bound adducts ($n > 1$) occurs. d) Difference spectrum, obtained by subtracting the on-resonance from an off-resonance ($\bar{\nu} = 1685 \text{ cm}^{-1}$) mass spectrum, showing the depletion (downward peaks) of the parent ions ($n > 1$) and the formation of the corresponding fragment ions ($n \leq 1$). Note that the ions with $n \leq 1$ are more strongly bound, making their dissociation less probable.

- 3) Evaporation of CH_3CHO to produce $[\text{P}(\text{O}_2)\text{VO}]^{+}$ can take place from either **4**, **5**, or **9**.

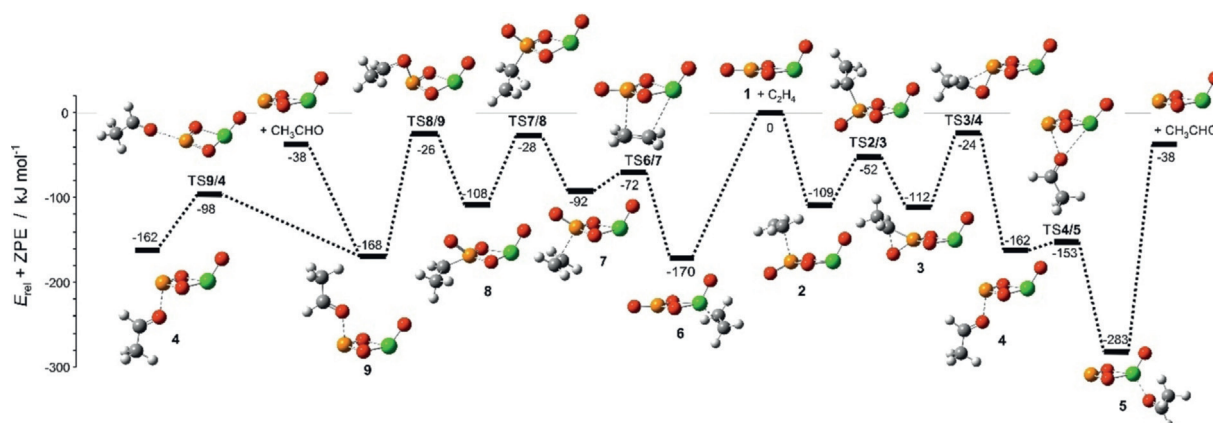


Figure 2. Simplified electronic ground-state PES for the reactions of $[\text{VPO}_4]^{+}$ with C_2H_4 , calculated at the B3LYP/def2-TZVPP level of theory. C gray, H white, V green, O red, P yellow. The relative energies $\Delta H_{0\text{K}}$ are given in kJ mol^{-1} and corrected for unscaled ZPE contributions.

In order to identify the structure of the reaction product(s), we turn to infrared photodissociation (IRPD) spectroscopy combined with messenger tagging to ensure probing in the linear absorption regime; this simplifies the interpretation of the IRPD spectra significantly.^[10] The IRPD experiments are performed on a cryogenic ion-trap tandem mass spectrometer^[11] using the widely tunable, intense IR radiation from the Fritz Haber Institute free electron Laser (FHI-FEL).^[12] As typical messengers, such as He or H₂, do not bind efficiently to cations at the present ion-trap temperature of 150 K, we exploit the fact that larger $[\text{VPO}_4, (\text{C}_2\text{H}_4)_n]^+$ adducts are formed, in which the additional C₂H₄ moieties are more weakly bound and function as messengers upon photoabsorption. This is demonstrated in the mass spectra shown in the bottom panels of Figure 1. The spectrum in Figure 1 c is obtained after irradiating all ions extracted from the ion trap on-resonance (1655 cm⁻¹), and the difference spectrum (Figure 1 d) is obtained by subtracting an off-resonance spectrum (1685 cm⁻¹) from this on-resonance spectrum. Using sufficiently attenuated laser pulse energies, photodissociation is only observed for the $n > 1$ adducts, that is, the corresponding peaks are depleted in the on-resonance spectrum (i.e., downward peaks in Figure 1 d), while the $n \leq 1$ peaks increase in intensity (i.e., upward peaks in Figure 1 d), suggesting that $[\text{VPO}_4, \text{C}_2\text{H}_4]^+ \cdot (\text{C}_2\text{H}_4)_{n-1}$ type complexes are present, containing a single, chemically transformed ethylene species, while the others remain physisorbed.

The IRPD spectrum of $[\text{VPO}_4, \text{C}_2\text{H}_4]^+ \cdot (\text{C}_2\text{H}_4)$ is shown in Figure 3 b and compared to the previously obtained spectrum of $[\text{VPO}_4]^+ \cdot \text{He}_2$ (Figure 3 a).^[8] The two spectra are distinctly different, showing that a reaction must have occurred. Note that the terminal P=O stretching band of $[\text{VPO}_4]^+$ at 1445 cm⁻¹ is not present in the spectrum of the C₂H₄ adduct, but has been replaced by a similarly intense band at higher energies (1653 cm⁻¹), which lies in the carbonyl stretching region.

In order to assign the IRPD spectrum of $[\text{VPO}_4, \text{C}_2\text{H}_4]^+ \cdot (\text{C}_2\text{H}_4)$, we compare it to the B3LYPD2/def2-tzvpp harmonic spectra of possible structural candidates in Figure 3 (see Figures S1 and S2 in the Supporting Information for additional information). Indeed, the best agreement is found for the global minimum-energy structure **5**, which is predicted to lie 283 kJ mol⁻¹ below the entrance channel and represents the final reaction product containing acetaldehyde bound to $[\text{P}(\text{O})_2\text{VO}]^+$. The exclusive formation of **5** rather than **4** or **9** (Figure 3 b, d, and e, respectively) as the long-lived $[\text{VPO}_3]^+/\text{CH}_3\text{CHO}$ intermediate in the ion trap is quite remarkable; after all, the OAT potential energy surface is rather complex and involves quite a number of isomeric intermediates and transition states. Nevertheless, most likely on thermochemical grounds, the CH₃CHO product undergoes an intracomplex migration from the P- to the V-center to

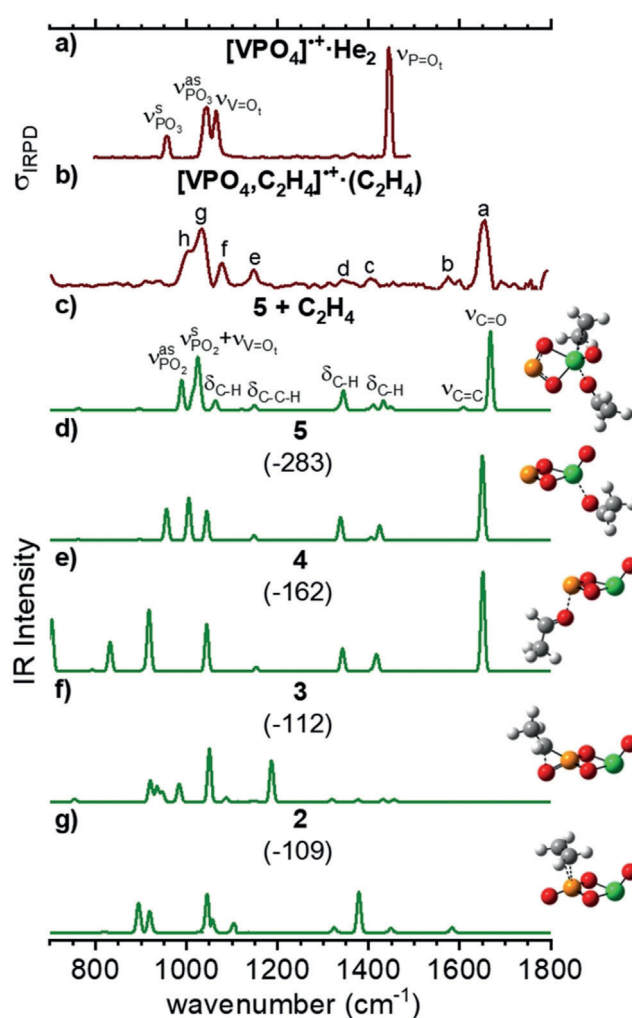


Figure 3. Experimental IRPD spectra (dark red) of a) $[\text{VPO}_4]^+ \cdot \text{He}_2$ at 15 K,^[8] b) $[\text{VPO}_4, \text{C}_2\text{H}_4]^+ \cdot (\text{C}_2\text{H}_4)$ at 150 K, and the harmonic B3LYPD2/def2-tzvpp IR spectra (green, Gaussian line function convolution FWHM = 10 cm⁻¹) of c) **5** + C₂H₄, d) **5**, e) **4**, f) **3**, and g) **2**. C gray, H white, V green, O red, P yellow. The zero-point vibration-corrected energies ($\Delta H_{0\text{K}}$, shown in parentheses) with respect to the separated reactants are given in kJ mol⁻¹. Harmonic frequencies of the V=O_i modes are scaled by 0.9167 and all other modes by 0.9832. See Table 1 for the band positions and assignments. Note that the calculated IR spectra of **4** and **9** (not shown) are practically indistinguishable.

Table 1: Experimental band positions (in cm⁻¹, see Figure 3 b), scaled harmonic vibrational wavenumbers (in cm⁻¹, see Figure 3 c), IR intensities (in parentheses, in km mol⁻¹) of **5** + C₂H₄, and band assignments.

Band	Exp.	B3LYPD2/def2-tzvpp	Assignment ^[d]
a	1653	1668 ^[b] (360)	$\nu(\text{C}=\text{O})$
b	1575	1608 ^[b] (13)	$\nu(\text{C}=\text{C})$
c	1404	1433 ^[b] (43)	$\delta(\text{C}-\text{H})$ in CH ₃ CH=O moiety
d	1347	1345 ^[b] (89)	$\delta(\text{C}-\text{H})$ in CH ₃ CH=O moiety
e	1147	1148 ^[b] (21)	$\delta(\text{C}-\text{C}-\text{H})$ in CH ₃ CH=O moiety
f	1078	1063 ^[b] (41)	$\delta(\text{C}-\text{H})$ in CH ₂ =CH ₂
g	1033	1025 ^[a,b] (242)	$\nu^s(\text{PO}_2) + \nu(\text{V}=\text{O}_i)$
h	999	989 ^[b] (136)	$\nu^{\text{as}}(\text{PO}_2)$

[a] Scaling factor: 0.9167 (VO stretches). [b] Scaling factor: 0.9832 (all other modes). [c] Stretching (ν), bending (δ), symmetric (s), antisymmetric (as).

form **5** (Figure 2). Note that the agreement of the IRPD spectrum with the predicted harmonic spectrum is improved after the second, weakly bound C₂H₄ molecule is considered in the calculations (see Table 1 for band assignments), highlighting its small but distinct perturbation. However, if this is considered, the complete IRPD spectrum is reproduced, demonstrating that the formation of other long-lived intermediates and products with this *m/z* ratio is insignificant.

Using C₂H₄ as a messenger tag raises the interesting question as to what the influence of the second C₂H₄ molecules is on the reaction pathway. To address this, we also performed experiments under single collision conditions (with respect to ion–ethylene collisions), but did not observe any substantial photodissociation of untagged [VPO₄C₂H₄]⁺. Note that the predicted dissociation energy of **5** is 283 kJ mol⁻¹, which would amount to the absorption of roughly 20 photons at 1000 cm⁻¹, which is unlikely under the present experimental conditions. This shows that for bare [VPO₄]⁺, chemisorption of C₂H₄ is highly favored over physisorption, and therefore the influence of the second C₂H₄ molecule is probably negligible under the present conditions.

Additional and independent spectroscopic support that the P-center represents the active site for the OAT from [VPO₄]⁺ to C₂H₄ is found in the IRPD spectrum of another product ion, namely that of (C₂H₄)_n-tagged [VPO₃]⁺. Although the yield of [VPO₃]⁺·(C₂H₄)₁₋₂ is small compared to that of [VPO₄C₂H₄]⁺·(C₂H₄) (see Figure 1), we were able to record an IRPD spectrum of [VPO₃]⁺·(C₂H₄)₂. The good agreement between the experimental and computational results (Figure S3) confirms that the P–O₂–V=O, and not the O=P–O₂–V structure is generated upon desorption of CH₃CHO from [VPO₄(C₂H₄)₂]⁺.

In summary, the present study has experimentally confirmed the previously predicted mechanism, which postulated that the P-atom represents the active site of the heteronuclear cluster [VPO₄]⁺ for the reaction of [VPO₄]⁺ with C₂H₄. Moreover, while in most ion/molecule reactions studied, characterization of the neutral product is based on circumstantial evidence,^[13] in the present case the OAT product was spectroscopically identified as CH₃CHO.

Acknowledgements

Generous financial support of the work at TU Berlin by the Fonds der Chemischen Industrie and the Deutsche Forschungsgemeinschaft (DFG) under Germany's Excellence Strategy—EXC 2008/1-390540038 (UniSysCat) is appreciated. The research of the Asmis group was funded by the DFG within the Collaborative Research Centre 1109 “Metal Oxide/Water Systems”. Y.-K.L. thanks the Alexander von Humboldt Foundation for a postdoctoral research fellowship. Insightful comments of a reviewer are appreciated.

Conflict of interest

The authors declare no conflict of interest.

Keywords: active site · cryogenic ion trap · heteronuclear oxide clusters · infrared photodissociation spectroscopy · olefin oxidation

How to cite: *Angew. Chem. Int. Ed.* **2019**, *58*, 18868–18872
Angew. Chem. **2019**, *131*, 19044–19048

- [1] H. S. Taylor, *J. Phys. Chem.* **1926**, *30*, 145–171.
- [2] a) H. S. Taylor, *Proc. R. Soc. London Ser. A* **1925**, *108*, 105–111; b) G.-M. Schwab, E. Pietsch, *Z. Phys. Chem.* **1928**, *1*, 385–408; c) G.-M. Schwab, E. Pietsch, *Z. Elektrochem. Angew. Phys. Chem.* **1929**, *35*, 135–141; d) G. Ertl, T. Gloyna, *Z. Phys. Chem.* **2003**, *217*, 1207–1220; e) K. Horn, *Science* **2004**, *305*, 483–484; f) J. M. Thomas, R. Raja, D. W. Lewis, *Angew. Chem. Int. Ed.* **2005**, *44*, 6456–6482; *Angew. Chem.* **2005**, *117*, 6614–6641; g) G. Ertl, *Angew. Chem. Int. Ed.* **2008**, *47*, 3524–3535; *Angew. Chem.* **2008**, *120*, 3578–3590; h) G. A. Somorjai, J. Y. Park, *Angew. Chem. Int. Ed.* **2008**, *47*, 9212–9228; *Angew. Chem.* **2008**, *120*, 9352–9368; i) A. Nilsson, J. LaRue, H. Öberg, H. Ogasawara, M. Dell'Angela, M. Beye, H. Öström, J. Gladh, J. K. Nørskov, W. Wurth, F. Abild-Petersen, L. G. M. Pettersson, *Chem. Phys. Lett.* **2017**, *675*, 145–173.
- [3] a) J. Sauer, H.-J. Freund, *Catal. Lett.* **2015**, *145*, 109–125; b) H. Schwarz, *Angew. Chem. Int. Ed.* **2015**, *54*, 10090–10100; *Angew. Chem.* **2015**, *127*, 10228–10239.
- [4] Z.-C. Wang, N. Dietl, R. Kretschmer, T. Weiske, M. Schlangen, H. Schwarz, *Angew. Chem. Int. Ed.* **2011**, *50*, 12351–12354; *Angew. Chem.* **2011**, *123*, 12559–12562.
- [5] S. Debnath, H. Knorke, W. Schöllkopf, S. Zhou, K. R. Asmis, H. Schwarz, *Angew. Chem. Int. Ed.* **2018**, *57*, 7448–7452; *Angew. Chem.* **2018**, *130*, 7570–7574.
- [6] For recent reviews on this method and numerous references, see: a) H. Schwarz, K. R. Asmis, *Chem. Eur. J.* **2019**, *25*, 2112–2126; b) D. Gerlich, *J. Chin. Chem. Soc.* **2018**, *65*, 637–653.
- [7] a) *Appl. Catal. A* **1997**, *157*, 1–425; b) I. E. Wachs, *Catal. Today* **2005**, *100*, 79–94; c) N. Nilius, T. Risse, S. Schauer mann, S. Shaikhutdinov, M. Sterrer, H.-J. Freund, *Top. Catal.* **2011**, *54*, 4–12.
- [8] N. Dietl, T. Wende, K. Chen, L. Jiang, M. Schlangen, X. Zhang, K. R. Asmis, H. Schwarz, *J. Am. Chem. Soc.* **2013**, *135*, 3711–3721.
- [9] a) K. R. Asmis, M. Brummer, C. Kaposta, G. Santambrogio, G. von Helden, G. Meijer, K. Rademann, L. Woste, *Phys. Chem. Chem. Phys.* **2002**, *4*, 1101–1104; b) N. Heine, K. R. Asmis, *Int. Rev. Phys. Chem.* **2015**, *34*, 1–34; c) N. Heine, K. R. Asmis, *Int. Rev. Phys. Chem.* **2016**, *35*, 507–507.
- [10] a) M. Brummer, C. Kaposta, G. Santambrogio, K. R. Asmis, *J. Chem. Phys.* **2003**, *119*, 12700–12703; b) K. R. Asmis, *Phys. Chem. Chem. Phys.* **2012**, *14*, 9270–9281.
- [11] a) D. J. Goebbert, T. Wende, R. Bergmann, G. Meijer, K. R. Asmis, *J. Phys. Chem. A* **2009**, *113*, 5874–5880; b) D. J. Goebbert, G. Meijer, K. R. Asmis, *AIP Conf. Proc.* **2009**, *1104*, 22–29.
- [12] W. Schöllkopf, S. Gewinner, H. Junkes, A. Paarmann, G. von Helden, H. Bluem, A. M. M. Todd in *Advances in X-Ray Free-Electron Lasers Instrumentation III, Vol. 9512* (Ed.: S. G. Biedron), Spie-Int. Soc Optical Engineering, Bellingham, **2015**.
- [13] See, for example, the OAT transfer from metal oxides to C₂H₄: a) A. E. Stevens, J. L. Beauchamp, *J. Am. Chem. Soc.* **1979**, *101*, 6449–6450; b) H. Kang, J. L. Beauchamp, *J. Am. Chem. Soc.* **1986**, *108*, 5663–5668; c) D. Schröder, H. Schwarz, *Angew. Chem. Int. Ed. Engl.* **1995**, *34*, 1973–1995; *Angew. Chem.* **1995**,

107, 2126–2150; d) D. R. Justes, R. Mitrić, N. A. Moore, V. Bonačić-Koutecký, A. W. Castleman, *J. Am. Chem. Soc.* **2003**, *125*, 6289–6299; e) J. Roithová, D. Schröder, *J. Am. Chem. Soc.* **2007**, *129*, 15311–15318; f) K. Chen, Z.-C. Wang, M. Schlagen, Y.-D. Wu, X. Zhang, H. Schwarz, *Chem. Eur. J.* **2011**, *17*, 9619–9625; g) for a rare exception in a unimolecular reaction, see: D.

Schröder, J. Müller, H. Schwarz, *Organometallics* **1993**, *12*, 1972–1975.

Manuscript received: August 29, 2019

Revised manuscript received: October 15, 2019

Accepted manuscript online: October 22, 2019

Version of record online: November 8, 2019



Supporting Information

Direct Identification of Acetaldehyde Formation and Characterization of the Active Site in the $[\text{VPO}_4]^{•+}/\text{C}_2\text{H}_4$ Couple by Gas-Phase Vibrational Spectroscopy

Ya-Ke Li, Sreekanta Debnath, Maria Schlangen, Wieland Schöllkopf, Knut R. Asmis, and Helmut Schwarz**

anie_201911040_sm_miscellaneous_information.pdf

Supporting Information

- 1) Experimental methods section
- 2) Computational section
- 3) Details regarding the structures in Figure 3
- 4) IRPD Spectroscopy of $[\text{VPO}_4, (\text{C}_2\text{H}_4)_2]^{*+}$
- 5) RPD Spectroscopy of $[\text{VPO}_3, (\text{C}_2\text{H}_4)_2]^{*+}$
- 6) References

1) Experimental methods section

The infrared photodissociation (IRPD) experiments are performed on a cryogenic ion trap tandem mass spectrometer^[1] using the widely tunable, intense IR radiation from the Fritz-Haber-Institute Free-Electron Laser (FHI FEL).^[2] $[\text{VPO}_4]^{*+}$ ions are generated as previously described.^[3] Briefly, $[\text{VPO}_4]^{*+}$ ions are produced by collision induced dissociation after the corresponding precursor is transferred to the gas phase using a commercial Z-spray electrospray ionization (ESI) source and a millimolar solution of VOCl_3 and $\text{PO}(\text{OEt})_3$ (both purchased from Sigma-Aldrich) in methanol, which were introduced through a stainless steel capillary to the ESI source by a syringe pump ($\sim 10 \mu\text{L min}^{-1}$). Nitrogen was used as nebulizing and drying gas at a source temperature of 80 °C. The best ion yield was achieved by adjusting the cone voltage (UC) to 170 V. The beam of cations pass through a 4 mm diameter skimmer and are collimated in a radio frequency (RF) decapole ion guide. The desired cations are mass-selected using a quadrupole mass filter, deflected 90° in an electrostatic quadrupole deflector, and focused into a cryogenic RF ring-electrode ion trap. The trap is continuously filled with a reactant gas/ buffer gas mix of 0.025 % C_2H_4 in He at an ion-trap temperature of 150 K. Many collisions of the trapped ions with the mixture gas provide gentle cooling of the internal degrees of freedom close to the ambient temperature. Under these conditions, only small amounts of $[\text{VPO}_3]^{*+}$ and C_2H_4 -tagged $[\text{VPO}_3]^{*+}$ ions $[\text{VPO}_3]^{*+} \cdot (\text{C}_2\text{H}_4)_{1-2}$ (see Fig. 1b and Fig. 3b) are formed.

For the IRPD experiments of the $[\text{VPO}_4, \text{C}_2\text{H}_4]^{*+}$ complex we used a second C_2H_4 molecule as a messenger tag (Fig. 3 and Fig. S2). All ions are extracted from the ion trap at 5 Hz and focused both temporally and spatially into the center of the extraction region of an orthogonally mounted reflection time-of-flight (TOF) tandem photofragmentation mass-spectrometer. Here, the ions are irradiated with a counter-propagating IR laser pulse produced by the FHI FEL ($700\text{--}1800 \text{ cm}^{-1}$, bandwidth: $\sim 0.5\%$ fwhm, pulse energy: 4–32 mJ). All parent and photofragment ions are then accelerated toward an MCP detector and monitored simultaneously. IRPD scans are recorded by averaging about 100 TOF mass spectra per wavelength step (3 cm^{-1}) and scanning the wavelength. Typically, at least three scans are summed to obtain the final IRPD spectrum. The photodissociation cross section σ_{IRPD} is determined as described previously.^[4]

2) Computational section

All calculations were performed using the Gaussian09 package.^[5] Geometries were optimized at the unrestricted UB3LYPD2 level of theory^[6] with the triple- ζ plus polarization basis sets def2-TZVP.^[7] Vibrational frequency analyses have been carried out at the same level of theory to characterize the

nature of stationary points as minima or transition structures, to derive the zero-point energy (ZPE) corrections, and to assign the IR relevant structures. All relative energies presented in this work are corrected for ZPE and given in kJ mol^{-1} . Intrinsic reaction coordinate (IRC)^[8] calculations or manual displacements along the reaction trajectory of the imaginary frequency were performed to link all transition states with the respective intermediates. All given ionic reactants, intermediates, and transition states have been located on the ground-state doublet potential energy surface.

It is known that B3LYP vibrational frequencies are systematically too large;^[9] however, the agreement with observed frequencies can be improved by appropriate scaling. Scaling then accounts for both anharmonicities and systematic errors of the calculated harmonic force constants (calculated harmonic wavenumbers are compared to observed fundamentals including anharmonicities). We use scaling parameters that were determined for small vanadium oxide cluster cations.^[10] The vanadyl ($V = O$) modes are scaled by 0.9167 and all other modes by 0.9832. The simulated linear absorption spectra are derived from scaled harmonic frequencies and intensities.

3) Details regarding the structures in Figure 3

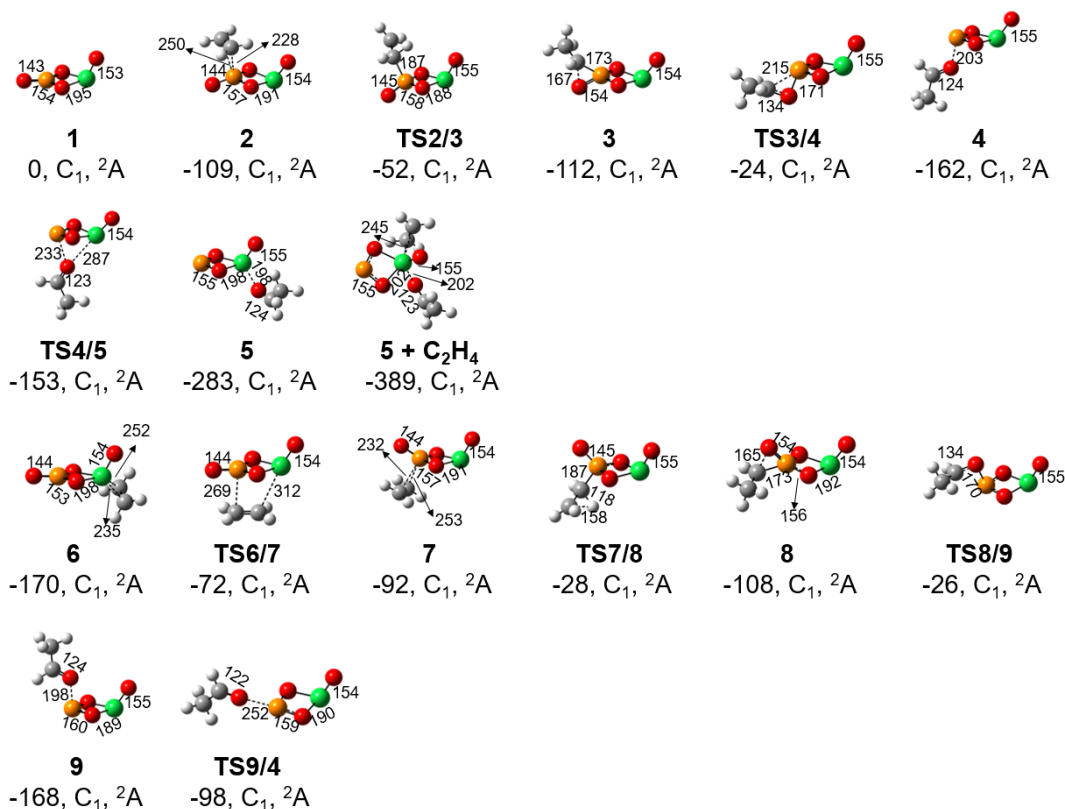


Figure S1. ZPE-corrected energy (ΔH_{0k}) with respect to the separated reactants (kJ mol^{-1}), symmetry, electronic state and bond lengths (\AA) of the B3LYPD2/def2-tzvp structures shown in Figures 2 and 3 (color code: yellow, P; green, V; red, O; gray, C; white, H).

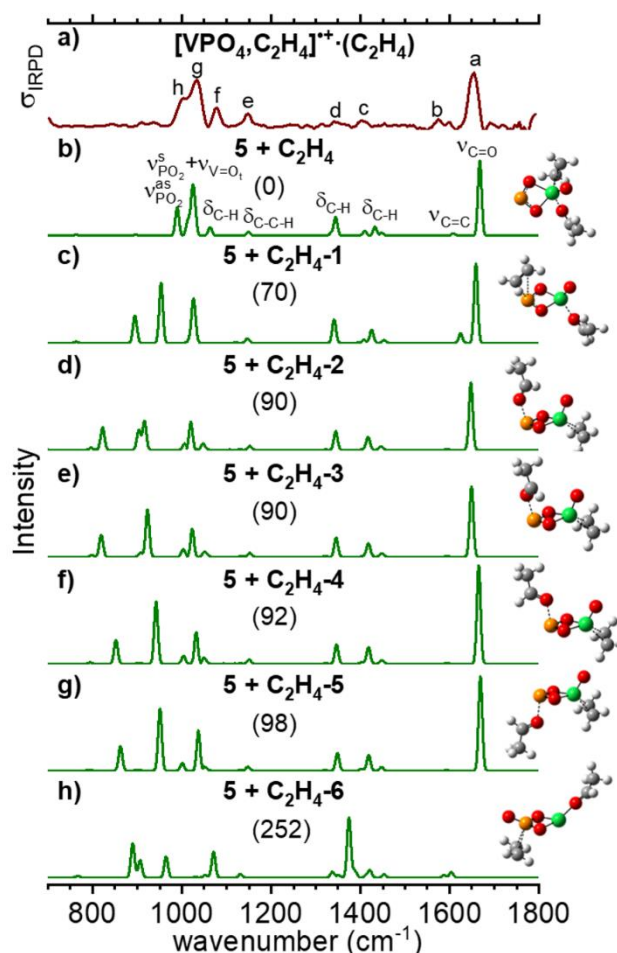
4) IRPD Spectroscopy of $[\text{VPO}_4, (\text{C}_2\text{H}_4)_2]^{\bullet+}$ 

Figure S2 Experimental IRPD spectra (dark red) of $[\text{VPO}_4, \text{C}_2\text{H}_4]^{\bullet+} \cdot (\text{C}_2\text{H}_4)$ at 150 K compared with calculated harmonic B3LYP2/def2-tzvpp spectra (green, Gaussian line function convolution, FWHM=10 cm^{-1}) of various isomers. Numbers in parenthesis indicates relative ZPE-corrected energies ($\Delta H_{0\text{K}}$, in kJ mol^{-1}) of the isomers (yellow, P; green, V; red, O; gray, C; white, H). Harmonic frequencies of the $\text{V}=\text{O}_t$ modes are scaled by 0.9167 and all other modes by 0.9832.

The band at 1653 cm^{-1} is assigned to the $\text{C}=\text{O}$ stretching mode. The weak band b (1575 cm^{-1}) is assigned to the $\text{C}=\text{C}$ stretching mode, which confirms that the integrity of the second ethylene, which acts as a tag, remains intact. The other two intense bands g (1033 cm^{-1}) and h (999 cm^{-1}) are assigned to the combination of symmetric PO_2 stretching with terminal $\text{V}=\text{O}_t$ stretching mode and antisymmetric PO_2 stretching mode, respectively. The terminal $\text{V}=\text{O}_t$ stretching mode at 1033 cm^{-1} is line with the IRPD data reported previously for $[\text{CeVO}_4]^{\bullet+}$,^[11] $[\text{V}_2\text{O}_4]^{\bullet+}$,^[10] $[\text{VPO}_4]^{\bullet+}$,^[3] and $[\text{AlVO}_4]^{\bullet+}$.^[12] The weak bands c (1404 cm^{-1}), d (1347 cm^{-1}), e (1147 cm^{-1}) are assigned to two $\text{C}-\text{H}$ bending modes and the $\text{C}-\text{C}-\text{H}$ bending mode in $\text{CH}_3\text{CH}=\text{O}$ moiety, respectively, and the weak band f (1078 cm^{-1}) is assigned to the $\text{C}-\text{H}$ bending mode in $\text{CH}_2=\text{CH}_2$.

5) IRPD Spectroscopy of $[\text{VPO}_3, (\text{C}_2\text{H}_4)_2]^{*+}$

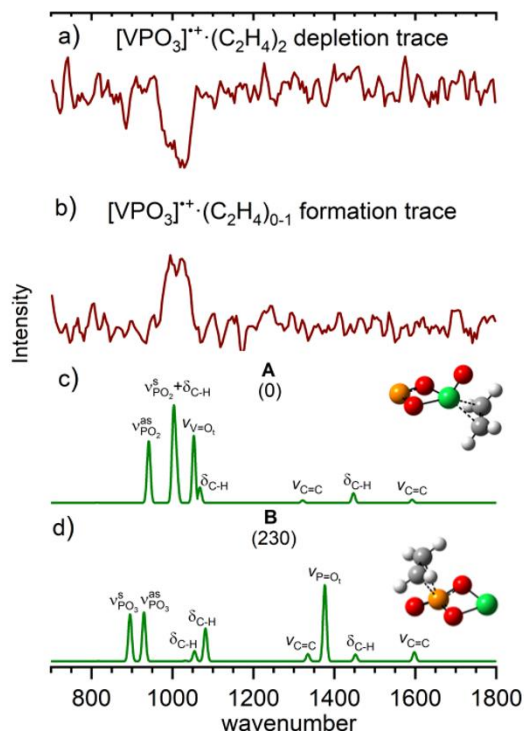


Figure S3. Experimental (dark red) (a) IRPD depletion trace of $[\text{VPO}_3]^{*+} \cdot (\text{C}_2\text{H}_4)_2$, (b) IRPD formation trace of $[\text{VPO}_3]^{*+} \cdot (\text{C}_2\text{H}_4)_{0.1}$ at 150 K, and the harmonic B3LYPD2/def2-tzvpp IR spectra (green, Gaussian line function convolution $\text{FWHM}=10 \text{ cm}^{-1}$) of structure c) **A** ($\text{PO}_2\text{VO}-\text{C}_2\text{H}_4$) and d) **B** ($\text{C}_2\text{H}_4-\text{OPO}_2\text{V}$) (color code: yellow, P; green, V; red, O; gray, C; white, H). The relative, ZPE-corrected energies ($\Delta H_{0\text{K}}$, shown in parentheses) are given in kJ mol^{-1} . Harmonic frequencies of the $\text{V}=\text{O}_t$ modes are scaled by 0.9167 and all other modes by 0.9832.

The reaction of $[\text{VPO}_4]^{*+}$ with C_2H_4 also yields small amounts of C_2H_4 -tagged $[\text{VPO}_3]^{*+}$ ions, which are formed by CH_3CHO desorption from $[\text{VPO}_4, \text{C}_2\text{H}_4]^{*+} \cdot (\text{C}_2\text{H}_4)_n$. We also measured IRPD spectra of these ions. The comparison in Fig. S3 shows that C_2H_4 -tagged $[\text{VPO}_3]^{*+}$ ions contain the $\text{P}-\text{O}_2-\text{V}=\text{O}$, and not the $\text{O}=\text{P}-\text{O}_2-\text{V}$, structure, yielding additional support that the P-center represents the active site for the OAT reaction of $[\text{VPO}_4]^{*+}$ with C_2H_4 .

6) References

- [1] a) D. J. Goebbert, T. Wende, R. Bergmann, G. Meijer, K. R. Asmis, *J. Phys. Chem. A* **2009**, *113*, 5874-5880; b) D. J. Goebbert, G. Meijer, K. R. Asmis, *AIP Conf. Proc.* **2009**, *1104*, 22-29.
- [2] W. Schöllkopf, S. Gewinner, H. Junkes, A. Paarmann, G. von Helden, H. Bluem, A. M. M. Todd, in *Advances in X-Ray Free-Electron Lasers Instrumentation Iii*, Vol. 9512 (Ed.: S. G. Biedron), Spie-Int Soc Optical Engineering, Bellingham, **2015**.
- [3] N. Dietl, T. Wende, K. Chen, L. Jiang, M. Schlangen, X. Zhang, K. R. Asmis, H. Schwarz, *J. Am. Chem. Soc.* **2013**, *135*, 3711-3721.

5. Catalytic Active Site Characterization of Heteronuclear Metal Oxide Clusters

- [4] a) N. Heine, K. R. Asmis, *Int. Rev. Phys. Chem.* **2016**, *35*, 507-507; b) N. Heine, K. R. Asmis, *Int. Rev. Phys. Chem.* **2015**, *34*, 1-34.
- [5] M. J. Frisch, G. W. Trucks, H. B. Schlegel, G. E. Scuseria, M. A. Robb, J. R. Cheeseman, G. Scalmani, V. Barone, B. Mennucci, G. A. Petersson, H. Nakatsuji, M. Caricato, X. Li, H. P. Hratchian, A. F. Izmaylov, J. Bloino, G. Zheng, J. L. Sonnenberg, M. Hada, M. Ehara, K. Toyota, R. Fukuda, J. Hasegawa, M. Ishida, T. Nakajima, Y. Honda, O. Kitao, H. Nakai, T. Vreven, J. A. M. Jr., J. E. Peralta, F. Ogliaro, M. Bearpark, J. J. Heyd, E. Brothers, K. N. Kudin, V. N. Staroverov, R. Kobayashi, J. Normand, K. Raghavachari, A. Rendell, J. C. Burant, S. S. Iyengar, J. Tomasi, M. Cossi, N. Rega, J. M. Millam, M. Klene, J. E. Knox, J. B. Cross, V. Bakken, C. Adamo, J. Jaramillo, R. Gomperts, R. E. Stratmann, O. Yazyev, A. J. Austin, R. Cammi, C. Pomelli, J. W. Ochterski, R. L. Martin, K. Morokuma, V. G. Zakrzewski, G. A. Voth, P. Salvador, J. J. Dannenberg, S. Dapprich, A. D. Daniels, Ö. Farkas, J. B. Foresman, J. V. Ortiz, J. Cioslowski, D. J. Fox, Gaussian 09, Revision D.01, Gaussian, Inc.: Wallingford CT, **2009**.
- [6] a) C. T. Lee, W. T. Yang, R. G. Parr, *Physical Review B* **1988**, *37*, 785-789; b) A. D. Becke, *J. Chem. Phys.* **1993**, *98*, 5648-5652; c) S. Grimme, *J. Comput. Chem.* **2006**, *27*, 1787-1799.
- [7] A. Schafer, C. Huber, R. Ahlrichs, *J. Chem. Phys.* **1994**, *100*, 5829-5835.
- [8] a) K. Fukui, *Acc. Chem. Res.* **1981**, *14*, 363-368; b) D. G. Truhlar, M. S. Gordon, *Science* **1990**, *249*, 491-498; c) C. Gonzalez, H. B. Schlegel, *J. Phys. Chem.* **1990**, *94*, 5523-5527.
- [9] a) A. P. Scott, L. Radom, *J. Phys. Chem.* **1996**, *100*, 16502-16513; b) M. D. Halls, J. Velkovski, H. B. Schlegel, *Theor. Chem. Acc.* **2001**, *105*, 413-421.
- [10] L. Jiang, T. Wende, P. Claes, S. Bhattacharyya, M. Sierka, G. Meijer, P. Lievens, J. Sauer, K. R. Asmis, *J. Phys. Chem. A* **2011**, *115*, 11187-11192.
- [11] K. R. Asmis, G. Meijer, M. Brümmer, C. Kaposta, G. Santambrogio, L. Woste, J. Sauer, *J. Chem. Phys.* **2004**, *120*, 6461-6470.
- [12] S. Debnath, H. Knorke, W. Schöllkopf, S. D. Zhou, K. R. Asmis, H. Schwarz, *Angew. Chem. Int. Ed.* **2018**, *57*, 7448-7452.

Chapter 6

CO₂ Adsorption on Ti₃O₆⁻

TiO₂ based materials have proved to be a promising candidate for photocatalytic CO₂ reduction and conversion. Many reports have showed that the oxygen deficient defect sites on titania surface are eventually the active sites for H₂O or CO₂ adsorption. In an earlier study published by our group, Ti₃O₆⁻ cluster is found to contain both Ti⁴⁺ and Ti³⁺ centres, where the later center contains the excess negative charge representing oxygen vacant defect site on titania surface.¹ Cryogenic ion trap vibrational spectroscopy in combination with high level quantum chemical calculations is used to gain a molecular level understanding of the CO₂ adsorption mechanism on titania with special emphasis on different CO₂ binding motifs.

6.1. CO₂ Adsorption on Ti₃O₆⁻: A Novel Carbonate Binding Motif

The published article “CO₂ Adsorption on Ti₃O₆⁻: A Novel Carbonate Binding Motif”^{2,3} presents different CO₂ binding motifs on Ti-oxide, with special mentioning of a newly found tridentate bridged carbonate binding pattern. Ti-oxide clusters were produced by ablation of a pure Ti-rod target in a dual channel laser ablation source and the CO₂ was added from the second reaction channel to produce [Ti₃O₆(CO₂)_n]⁻ (n=1, 2) clusters. Structural characterization of the mentioned ions were performed by comparing the measured D₂-tagged IRPD spectra to the DFT predicted IR harmonic spectra. Chemical adsorption of the first two CO₂ to the Ti₃O₆⁻ cluster anion was found, by incorporating a formally doubly negatively charged either doubly or triply coordinated O atom to form a bidentate (asymmetric) or tridentate (symmetric) bridging carbonate di-anion (CO₃²⁻), respectively, of which the latter has not been reported previously. Each type of formed carbonate has their distinguishable characteristic IR signature within 400-2400 cm⁻¹. Interestingly, the tridentate binding motif exhibits a characteristic IR signature in the form of an intense doublet of peaks near 1400 cm⁻¹ stemming from two antisymmetric carbonate stretching modes, which has been assigned previously to the signature of HCO₃⁻ present at the CO₂ adsorbed wet titania surface.^{4,5} This finding asks for additional scrutiny on the role of (HCO₃⁻) species in the CO₂ activation/conversion process at titania-interface.

1. Weichman, M.L., et al., *Journal of Chemical Physics*, 2016, **144**, 1-11
2. Debnath, S., et al., *The Journal of Physical Chemistry C*, 2019, **123**, 8439-8446
3. Debnath, S., et al., *The Journal of Physical Chemistry C*, 2020, **124**, 6952-6953
4. Mino, L., *The Journal of Physical Chemistry C*, 2014, **118**, 25016-25026.
5. Su, W., et al., *The Journal of Physical Chemistry C*, 2008, **112**, 7710-7716

Declaration of Contribution:

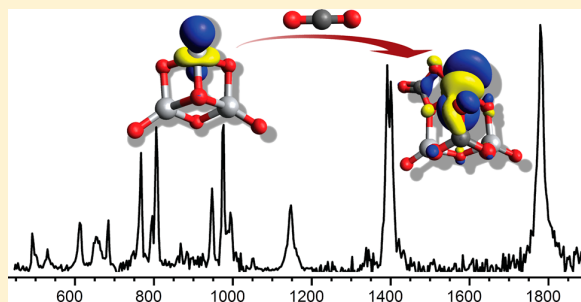
Matias R. Fagiani, Xiaowei Song and I planned and performed the experimental work, including the measurement of all IRPD spectra and data evaluation. I did part of the DFT ($n=1$ CO₂ isomers) and CCSD(t) ($n=1, 2$ CO₂ isomers) calculations. I did the data interpretation, made all the figures and wrote the first version of the manuscript. Other contributions of the co-authors are listed below:

Marissa L. Weichman	Assisted during the beam time measurements. Gave valuable suggestions for the preliminary DFT calculations.
Min Gao	Did part of the DFT ($n=2$ CO ₂ isomers) and CCSD(t) calculations.
Wieland Schöllkopf	Evening operator of the FHI-FEL.
Andrey Lyalin, Satoshi Maeda, Tetsuya Taketsugu	Supervised all the theoretical calculations and revised the manuscript.
Daniel M. Neumark	Framed the principal idea and revised the manuscript.
Knut R. Asmis	Coordinated the project, Framed the principal idea, supervised the research, helped in data interpretation and revised the manuscript.

CO₂ Adsorption on Ti₃O₆⁻: A Novel Carbonate Binding MotifSreekanta Debnath,^{†,‡} Xiaowei Song,[‡] Matias R. Fagiani,^{†,‡} Marissa L. Weichman,^{§,||} Min Gao,^{⊥,‡} Satoshi Maeda,^{#,○} Tetsuya Taketsugu,^{#,○,□} Wieland Schöllkopf,[‡] Andrey Lyalin,^{*,□} Daniel M. Neumark,^{*,§,△} and Knut R. Asmis^{*,†}[†]Wilhelm-Ostwald-Institut für Physikalische und Theoretische Chemie, Universität Leipzig, Linnéstrasse 2, D-04103 Leipzig, Germany[‡]Fritz-Haber-Institut der Max-Planck-Gesellschaft, Faradayweg 4-6, D-14195 Berlin, Germany[§]Department of Chemistry, University of California, Berkeley, California 94720, United States[⊥]Institute for Catalysis, Hokkaido University, Sapporo 001-0021, Japan[#]Department of Chemistry, Faculty of Science, Hokkaido University, Sapporo 060-0810, Japan[○]Institute for Chemical Reaction Design and Discovery (WPI-ICReDD), Hokkaido University, Sapporo 001-0021, Japan[□]Global Research Center for Environment and Energy based on Nanomaterials Science (GREEN), National Institute for Material Science (NIMS), Tsukuba 305-0044, Japan[△]Chemical Sciences Division, Lawrence Berkeley National Laboratory, Berkeley, California 94720, United States

Supporting Information

ABSTRACT: CO₂ adsorption on Ti₃O₆⁻, which serves as a model for an oxygen vacancy on a titania surface, is studied using infrared photodissociation (IRPD) spectroscopy in combination with density functional theory (DFT) and coupled cluster computations, as well as a recently developed multi-component artificial force induced reaction method. The IRPD spectra of D₂-tagged [(Ti₃O₆)(CO₂)_n]⁻, with *n* = 1, 2, are reported in the spectral window of 450–2400 cm⁻¹ and assigned based on a comparison to harmonic IR spectra from the DFT calculations. We find that CO₂ binding leaves the unpaired electron largely unperturbed. The first two CO₂ molecules adsorb chemically to Ti₃O₆⁻ by incorporating a formally doubly negatively charged, either doubly or triply coordinated O atom to form a bidentate or tridentate bridging carbonate dianion (CO₃²⁻), respectively. The latter binding motif exhibits a characteristic IR signature in the form of an intense doublet of peaks near 1400 cm⁻¹ stemming from two antisymmetric carbonate stretching modes.



1. INTRODUCTION

Steadily growing global energy consumption has led to a sharp rise in atmospheric CO₂ levels, one of the factors contributing to anthropogenic climate change. Hence, there is an increasing demand for efficient methods to reduce atmospheric CO₂ and convert it into value-added chemicals using heterogeneous catalysts.^{1,2} TiO₂-based materials have been identified as promising, cost-efficient candidates for CO₂ sequestration and conversion, considering their relative abundance in earth's crust in combination with their photocatalytic activity.^{3–5} To enhance the photocatalytic efficiency, it is necessary to develop an understanding of the fundamental processes occurring at the TiO₂ interface. Adsorption studies of CO₂ on titania, for example, have focused on a molecular level characterization of chemi- versus physisorption, that is, formation of bicarbonate or carbonate versus CO₂ binding exclusively to a metal center through one of its oxygen atoms, and are typically discussed in the context of Lewis acids and bases, finding that stronger CO₂

binding is promoted by higher oxygen basicity as well as higher metal acidity.^{6–9} Here, we employ a complementary approach to shed new light on TiO₂–CO₂ interactions. We use infrared photodissociation (IRPD) spectroscopy, combined with density functional theory (DFT) calculations, to study CO₂ adsorption by the radical anion Ti₃O₆⁻ in the gas phase. This cluster represents a model for oxygen vacancies on titania surfaces.¹⁰ The goal of the present study is identifying the vibrational signatures of characteristic binding motifs in the vicinity of such defect sites.

The C_s structure of Ti₃O₆⁻ (see Figure 1), characterized previously by IRPD spectroscopy,¹⁰ exhibits two 4-fold coordinated Ti⁴⁺ centers and one triply coordinated Ti³⁺

Special Issue: Hans-Joachim Freund and Joachim Sauer Festschrift

Received: November 3, 2018

Revised: December 7, 2018

Published: December 12, 2018

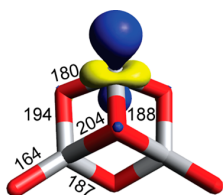


Figure 1. Spin density plot of the singly occupied molecular orbital in the Ti_3O_6^- anion from $\omega\text{B97XD/ aug-cc-pVTZ}$ calculations. The unpaired electron is localized at the under coordinated Ti^{3+} center. Bond lengths (in pm) are also shown.

center. The latter carries the spin density and represents the reactive center for hydrogen dissociation¹¹ as well as water adsorption.¹² CO_2 adsorption could be favorable at this site as it represents an electron donor site for the π acceptor CO_2 . However, there are many possible binding motifs known from CO_2 adsorption studies on titania surfaces^{7,8,13,14} and on neutral and small anionic titanium oxide clusters in the gas phase.^{15,16} These include chemisorbed monodentate, bridging bidentate, chelating bidentate and tridentate carbonates, oxalates, as well as configurations with linear and bent physisorbed CO_2 . A priori, it is unclear which binding motifs are preferred in the $[\text{Ti}_3\text{O}_6(\text{CO}_2)_n]^-$ system. Our results show that two types of tridentate carbonates, each with its own characteristic IR signature, are formed, an asymmetric and a symmetric one, of which the latter has not been reported previously.

2. EXPERIMENTAL AND COMPUTATIONAL METHODS

Experimental Methods. The IRPD experiments were carried out with an ion trap tandem mass spectrometer described previously.^{17,18} In brief, $[\text{Ti}_3\text{O}_6(\text{CO}_2)_n]^-$ ($n = 1, 2$) clusters are produced in a dual gas channel pulsed laser-vaporization source operated at 50 Hz.^{11,19} The beam of ions

passes through a 4 mm diameter skimmer and is collimated in a radio frequency (RF) decapole ion-guide filled with He buffer-gas. Ions of interest are mass-selected according to their mass/charge ratio using a quadrupole mass-filter (see Figure S1 for a characteristic mass spectrum of the $[\text{Ti}_3\text{O}_6(\text{CO}_2)_n]^-$ clusters studied here). The mass-selected beam is focused into a cryogenically cooled RF ring-electrode ion trap. The trap is continuously filled with buffer gas (10% D_2 in He) at a trap temperature of 13–15 K, which allows for the accumulation and thermalization of the trapped ions. Inside the trap, ions undergo three-body collisions with the buffer gas, which promote the formation of weakly bound ion- D_2 complexes.²⁰ Ions are extracted from the ion trap at 5 Hz and are focused into the center of the extraction region of a time-of-flight (TOF) mass spectrometer, where they are irradiated by an intense and wavelength-tunable IR laser pulse from the IR free electron laser FHI FEL.²¹ When resonant with a rovibrational transition, the initially internally cold parent ions can absorb one (or more) photon(s), leading to loss of messenger molecules via intramolecular vibrational predissociation. At sufficiently high pulse energies, loss of the more strongly bound CO_2 molecules is also observed.

The TOF intensities of all ions are monitored simultaneously as the FEL wavelength is scanned from 450 to 2400 cm^{-1} in 3 cm^{-1} steps; for each wavelength step, ~ 100 TOF traces are acquired and averaged. Over this wavelength range, the FHI FEL has a spectral bandwidth ranging from 2 cm^{-1} fwhm at 450 to 7 cm^{-1} fwhm at 1200 cm^{-1} , and a typical energy output of 10–30 mJ/pulse. Attenuated laser pulses using 12–33% of the full FEL power are employed in a particular spectral window to ensure operation within a linear absorption regime and to avoid saturation. Typically, at least three scans are summed, the photodissociation cross section σ_{IRPD} is determined as described previously,^{22,23} and the data obtained in separately scanned ranges are stitched together to obtain the final IRPD spectrum.

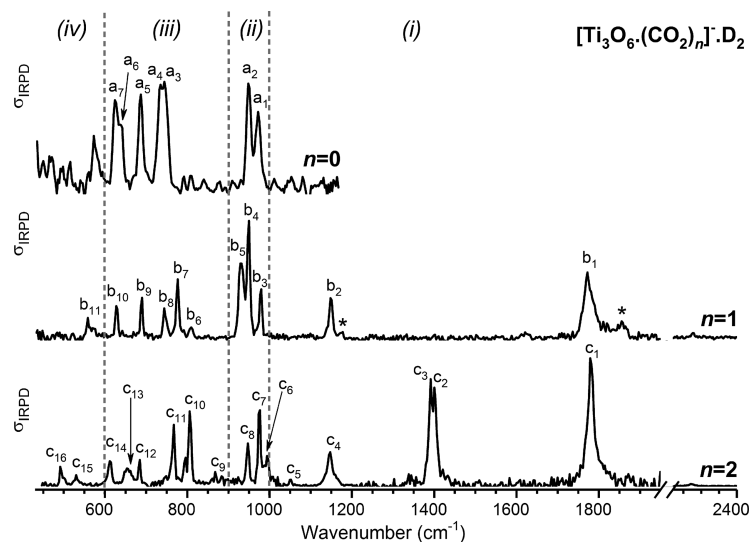


Figure 2. Experimental IRPD spectra of D_2 -tagged $[\text{Ti}_3\text{O}_6(\text{CO}_2)_n]^-$ with $n = 0, 1$ and 2 . See Table 2 for band positions and assignments. Four characteristic spectral regions are indicated by the dashed lines: (i) antisymmetric O–C–O stretching modes ($>1000 \text{ cm}^{-1}$), (ii) symmetric O–C–O and terminal Ti–O stretching modes ($1000\text{--}900 \text{ cm}^{-1}$), (iii) stretching modes associated with Ti–O–Ti bridges and O–C–O bending modes ($900\text{--}600 \text{ cm}^{-1}$), and (iv) low frequency bending, wagging, rocking, and ring breathing modes ($<600 \text{ cm}^{-1}$).

Computational Methods. DFT calculations were carried out using the Gaussian 09 (rev. C01) program package²⁴ to find relative energies, optimized geometries, BSSE-corrected binding energies, harmonic vibrational frequencies, and IR intensities of the lowest-lying [Ti₃O₆(CO₂)_{n=1-2}][−] isomers. We use the range-separated hybrid ω B97X-D functional²⁵ which includes dispersion interactions. It has been shown to perform well for geometry optimization of transition metal compounds²⁶ and has provided satisfactory results in our previous work on [(TiO₂)_{n=2-4}(D₂O)_{m=1-3}][−].¹² The aug-cc-pVTZ basis set^{27,28} was used for all atoms, with full treatment of all electrons.

Single point CCSD(T) calculations²⁹⁻³³ of all the lowest lying isomers (for $n = 2$ aug-cc-pVDZ optimized geometries were taken for CCSD(T) calculation) were performed with the def2-TZVP^{34,35} basis set using the TURBOMOLE 6.6 programs.³⁶ In the search of energetically low-lying structures of bare and D₂-tagged [Ti₃O₆(CO₂)_{n=1-2}][−] isomers, the multicomponent artificial force induced reaction (MC-AFIR) method implemented in the GRRM program was used,^{37,38} where geometries obtained by the MC-AFIR calculations utilizing the PBE functional and DZP basis set of the SIESTA program³⁹ were reoptimized at the aforementioned computational level using Gaussian 09 (rev. C01).²⁴

3. RESULTS

The experimental IRPD spectra of the D₂-tagged anions [Ti₃O₆(CO₂)_n][−], with $n = 0-2$, are shown in Figure 2 in the spectral region 450–2400 cm^{−1}. Experimental band positions and band assignments (vide infra) are summarized in Table 1. Based on our previous studies of titanium oxide anions^{10,12} and CO₂ adsorption,⁴⁰ we group characteristic normal modes into four spectral regions, labeled (i) to (iv) in Figure 2: (i) antisymmetric O–C–O stretching modes (>1000 cm^{−1}), (ii) symmetric O–C–O and terminal Ti–O stretching modes (1000–900 cm^{−1}), (iii) the stretching modes associated with Ti–O–Ti bridges and O–C–O bending modes (900–600 cm^{−1}), and (iv) low frequency bending, wagging, rocking, and ring breathing modes (<600 cm^{−1}). No evidence is found for the IR signature of physisorbed CO₂, which would be above 2000 cm^{−1}, close to the absorption of neutral CO₂ (2349 cm^{−1}).⁴¹

The IRPD spectrum of D₂-tagged [Ti₃O₆(CO₂)_n][−] for $n = 0$ has been discussed in detail previously.¹⁰ Briefly, no absorption is observed in the region (i). The two characteristic peaks in region (ii) are the symmetric (a_1 , 972 cm^{−1}) and antisymmetric (a_2 , 948 cm^{−1}) terminal Ti–O stretching modes. Six vibrational bands that show decreasing IR intensity with decreasing frequency are observed below 750 cm^{−1} and attributed to Ti–O–Ti bridge stretching modes.

The IRPD spectrum for $n = 1$ (center panel in Figure 2) looks similar to that for $n = 0$ below 950 cm^{−1}, suggesting that the core structure remains intact upon adsorption of the first CO₂ molecule. The signal-to-noise ratio is slightly better in the present spectra ($n = 1, 2$) compared to the previously published one ($n = 0$), mainly a result of improved source conditions.¹⁰ The intense peaks observed above 950 cm^{−1} at 1773 cm^{−1} (b_1), 1144 cm^{−1} (b_2), and 984 cm^{−1} (b_3) signal that CO₂ is preferentially chemisorbed. This particular carbonate stretch pattern, with no absorption in the 1200–1600 cm^{−1} region, fits best with a bridging bidentate carbonate species,^{7,8} as discussed in more detail in Section 4. There is a weak

Table 1. Experimental Band Positions (in cm^{−1}) from the IRPD Spectra of D₂-Tagged [Ti₃O₆(CO₂)_n][−], Shown in Figure 2, and ω B97XD/aug-cc-pVTZ Harmonic Frequencies Scaled by 0.96 (in cm^{−1}) of Isomers 1b ($n = 1$) and 2a ($n = 2$), as Well as Band Assignments

n	label	experiment (cm ^{−1})	theory (cm ^{−1})	assignment
1	b_1	1773	1761	terminal C=O stretch
	b_2	1144	1157	antisym. CO ₂ stretch
	b_3	984	1017	sym. CO ₂ stretch
	b_4	954	993	terminal Ti–O stretch (sym.)
	b_5	936	965	terminal Ti–O stretch (antisym.)
	b_6	813	748	in-plane CO ₃ bend
	b_7	780	726	antisym. Ti–O–Ti ring stretch
	b_8	747	692	antisym. ring breathing
	b_9	693	656	in-plane CO ₃ bend
	b_{10}	630	614	O–(Ti) ₃ stretch
	b_{11}	561	565	O–(Ti) ₃ bend
2	c_1	1779	1778	terminal C=O stretch
	c_2	1400	1415	antisym. CO ₃ stretch
	c_3	1391	1382	antisym. CO ₃ stretch
	c_4	1147	1155	antisym. CO ₂ stretch
	c_5	1052	1048	sym CO ₃ stretch
	c_6	994	1022	terminal Ti–O stretch (sym.)
	c_7	976	994	terminal Ti–O stretch (antisym.)
	c_8	947	954	sym. CO ₂ stretch
	c_9	867	874	CO ₃ umbrella motion
	c_{10}	806	776	antisym. Ti–O–Ti ring stretch
	c_{11}	767	756	in-plane CO ₂ bend
	c_{12}	684	672	antisym. Ti–O–Ti ring stretch
	c_{13}	653	651	in-plane CO ₂ /CO ₃ bend
	c_{14}	612	602	sym. Ti–O–Ti ring stretch
	c_{15}	530	530	antisym. ring breathing
	c_{16}	491	484	antisym. ring breathing

feature at 2285 cm^{−1}, indicative of another isomer containing a physisorbed CO₂, but its contribution is negligible.

The IRPD spectrum for $n = 2$ (bottom panel in Figure 2) shows similarities to the $n = 1$ spectrum over large parts of the spectral range. The carbonate stretching bands c_1 , c_4 , and c_6 in the $n = 2$ spectrum are found nearly unshifted from the positions in the $n = 1$ spectrum, where they correspond to bands b_1 , b_2 , and b_3 . The persistence of these bands supports an identical bridging bidentate binding motif for one of the two CO₂ molecules in the $n = 2$ species. There are, however, two new, closely spaced features at 1400 cm^{−1} (c_2) and 1391 cm^{−1} (c_3) that cannot be attributed to any of the known CO₂ binding motifs,^{7,8} including those proposed in a recent computational study on neutral Ti₃O₆(CO₂)_n clusters.¹⁵

4. ANALYSIS AND DISCUSSION

In order to assign the IRPD spectra, we performed geometry optimizations and harmonic frequency calculations using DFT. The ω B97XD/aug-cc-pVTZ relative electronic energies ΔE_{DFT} and zero-point energy (ZPE) corrected relative energies $\Delta E_{0,\text{DFT}}$ are listed in Table 2. To obtain more accurate electronic energies, we also calculated CCSD(T)/def2-TZVP single-point energies $\Delta E_{\text{CCSD(T)}}$ at the optimized ω B97XD/aug-cc-pVTZ geometry; these are also listed in Table 2. The six

Table 2. ω B97XD/aug-cc-pVTZ Relative Electronic Energies ΔE_{DFT} and ZPE-Corrected Relative Energies $\Delta E_{0,\text{DFT}}$ of the Lowest-Energy Minimum-Energy Isomers of $[\text{Ti}_3\text{O}_6(\text{CO}_2)_{n=1,2}]^{-a}$

<i>n</i>	isomer	ΔE_{DFT}^b	$\Delta E_{0,\text{DFT}}^c$	$\Delta E_{\text{CCSD(T)}}^b$	$\Delta E_{0,\text{CCSD(T)/DFT}}^c$
1	1a	0.0	0.0	0.0	0.0
	1b	19.1	18.0	0.0	-0.8
	1c	12.0	11.9	10.5	11.2
	1d	37.4	39.2	81.7	84.4
	1e	45.1	38.2	156.0	149.9
	1f	53.4	46.2	130.2	123.8
2	2a	0.0	0.0	0.0	0.0
	2b	18.5	17.8	14.9	14.2
	2c	24.5	24.2	41.8	41.6
	2d	32.5	30.6	27.4	25.4
	2e	39.2	38.8	75.4	75.1
	2f	41.4	40.1	47.5	46.2

^aCCSD(T)/def2-TZVP relative electronic energies $\Delta E_{\text{CCSD(T)}}$ at the DFT minimum-energy geometry and ZPE-corrected relative electronic energies $\Delta E_{0,\text{CCSD(T)/DFT}}$ using the DFT ZPE-correction are also shown. All energies are given in kJ/mol. ^bAbsolute energies: -3189.03837 au (1a, DFT), -3182.85095 au (1a, CCSD(T)), -3377.67800 au (2a, DFT), -3370.61920 au (2a, CCSD(T)). ^cZero-point-energy (ZPE) determined from ω B97XD/aug-cc-pVTZ harmonic vibrational frequencies.

lowest minimum-energy structures for $n = 1$ and $n = 2$ are shown in Figure 3. The isomers are labeled with $n\mathbf{x}$, where n is the number of CO₂ molecules adsorbed to Ti₃O₆⁻ and $x = \mathbf{a}, \mathbf{b}, \mathbf{c}, \dots$ indicates the energetic ordering. See Tables 2 and S3 for the isomer energies and Figures S2 and S3 for the harmonic IR spectra of all the considered isomers.

For $[\text{Ti}_3\text{O}_6(\text{CO}_2)]^-$, we considered the six structures (1a–1f) shown in Figure 3. Their relative energies are listed in Table 2. Chemisorption, that is, carbonate formation (1a–1d), is preferred over physisorption, with a counterpoise-corrected DFT CO₂ binding energy of 139 kJ/mol (1a). Note that the physisorbed complexes (1e, 1f) are predicted to lie even higher in energy when the CCSD(T) energies are considered (see Table 2). Structure 1a represents the global minimum-energy structure using DFT. Structure 1b is predicted to be 19 kJ/mol higher in energy. However, when the CCSD(T) energies are considered, structures 1a and 1b are nearly isoenergetic, with 1b predicted only +0.3 kJ/mol higher in energy. Moreover, when the harmonic vibrational ZPEs from DFT are combined with the CCSD(T) electronic energies, the energetic ordering is reversed and 1b is indeed slightly favored by 0.8 kJ/mol. Both of these structures exhibit carbonate binding motifs, but in different binding environments and with different formal charges on the carbonate moiety: -1.039 |e| (1a) versus -1.126 |e| (1b) (see Figure S6 and Table S1). Structure 1a contains a tridentate, quasi-symmetric carbonate moiety, (C(-O)₃)²⁻, that exhibits three similar C–O bonds (~131 pm, see SI) and forms three Ti–O bonds, one to each of the three Ti centers. On the other hand, 1b contains an asymmetric tridentate carbonate moiety, (O=C(-O)₂)²⁻, that involves a bridging O atom and only two Ti-centers. The higher energy chemisorbed structures involve an asymmetric bidentate carbonate species bound to a single Ti-center (1c, $\Delta E_{\text{CCSD(T)}} = 11$ kJ/mol) and a quasi-symmetric tetradentate carbonate species bound to two Ti-centers involving a bridging O atom (1d, +82 kJ/mol). Dixon and co-workers¹⁵ find structures similar to 1b to 1d for neutral chemisorbed

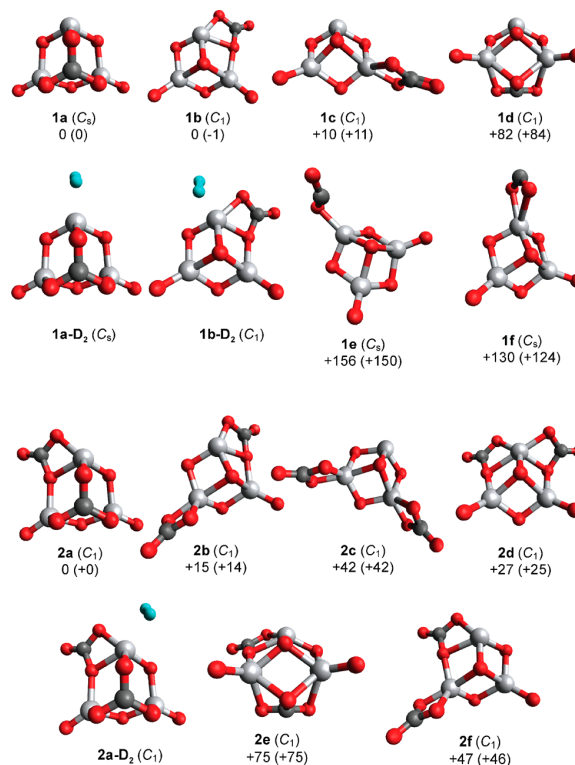


Figure 3. ω B97X-D/aug-cc-pVTZ minimum-energy structures, symmetry (in parentheses) and relative CCSD(T) single-point energy (in kJ·mol⁻¹) of energetically low-lying $[\text{Ti}_3\text{O}_6(\text{CO}_2)_{n=1,2}]^-$ isomers. The ZPE-corrected energies are given in parentheses. The isomers are labeled with $n\mathbf{x}$, where n is the number of CO₂ molecules adsorbed and $x = \mathbf{a}, \mathbf{b}, \mathbf{c}, \dots$, which indicates the energetic ordering. Atoms in gray represent Ti, dark gray represents C, red represents O, and blue represents H. The structures of D₂-tagged species for 1a, 1b, and 2a are also shown.

$[\text{Ti}_3\text{O}_6(\text{CO}_2)]$ clusters of which the neutral structure corresponding to 1d was found to be the lowest in energy. Interestingly, they did not consider the tridentate symmetric carbonate motif of 1a. We determined the optimized geometry of the neutral analogue of 1a and find that it lies 20 kJ/mol above the 1d analogue using DFT (see Table S1). However, when the CCSD(T) energies are considered, the order is reversed; the 1a analogue is predicted 11 kJ/mol below the 1d analogue and thus is likely the ground state structure of neutral $[\text{Ti}_3\text{O}_6(\text{CO}_2)]$. Formation of the physisorbed species 1e (+130 kJ/mol) and 1f (+156 kJ/mol) is less favorable compared to the corresponding neutral clusters and contain bent CO₂ moieties (see SI for geometric parameters), indicating partial charge transfer to the CO₂.

Messenger-tagging with D₂ also plays a significant role for the energetic ordering of the isomers. We calculated counterpoise-corrected D₂ binding energies for 1a·D₂ and 1b·D₂ and find that 1b (21 kJ/mol) binds D₂ more than twice as strong as 1a (9.0 kJ/mol). This is presumably due to the higher positive atomic charge on the corresponding Ti atom in 1b (0.86 |e|) versus 1a (0.59 |e|). Hence, messenger tagging favors the formation of 1b·D₂.

For $n = 2$, we considered the six structures shown in Figure 3. Their relative DFT and CCSD(T) energies are listed in Table 2. Independent of the computational method used, 2a is

predicted to lie lowest in energy followed by **2b**, which lies about 15 kJ/mol higher. Structure **2a** consists of two chemisorbed CO₂ molecules in the form of a bidentate (**1b**) and tridentate (**1a**) bridged carbonate, the two most stable $n = 1$ motifs. Structure **2b** corresponds to the combination of the **1b/1c** motifs, while the higher energy isomers **2d** (+27 kJ/mol), **2c** (+42 kJ/mol), and **2e** (+75 kJ/mol) then represent the **1b/1b**, **1c/1c**, and **1b/1d** combinations, respectively. Structure **2f** (+48 kJ/mol) exhibits similar CO₂ binding motifs as **2b**, but here the two carbonate groups share a Ti⁴⁺ center.

In order to assign the IRPD spectra of the D₂-tagged [Ti₃O₆(CO₂)_{*n*}]⁻ anions with $n = 1$ and 2, we compare them to the calculated harmonic spectra of the three lowest energy isomers (without tag) in Figures 4 and 5, respectively (see Figures S2

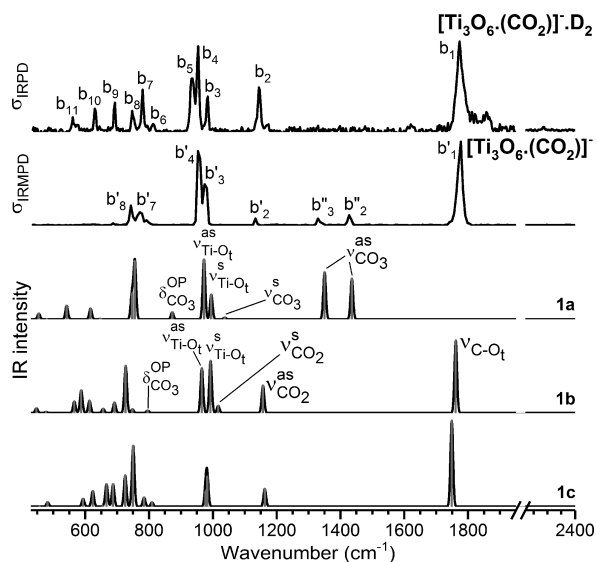


Figure 4. Experimental IRPD and IRMPD spectra of D₂-tagged [Ti₃O₆(CO₂)⁻] and calculated IR spectra of the three energy isomers (**1a–1c**) of the untagged anions. The IRPD spectrum (top panel), measured with an attenuated (14%) laser beam, shows the D₂-loss channel, while the IRMPD spectrum (second panel from top), measured with a nonattenuated laser beam, shows the CO₂-loss channel. The calculated IR spectra (lower panels), derived from ω B97XD/aug-cc-pVTZ harmonic frequencies (scaled by 0.96) and intensities, are plotted with sticks (gray) and a 10 cm⁻¹ fwhm Gaussian line shape convolution. See Table 1 for band assignments.

and S3 for a comparison to the spectra of all isomers, also including isomers with D₂ tag). For $n = 1$ (see Figure 4), we find the best agreement of the experimental D₂-loss IRPD spectrum with the simulated spectrum of **1b**. It reproduces all of the observed bands b₁ to b₁₁ satisfactorily (see Table 1). The three absorption bands b₁ (1773 cm⁻¹), b₂ (1144 cm⁻¹), and b₃ (984 cm⁻¹) are assigned to the terminal C=O (1761 cm⁻¹), antisymmetric CO₂ (1157 cm⁻¹), and symmetric CO₂ (1017 cm⁻¹) stretching modes, respectively, of the bridging bidentate carbonate moiety. Bands b₄ (954 cm⁻¹) and b₅ (936 cm⁻¹) correspond to the symmetric (993 cm⁻¹) and antisymmetric (965 cm⁻¹) combinations of the terminal Ti–O stretching modes, followed by CO₃ bending (b₆, b₉) and Ti–O–Ti stretching and bending modes at lower energies. Note that the weak features at 1855 and 1174 cm⁻¹ (marked with an asterisk in Figure 2) are not reproduced by the harmonic spectrum and we therefore attribute them to

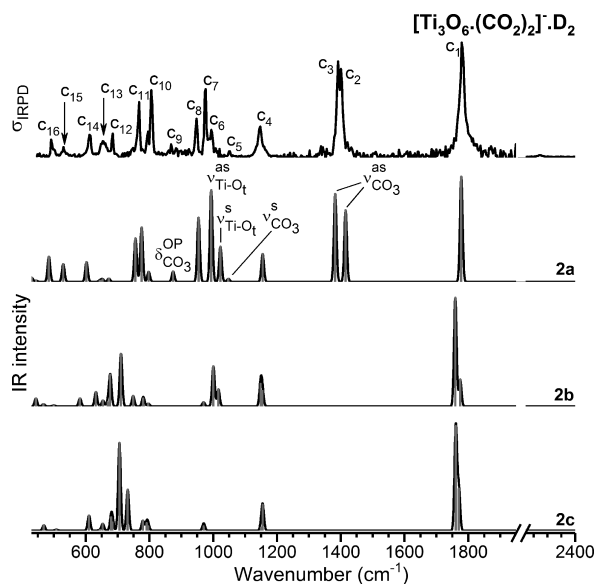


Figure 5. Experimental IRPD spectra of D₂-tagged [Ti₃O₆(CO₂)₂]⁻ (top panel) and calculated IR spectra (lower panels) of the three low-energy isomers (**2a–2c**) of the untagged anions. The calculated IR spectra, derived from ω B97XD/aug-cc-pVTZ harmonic frequencies (scaled by 0.96) and intensities, are plotted with sticks (gray) and a 10 cm⁻¹ fwhm Gaussian line shape convolution. See Table 1 for band assignments.

excitation of antisymmetric CO₂ stretching mode/triply coordinated O atom stretching mode and carbonate bending mode/ring breathing mode combination bands, respectively. The spectrum of **1c**, on the other hand, does not reproduce the characteristic triplet b₃–b₅ around 1000 cm⁻¹, because one of the Ti=O sites is occupied. The spectrum of **1a** exhibits two characteristic antisymmetric stretching modes of the symmetrically bound carbonate species at 1436 and 1350 cm⁻¹, which are not observed in the D₂-loss channel.

Interestingly, we do find evidence for the population of (bare) **1a** when monitoring the CO₂-loss channel as part of IRMPD measurements using higher pulse energies (~8 vs 1 mJ). In addition to the features previously attributed to **1b**, the corresponding IRMPD spectrum (see second trace from top in Figure 4) exhibits two weaker peaks at 1427 (b₂'') and 1329 cm⁻¹ (b₃''), which we assign to the two antisymmetric stretching modes of the tridentate carbonate in **1a**. This observation confirms that **1a** lies close in energy to **1b** in the absence of tagging and both are formed and present initially in the ion trap, but subsequent D₂-tagging then favors the formation **1b**-D₂ over **1a**-D₂.

The IRPD spectrum of the $n = 2$ cluster is compared to the harmonic spectra of the three lowest energy isomers in Figure 5. Only the spectrum of the lowest energy isomer **2a** reproduces the characteristic IR signature in the C–O stretching region. The four bands at 1779 (c₁), 1400 (c₂), 1391 (c₃) and 1147 cm⁻¹ (c₄) are assigned to the terminal C=O (1778 cm⁻¹) and antisymmetric CO₂ stretch (1155 cm⁻¹) of the bidentate carbonate as well as the two antisymmetric CO₃ stretches (1415 and 1382 cm⁻¹) of the tridentate carbonate. Note that the calculated splitting of the antisymmetric CO₃ stretches of 33 cm⁻¹ for the untagged cluster (spectrum **2a** in Figure 5) is substantially larger than the experimental value of 9 cm⁻¹ (for the tagged cluster), but is

reduced to 2 cm⁻¹ when D₂-tagging is explicitly considered (see Figure S3). This is the only band that shows such a pronounced messenger-tag induced shift. The bands at lower energies can then be assigned as follows. Bands c₅ (1052 cm⁻¹) and c₈ (947 cm⁻¹) are the symmetric CO₃ (1048 cm⁻¹) and CO₂ (954 cm⁻¹) stretches of the tridentate and bidentate bridging carbonates, respectively. The symmetric (1022 cm⁻¹) and antisymmetric (994 cm⁻¹) combinations of the terminal Ti–O stretches correspond to bands c₆ (994 cm⁻¹) and c₇ (976 cm⁻¹), followed by Ti–O–Ti ring stretching (c₁₀, c₁₂), CO₃/CO₂ bending modes (c₉, c₁₁, c₁₃), and Ti–O–Ti ring breathing modes (c₁₄–c₁₆) at lower energies (see Table 1). The spectra of 2b and 2c, on the other hand, cannot recover the experimental spectrum, in particular the characteristic doublet of the tridentate carbonate moiety around 1400 cm⁻¹ (c₂, c₃) is absent from these spectra.

The similarities in the IRPD spectra of D₂-tagged [Ti₃O₆(CO₂)_{0–2}]⁻ anions show that addition of up to two CO₂ molecules to Ti₃O₆⁻ leads to local perturbations rather than overall structural changes. For example, the two terminal Ti=O bonds remain intact and slightly increase in bond strength upon CO₂ addition, indicated by a small, but consistent, blue-shift of the corresponding stretching modes from 970/948 cm⁻¹ (*n* = 0) to 984/954 cm⁻¹ in the *n* = 1 cluster and 994/976 cm⁻¹ in the *n* = 2 cluster, concomitant with a predicted shortening of the terminal Ti–O bonds from 164 pm (*n* = 0) to 162 pm (*n* = 2). Similarly, the two stretching modes associated with the bidentate carbonate species are also slightly blue-shifted from 1773/1144 cm⁻¹ (*n* = 1) to 1779/1147 cm⁻¹ (*n* = 2). The spectral changes in regions (iii) and (iv) (<900 cm⁻¹) are slightly more pronounced, but also not dramatic. Finally, calculation of the spin density for the *n* = 0–2 anions (see Figure S5) confirms that the localized, unpaired electron remains nearly unperturbed upon CO₂ adsorption. On the other hand, D₂-tagging leads to more substantial effects, for example, the symmetric CO₂ stretch in the spectrum of 1b is red-shifted by 61 cm⁻¹ and its IR intensity increases by a factor of 6 (from 99 to 626 km/mol) upon D₂-tagging (see Figure S2) as a result of electron delocalization from the Ti³⁺ center to the D₂ molecule.

5. CONCLUSIONS

In summary, we find that the first two CO₂ molecules adsorb chemically to Ti₃O₆⁻, leaving the unpaired electron largely unperturbed. CO₂ activation in this case involves the incorporation of a formally doubly negatively charged, either doubly or triply coordinated O atom to form a bidentate or tridentate bridging carbonate dianion (CO₃²⁻), respectively. The bidentate binding motif described here is well-known from CO₂ adsorption studies on TiO₂ anatase surfaces^{7,8,13,14} and has also been predicted as a particular stable motif for CO₂ adsorption on neutral gas phase titanium oxide clusters.¹⁵ The tridentate binding motif is identified here experimentally for the first time and exhibits a characteristic IR signature in the form of an intense doublet of peaks near 1400 cm⁻¹, which correspond to two antisymmetric carbonate stretching modes.

The present results have several implications for understanding CO₂ activation/conversion in general and CO₂ adsorption at titania interfaces in particular. For example, the characterization of the role of bicarbonate (HCO₃⁻) species in such processes using IR spectroscopy may require additional scrutiny, since the characteristic doublet of the tridentate carbonate binding motif lies in the same spectral region that

has typically been attributed to HCO₃⁻.^{8,14} Moreover, recent DFT calculations suggest that a tridentate binding motif plays a central role in the oxygen exchange mechanism on a defective anatase surface.⁴² However, the prediction of the reaction barriers for such rather complex systems using DFT depends intimately on the specific value of the Hubbard *U* correction used to describe the on-site Coulomb interaction.^{43,44} Gas phase clusters such as those studied here represent ideal model systems to accurately test more such approximate computational methods, since smaller clusters are amenable to higher level calculations.^{19,45,46}

The present study also demonstrates the high potential of calculations based on the AFIR method for investigation of chemical reactions on small atomic clusters. In future IRPD studies, we will try to obtain a molecular level understanding of how water coadsorption influences CO₂ activation in these model systems and how this ultimately can be exploited for the catalytic conversion of CO₂ to value-added chemicals.

■ ASSOCIATED CONTENT

Supporting Information

The Supporting Information is available free of charge on the ACS Publications website at DOI: 10.1021/acs.jpcc.8b10724.

Quadrupole mass spectra; experimental spectra compared to computed spectra for all the isomers; additional possible isomers, spin densities, and NBO charges; isomer energies; Cartesian atomic coordinates of all calculated isomers (PDF).

■ AUTHOR INFORMATION

Corresponding Authors

*E-mail: knut.asmis@uni-leipzig.de.

*E-mail: dneumark@berkeley.edu.

*E-mail: lyalin.andrey@nims.go.jp.

ORCID

Satoshi Maeda: 0000-0001-8822-1147

Tetsuya Taketsugu: 0000-0002-1337-6694

Wieland Schöllkopf: 0000-0003-0564-203X

Knut R. Asmis: 0000-0001-6297-5856

Present Address

^{||}JILA, National Institute of Standards and Technology, Boulder, Colorado 80305, U.S.A.

Notes

The authors declare no competing financial interest.

■ ACKNOWLEDGMENTS

This work has been supported by the German Research Foundation (DFG) within the CRC 1109 “Metal Oxide–Water Systems”. X.S. thanks the Alexander-von-Humboldt Foundation for a postdoctoral research fellowship. M.L.W. thanks the National Science Foundation for a graduate research fellowship. D.M.N. thanks the Air Force Office of Scientific Research for funding this research (No. FA9550-16-1-0097). M.G., S.M., T.T., and A.L. are grateful for financial support from the programs of the Ministry of Education, Culture, Sports, Science and Technology (MEXT, Japan) on the “Development of Environmental Technology using Nanotechnology” and “Priority Issue on Post-K computer” (development of new fundamental technologies for high-efficiency energy creation, conversion/storage and use). Institute for Chemical Reaction Design and Discovery

(ICRD) was established by World Premier International Research Initiative (WPI), MEXT, Japan. A.L. and T.T. gratefully acknowledge the financial support of JSPS KAKENHI Grant Nos. 15K05387 and 16KT0047, respectively.

REFERENCES

- Habisreutinger, S. N.; Schmidt-Mende, L.; Stolarczyk, J. K. Photocatalytic reduction of CO₂ on TiO₂ and other semiconductors. *Angew. Chem., Int. Ed.* **2013**, *52*, 7372–7408.
- Civiš, S.; Ferus, M.; Knížek, A.; Kubelík, P.; Kavan, L.; Zúkalová, M. Photocatalytic transformation of CO₂ to CH₄ and CO on acidic surface of TiO₂ anatase. *Opt. Mater.* **2016**, *56*, 80–83.
- Linsebigler, A. L.; Lu, G.; Yates, J. T. Photocatalysis on TiO₂ surfaces: Principles, mechanisms, and selected results. *Chem. Rev.* **1995**, *95*, 735–758.
- Thompson, T. L.; Yates, J. T. Surface science studies of the photoactivation of TiO₂: New photochemical processes. *Chem. Rev.* **2006**, *106*, 4428–4453.
- Guo, Q.; Zhou, C.; Ma, Z.; Ren, Z.; Fan, H.; Yang, X. Elementary photocatalytic chemistry on TiO₂ surfaces. *Chem. Soc. Rev.* **2016**, *45*, 3701–3730.
- Martra, G. Lewis acid and base sites at the surface of microcrystalline TiO₂ anatase: relationships between surface morphology and chemical behaviour. *Appl. Catal., A* **2000**, *200*, 275–285.
- Liao, L. F.; Lien, C. F.; Shieh, D. L.; Chen, M. T.; Lin, J. L. FTIR study of adsorption and photoassisted oxygen isotopic exchange of carbon monoxide, carbon dioxide, carbonate, and formate on TiO₂. *J. Phys. Chem. B* **2002**, *106*, 11240–11245.
- Mino, L.; Spoto, G.; Ferrari, A. M. CO₂ capture by TiO₂ anatase surfaces: A combined DFT and FTIR study. *J. Phys. Chem. C* **2014**, *118*, 25016–25026.
- He, H.; Zapol, P.; Curtiss, L. A. A theoretical study of CO₂ anions on anatase (101) surface. *J. Phys. Chem. C* **2010**, *114*, 21474–21481.
- Weichman, M. L.; Song, X. W.; Fagiani, M. R.; Debnath, S.; Gewinner, S.; Schöllkopf, W.; Neumark, D. M.; Asmis, K. R. Gas phase vibrational spectroscopy of cold (TiO₂)_n⁻ (n = 3–8) clusters. *J. Chem. Phys.* **2016**, *144*, 124308.
- Song, X. W.; Fagiani, M. R.; Debnath, S.; Gao, M.; Maeda, S.; Taketsugu, T.; Gewinner, S.; Schöllkopf, W.; Asmis, K. R.; Lyalin, A. Excess charge driven dissociative hydrogen adsorption on Ti₂O₄⁻. *Phys. Chem. Chem. Phys.* **2017**, *19*, 23154–23161.
- Weichman, M. L.; Debnath, S.; Kelly, J. T.; Gewinner, S.; Schöllkopf, W.; Neumark, D. M.; Asmis, K. R. Dissociative water adsorption on gas-phase titanium dioxide cluster anions probed with infrared photodissociation spectroscopy. *Top. Catal.* **2018**, *61*, 92–105.
- Freund, H. J.; Roberts, M. W. Surface chemistry of carbon dioxide. *Surf. Sci. Rep.* **1996**, *25*, 225–273.
- Su, W. G.; Zhang, J.; Feng, Z. C.; Chen, T.; Ying, P. L.; Li, C. Surface phases of TiO₂ nanoparticles studied by UV Raman spectroscopy and FT-IR spectroscopy. *J. Phys. Chem. C* **2008**, *112*, 7710–7716.
- Flores, L. A.; Murphy, J. G.; Copeland, W. B.; Dixon, D. A. Reaction of CO₂ with groups 4 and 6 transition metal oxide clusters. *J. Phys. Chem. A* **2017**, *121*, 8719–8727.
- Dodson, L. G.; Thompson, M. C.; Weber, J. M. Interactions of molecular titanium oxides TiO_x (x = 1–3) with carbon dioxide in cluster anions. *J. Phys. Chem. A* **2018**, *122*, 6909–6917.
- Goebbert, D. J.; Meijer, G.; Asmis, K. R. 10K ring electrode trap - tandem mass spectrometer for infrared spectroscopy of mass selected ions. *AIP Conf. Proc.* **2008**, *1104*, 22–29.
- Goebbert, D. J.; Garand, E.; Wende, T.; Bergmann, R.; Meijer, G.; Asmis, K. R.; Neumark, D. M. Infrared spectroscopy of the microhydrated nitrate ions NO₃⁻(H₂O)_{1–6}. *J. Phys. Chem. A* **2009**, *113*, 7584–7592.
- Fagiani, M. R.; Song, X.; Debnath, S.; Gewinner, S.; Schöllkopf, W.; Asmis, K. R.; Bischoff, F. A.; Müller, F.; Sauer, J. Dissociative water adsorption by Al₃O₄⁺ in the gas phase. *J. Phys. Chem. Lett.* **2017**, *8*, 1272–1277.
- Brümmer, M.; Kaposta, C.; Santambrogio, G.; Asmis, K. R. Formation and photodepletion of cluster ion-messenger atom complexes in a cold ion trap: Infrared spectroscopy of VO⁺, VO₂⁺, and VO₃⁺. *J. Chem. Phys.* **2003**, *119*, 12700–12703.
- Schöllkopf, W.; Gewinner, S.; Junkes, H.; Paarmann, A.; von Helden, G.; Bluem, H.; Todd, A. M. M. The new IR and THz FEL facility at the Fritz Haber Institute in Berlin. *Proc SPIE*, **2015**, *9512*, 95121L.
- Heine, N.; Asmis, K. R. Cryogenic ion trap vibrational spectroscopy of hydrogen-bonded clusters relevant to atmospheric chemistry. *Int. Rev. Phys. Chem.* **2015**, *34*, 1–34.
- Heine, N.; Asmis, K. R. Cryogenic ion trap vibrational spectroscopy of hydrogen-bonded clusters relevant to atmospheric chemistry (vol 34, pg 1, 2015). *Int. Rev. Phys. Chem.* **2016**, *35*, 507–507.
- Frisch, M. J.; Trucks, G. W.; Schlegel, H. B.; Scuseria, G. E.; Robb, M. A.; Cheeseman, J. R.; Scalmani, G.; Barone, V.; Mennucci, B.; Petersson, G. A.; et al. *Gaussian 09*, version D01; Gaussian, Inc.: Wallingford, CT, U.S.A., 2009.
- Chai, J.-D.; Head-Gordon, M. Long-range corrected hybrid density functionals with damped atom-atom dispersion corrections. *Phys. Chem. Chem. Phys.* **2008**, *10*, 6615–6620.
- Minenkov, Y.; Singstad, A.; Occhipinti, G.; Jensen, V. R. The accuracy of DFT-optimized geometries of functional transition metal compounds: a validation study of catalysts for olefin metathesis and other reactions in the homogeneous phase. *Dalton Trans.* **2012**, *41*, 5526–5541.
- Kendall, R. A.; D, T. H., Jr.; Harrison, R. J. Electron affinities of the first-row atoms revisited. Systematic basis sets and wave functions. *J. Chem. Phys.* **1992**, *96*, 6796–6806.
- Davidson, E. R. Comment on “Comment on Dunning’s correlation-consistent basis sets. *Chem. Phys. Lett.* **1996**, *260*, 514–518.
- Noga, J.; Bartlett, R. J. The full CCSDT model for molecular electronic structure. *J. Chem. Phys.* **1987**, *86*, 7041–7050.
- Urban, M.; Noga, J.; Cole, S. J.; Bartlett, R. J. Towards a full CCSDT model for electron correlation. *J. Chem. Phys.* **1985**, *83*, 4041–4046.
- Stanton, J. F. Why CCSD(T) works: a different perspective. *Chem. Phys. Lett.* **1997**, *281*, 130–134.
- Raghavachari, K.; Trucks, G. W.; Pople, J. A.; Head-Gordon, M. A fifth-order perturbation comparison of electron correlation theories. *Chem. Phys. Lett.* **1989**, *157*, 479–483.
- Bartlett, R. J.; Musial, M. Coupled-cluster theory in quantum chemistry. *Rev. Mod. Phys.* **2007**, *79*, 291–352.
- Weigend, F.; Ahlrichs, R. Balanced basis sets of split valence, triple zeta valence and quadruple zeta valence quality for H to Rn: Design and assessment of accuracy. *Phys. Chem. Chem. Phys.* **2005**, *7*, 3297–3305.
- Hellweg, A.; Hättig, C.; Höfener, S.; Klopper, W. Optimized accurate auxiliary basis sets for RI-MP2 and RI-CC2 calculations for the atoms Rb to Rn. *Theor. Chem. Acc.* **2007**, *117*, 587–597.
- Ahlrichs, R.; Bär, M.; Häser, M.; Horn, H.; Kölmel, C. Electronic structure calculations on workstation computers: The program system turbomole. *Chem. Phys. Lett.* **1989**, *162*, 165–169.
- Maeda, S.; Ohno, K.; Morokuma, K. Systematic exploration of the mechanism of chemical reactions: the global reaction route mapping (GRRM) strategy using the ADDF and AFIR methods. *Phys. Chem. Chem. Phys.* **2013**, *15*, 3683–3701.
- Maeda, S.; Harabuchi, Y.; Sumiya, Y.; Takagi, M.; Suzuki, K.; Hatanaka, M.; Osada, Y.; Taketsugu, T.; Morokuma, K.; Ohno, K. GRRM, a developmental version at Hokkaido University; <https://afir.sci.hokudai.ac.jp> (accessed 29 August, 2018).

(39) José, M. S.; Emilio, A.; Julian, D. G.; Alberto, G.; Javier, J.; Pablo, O.; Daniel, S.-P. The SIESTA method for ab initio order- N materials simulation. *J. Phys.: Condens. Matter* **2002**, *14*, 2745.

(40) Miller, G. B. S.; Esser, T. K.; Knorke, H.; Gewinner, S.; Schoellkopf, W.; Heine, N.; Asmis, K. R.; Uggerud, E. Spectroscopic identification of a bidentate binding motif in the anionic magnesium-CO₂ complex ([ClMgCO₂]⁻). *Angew. Chem., Int. Ed.* **2014**, *53*, 14407–14410.

(41) Shimanouchi, T. *Tables of molecular vibrational frequencies consolidated*; National Bureau of Standards, 1972; Vol. 1, pp 1–160.

(42) Sorescu, D. C.; Civiš, S.; Jordan, K. D. Mechanism of oxygen exchange between CO₂ and TiO₂(101) anatase. *J. Phys. Chem. C* **2014**, *118*, 1628–1639.

(43) Anisimov, V. I.; Zaanen, J.; Andersen, O. K. Band theory and Mott insulatoras - Hubbard-U instead of Stoner-I. *Phys. Rev. B: Condens. Matter Mater. Phys.* **1991**, *44*, 943–954.

(44) Dudarev, S. L.; Botton, G. A.; Savrasov, S. Y.; Humphreys, C. J.; Sutton, A. P. Electron-energy-loss spectra and the structural stability of nickel oxide: An LSDA+U study. *Phys. Rev. B: Condens. Matter Mater. Phys.* **1998**, *57*, 1505–1509.

(45) Burow, A. M.; Wende, T.; Sierka, M.; Włodarczyk, R.; Sauer, J.; Claes, P.; Jiang, L.; Meijer, G.; Lievens, P.; Asmis, K. R. Structures and vibrational spectroscopy of partially reduced gas-phase cerium oxide clusters. *Phys. Chem. Chem. Phys.* **2011**, *13*, 19393–19400.

(46) Jiang, L.; Wende, T.; Claes, P.; Bhattacharyya, S.; Sierka, M.; Meijer, G.; Lievens, P.; Sauer, J.; Asmis, K. R. Electron distribution in partially reduced mixed metal oxide systems: Infrared spectroscopy of Ce_mV_nO_o⁺ gas phase clusters. *J. Phys. Chem. A* **2011**, *115*, 11187–11192.

Correction to “CO₂ Adsorption on Ti₃O₆⁻: A Novel Carbonate Binding Motif”

Sreekanta Debnath, Xiaowei Song, Matias R. Fagiani, Marissa L. Weichman, Min Gao, Satoshi Maeda, Tetsuya Taketsugu, Wieland Schöllkopf, Andrey Lyalin,* Daniel M. Neumark,* and Knut R. Asmis*

J. Phys. Chem. C 2019, 123, 13, 8439–8446. DOI: 10.1021/acs.jpcc.8b10724Cite This: *J. Phys. Chem. C* 2020, 124, 6952–6953

Read Online

ACCESS |

Metrics & More

Article Recommendations

Supporting Information

The published article contained erroneous CCSD(T) electronic energies. This concerns all CCSD(T) energies mentioned in the article, including values in Figure 3 and Table 2 as well as Figure S4 and Tables S2 and S3 of the

Table 2. ω B97XD/aug-cc-pVTZ and CCSD(T)/def2-TZVP Relative Electronic Energies, ΔE_{DFT} and $\Delta E_{\text{CCSD(T)}}$, as Well as ZPE-Corrected Energies ΔE_0 (All Energies in kJ/mol) of the Lowest-Energy Minimum-Energy Isomers of $[\text{Ti}_3\text{O}_6(\text{CO}_2)_{n=1,2}]^-$ at the Corresponding ω B97XD/aug-cc-pVTZ Minimum-Energy Geometry^a

<i>n</i>	isomer	ΔE_{DFT}^a	$\Delta E_{0,\text{DFT}}^b$	$\Delta E_{\text{CCSD(T)}}^a$	$\Delta E_{0,\text{CCSD(T)/DFT}}^b$
1	1a	0.0	0.0	0.0	0.0
	1b	19.1	18.0	17.6	16.4
	1c	12.0	11.9	5.3	5.2
	1d	37.4	39.2	18.2	20.1
	1e	45.1	38.2	17.5	10.7
	1f	53.4	46.2	16.3	9.1
2	2a	0.0	0.0	0.0	0.0
	2b	18.5	17.8	8.0	7.2
	2c	24.5	24.2	7.8	7.5
	2d	32.5	30.6	22.8	20.8
	2e	39.2	38.8	12.6	12.3
	2f	41.4	40.1	27.0	25.8

^aAbsolute energies: −3189.03837 au (1a, DFT), −3186.14665 au (1a, CCSD(T)), −3377.67800 au (2a, DFT), −3374.51650 au (2a, CCSD(T)). ^bZPE determined from ω B97XD/aug-cc-pVTZ harmonic vibrational frequencies.

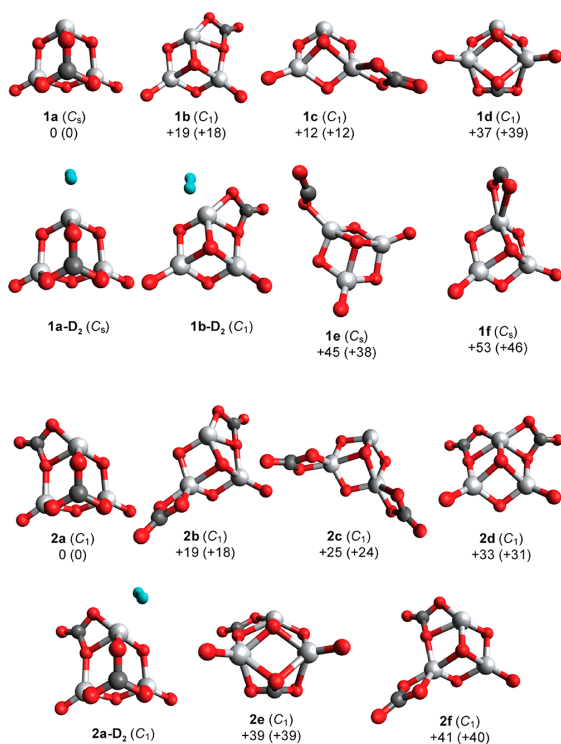


Figure 3. ω B97XD/aug-cc-pVTZ minimum-energy structures, symmetry (in parentheses) and relative energy ΔE_{DFT} (in kJ·mol⁻¹) of energetically low-lying $[\text{Ti}_3\text{O}_6(\text{CO}_2)_{n=1,2}]^-$ isomers. The ZPE-corrected energies $\Delta E_{0,\text{DFT}}$ are given in parentheses. The isomers are labeled with *nx*, where *n* is the number of CO₂ molecules adsorbed and *x* = a, b, c, ... indicates the energetic ordering. Atoms in gray represent Ti, dark gray C, red O, and blue H. The structures of D₂-tagged species for 1a, 1b, and 2a are also shown.

Supporting Information. In addition, the calculated spectra of 1e and 1f were incorrectly labeled in Figure S2. Corrected Table 2 and Figure 3 are presented here, and the corrected Supporting Information figures and tables are deposited. These corrections do not affect the main conclusions drawn in the paper.

Page 8442, second paragraph (left column): “Note that the physisorbed complexes (1e, 1f) are predicted to lie even higher in energy when the CCSD(T) energies are considered (see Table 2).”

Published: March 16, 2020



ACS Publications

© 2020 American Chemical Society

6952

https://dx.doi.org/10.1021/acs.jpcc.0c01893
J. Phys. Chem. C 2020, 124, 6952–6953

Corrected: “Note that the physisorbed complexes (**1e**, **1f**) are predicted to lie lower in energy when the CCSD(T) energies are considered (see Table 2).

Page 8442, second paragraph (left column): “However, when the CCSD(T) energies are considered, structures **1a** and **1b** are nearly isoenergetic, with **1b** predicted only +0.3 kJ/mol higher in energy. Moreover, when the harmonic vibrational ZPEs from DFT are combined with the CCSD(T) electronic energies, the energetic ordering is reversed and **1b** is indeed slightly favored by 0.8 kJ/mol.”

Corrected: “However, when the CCSD(T) energies are considered, the energy difference between structures **1a** and **1b** is reduced from 18 kJ/mol ($\Delta E_{0,\text{DFT}}$) to 16 kJ/mol ($\Delta E_{0,\text{CCSD(T)}}$).”

Page 8442, first paragraph (right column): “We determined the optimized geometry of the neutral analogue of **1a** and find that it lies 20 kJ/mol above the **1d** analogue using DFT (see Table S1). However, when the CCSD(T) energies are considered, the order is reversed; the **1a** analogue is predicted 11 kJ/mol below the **1d** analogue and thus is likely the ground state structure of neutral [Ti₃O₆(CO₂).”

Corrected: “We determined the optimized geometry of the neutral analogue of **1a** and find that it lies 20 kJ/mol above the **1d** analogue using DFT (see Table S2). When the CCSD(T) energies are considered, the order is confirmed; the **1a** analogue is predicted 32 kJ/mol above the **1d** analogue.”

■ ASSOCIATED CONTENT

SI Supporting Information

The Supporting Information is available free of charge at <https://pubs.acs.org/doi/10.1021/acs.jpcc.0c01893>.

Corrected Figures S2 and S4 and Tables S2 and S3 (PDF)

■ ACKNOWLEDGMENTS

We thank Prof. David A. Dixon (University of Alabama) for drawing our attention to this issue.

Supporting Information

CO₂ Adsorption on Ti₃O₆⁻: A Novel Carbonate Binding Motif

Sreekanta Debnath,^{a,b} Xiaowei Song,^b Matias R. Fagiani,^{a,b} Marissa L. Weichman,^{c,†} Min Gao,^{d,e}
Satoshi Maeda,^{e,f} Tetsuya Taketsugu,^{e,f,g} Wieland Schöllkopf,^b Andrey Lyalin,^{g,*} Daniel M.
Neumark,^{c,h,*} Knut R. Asmis^{a,*}

^a Wilhelm-Ostwald-Institut für Physikalische und Theoretische Chemie, Universität Leipzig,
Linnéstrasse 2, D-04103 Leipzig, Germany

^b Fritz-Haber-Institut der Max-Planck-Gesellschaft, Faradayweg 4-6, D-14195 Berlin, Germany

^c Department of Chemistry, University of California, Berkeley, California 94720, United States

^d Institute for Catalysis, Hokkaido University, Sapporo 001-0021, Japan

^e Department of Chemistry, Faculty of Science, Hokkaido University, Sapporo 060-0810, Japan

^f Institute for Chemical Reaction Design and Discovery (WPI-ICRD), Hokkaido University, Kita
21, Nishi 10, Kita-ku, Sapporo 001-0021, Japan

^g Global Research Center for Environment and Energy based on Nanomaterials Science
(GREEN), National Institute for Material Science (NIMS), Tsukuba 305-0044, Japan.

^h Chemical Sciences Division, Lawrence Berkeley National Laboratory, Berkeley, California
94720, United States

†Current affiliation: JILA, National Institute of Standards and Technology, Boulder, Colorado
80305, USA

S1. Quadrupole mass spectra

S2. Experimental spectra compared to computed spectra for all the isomers

S3. Additional possible isomers, spin densities and NBO charges

S4. Isomer energies

S5. Cartesian atomic coordinates of all calculated isomers

S1. Quadrupole mass spectra

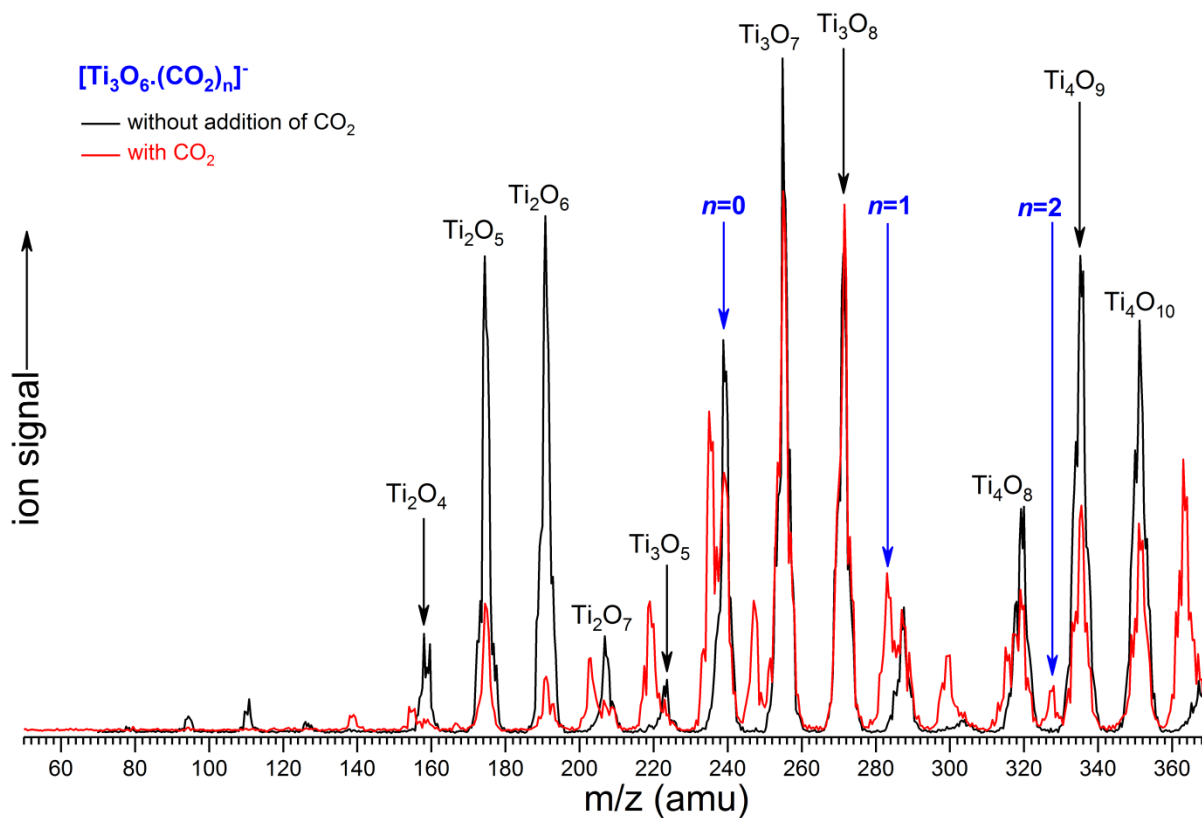


Fig.S1: Quadrupole mass spectrum of the ions produced by pulsed laser vaporization of a pure Ti metal rod and quenching in a gas pulse of 0.75 % O₂ seeded in He. Pure CO₂ was added from a second gas channel to the source block to get CO₂ reaction product.

S2. Experimental spectra compared to computed spectra for all the isomers

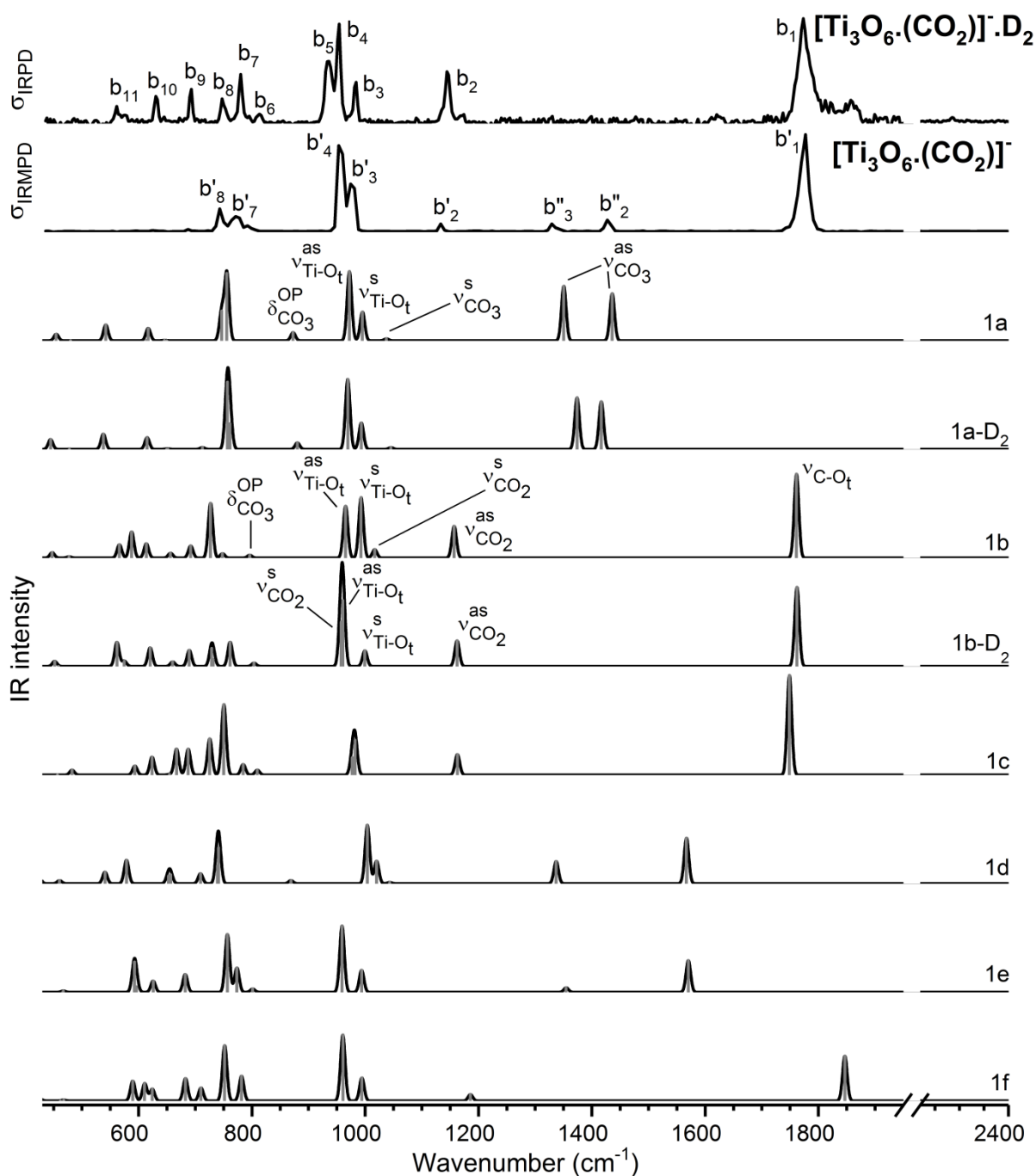


Fig.S2: Experimental IRPD spectra of D₂ tagged [Ti₃O₆.(CO₂)]⁻ (D₂ loss – top trace, CO₂ loss – second trace from the top) compared with calculated harmonic spectrum (using Gaussian convolution, FWHM=10) of different possible isomers for the species, using ωB97XD/aug-cc-pVTZ level of theory and numbers in parenthesis indicates relative energy of the isomers. A scaling factor of 0.96 is used for the whole region.

6. CO₂ Adsorption on Ti₃O₆⁻

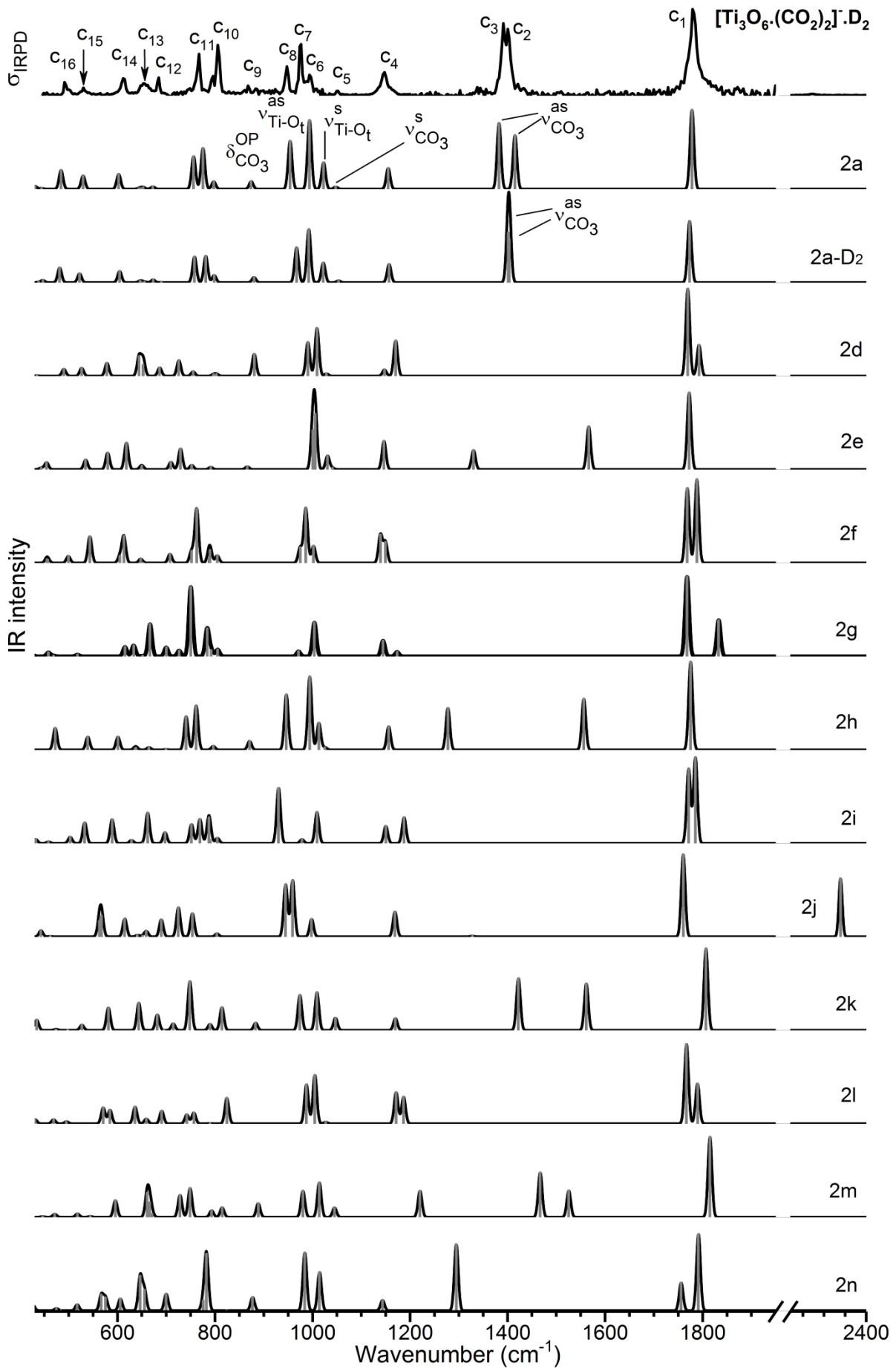


Fig.S3: Experimental IRPD spectra of D₂ tagged [Ti₃O₆.(CO₂)₂]⁻ (top trace) compared with calculated harmonic spectrum (using Gaussian convolution, FWHM=10) of different possible isomers for the species, using ωB97XD/aug-cc-pVTZ level of theory and numbers in parenthesis indicates relative energy of the isomers. A scaling factor of 0.96 is used for the whole region.

S3. Additional possible isomers, spin densities and NBO charges

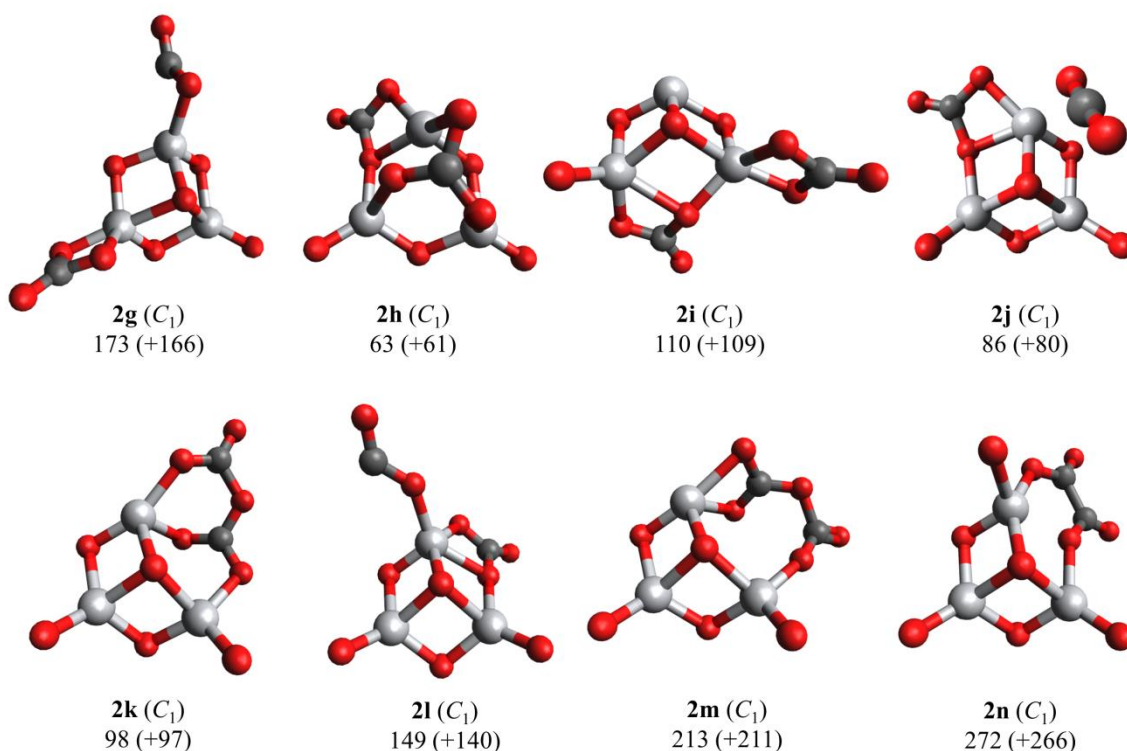


Fig.S4: ωB97X-D/aug-cc-pVTZ minimum-energy structures, symmetry (in parentheses) and relative CCSD(T) single-point energy (in kJ·mol⁻¹) of energetically low-lying [Ti₃O₆(CO₂)₂]⁻ isomers (2a-2f in main manuscript). The ZPE-corrected energies are given in parentheses. The isomers are labelled with *nx*, where *n* is the number of CO₂ molecules adsorbed and *x* = g, h, i, ... indicates the energetic ordering. Atoms in grey represent Ti, dark grey C, and red O. .

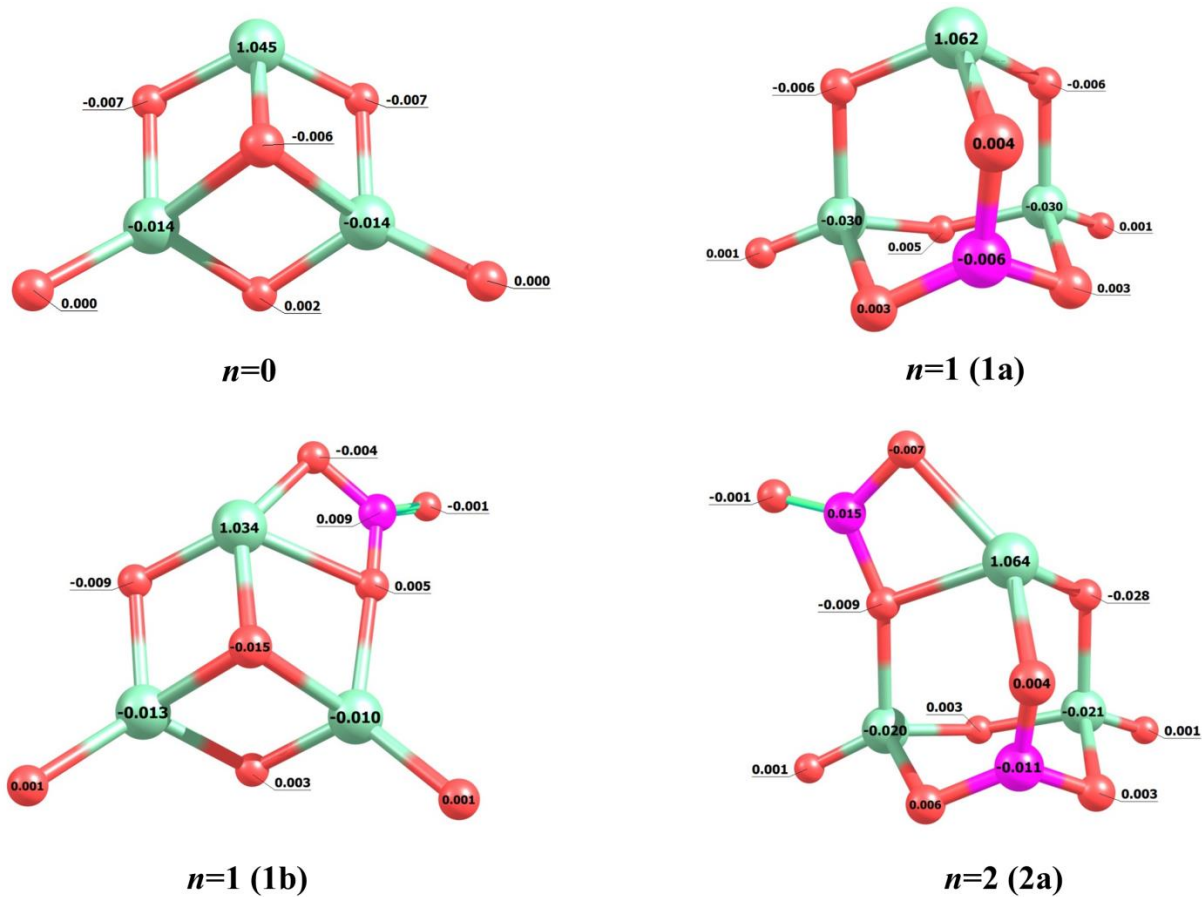


Fig.S5: Spin density plot of [Ti₃O₆.(CO₂)_{n=0-2}]⁻ clusters. (Colour code : sky blue: Ti, orange red: O, pink: C)

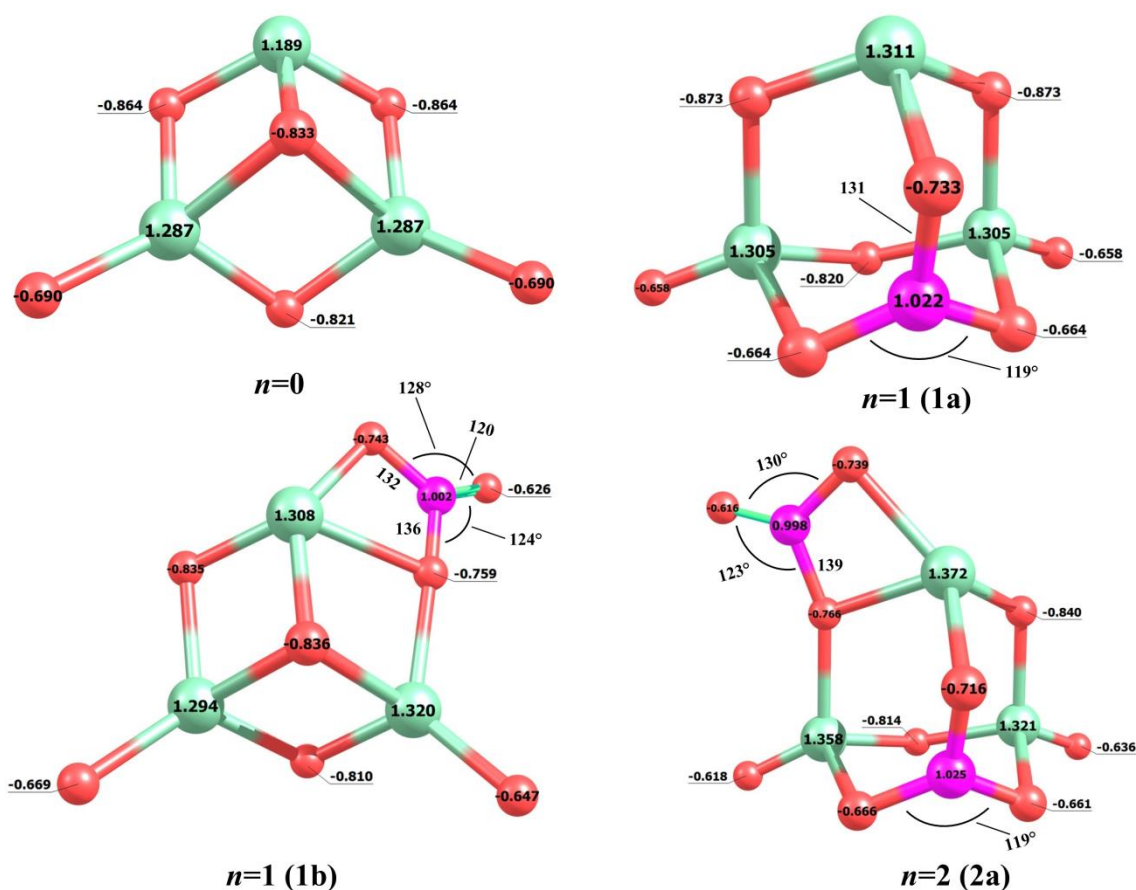


Fig.S6: NBO charges on the C and O atoms of the adsorbed CO₂ on Ti₃O₆⁻ cluster forming [Ti₃O₆.(CO₂)_{n=0-2}]⁻ clusters. Bond lengths (in pm) and bond angles (in degrees) are also shown. (Colour code : sky blue: Ti, orange red: O, pink: C)

Table.S1: Spin densities and NBO charges on different atoms of [Ti₃O₆.(CO₂)_{n=0-2}]⁻ clusters. Ti atom of the Ti³⁺ center is named as Ti_a and then anticlockwise other Ti atoms named as b, c. For bidentate bridged CO₃⁻, free C-O oxygen named as O_a and then same naming as Ti atoms, and for the tridentate CO₃⁻ the oxygen connected to the Ti³⁺ centre named as O_a and then followed same naming as above. All the calculations are performed with ωB97XD/aug-cc-pVTZ level of theory.

Isomer	Spin densities			NBO charges				
	Ti _a	Ti _b	Ti _c	C	O _a	O _b	O _c	CO ₃ ⁻
Ti ₃ O ₆	1.044	-0.013	-0.013			n.a		
1a	1.064	-0.030	-0.030	1.022	-0.733	-0.664	-0.664	-1.039
1b	1.034	-0.012	-0.011	1.002	-0.626	-0.743	-0.759	-1.126
2a	1.062	-0.019	-0.023	1.025	-0.716	-0.666	-0.661	-1.018
				0.998	-0.616	-0.766	-0.739	-1.123

S4. Isomer energies

Table.S2: ω B97XD/aug-cc-pVTZ relative electronic energies ΔE_{DFT} and ZPE-corrected relative energies $\Delta E_{0,\text{DFT}}$ of the **neutral** analogues of $[\text{Ti}_3\text{O}_6(\text{CO}_2)_{n=1,2}]^-$. CCSD(T)/def2-TZVP relative electronic energies $\Delta E_{\text{CCSD(T)}}$ at the DFT minimum-energy geometry and ZPE-corrected relative electronic energies $\Delta E_{0,\text{CCSD(T)/DFT}}$ using the DFT ZPE-correction are also shown. All energies are given in kJ/mol

isomer	label (Dixon et.al)	ΔE_{DFT}^a	$\Delta E_{0,\text{DFT}}^b$	$\Delta E_{\text{CCSD(T)}}^a$	$\Delta E_{0,\text{CCSD(T)/DFT}}^b$
<i>n</i> =1					
1a	n.a	19.6	18.3	0.0	0.0
1b	3-4 Bc	28.4	25.2	8.9	7.0
1d	3-4 Ba	0.0	0.0	11.0	12.3

^a Absolute energies: -3188.90843 a.u (**1a**, DFT), -3182.69384 a.u (**1a**, CCSD(T)),
-3188.90509 a.u (**1b**, DFT), -3182.69046 a.u (**1b**, CCSD(T)),
-3188.91590 a.u (**1d**, DFT), -3182.68965 a.u (**1d**, CCSD(T)),

^b ZPE determined from ω B97XD/aug-cc-pVTZ harmonic vibrational frequencies.

Table.S3: ω B97XD/aug-cc-pVTZ relative electronic energies ΔE_{DFT} and ZPE-corrected relative energies $\Delta E_{0,\text{DFT}}$ of the lowest-energy minimum-energy isomers of $[\text{Ti}_3\text{O}_6(\text{CO}_2)_2]^-$. CCSD(T)/def2-TZVP relative electronic energies $\Delta E_{\text{CCSD(T)}}$ at the DFT minimum-energy geometry and ZPE-corrected relative electronic energies $\Delta E_{0,\text{CCSD(T)/DFT}}$ using the DFT ZPE-correction are also shown. All energies are given in kJ/mol.

isomer	ΔE_{DFT}^a	$\Delta E_{0,\text{DFT}}^b$	$\Delta E_{\text{CCSD(T)}}^a$	$\Delta E_{0,\text{CCSD(T)/DFT}}^b$
<i>n</i> =2				
2a	0.0	0.0	0.0	0.0
2b	18.5	17.8	14.9	14.2
2c	24.5	24.2	41.8	41.6
2d	32.5	30.6	27.4	25.4
2e	39.2	38.8	75.4	75.1
2f	41.4	40.1	47.5	46.2
2g	48.1	41.1	173.2	166.2
2h	47.9	46.5	62.8	61.4
2i	67.4	66.3	110.4	109.3
2j	82.0	77.0	85.6	80.5
2k	93.6	92.9	98.1	97.5

2l	105.0	95.7	149.4	140.1
2m	119.2	118.0	212.6	211.4
2n	213.0	206.6	272.0	265.6

S5. Cartesian atomic coordinates of all calculated isomers

Table S4: Optimized Cartesian coordinates (Å) of the low-lying [Ti₃O₆·(CO₂)_n]⁻ isomers (n=1,2) calculated with ωB97XD/aug-cc-pVTZ.

Isomer		x	y	z
1a	Ti	0.656893	-0.412899	1.592554
	Ti	-1.942848	0.040596	0.000000
	Ti	0.656893	-0.412899	-1.592554
	O	1.401944	-0.867598	-2.964180
	O	1.339432	-1.066624	-0.000000
	O	-1.257310	-0.672020	1.477161
	O	1.401944	-0.867598	2.964180
	O	-1.257310	-0.672020	-1.477161
	O	0.656893	1.569963	-1.116053
	C	0.047059	1.706780	0.000000
	O	-1.247861	1.885156	0.000000
	O	0.656893	1.569963	1.116053
	1a-D2	Ti	0.718989	-0.418080
Ti		-1.924554	-0.016013	-0.000000
Ti		0.718989	-0.418080	-1.593425
O		1.467674	-0.869631	-2.965628
O		1.393085	-1.080312	0.000000
O		-1.196166	-0.673997	1.482950
O		1.467674	-0.869631	2.965628
O		-1.196166	-0.673997	-1.482950
O		0.718989	1.552701	-1.115609
C		0.101200	1.692596	-0.000000
O		-1.182670	1.872413	-0.000000
O		0.718989	1.552701	1.115609
D		-3.532073	1.391555	-0.000000
D	-3.901702	0.718676	-0.000000	
1b	Ti	1.926826	-0.500417	-0.299269
	Ti	-0.606592	-1.268923	0.552455
	Ti	0.030153	1.583162	0.030137
	O	3.505320	-0.752946	0.021334
	O	0.712622	-1.997597	-0.410413
	O	1.361585	1.093658	-1.136124
	O	0.639434	0.067323	1.139497
	O	-1.646418	0.500683	-0.097076
	O	0.072679	3.091645	0.630682
	C	-2.761399	-0.250167	-0.306470
	O	-3.786253	0.189915	-0.744438
	O	-2.501483	-1.493066	0.047253

6. CO₂ Adsorption on Ti₃O₆⁻

1b-D2	Ti	1.982218	-0.395049	-0.264622
	Ti	-0.607473	-1.312037	0.307194
	Ti	0.025407	1.568160	0.069267
	O	3.534460	-0.716705	0.128893
	O	0.738074	-1.843155	-0.706431
	O	1.495896	1.256171	-1.001266
	O	0.625138	0.034703	1.130454
	O	-1.519482	0.388925	-0.469123
	O	-0.115256	3.019194	0.788849
	C	-2.770015	-0.171337	-0.308646
	O	-3.780558	0.405821	-0.595176
	O	-2.622610	-1.376179	0.181803
	D	-0.757532	-2.868723	1.683684
	D	-0.271021	-2.397091	2.043717
1c	Ti	-1.770986	-0.982807	-0.081115
	Ti	-1.287389	1.640100	0.321034
	Ti	0.919320	0.058022	-0.303703
	O	-2.650518	-2.254809	0.427895
	O	-2.612711	0.711815	-0.458906
	O	-0.133604	-1.178224	-1.045570
	O	-0.671681	0.119096	1.152836
	O	0.280598	1.765616	-0.618638
	O	2.198132	-0.348614	1.090321
	C	3.206867	-0.317311	0.216285
	O	2.695671	-0.054529	-0.998629
	O	4.371366	-0.489483	0.463885
	1d	Ti	0.354865	0.107221
Ti		-1.847590	0.690606	-0.000000
Ti		0.354865	0.107221	-1.589660
O		-1.531060	-0.134776	1.578155
O		0.917248	-1.917732	1.142569
O		0.917248	0.803919	2.930699
O		-1.531060	-0.134776	-1.578155
O		0.917248	0.803919	-2.930699
O		0.917248	-1.917732	-1.142569
C		1.239103	-1.477370	0.000000
O		1.743480	-0.251093	0.000000
O		-0.150560	1.367417	-0.000000
1e		Ti	1.222410	-1.399769
	Ti	1.222410	1.399769	-0.043028
	Ti	-1.200514	0.000000	-0.175592
	O	0.267256	0.000000	1.029654
	O	2.284185	-0.000000	-0.658064
	O	1.894844	2.729813	0.620773
	O	1.894844	-2.729813	0.620773
	O	-0.527698	-1.439028	-0.917989
	O	-0.527698	1.439028	-0.917989
	C	-3.562425	0.000000	0.453117
	O	-3.321163	0.000000	-0.762395
	O	-2.714594	0.000000	1.364929

1f	Ti	0.997345	0.788764	1.403082
	Ti	-0.600454	-1.024079	0.000000
	Ti	0.997345	0.788764	-1.403082
	O	0.997345	1.730171	-2.734645
	O	2.173963	1.121648	-0.000000
	O	-0.447813	0.860776	-0.000000
	O	0.401827	-1.074817	1.444461
	O	0.401827	-1.074817	-1.444461
	O	0.997345	1.730171	2.734645
	C	-2.912387	-1.472840	0.000000
	O	-2.091859	-2.429624	0.000000
	O	-4.082494	-1.280863	0.000000
	2a	Ti	0.363085	1.738179
Ti		0.679669	-1.592185	0.216930
Ti		-2.038259	-0.291691	-0.636957
O		0.864441	3.263336	-0.169311
O		1.588076	0.170100	-0.290857
O		-1.104460	1.277859	-1.011040
O		-1.983229	-0.176801	1.381653
O		-0.741712	-1.723288	-0.818168
O		-3.485185	-0.486900	-1.336924
C		2.783677	-0.475292	-0.556209
O		3.769378	0.098071	-0.914594
O		2.595142	-1.751204	-0.332469
C		-0.768433	-0.017974	1.757783
O		-0.242042	1.153832	1.796971
O		-0.034205	-1.054388	2.009382
2a-D2	Ti	0.292832	1.799661	0.039423
	Ti	0.741453	-1.589325	0.147932
	Ti	-2.029582	-0.288403	-0.662467
	O	0.753152	3.342105	-0.062627
	O	1.557653	0.271879	-0.243090
	O	-1.146432	1.318735	-0.985263
	O	-1.992258	-0.233145	1.351106
	O	-0.684690	-1.675028	-0.876466
	O	-3.467004	-0.509522	-1.375928
	C	2.762369	-0.297273	-0.596101
	O	3.710061	0.339746	-0.952172
	O	2.644049	-1.595488	-0.454404
	C	-0.784720	-0.044060	1.746802
	O	-0.310175	1.148863	1.830736
	O	-0.018610	-1.055326	1.966142
	D	1.054047	-3.636305	0.692777
	D	0.610626	-3.420754	1.271200
2b	Ti	-1.402867	-0.169791	0.338281
	Ti	1.039363	-1.256387	-0.576252
	Ti	0.858378	1.594262	0.005765
	O	-3.113749	-0.488674	1.107297
	O	-0.425302	-1.730638	0.416063
	O	-0.593232	1.232807	1.138679

6. CO₂ Adsorption on Ti₃O₆⁻

	O	0.073669	0.244075	-1.142431
	O	2.326667	0.277612	0.198689
	O	1.062571	3.096607	-0.554106
	C	3.340889	-0.633824	0.279534
	O	4.430424	-0.376005	0.697554
	O	2.889886	-1.790086	-0.164663
	C	-3.735318	-0.254444	-0.062745
	O	-2.797730	0.056225	-0.965350
	O	-4.918283	-0.317954	-0.255755
2c	Ti	-1.464895	-0.030387	-0.279266
	Ti	-0.001343	2.168161	0.451412
	Ti	1.466075	-0.028286	-0.277947
	O	-3.055806	-0.774488	-1.004815
	O	-1.551335	1.801306	-0.456206
	O	0.001541	-0.690756	-1.147614
	O	-0.000448	0.493100	1.116324
	O	1.550353	1.803742	-0.454173
	O	3.057553	-0.771116	-1.003734
	C	-3.420491	-1.283086	0.187672
	O	-2.464221	-0.966090	1.068205
	O	-4.423272	-1.901416	0.411804
	C	3.420440	-1.283312	0.187743
	O	4.422122	-1.903635	0.411253
	O	2.463999	-0.966943	1.068349
2d	Ti	-1.534432	-1.349231	0.065669
	Ti	0.083113	1.172001	0.485455
	Ti	1.266889	-1.412798	-0.313338
	O	-2.583501	-2.306994	0.841123
	O	-1.896696	0.525806	-0.347516
	O	-0.269187	-2.145068	-1.037105
	O	0.042811	-0.642225	1.065796
	O	1.620196	0.539341	-0.714393
	O	2.425027	-2.423874	0.180295
	C	-2.239024	1.838433	-0.393539
	O	-3.289564	2.240417	-0.800353
	O	-1.224571	2.554157	0.060148
	C	2.504142	1.429410	-0.075397
	O	1.837900	2.046582	0.857943
	O	3.645931	1.533554	-0.408148
2e	Ti	-0.346440	1.485635	-0.490685
	Ti	-0.764220	-1.494355	-0.414672
	Ti	1.918058	-0.699877	-0.040013
	O	-0.704786	2.681719	-1.493627
	O	-1.876453	0.300465	-0.059177
	O	1.703169	1.454734	0.003421
	O	0.338720	-0.210083	-1.264163
	O	0.719725	-2.112814	0.384549
	O	3.288651	-1.218180	-0.706485
	C	-2.919064	-0.449992	0.398065
	O	-3.945504	0.015060	0.799504

	O	-2.583590	-1.721840	0.306270
	C	1.285722	1.251039	1.246209
	O	1.872861	0.324666	1.868662
	O	0.191869	1.834129	1.527608
2f	Ti	1.034812	-0.125925	0.196037
	Ti	-1.726445	0.728934	-0.690407
	Ti	-1.296042	-1.795105	0.329125
	O	2.786413	0.379794	0.764577
	O	0.080629	1.586586	0.069783
	O	0.298453	-1.245484	1.316678
	O	-0.465875	-0.657169	-1.050519
	O	-2.675122	-0.487172	0.239195
	O	-1.648185	-3.350444	0.030624
	C	-0.579899	2.775998	0.256416
	O	-0.074369	3.741829	0.740874
	O	-1.808197	2.628739	-0.191886
	C	3.354023	-0.277848	-0.257127
	O	2.364531	-0.836716	-0.973417
	O	4.527234	-0.355312	-0.490948
2g	Ti	1.339208	-0.209513	-0.348335
	Ti	-1.472095	-0.357518	-0.014001
	Ti	-0.311707	2.126530	-0.007138
	O	2.919605	-1.056004	-0.962786
	O	-0.155744	-1.134588	-0.966222
	O	1.271892	1.497878	-0.855820
	O	-0.193717	0.445905	1.024970
	O	-1.869721	1.202981	-0.717292
	O	-0.422075	3.581167	0.701572
	C	-3.362184	-1.813103	0.027142
	O	-2.831965	-1.354418	1.087423
	O	-4.265983	-2.519498	-0.271562
	C	3.342964	-1.286243	0.296898
	O	4.360904	-1.841252	0.602867
	O	2.423852	-0.786284	1.129871
2h	Ti	0.419048	1.655328	0.282597
	Ti	0.700604	-1.299576	0.028871
	Ti	-2.065528	0.023962	-0.697882
	O	0.804353	3.038305	1.019517
	O	1.791206	0.407301	-0.451770
	O	-1.146155	1.661572	-0.634005
	O	-0.042130	0.054156	1.488345
	O	-0.683002	-1.244574	-1.101053
	O	-3.406209	-0.009739	-1.599413
	C	2.938731	-0.346488	-0.629742
	O	3.989187	0.136787	-0.935630
	O	2.633487	-1.598550	-0.405625
	C	-1.014859	-0.873320	1.564298
	O	-0.576059	-2.045681	1.678905
	O	-2.206424	-0.528932	1.302450
2i	Ti	1.909295	0.083380	0.631582

6. CO₂ Adsorption on Ti₃O₆⁻

	Ti	0.684422	-1.999391	-0.697046
	Ti	-1.143036	0.010279	-0.167634
	O	2.760056	0.001214	1.994244
	O	2.304594	-1.298037	-0.682337
	O	0.165869	1.373590	0.113267
	O	0.218038	-1.109665	0.834082
	O	-0.739008	-1.078040	-1.528209
	O	-2.818461	0.829240	-0.531892
	C	-3.419280	0.179052	0.480304
	O	-2.485525	-0.576225	1.072084
	O	-4.575111	0.257719	0.786925
	C	1.061301	2.245365	-0.507915
	O	2.261916	1.821972	-0.274265
	O	0.686742	3.200683	-1.122172
2j	Ti	-1.725432	-0.761587	-0.787115
	Ti	0.455350	0.988063	-0.674422
	Ti	0.463694	-1.592881	0.738784
	O	-3.357641	-0.708536	-0.722307
	O	-0.750942	0.507880	-1.893094
	O	-0.777599	-2.333859	-0.405101
	O	-0.647550	0.028545	0.704377
	O	1.830734	-0.514426	-0.276762
	O	0.736984	-2.322565	2.165310
	C	2.886744	0.379603	-0.351895
	O	4.024134	0.046794	-0.169016
	O	2.406599	1.557552	-0.642050
	C	-1.244536	2.583433	1.271892
	O	-0.469641	2.785805	0.417544
	O	-2.009167	2.488149	2.118671
2k	Ti	-2.199166	-0.891126	0.144154
	Ti	0.546372	-1.364903	-0.114911
	Ti	-0.938882	1.641496	-0.073828
	O	-3.539569	-1.432815	-0.602320
	O	-0.837801	-2.202594	0.612962
	O	-2.237580	0.808817	0.926093
	O	-0.695876	-0.097909	-0.954474
	O	2.869012	0.922219	0.113810
	O	-1.510181	2.837146	-0.999919
	C	3.383951	-0.358349	-0.328671
	O	4.573164	-0.454903	-0.333250
	O	2.483283	-1.172795	-0.723145
	C	1.664523	0.980725	0.678595
	O	1.220778	-0.030030	1.290914
	O	1.015524	2.046046	0.529497
2l	Ti	0.776065	-1.804895	-0.667733
	Ti	-0.980681	0.347278	-0.173527
	Ti	1.927430	0.348128	0.726696
	O	0.721669	-3.421758	-0.600114
	O	-0.685319	-0.729634	-1.477167
	O	2.414747	-0.935869	-0.503344

	O	0.225051	-0.663325	0.894478
	O	0.683161	1.692303	-0.035581
	O	2.887600	0.581246	2.007745
	C	-0.054129	2.662327	-0.651147
	O	0.363829	3.746982	-0.924387
	O	-1.246051	2.156962	-0.863226
	C	-3.648943	-0.783694	0.587941
	O	-4.655074	-0.846151	1.215444
	O	-2.670048	0.061361	0.648608
2m	Ti	2.352138	-0.006008	-0.403880
	Ti	0.311703	-1.741441	0.297889
	Ti	0.056875	1.598629	0.235898
	O	3.881156	0.224078	0.092745
	O	1.777539	-1.854033	-0.684234
	O	1.403432	1.466421	-1.025516
	O	0.831376	-0.075972	0.981880
	O	0.243463	2.858088	1.227401
	O	-1.285067	-1.345518	-0.908513
	C	-2.970864	0.709201	-0.402261
	O	-1.856136	1.261782	-0.154822
	O	-3.937798	1.113460	-0.971031
	C	-2.029590	-1.390816	0.122742
	O	-3.087046	-0.601788	0.204792
	O	-1.702547	-2.126052	1.089692
2n	Ti	2.142691	-0.591390	-0.613044
	Ti	-0.431145	-1.188493	0.401449
	Ti	0.761356	1.668743	0.322861
	O	3.628681	-1.228473	-0.489639
	O	0.575883	-1.726900	-0.911907
	O	1.944880	1.231167	-1.008229
	O	1.060469	-0.144404	1.021252
	O	-1.071737	0.828039	0.007147
	O	1.069092	2.974247	1.227933
	C	-2.332079	1.007741	-0.379838
	O	-2.805924	2.055617	-0.695551
	O	-2.306115	-1.345037	-0.064298
	C	-3.096663	-0.352045	-0.370182
	O	-4.266078	-0.413094	-0.624531
	O	-0.558078	-2.417302	1.794355

Chapter 7

Conclusion and Outlook

7.1 Conclusion

With the results presented in this doctoral thesis, action spectroscopy of size selected cluster ions in combination with high level quantum chemical calculations proved to be an ideal tool to gain molecular level insight into the structure – reactivity relationship of this unique form of matter.

Chapter 4 describes the effect of atomic Fe- impurity into small Al- oxide clusters in terms of structural change and preferred doping site. It is found that the smallest cluster ($n = 1$) of the Al/Fe- mixed metal oxides $[(Al_2O_3)_n(FeO)]^+$ adopts a different structural motif than that of the pure Al- oxide¹ and the degree of structural agreement increases with increasing size. The structural trend evolves from bi-cyclic planar ($n = 1$) to quasi 2D ($n = 2$) to 3D cage type ($n \geq 3$) geometry with increasing cluster size.

The Fe- atom is found to preferentially occupy the outer ring of the cluster with a more relaxing 3-fold coordinated geometry than 4-fold coordination. The reason behind this selectivity is attributed to the larger size and d-type valence orbitals of the Fe- atom. This finding is in line with the distinctive doping site of Fe-doped nanoparticles or nanocrystals, where the dopant Fe-atoms replace Al-atoms of the Al_2O_3 network, mostly in the surface, inducing only minor distortions of the network.² Moreover, high propensity of populating the surface by the dopant molecules support the observation of increased photocatalytic efficiency of zeolites³ when doped with transition metals, in particular with iron atoms.^{4, 5}

Proper care must be taken during mass analysis of these mixed metal oxide clusters. At the ion source, both mixed- and pure- metal oxides are formed as the target rod is composed of both the elements. The clusters are mass-selected by their m/z ratio; as a result, separating isobaric compounds remain difficult without very high resolution mass spectrometer, resulting, contribution from all the overlapping masses in the measured IRPD spectra. By choosing the system in an intelligent way, one can avoid the problem with mass overlapping. Furthermore, if any of the metal elements have an abundant isotope which favours mass separation of the isobaric compounds, then, using an isotopically enriched target is beneficial. In case, this option is unattainable, isobaric compounds can also be separated by their tagging efficiency. In a favourable experimental condition one of the isobaric compound forms multiple tagging signal whereas the other one forms one or no tag. Then the IRPD spectra can be generated by looking at the depletion channel of each tag. IR²MS² technique (detailed description can be found in ref.^{6, 7}) is another smart tool to measure

individual IRPD spectra of the isobaric species. In a worst case scenario, where none of the above method is applicable, IRPD spectrum of the pure metal oxide is measured separately using a single-metal target rod and then subtracted from the overlapping spectra of isobaric compounds. Here, both the spectra must have to be measured with identical trapping conditions (e.g. identical trap temperature and messenger gas). In the particular study reported in chapter 4, for small $[(\text{Al}_2\text{O}_3)_n\text{FeO}]^+$ ($n = 1-2$) clusters no isobaric species was found. In case of bigger clusters ($n = 3-5$), the isobaric species contains at least 3 Fe- atoms (FeO_{10} same mass with Fe_3O_3 , $m/z = 216$ amu) i.e. $\text{Al}_6\text{FeO}_{10}$ and $\text{Al}_6\text{Fe}_3\text{O}_3$, $\text{Al}_8\text{FeO}_{14}$ and $\text{Al}_8\text{Fe}_3\text{O}_7$, $\text{Al}_{10}\text{FeO}_{16}$ and $\text{Al}_{10}\text{Fe}_3\text{O}_9$ are isobars. However, multiple Fe-atom containing clusters were non-abundant in the mass spectra obtained from the Al/Fe mixed metal rod, so the isobaric contribution from the high Fe- containing clusters were neglected. Possibly because of the above mentioned limitations, gas phase experiments on mixed metal oxide clusters are scarce. Thus, the insights obtained from this study are of fundamental relevance for the molecular level understanding of Fe- doped metal oxide nanoparticles or nanocrystals.

Chapter 5 provides a molecular level understanding of the active site(s) in heteronuclear-metal oxide clusters, towards oxygen atom transfer reaction (OAT). In particular, Al-O_t unit of $[\text{AlVO}_4]^{+\bullet}$ cluster was experimentally identified as the active site for the conversion of CO to CO₂. On the other hand, the P=O_t unit of $[\text{VPO}_4]^{+\bullet}$ cluster was found to provide the oxygen atom for the conversion of ethylene to acetaldehyde. Generally, because of having high activation barrier, these oxidation reactions do not occur directly in room or elevated temperatures. Here, catalysts play a role to bypass the activation barrier by opening up new energetically favourable pathways. $[\text{AlVO}_4]^{+\bullet}$ or $[\text{VPO}_4]^{+\bullet}$ cluster serves as gas phase model systems to study OAT reactions as part of more complex catalytic cycles. Mass spectrometry or CID studies can provide quantitative results concerning yield of these conversion processes, but messenger tagged IRPD spectroscopy proved to be a phenomenal tool for the unambiguous assignment of the active site(s) in the catalyst models. Moreover, identification of neutral CH₃CHO as a reaction product for the $[\text{VPO}_4]^{+\bullet}/\text{C}_2\text{H}_4$ reaction couple, deserves a special mentioning because in most of the ion/molecule reactions the neutral product is usually identified in an indirect way.

The study of CO₂ activation with $[\text{Ti}_3\text{O}_6]^-$ cluster in chapter 6 sheds new light to the chemical understanding of oxygen vacancy defect site on titania surface. An asymmetric bridged bidentate and a symmetric tridentate bridged carbonate binding motif of chemisorbed CO₂ on Ti_3O_6^- is identified. The tridentate binding motif is reported here for the first time, whose characteristic IR signature questions the till date assignment of bicarbonate species formed on wet TiO₂ surface in presence of CO₂.

The molecular level insights obtained on the structure-reactivity relationship by studying the pure- and mixed- metal oxide model systems with atmospherically relevant ligands are of fundamental importance in contemporary science. The theoretically tractable model system studies make it possible to test and confirm

quantum chemical predictions of structure and reactivity of metal oxide clusters. Potential interdisciplinary application of these studies also cannot be ignored. The characteristic infrared signatures of the studied species can be grouped and used in surface science for structural assignment, as performing high level theoretical calculations for complex surfaces are expensive and difficult with the state-of-art resources. Understanding of the active sites in an atomistic level may help in design new material or functional building blocks for industrially important heterogeneous catalysts or fuel cells for example.

Although most of the open questions discussed in the first chapter (see section 1.4, 1.5 and 1.6) could be answered with the presented results. Some of the remaining challenges and new questions that arise while solving the stated ones are summarized in the following final section of this thesis. In particular, improvements to the present experimental setup are also discussed in the following section.

7.2 Outlook

The stability of the ion signal at the source region remains the main parameter that determines the signal-to-noise ratio in measured IRPD spectra. The ion spray source is comparatively more stable than the laser vaporization source. By replacing the solenoid general valve (*Parker, series 99*) with a copper Even-Lavie valve (EL valve) which produces shorter ($\sim 25 \mu\text{s}$) and denser gas pulses, clustering efficiency of the vaporization source can be improved. The later valve is made to be operated in a wide range of temperature (10 K - 400 K) and repetition rate (0 - 600 Hz) without adjustment. The shorter pulse and low repetition rate (10-50 Hz) helps in achieving low background pressure in the pumping chamber thus facilitates cluster growth and cooling of large molecules to lower temperature.⁸ A cryogenic motor can then be coupled with the source block, allowing cryogenic cooling of the whole assembly; leading to enhanced clustering efficiency compared to the present setup where the temperature range is limited up to ~ 200 K. Incorporation of the EL valve was tasted and the outcome is stated in the following. With the state-of-art experimental set-up (described in section 3.1) ~ 4 -6 bar backing pressure at the general valve is used for normal operation. Using the EL valve, no cluster formation was observed with this low backing pressure. When comparatively higher pressure (~ 15 bars) was used, cluster generation was observed but with very low yield. This insight and literature survey^{9, 10} suggested that the EL valve requires higher backing pressure (~ 50 bars) for best results, which was not possible to achieve with the present design of the gas inlet. Modification of the gas inlet system to attain high backing pressure will enable to use the EL valve and possibly will lead to better signal stability.

With the rod target in the laser vaporization source, only the surface of the rod gets ablated. So, a large portion of the target remains unused. This becomes a concern, when working with expensive materials, say gold, boron or mixed metals like Ni/Al, Fe/Si. Design and implementation of a “*disk target*”¹¹ source is advantageous in this particular regard.

Mounting another ion detector directly after the quadrupole mass filter in the present experimental setup, will open the possibility of signal monitoring and optimizing before going to the RET region. This will also be helpful to locate the problem by ensiling the front and back of the machine in case of any signal issue. This modification is already implemented in a similar setup which was built and been used by our group and proved to be beneficial.⁶ Design and adaptation of a linear nano-spray ion source, similar to the later setup⁶ would also widen the choice and control of system to be investigated.

Another desirable improvement of the experimental setup is the addition of a second cryogenic ion trap, similar to ref.¹², separated from the existing one by another mass-selection stage. The improved set-up will facilitate to perform multiple reactions (see below) with the formed clusters at the source. Furthermore, one trap can be used for performing reaction while the other one will allow messenger complex formation of the reaction product. This configuration can be used, for example:

- i. To study reactivity of the activated CO_2 described in chapter 6 with H_2O in a second step.
- ii. To measure He- tagged spectra of $[(\text{AlVO}_3)\text{CO}_6]^{\bullet+}$ (see chapter 5.1).
- iii. To measure spectra of $[\text{VPO}_4(\text{C}_2\text{H}_4)]^{\bullet+}$ with He- tag (see chapter 5.2).

The photocatalytic active site in zeolite molecular sieves is found to be the $[\text{Fe}^{2+}\text{-O}]^*$ charge transfer excited state. The nature of this active site is also studied and summarized by a parallel study reported in ref.¹. Possible next steps are to investigate the catalytic activities of this cluster model. Theoretical calculation by the group of Prof. Sauer, predicts $\text{Al}_2\text{FeO}_4^+$, which contains the $[\text{Fe}^{2+}\text{-O}]^*$ unit can actually activate methane. It would therefore be interesting to experimentally verify this prediction. A similar study is already been done and reported in ref.¹³, where it was shown experimentally that $\text{Al}_8\text{O}_{12}^+$ activates methane by abstraction of a hydrogen atom but the reactivity is inhibited by replacing one Al- with an Fe- atom. Since, Fe- doped metal oxide (e.g. Zn-, Ti- oxide) nanoparticles¹⁴⁻¹⁸ got much attention for their elevated catalytic efficiency, other compelling experiments can be (i) studying structural evolution and active site characterization of Zn- and Ti- oxide clusters with Fe- atom impurity and (ii) testing their catalytic activity.

Similar to the studies shown in chapter 5 and 6, cryogenic ion trap vibrational spectroscopy in combination with electronic structure calculations can be applied to investigate potentially interesting heterogeneous catalysis reactions with suitable pure- and mixed- metal oxide clusters.¹⁹⁻²² Experiments, involving coupling of methane or water with carbon dioxide²³ can be performed with a modified experimental set-up having two ion traps (discussed above). The area of reactivity studies can also be extended towards using metal- carbides²⁴ or nitrides.

Preliminary results on understanding water interaction with Fe- oxides having mixed valence Fe-atoms is presented in Appendix B. These clusters show high multi-reference character, so, theoretical calculations predicting unambiguous structure

and reactivity becomes expensive. However, these studies are demanding for a molecular level understanding of water adsorption process as a function of oxidation state. Here, interaction of the first two water molecules with the Fe-oxide clusters is shown and dissociative water adsorption is predicted in both the cases. In future experiments it will be interesting to explore further evolution of hydration shell and to know at which step molecular water adsorption is happening.

The potential of cryogenic ion trap vibrational spectroscopy is enhanced and widened by coupling this technique with widely tunable and intense IR light source, the FHI-FEL. Proposed upgrade of the FHI-FEL will allow exploring spectral features at the far-infrared and terahertz (THz) region.²⁵ Moreover, two colour IR experiments can also be performed on implementation of this upgrade.

References:

1. J. B. S. F. Müller, F. A. Bischoff, L. Gagliardi, J. Sauer, S. Debnath, M. Jorewitz, K. R. Asmis, *manuscript under preparation*.
2. A. Khodadadi, M. Farahmandjou, M. Yaghoubi and A. R. Amani, *International Journal of Applied Ceramic Technology*, 2019, **16**, 718-726.
3. G. Yan, X. Wang, X. Fu and D. Li, *Catalysis today*, 2004, **93**, 851-856.
4. Y. Tong, Y. Zhang, N. Tong, Z. Zhang, Y. Wang, X. Zhang, S. Zhu, F. Li and X. Wang, *Catalysis Science & Technology*, 2016, **6**, 7579-7585.
5. G. Panov, G. Sheveleva, A. e. a. Kharitonov, V. Romannikov and L. Vostrikova, *Applied Catalysis A: General*, 1992, **82**, 31-36.
6. N. Heine, PhD thesis, Freie Universität Berlin, 2014.
7. M. R. Fagiani, PhD Thesis, Freie Universität Berlin, 2017.
8. U. Even, *EPJ Techniques and Instrumentation*, 2015, **2**, 17.
9. R. Katzy, M. Singer, S. Izadnia, A. LaForge and F. Stienkemeier, *Review of Scientific Instruments*, 2016, **87**, 013105.
10. M. Hillenkamp, S. Keinan and U. Even, *The Journal of chemical physics*, 2003, **118**, 8699-8705.
11. M. A. Duncan, *Review of Scientific Instruments*, 2012, **83**, 041101.
12. B. M. Marsh, J. M. Voss and E. Garand, *The Journal of Chemical Physics*, 2015, **143**, 204201.
13. M. Jorewitz, PhD Thesis, Universität Leipzig, 2019.
14. R. Saleh and N. F. Djaja, *Superlattices and Microstructures*, 2014, **74**, 217-233.
15. Z. Li, W. Shen, W. He and X. Zu, *Journal of Hazardous Materials*, 2008, **155**, 590-594.
16. S. Sood, A. Umar, S. K. Mehta and S. K. Kansal, *Journal of Colloid and Interface Science*, 2015, **450**, 213-223.
17. A. Singhal, S. N. Achary, J. Manjanna, O. D. Jayakumar, R. M. Kadam and A. K. Tyagi, *The Journal of Physical Chemistry C*, 2009, **113**, 3600-3606.
18. M. Zhou, J. Yu, B. Cheng and H. Yu, *Materials Chemistry and Physics*, 2005, **93**, 159-163.
19. J. Li, C. Geng, T. Weiske and H. Schwarz, *Angewandte Chemie International Edition*, **n/a**.
20. S. Zhou, X. Sun, L. Yue, M. Schlangen and H. Schwarz, *Chemistry – A European Journal*, 2019, **25**, 2967-2971.
21. C. Geng, J. Li, T. Weiske and H. Schwarz, *Journal of the American Chemical Society*, 2018, **140**, 9275-9281.
22. S. Zhou, J. Li, M. Schlangen and H. Schwarz, *Angewandte Chemie International Edition*, 2017, **56**, 413-416.
23. J. Li, P. González-Navarrete, M. Schlangen and H. Schwarz, *Chemistry–A European Journal*, 2015, **21**, 7780-7789.

7. Conclusion and Outlook

24. J. Li, C. Geng, T. Weiske and H. Schwarz, *Angewandte Chemie International Edition*, 2020, DOI: 10.1002/anie.202001599, 7.
25. W. Schöllkopf, S. Gewinner, H. Junkes, A. Paarmann, G. von Helden, H. Bluem and A. M. Todd, *The new IR and THz FEL facility at the Fritz Haber Institute in Berlin*, SPIE, 2015.

Appendix A

A.1. Supporting Information:

Infrared Photodissociation Spectroscopy of $[(\text{Al}_2\text{O}_3)_n\text{FeO}]^+$ with $n = 2-5$: Influence of Fe-Impurities on Structure and Other Properties

The following section contains the supporting information for the ready to submit manuscript presented in section 4.1:

:- Supporting Information :-

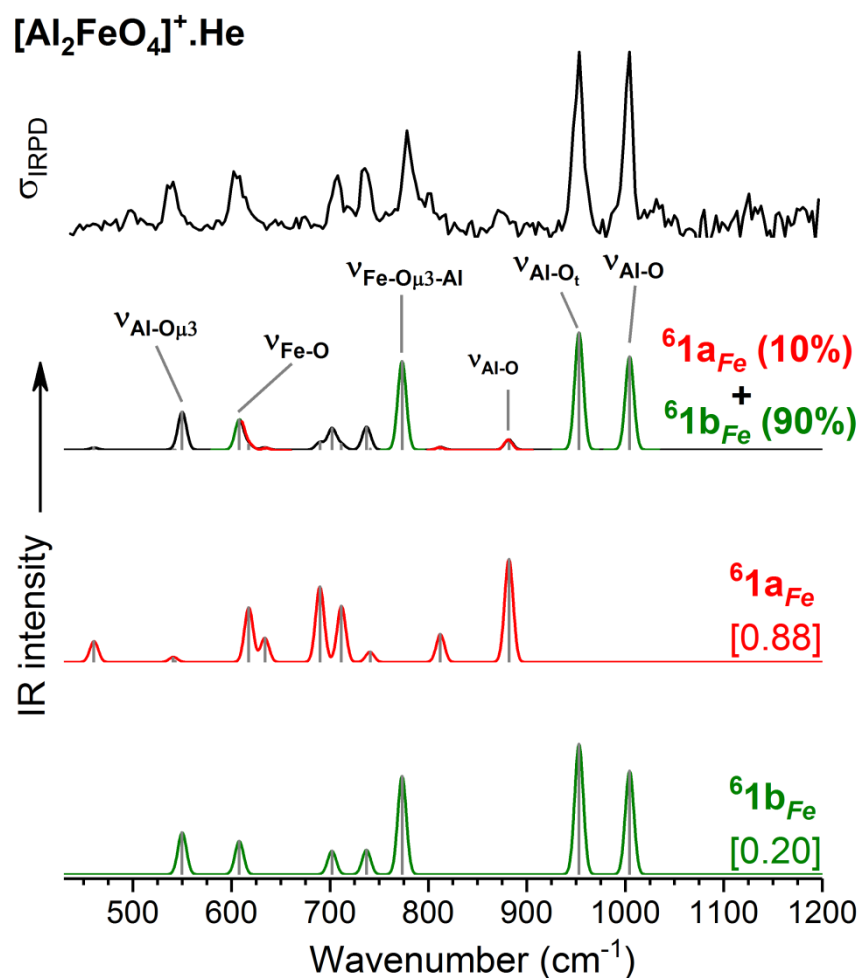
 $n = 1$ 

Figure S1. Experimental IRPD spectra of He-tagged (Al₂FeO₄)⁺ (top trace) compared with simulated IR spectra (lower traces) of the two lowest-energy isomers (⁶1a_{Fe} - ⁶1b_{Fe}).¹ The calculated IR spectra, derived from TPSSh/def2-TZVP harmonic frequencies (scaled by 1.0166) and intensities are plotted with sticks (gray) and a 10 cm⁻¹ FWHM Gaussian line shape convolution. Each sum spectrum is colour coded using Red and Green for individual and black for common contributions.

$n = 2$

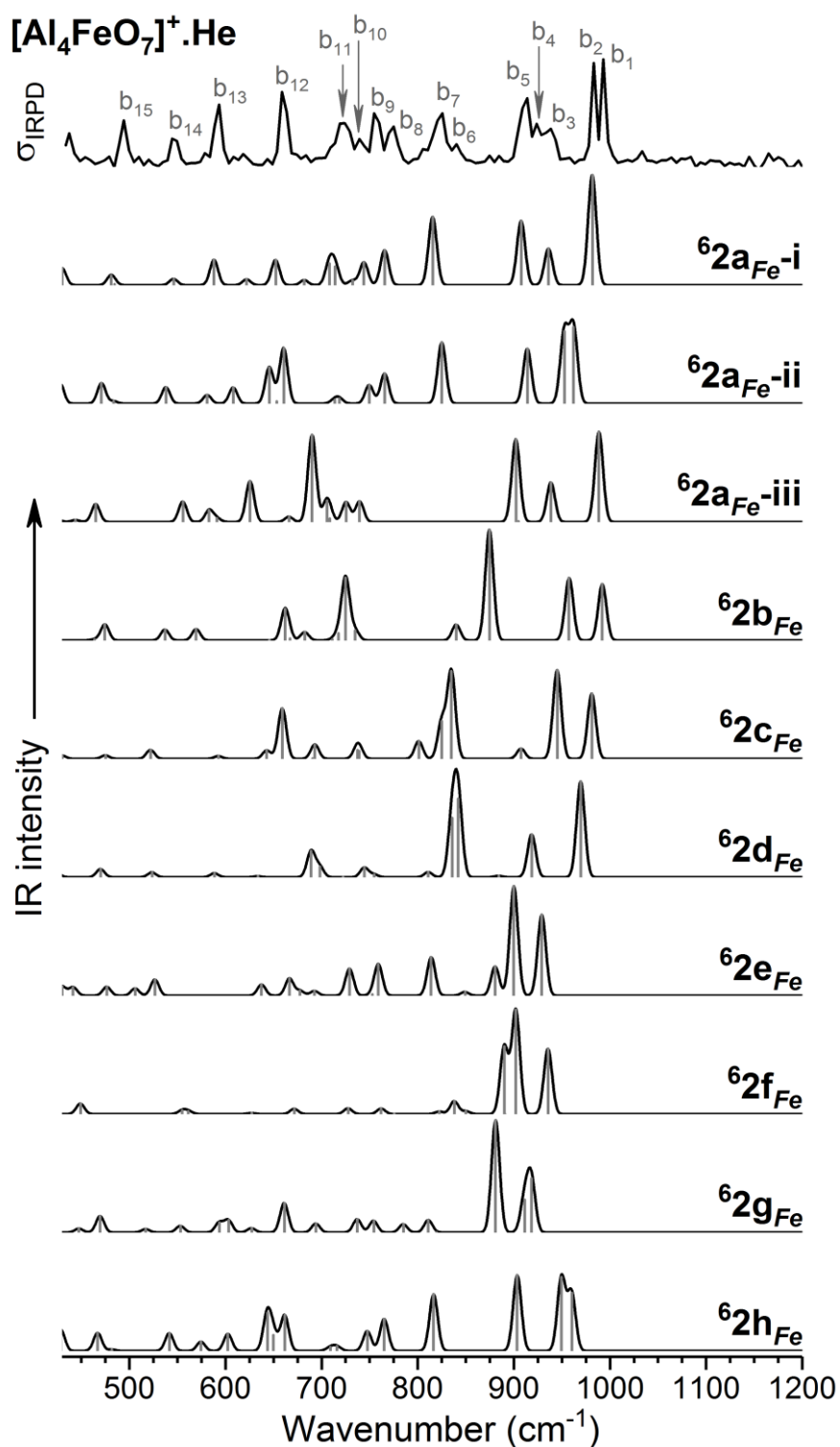


Figure S2. Experimental IRPD spectra of He-tagged $(\text{Al}_4\text{FeO}_7)^+$ (top trace) compared with simulated IR spectra (lower traces) of all calculated isomers (${}^62a_{\text{Fe-i}}$ - ${}^62h_{\text{Fe}}$) with **sextet spin** state. The calculated IR spectra, derived from TPSSh/def2-TZVP harmonic frequencies (scaled by 1.0) and intensities are plotted with sticks (gray) and a 10 cm^{-1} FWHM Gaussian line shape convolution. See Fig.S8 for the structures and relative energies of the contributing isomers.

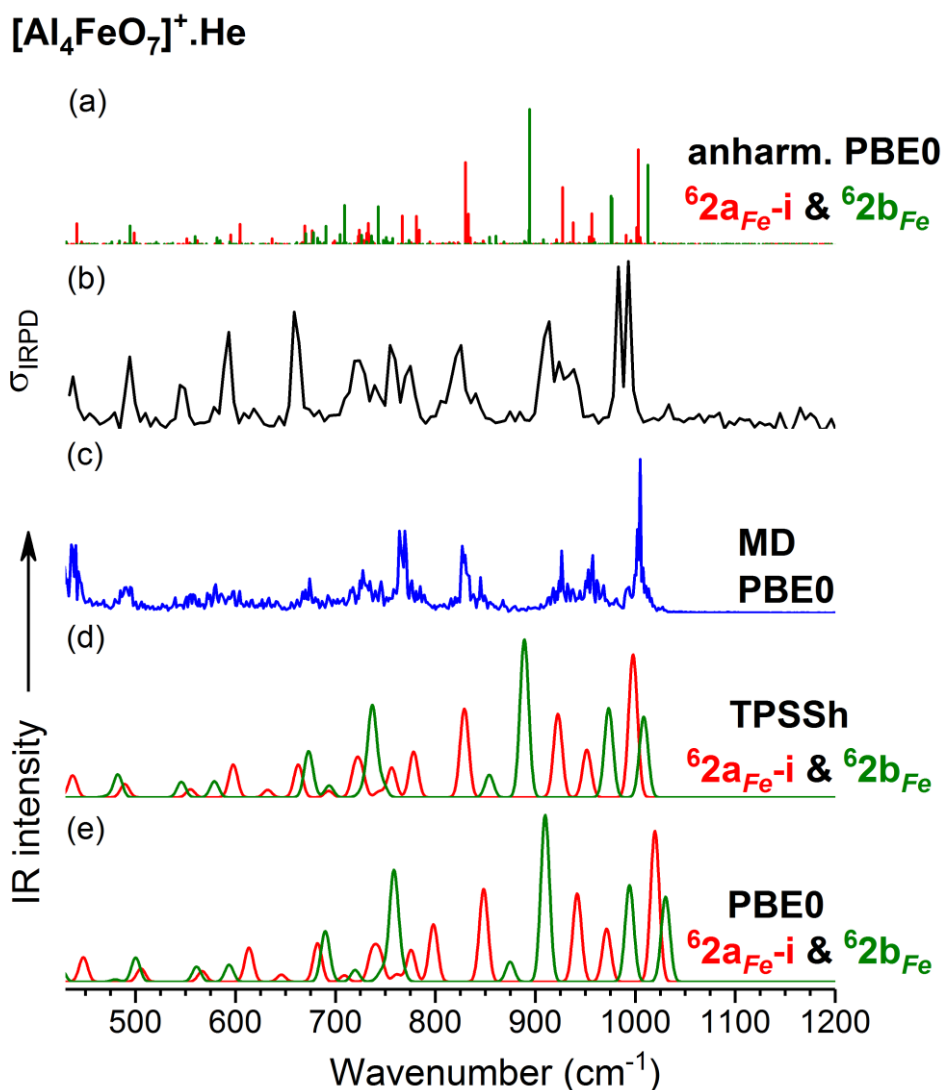
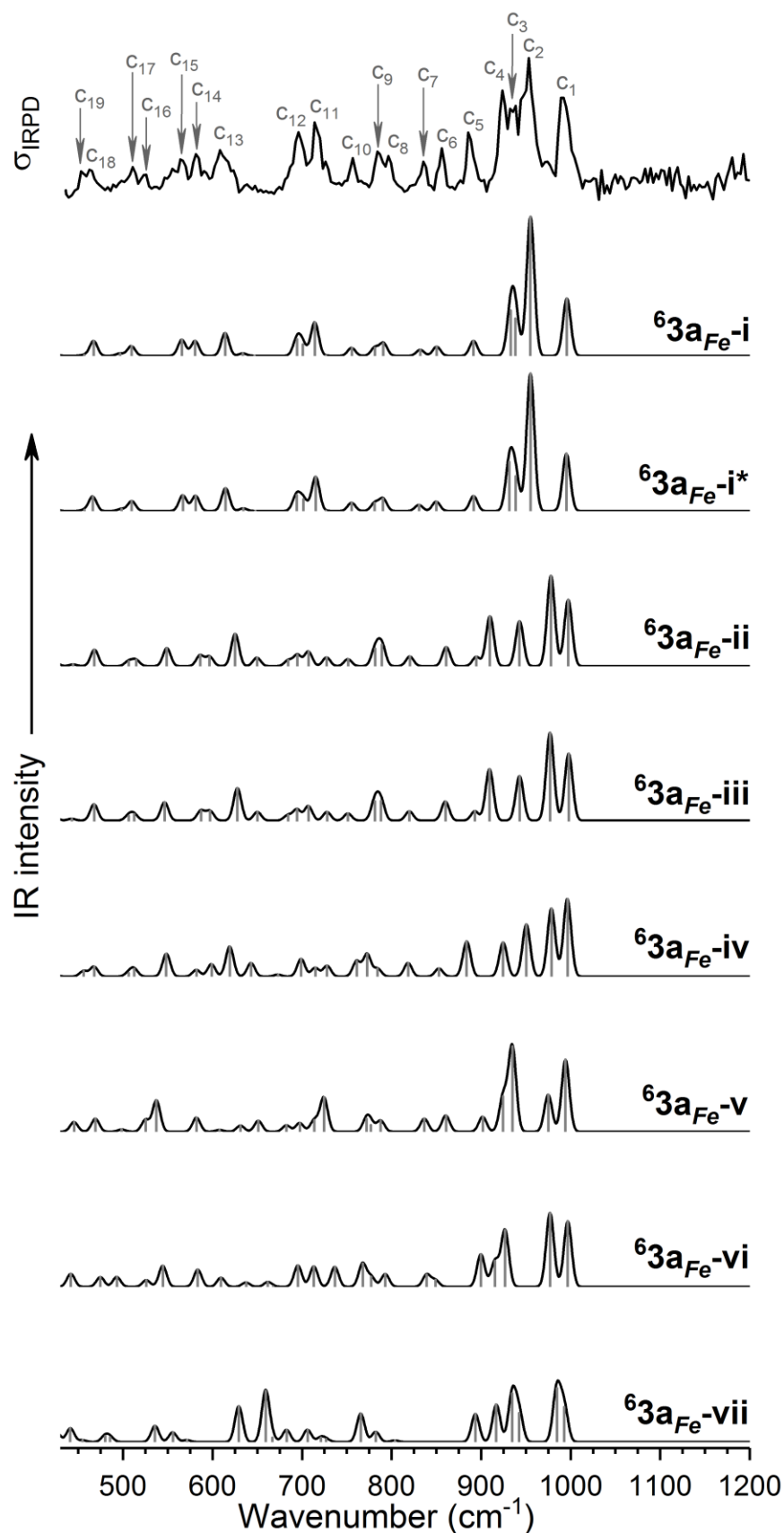


Figure S3. The experimental IRPD spectrum (black) is compared with calculated harmonic, anharmonic and MD simulation spectra of the lowest energy isomers. In the lowest panel harmonic IR spectra of ${}^62a_{Fe-i}$ (red) and ${}^62b_{Fe}$ (green) on the PBE0 level are seen. Above, the harmonic spectra for the same isomers on the TPSSh level are shown. The blue trace results from a Fourier transformation of the total dipole moment of ${}^62a_{Fe-i}$ captured during a 40 ps molecular dynamics simulation on the PBE0-PES. It can be seen, that the doublet peak is emerging at about 994 cm⁻¹. In the topmost panel the anharmonic PBE0 frequencies for both relevant isomers are given as stick spectrum. They suggest that the doublet is resulting from the highest energy vibration of both isomers.

$n=3$

$[\text{Al}_6\text{FeO}_{10}]^+ \cdot \text{He}$



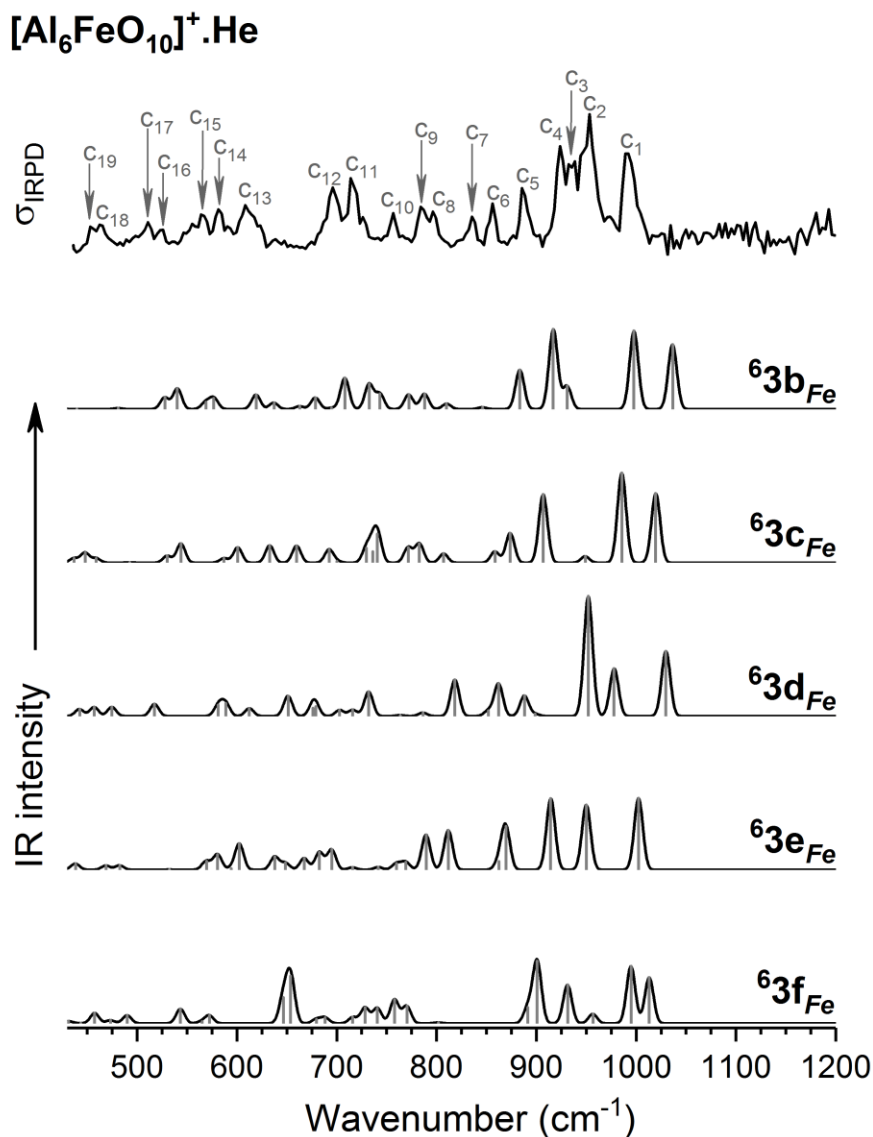
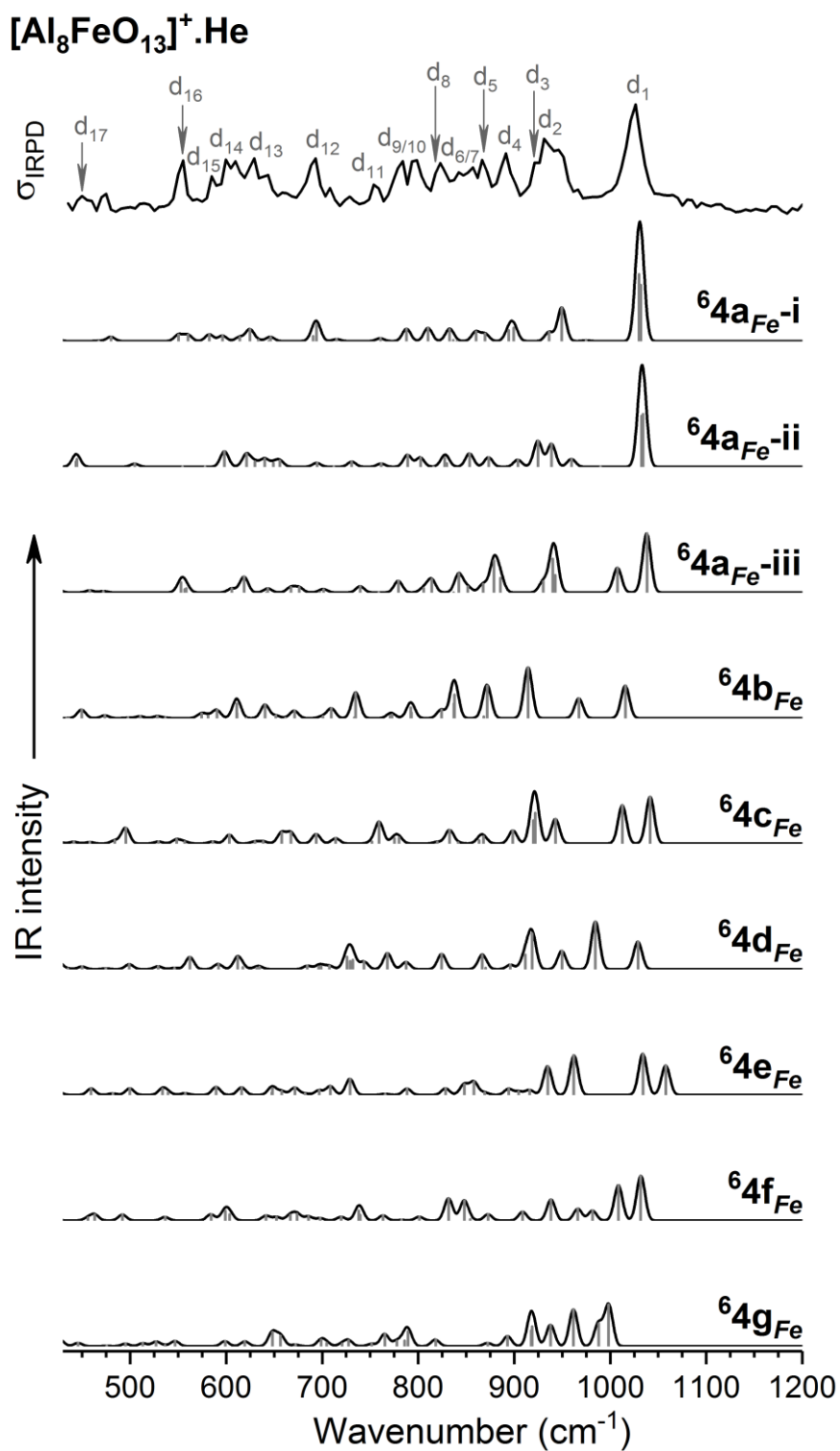


Figure S4. Experimental IRPD spectra of He-tagged $[\text{Al}_6\text{FeO}_{10}]^+$ (top trace) compared with simulated IR spectra (lower traces) of all calculated isomers (${}^{63}\text{a-i}_{\text{Fe}} - {}^{63}\text{f}_{\text{Fe}}$). The calculated IR spectra, derived from TPSSh/def2-TZVP harmonic frequencies (scaled by 1.0166) and intensities are plotted with sticks (gray) and a 10 cm^{-1} FWHM Gaussian line shape convolution. See Fig.S8 for the structures and relative energies of the contributing isomers.

$n=4$



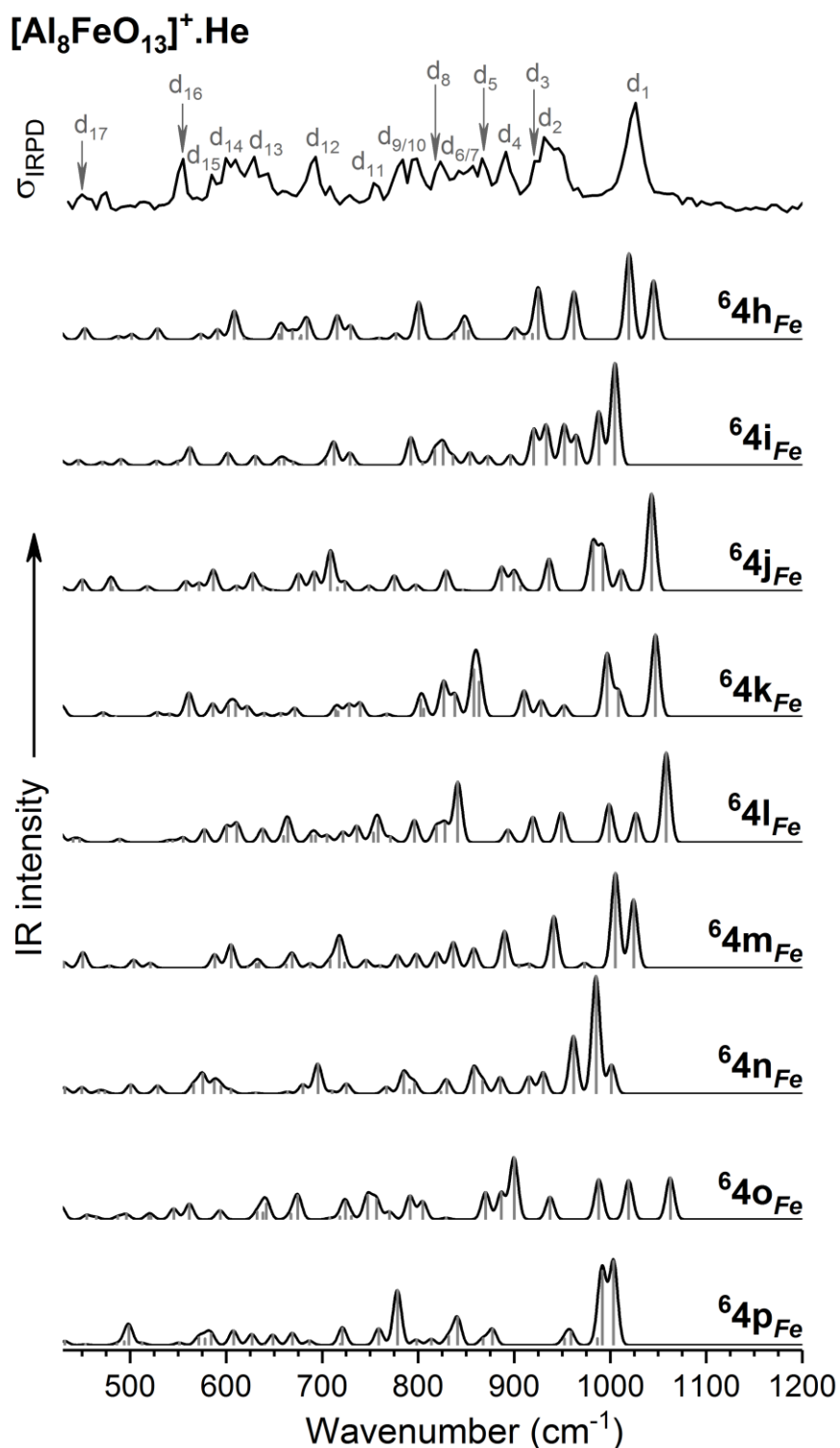
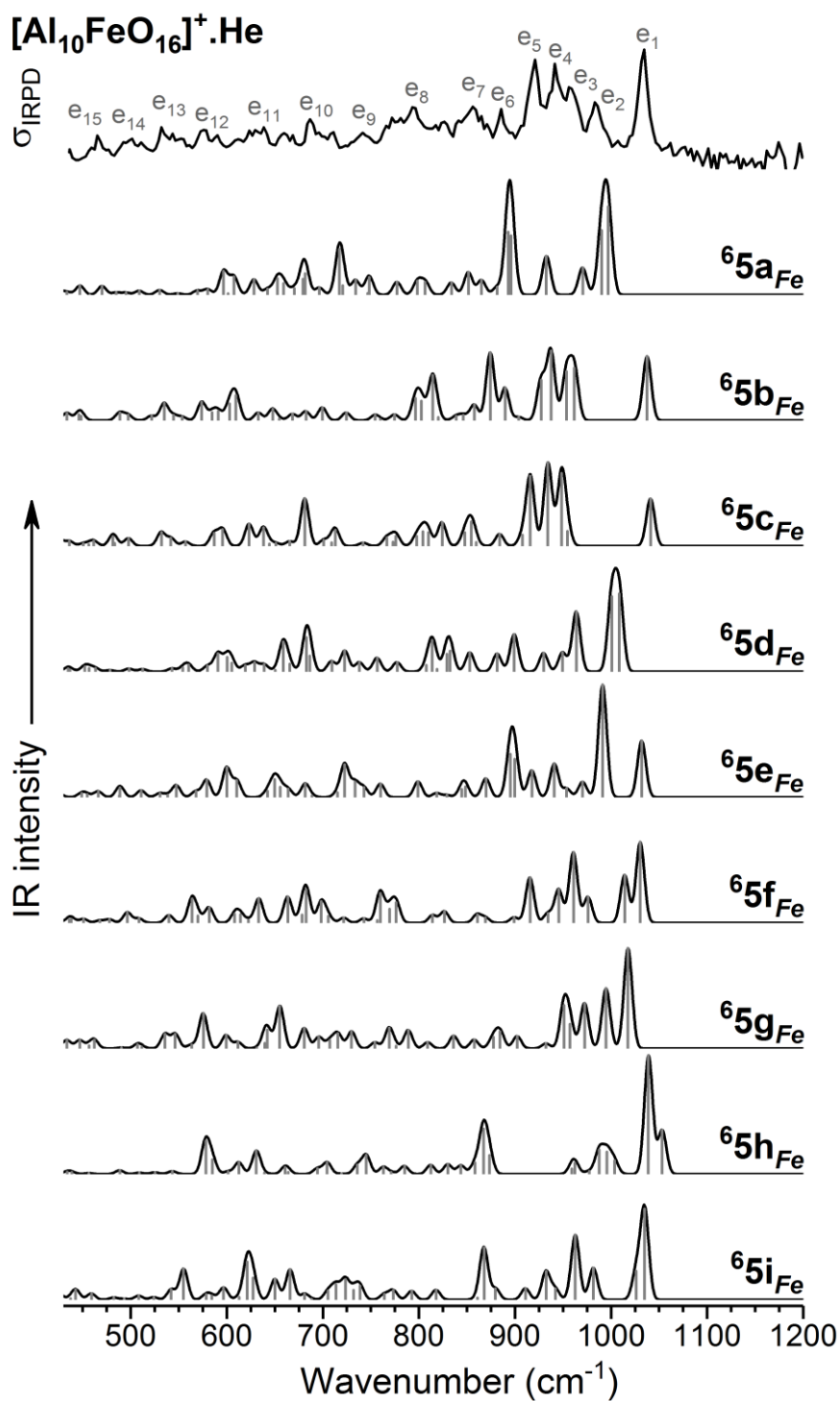


Figure S5. Experimental IRPD spectra of He-tagged (Al₈FeO₁₃)⁺ (top trace) compared with simulated IR spectra (lower traces) of all calculated isomers (^{64a-i}Fe - ^{64p}Fe). The calculated IR spectra, derived from TPSSh/def2-TZVP harmonic frequencies (scaled by 1.0166) and intensities are plotted with sticks (gray) and a 10 cm⁻¹ FWHM Gaussian line shape convolution. See Fig.S8 for the structures and relative energies of the contributing isomers.

$n=5$



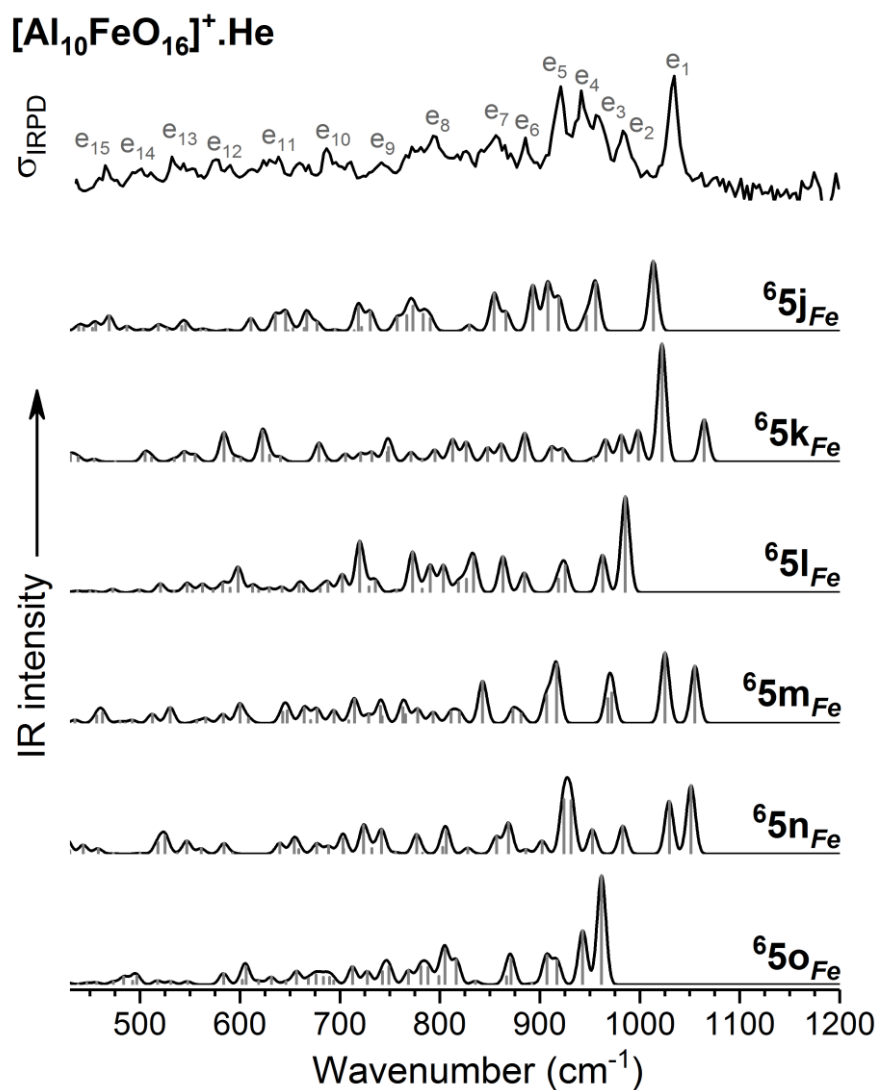


Figure S6. Experimental IRPD spectra of He-tagged $[\text{Al}_{10}\text{FeO}_{16}]^+$ (top panel) compared with simulated IR spectra (lower traces) of all calculated isomers (${}^65\text{a}_{\text{Fe}}$ - ${}^65\text{o}_{\text{Fe}}$). The calculated IR spectra, derived from TPSSh/def2-TZVP harmonic frequencies (scaled by 1.0166) and intensities are plotted with sticks (gray) and a 10 cm^{-1} FWHM Gaussian line shape convolution. See Fig.S8 for the structures and relative energies of the contributing isomers.

Table S1: TPSSh/def2-TZVP Relative Electronic energies ΔE_{DFT} and ZPE-Corrected relative energies $\Delta E_{0,DFT}$ of all calculated isomers of $[(Al_2O_3)_n(FeO)]^+$ ($n=2-5$)

n	Isomer	ΔE_{DFT}	$\Delta E_{0,DFT}$
2	${}^62a_{Fe-i}$	0	0
	${}^62a_{Fe-ii}$	53	52
	${}^62a_{Fe-iii}$	96	95
	${}^62b_{Fe}$	6	5
	${}^62c_{Fe}$	32	31
	${}^62d_{Fe}$	32	32
	${}^62e_{Fe}$	44	44
	${}^62f_{Fe}$	49	48
	${}^62g_{Fe}$	50	49
	${}^62h_{Fe}$	54	53
3	${}^63a_{Fe-i}$	0	0
	${}^63a_{Fe-i}^*$	0	0
	${}^63a_{Fe-ii}$	23	23
	${}^63a_{Fe-iii}$	23	23
	${}^63a_{Fe-iv}$	27	26
	${}^63a_{Fe-v}$	61	59
	${}^63a_{Fe-vi}$	62	61
	${}^63a_{Fe-vii}$	76	74
	${}^63b_{Fe}$	16	16
	${}^63c_{Fe}$	24	24
	${}^63d_{Fe}$	25	24
	${}^63e_{Fe}$	35	35
	${}^63f_{Fe}$	79	77
	4	${}^64a_{Fe-i}$	0
${}^64a_{Fe-ii}$		14	13
${}^64a_{Fe-iii}$		20	20
${}^64b_{Fe}$		47	49
${}^64c_{Fe}$		53	51
${}^64d_{Fe}$		64	63
${}^64e_{Fe}$		65	64
${}^64f_{Fe}$		71	68
${}^64g_{Fe}$		75	74
${}^64h_{Fe}$		81	79
${}^64i_{Fe}$		84	82
${}^64j_{Fe}$		85	83
${}^64k_{Fe}$		88	84
${}^64l_{Fe}$		90	87
${}^64m_{Fe}$		91	89
${}^64n_{Fe}$		91	90
${}^64o_{Fe}$		97	95
${}^64p_{Fe}$	106	104	
5	${}^65a_{Fe}$	0	0
	${}^65b_{Fe}$	10	10
	${}^65c_{Fe}$	18	17
	${}^65d_{Fe}$	26	26

${}^65e_{Fe}$	31	29
${}^65f_{Fe}$	45	42
${}^65g_{Fe}$	80	76
${}^65h_{Fe}$	81	77
${}^65i_{Fe}$	91	88
${}^65j_{Fe}$	89	88
${}^65k_{Fe}$	101	98
${}^65l_{Fe}$	113	113
${}^65m_{Fe}$	129	124
${}^65n_{Fe}$	130	125
${}^65o_{Fe}$	150	150

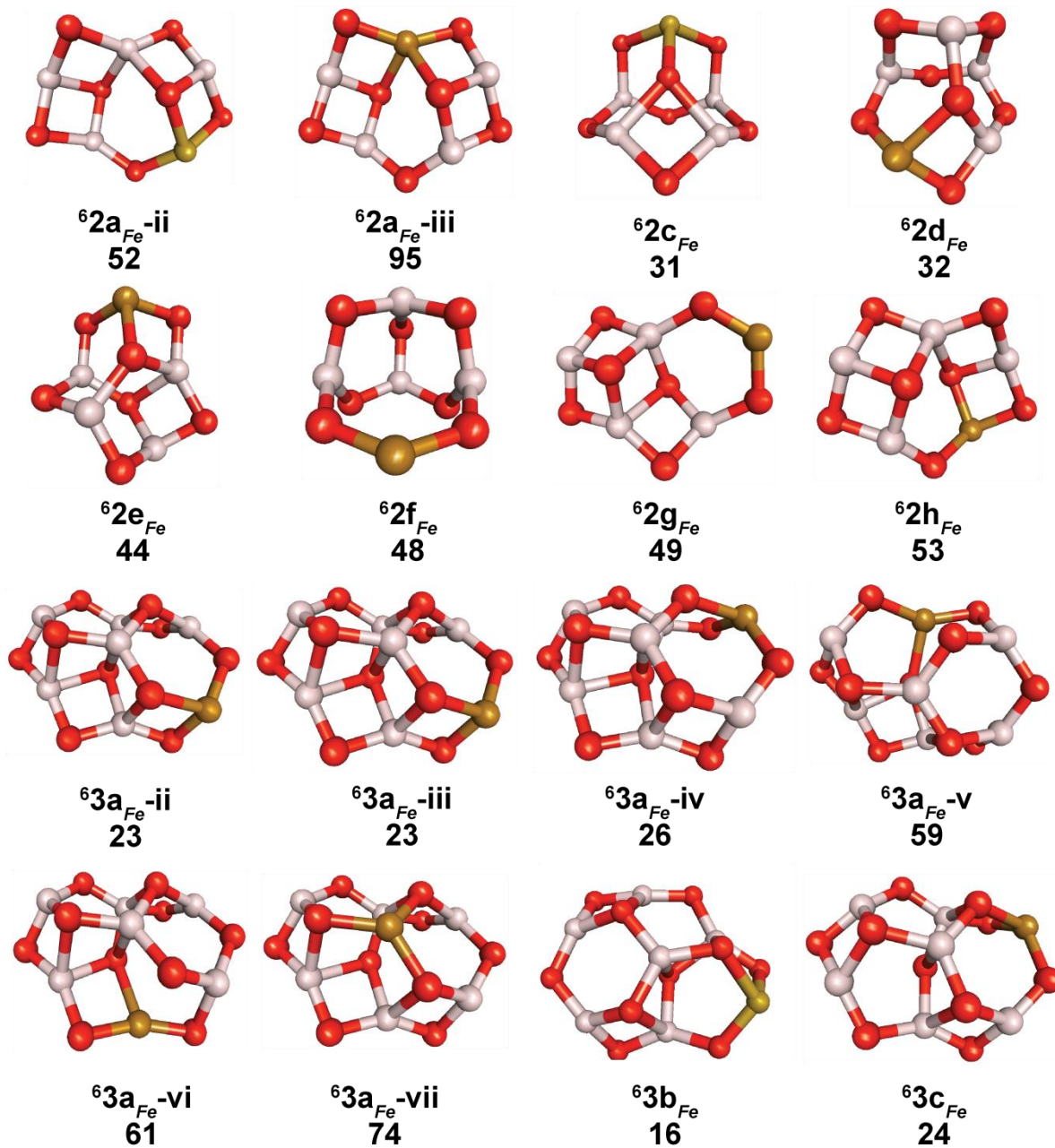
Table S2: Experimental Band Positions (in cm^{-1}) from the IRPD Spectra of He-tagged $[(\text{Al}_2\text{O}_3)_n(\text{FeO})]^+$ ($n = 1-5$), Shown in Figure 1, and TPSSH/def2-TZVP Harmonic frequencies (in cm^{-1}) scaled with 1.0166, of the contributing Isomers as well as Band Assignments

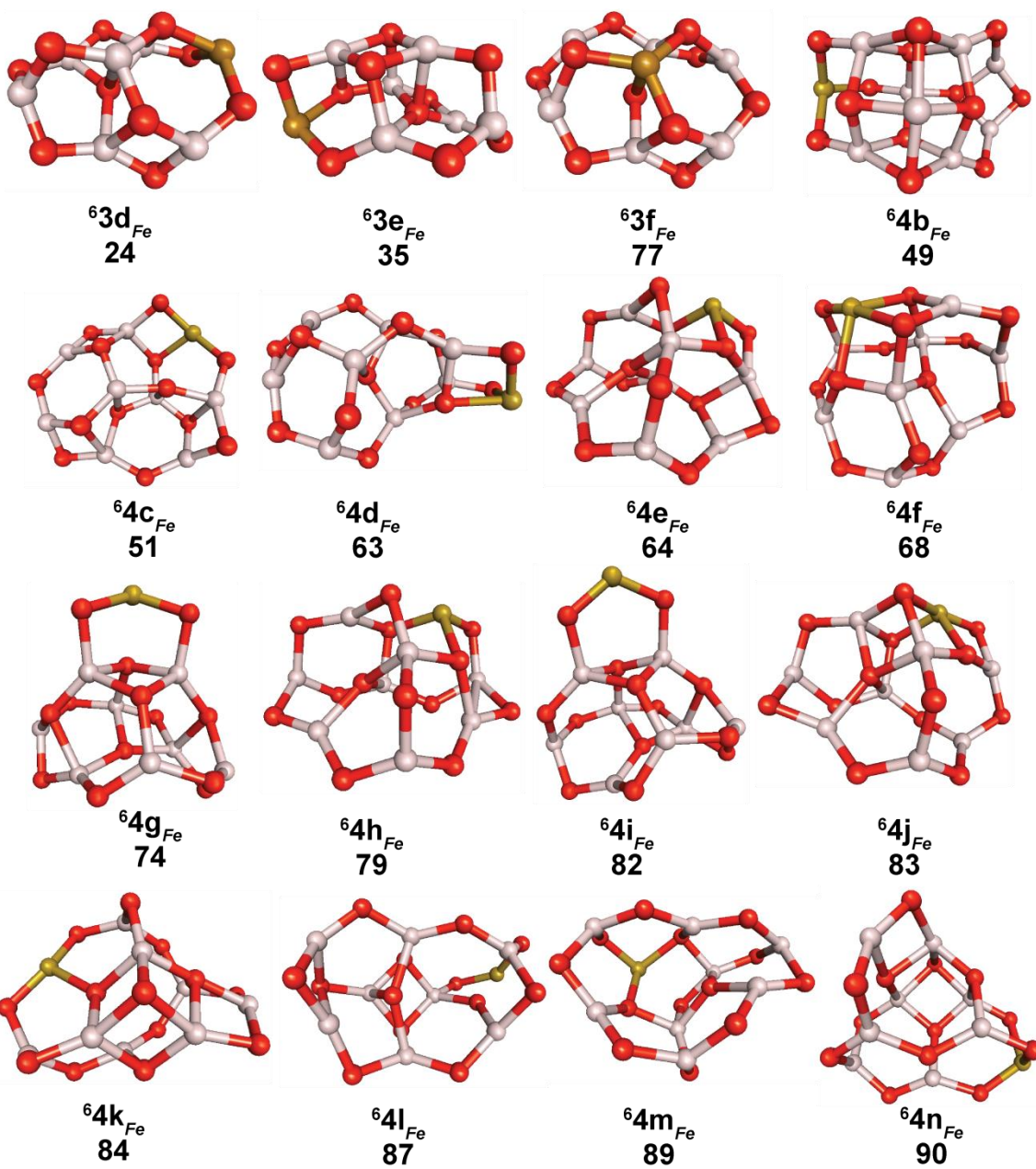
<i>n</i>	experiment	theory	assignment
2	454	438	Framework
	494	490	Al- $\text{O}_{\mu 3}$ stretch
	549	556	Fe- $\text{O}_{\mu 3}$ stretch
	593	599	Al- $\text{O}_{\mu 3}$ stretch
	619	632	Fe- μ_2 -O stretch
	659	663	
	724	718 727	
	739	745	Fe/Al- $\text{O}_{\mu 2/\mu 3}$ -Al stretch
	755	756	
	775	779 829	
	825	854	Al $_{\mu 4}$ -O stretch
	914	923	
	938	952	Al- $\text{O}_{\mu 2}$ -Al stretch
	983	973	
993	998		
3	452	457	Framework
	465	467	
	511	510	

A.1. Supporting Information: Infrared Photodissociation Spectroscopy of $[(Al_2O_3)_nFeO]^+$ with $n = 2-5$:
Influence of Fe-Impurities on Structure and Other Properties

	564	566	FeAl ₂ -O _{μ3} out of plane bend
	582	580	Al ₃ -O _{μ3} out of plane bend
	608	613	Al-O _{μ4} stretch
	696	694	Fe/Al-O _{μ3/μ2}
		701	
	714	714	Fe-O _{μ2} stretch
	757	755	Fe/Al-O _{μ2/μ3} stretch
	784	781	Al _{μ3/μ4} -O stretch
	796	791	
	835	832	Al _{μ4} -O _{μ3} stretch
	856	851	
	886	891	Al _{μ4} -O _{μ2} -Al/Fe stretch
	924	931	Al-O _{μ2} stretch
	938	939	Al _{μ4} -O _{μ2} sym stretch
	953	955	Al _{μ4} -O _{μ2} anti sym stretch
	992	996	Al _{μ3} -O _{μ2} stretch
4	475	443	Framework
	515	480	
	555	549	
		560	
	585	573	Fe/Al-O _{μ2/μ3} stretch
		583	
	600	598	
		615	
	629	624	Al-O _{μ2/μ3} stretch
		647	
		691	
	693	694	
		760	Fe/Al-O _{μ2/μ3} stretch
	754	765	
	784	788	Al-O _{μ2/μ3} stretch
	799	809	
	823	831	Fe/Al-O _{μ2/μ3} stretch
	842	823	
	857	860	Al-O _{μ3} stretch
		870	
	867	874	Al _{μ4} -O _{μ2} -Al _{μ3} stretch
		894	Al/Fe-O _{μ2} stretch
	891	900	Al-O _{μ2/μ3} stretch
		937	
	931	950	Al _{μ4} -O _{μ3} stretch
	1026	1030	Al _{μ3} -O _{μ2} stretch

5	465	447	Framework
	502	488	
		497	Fe/Al-O _{μ3} in plane bend
	532	535	Fe/Al-O stretch
	579	573	Al-O _{μ3} out of plane bend
	639	627	Al-O _{μ3} out of plane bend
	687	717	Fe-O _{μ2} stretch
	741	748	Fe-O _{μ2} -Al _{μ4} stretch
	796	796	
		802	Fe/Al-O stretch
	856	858	Al _{μ4} -O _{μ3} stretch
	886	890	
	921	927	Al _{μ3} -O _{μ2} -Al _{μ4} stretch
	941	937	
	959	954	
		962	Al-O _{μ2} stretch
		990	Al _{μ3} -O _{μ2} stretch
	983	997	Al _{μ4} -O _{μ2} stretch
	1034	1037	Al _{μ3} -O _{μ2} stretch





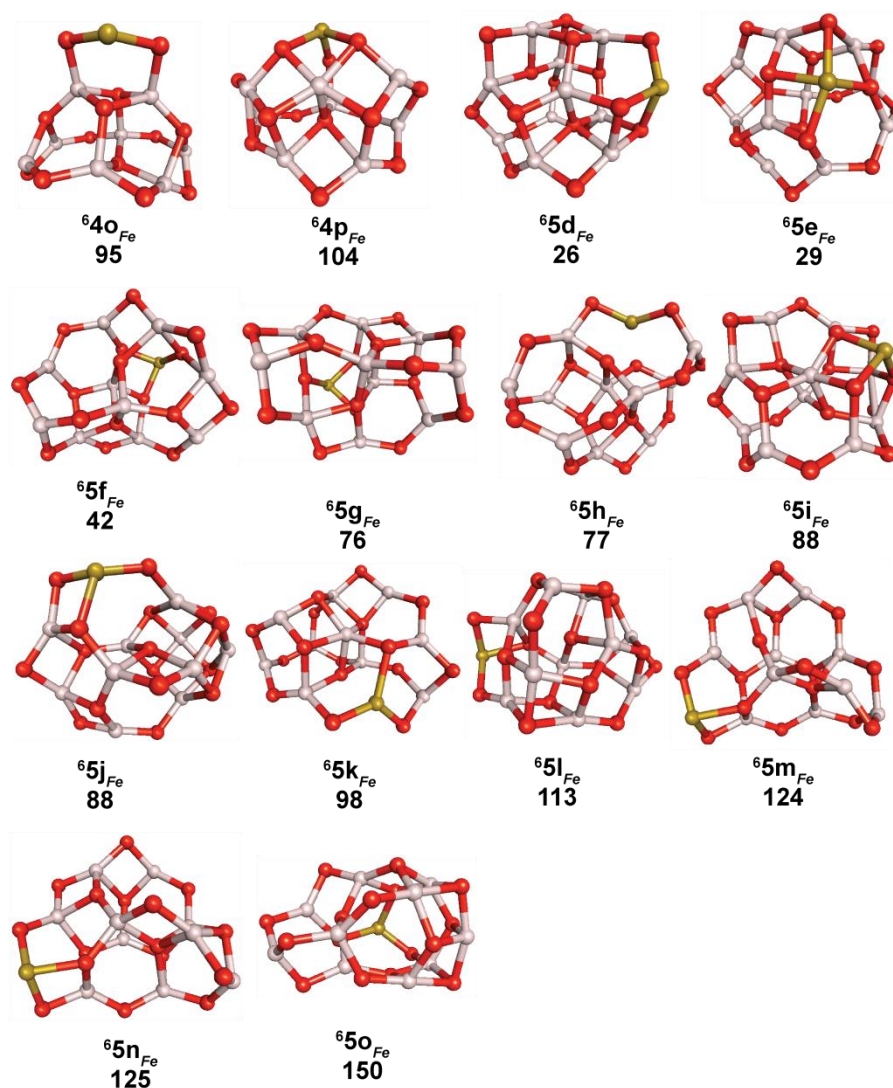


Figure S7. TPSSH/def2-TZVP minimum-energy structures of all the calculated isomers of $[(\text{Al}_2\text{O}_3)_n(\text{FeO})]^+$ ($n=2-5$). The ZPE-corrected DFT energies are given at the bottom. The isomers are labeled with nx , where n is the number of (Al_2O_3) unit and $x = \text{a}, \text{b}, \text{c}, \dots$, which indicates the energetic ordering. Atoms in white= Al, yellow= Fe, red= O.

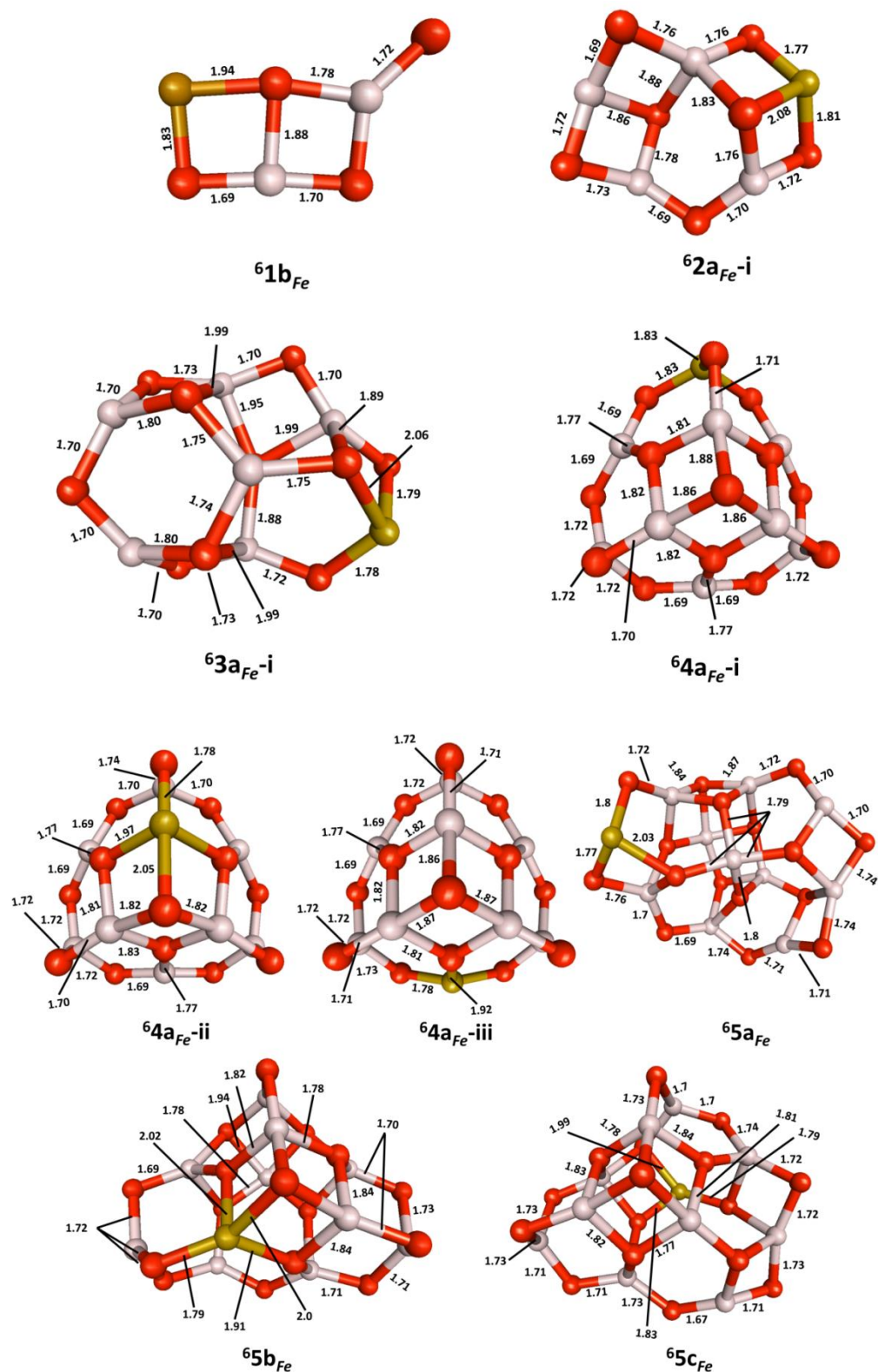


Figure S8. TPSSH/def2-TZVP minimum-energy structures (ball and stick) of low-energy isomers that are found to contribute to the IRPD spectra of $[(\text{Al}_2\text{O}_3)_n(\text{FeO})]^+$ ($n=1-5$).¹ The isomers are labeled with nx , where n is the number of (Al_2O_3) unit and $x = a, b, c, \dots$, which indicates the energetic ordering. Different bond lengths in Å unit are indicated. Atoms in white/blue= Al, yellow= Fe, red= O, and green= He.

Table S3: Cosine score²⁻³ of low energy isomers of $[(Al_2O_3)_n(FeO)]^+$ ($n=2-5$), calculated using equation 1 and 2 from the main manuscript.

n=	Isomer	Score
2	⁶ 2a _{Fe-i}	0.63
	⁶ 2b _{Fe}	0.21
	⁶ 2a _{Fe-i} + ⁶ 2b _{Fe} (80/20)	0.63
	⁶ 2a _{Fe-i} + ⁶ 2b _{Fe} (90/10)	0.64
	⁶ 2a _{Fe-i} + ⁶ 2b _{Fe} (70/30)	0.61
3	⁶3a_{Fe-i}	0.87
	⁶ 3a _{Fe-ii}	0.61
	⁶ 3b _{Fe}	0.55
4	⁶ 4a _{Fe-i}	0.69
	⁶ 4a _{Fe-ii}	0.67
	⁶ 4a _{Fe-iii}	0.68
	⁶4a_{Fe-i} + ⁶4a_{Fe-iii} (50/50)	0.77
	⁶ 4a _{Fe-i} + ⁶ 4a _{Fe-iii} (40/60)	0.77
	⁶ 4a _{Fe-i} + ⁶ 4a _{Fe-iii} (60/40)	0.76
	⁶ 4a _{Fe-i} + ⁶ 4a _{Fe-ii} (60/40)	0.70
	⁶ 4a _{Fe-i} + ⁶ 4a _{Fe-ii} (70/30)	0.70
	⁶ 4a _{Fe-i} + ⁶ 4a _{Fe-ii} (50/50)	0.70
	⁶ 4a _{Fe-ii} + ⁶ 4a _{Fe-iii} (50/50)	0.74
	⁶ 4a _{Fe-ii} + ⁶ 4a _{Fe-iii} (60/40)	0.73
	⁶ 4a _{Fe-ii} + ⁶ 4a _{Fe-iii} (40/60)	0.74
5	⁶ 5a _{Fe}	0.52
	⁶ 5b _{Fe}	0.79
	⁶ 5c _{Fe}	0.80
	⁶5a_{Fe} + ⁶5c_{Fe} (30/70)	0.84
	⁶ 5a _{Fe} + ⁶ 5c _{Fe} (20/80)	0.84
	⁶ 5a _{Fe} + ⁶ 5c _{Fe} (40/60)	0.83
	⁶5a_{Fe} + ⁶5b_{Fe} (30/70)	0.83
	⁶ 5a _{Fe} + ⁶ 5b _{Fe} (20/80)	0.83
	⁶ 5a _{Fe} + ⁶ 5b _{Fe} (40/60)	0.81
	⁶ 5b _{Fe} + ⁶ 5c _{Fe} (50/50)	0.85
	⁶ 5b _{Fe} + ⁶ 5c _{Fe} (60/40)	0.85
⁶ 5b _{Fe} + ⁶ 5c _{Fe} (40/60)	0.85	

References:

1. Fabian Müller, J. B. S., Florian A. Bischoff, Laura Gagliardi, Joachim Sauer, Sreekanta Debnath, Marcel Jorewitz, Knut R. Asmis,. The $[FeAl_2O_4]^+$ radical cation and its ability to activate C-H bonds.
2. Kempkes, L. J. M.; Martens, J.; Berden, G.; Houthuijs, K. J.; Oomens, J. Investigation of the position of the radical in z3-ions resulting from electron transfer dissociation using infrared ion spectroscopy. *Faraday Discussions* **2019**, *217* (0), 434-452.
3. van Outersterp, R. E.; Houthuijs, K. J.; Berden, G.; Engelke, U. F.; Kluijtmans, L. A. J.; Wevers, R. A.; Coene, K. L. M.; Oomens, J.; Martens, J. Reference-standard free metabolite identification using infrared ion spectroscopy. *International Journal of Mass Spectrometry* **2019**, *443*, 77-85.

Appendix B

Fe-Oxides

Experimental Details:

IRPD experiments are conducted using the cryogenic ion trap tandem mass spectrometer described in chapter 3.3. A pulsed beam of cationic iron-oxide clusters is formed by laser vaporization with the source described in Section 3.1. Vaporization is induced by focusing (30 cm focal length) the second harmonic output (532 nm) of a pulsed 50 Hz Nd:YAG laser (Soliton, Nano LG 100-50) onto the surface of a moving Fe-rod target. The ablated plasma is then entrained in a carrier gas pulse of 0.65% O₂ seeded in helium, Fe-oxide clusters Fe_xO_y⁺ are subsequently formed through expansion in a clustering channel ending with a cone shape nozzle held at a temperature of 270 K. In order to obtain a stable cluster signal, the turning speed of the rod is set to ~3 turns per minute and laser pulse energies of up to 7 mJ are applied. Using a backing pressure of ~4.5 bar, Fe_xO_y⁺ clusters are efficiently produced in the mass range from 40 to 600 amu (see Fig.B.2.1). The time delay between laser Q-switch and opening of the pulsed valve is optimized to enhance the formation of the clusters of interest. In order to form Fe-oxide/water complexes, a flow of helium at 1.5 bar passes through a bubbler containing H₂O at room temperature (294 K). Water vapour mixes with He and the gas mixture is injected with the second pulsed valve in the source block expanding through the separated gas channel. Fe_xO_y⁺(H₂O)_n complexes with $n \leq 5$ are efficiently formed. The beam of ions passes a 4 mm diameter skimmer, is then collimated in a RF buffer-gas-filled decapole ion-guide and ions of interest are selected according to their mass/charge ratio using a quadrupole mass-filter. The mass-selected beam is focused into a cryogenically-cooled RF ring electrode ion-trap. The trap is continuously filled with He- buffer gas at a trap temperature of 14 K, which allows for the accumulation and thermalization of the trapped ions. Inside the ion trap, ions undergo three-body collisions with the buffer gas, which promote the formation of weakly bound ion-He complexes. After an ion trap fill time of 199 ms all ions are extracted from the ion trap and focused in the center of the extraction region of TOF mass spectrometer, where they are irradiated by an intense and wavelength-tunable IR laser pulse. When resonant with a vibrational transition, the parent ions can absorb a photon, eventually leading to loss of one or more messenger molecules via intramolecular vibrational predissociation. For the larger water complexes ($n \geq 2$) ion-messenger complex formation is not efficient and the vibrational spectra are measured via IRMPD. For the lower-energy spectral range (1800-300 cm⁻¹), the FHI FEL was used and the OPO/OPA laser, operating at 10 Hz, provided access to frequencies ranging from 4000-3000 cm⁻¹. The infrared photodissociation cross sections σ_{IRPD} is obtained as described in Section 3.4. The IRMPD vibrational spectrum is obtained monitoring the fragment originated by the loss of first H₂O molecule. Each spectrum is averaged over at least 60 measurements.

B.1. Structure and Reactivity of Mixed Valence Fe-Oxides, Fe_3O_3^+ and Fe_4O_5^+ : Towards Water

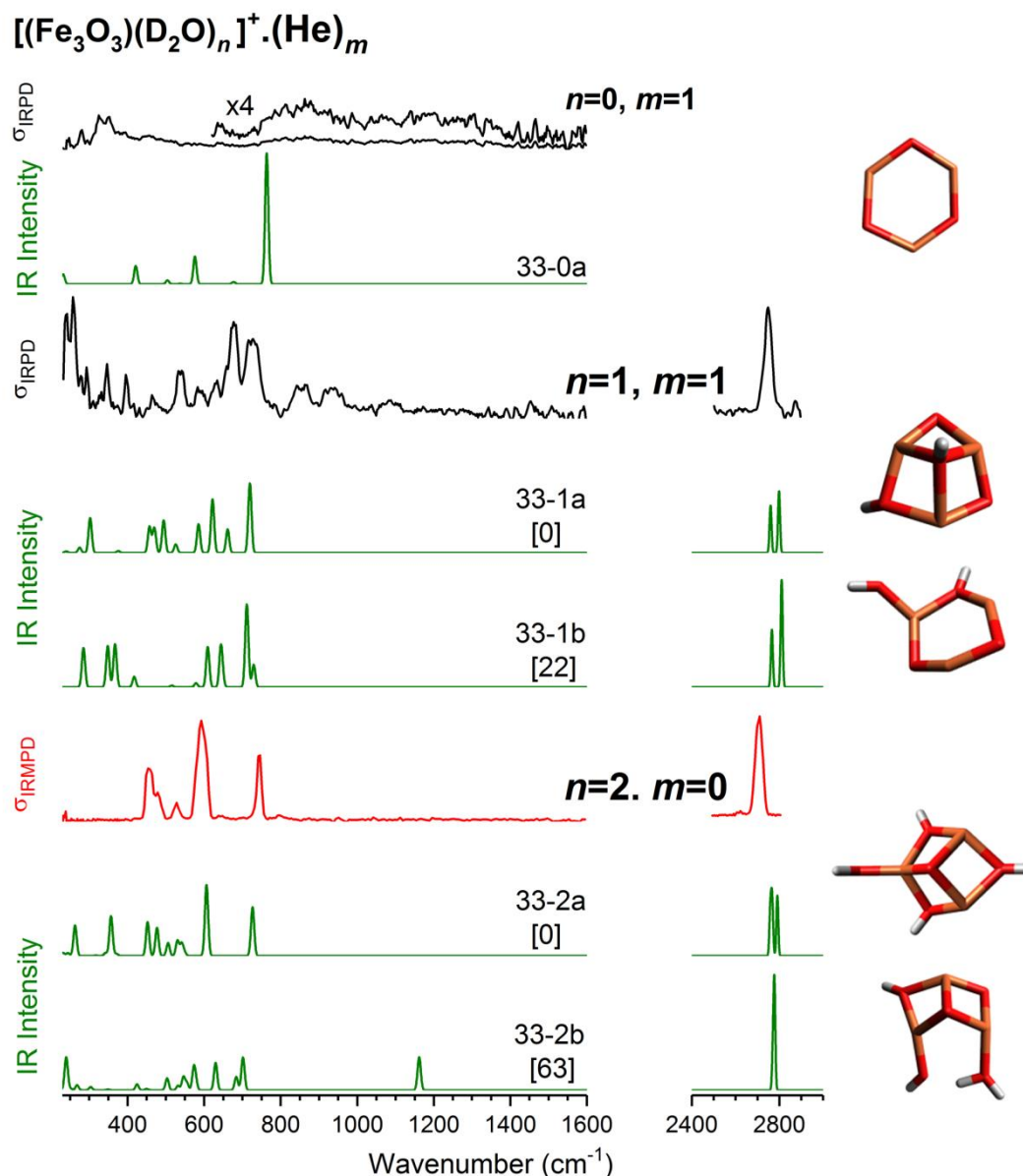


Figure B.1.01. Experimental IRPD spectra of He-tagged (black)/ untagged (red) $[(\text{Fe}_3\text{O}_3)(\text{D}_2\text{O})_n]^+$ ($n=0-2$) compared with simulated IR spectra (green) of the lowest-energy isomers. The calculated IR spectra, derived from TPSSh/def2-TZVP harmonic frequencies (not scaled) and intensities are plotted with 10 cm^{-1} fwhm Gaussian line shape convolution. Isomers are labelled with xy-nm, where x is the number of Fe atoms, y number of oxygen atoms, n number of water molecules and m = a, b,..., indicates energetic ordering of the isomers. DFT calculated relative energies are given in the parenthesis bottom to the isomer labelling. (Fe: Brown, O: Red, H: White)

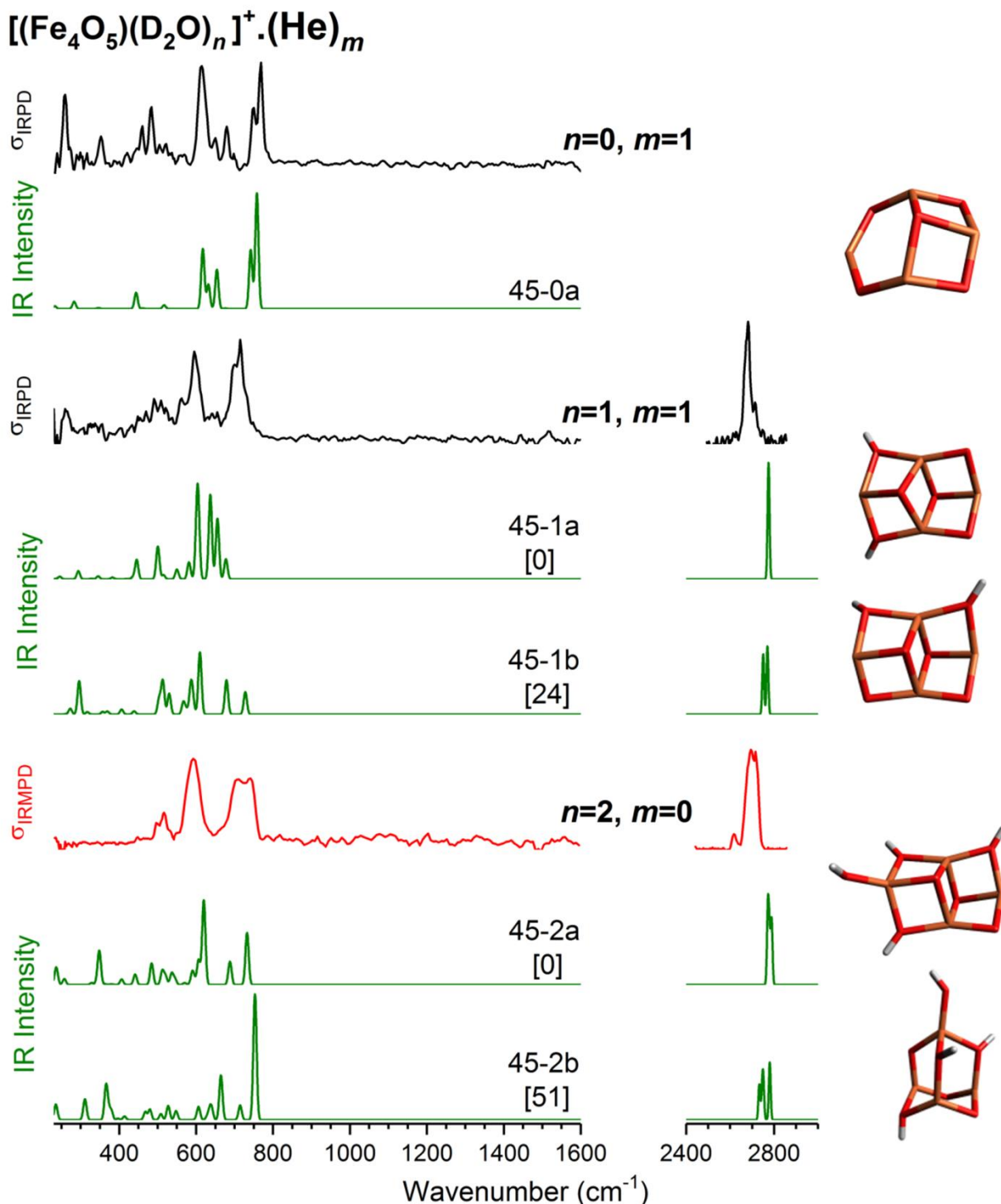


Figure B.1.02. Experimental IRPD spectra of He-tagged (black)/ untagged (red) $[(\text{Fe}_4\text{O}_5)(\text{D}_2\text{O})_n]^+$ ($n=0-2$) compared with simulated IR spectra (green) of the lowest-energy isomers. The calculated IR spectra, derived from TPSSh/def2-TZVP harmonic frequencies (not scaled) and intensities are plotted with 10 cm^{-1} fwhm Gaussian line shape convolution. Isomers are labelled with xy-nm, where x is the number of Fe atoms, y number of oxygen atoms, n number of water molecules and m = a, b, ..., indicates energetic ordering of the isomers. DFT calculated relative energies are given in the parenthesis bottom to the isomer labelling. (Fe: Brown, O: Red, H: White).

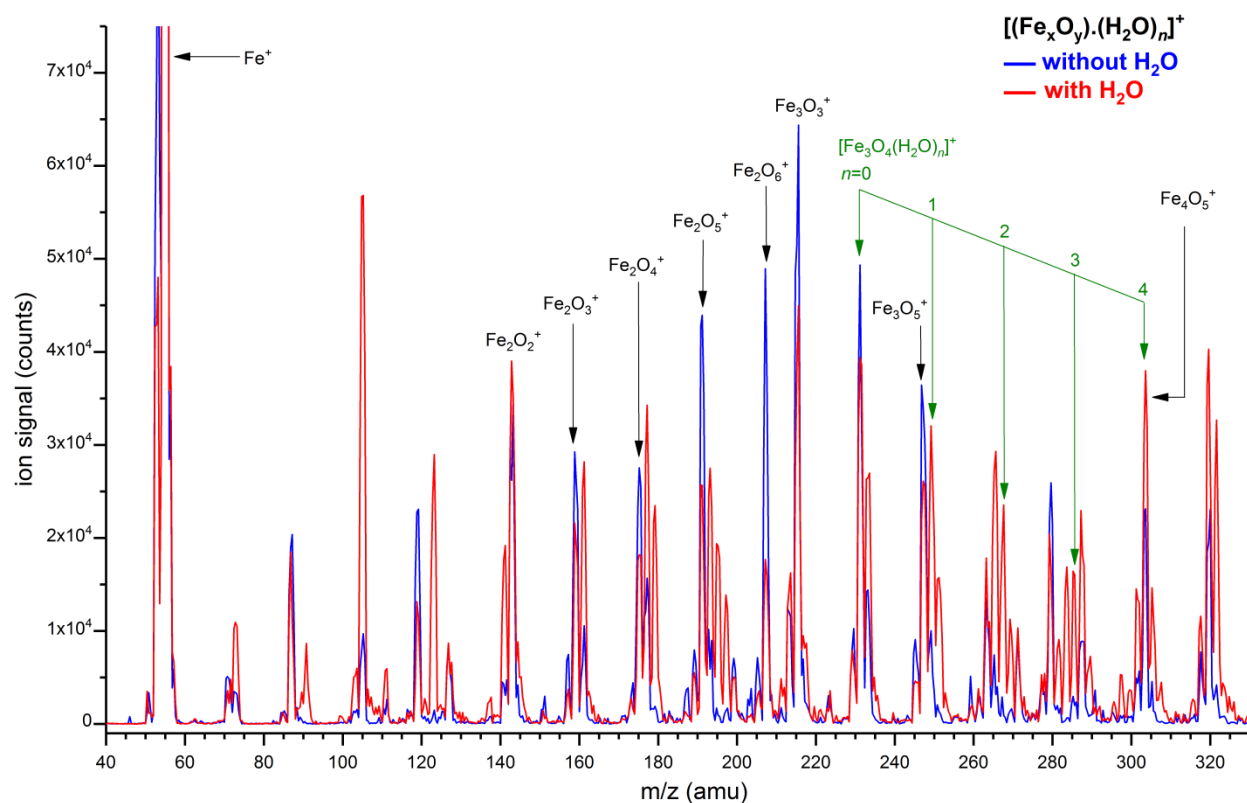
B.2. $\text{Fe}_3\text{O}_4 \cdot (\text{H}_2\text{O})^+_{n=0-4}$ 

Figure B.2.01. Quadrupole mass spectrum of the ions produced by pulsed laser vaporization of a pure Fe metal rod and quenching in a gas pulse of 0.65 % O₂ seeded in He. Pure H₂O was added from the second gas channel of the source block to get H₂O adsorbed product.

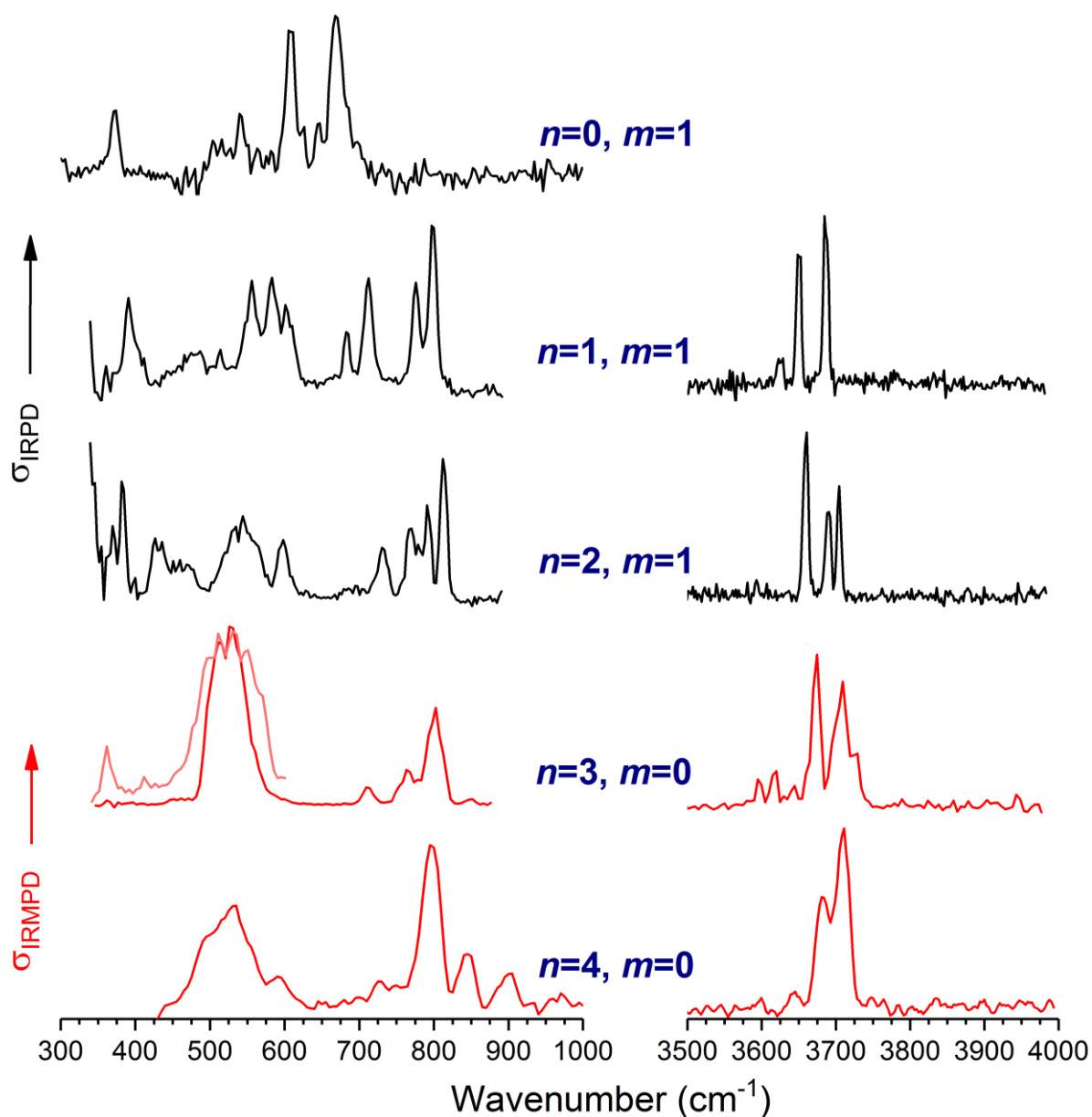


Figure B.2.02. Experimental IRPD spectra of He-tagged (black)/untagged (red) $[(Fe_3O_4)(H_2O)_n]^+$ ($n=0-4$) clusters. He-tagging of $n=3$ and 4 clusters were not achieved, so their IR spectra is generated looking at the first H_2O depletion channel.

Appendix C

Microhydration of Salts

Experimental Details:

IRPD experiments are performed using a cryogenic ion trap tandem mass spectrometer described in the chapter 3.3. In brief, microhydrated magnesium nitrate cations $[\text{MgNO}_3 \cdot (\text{H}_2\text{O})_n]^+$ / iron-hydroxy-chloride cations $[\text{Fe}(\text{OH})(\text{Cl}) \cdot (\text{H}_2\text{O})_n]^+$ are continuously generated in a modified Z-spray ionization source (see chapter 3.2) using a 10 mM aqueous solution of magnesium nitrate / $\text{FeCl}_3 \cdot 6\text{H}_2\text{O}$ salt in pure distilled water. Formed ions pass through a 4-mm diameter skimmer and are collimated in a radio frequency (RF) decapole ion-guide. The ions are then mass-selected with a quadrupole mass-filter, deflected 90° by an electrostatic quadrupole deflector, and focused into a cryogenic RF ring-electrode ion trap. The trap is continuously filled with a buffer gas mixture, either He- or 10% D_2 and held at 10K (when pure He- is used) or 18 K (when 10% D_2 is used) depending on the used buffer gas, which allows for the accumulation and thermalization of the trapped ions. At sufficiently low ion-trap temperatures, ion-messenger complexes are formed via three-body collisions. The ions are accumulated in the trap either for 100 ms or 200 ms, depending on the IR laser used, then extracted and focused both temporally and spatially into the extraction region of an orthogonal time-of-flight (TOF) mass spectrometer. Here, the ions are irradiated with a counter-propagating IR laser pulse generated either by the FHI FEL (described in section 3.5) or a table-top OPO/OPA laser system. For the lower-energy spectral range ($1800\text{-}300\text{ cm}^{-1}$), the FHI FEL was used and the OPO/OPA laser, operating at 10 Hz, provided access to frequencies ranging from $4000\text{-}3000\text{ cm}^{-1}$. In both energy regions, the laser beam was attenuated in order to minimize multi-photon excitation. Following the interaction with the IR laser pulse, all parent and photofragment ions are accelerated towards a microchannel plate detector and monitored as a function of irradiated wavelength. IRPD scans are recorded by averaging over 100 time-of-flight mass spectra per wavelength step (3 cm^{-1} for both the FHI FEL and the OPO/OPA system). Typically, at least three scans are summed to obtain the final IRPD spectrum. The IRPD cross section, σ_{IRPD} , is obtained as described in section 3.4.

C.1. Infrared Spectroscopic Snapshots of MgNO_3 Solvation in Water: $[\text{MgNO}_3 \cdot (\text{H}_2\text{O})_n]^+$

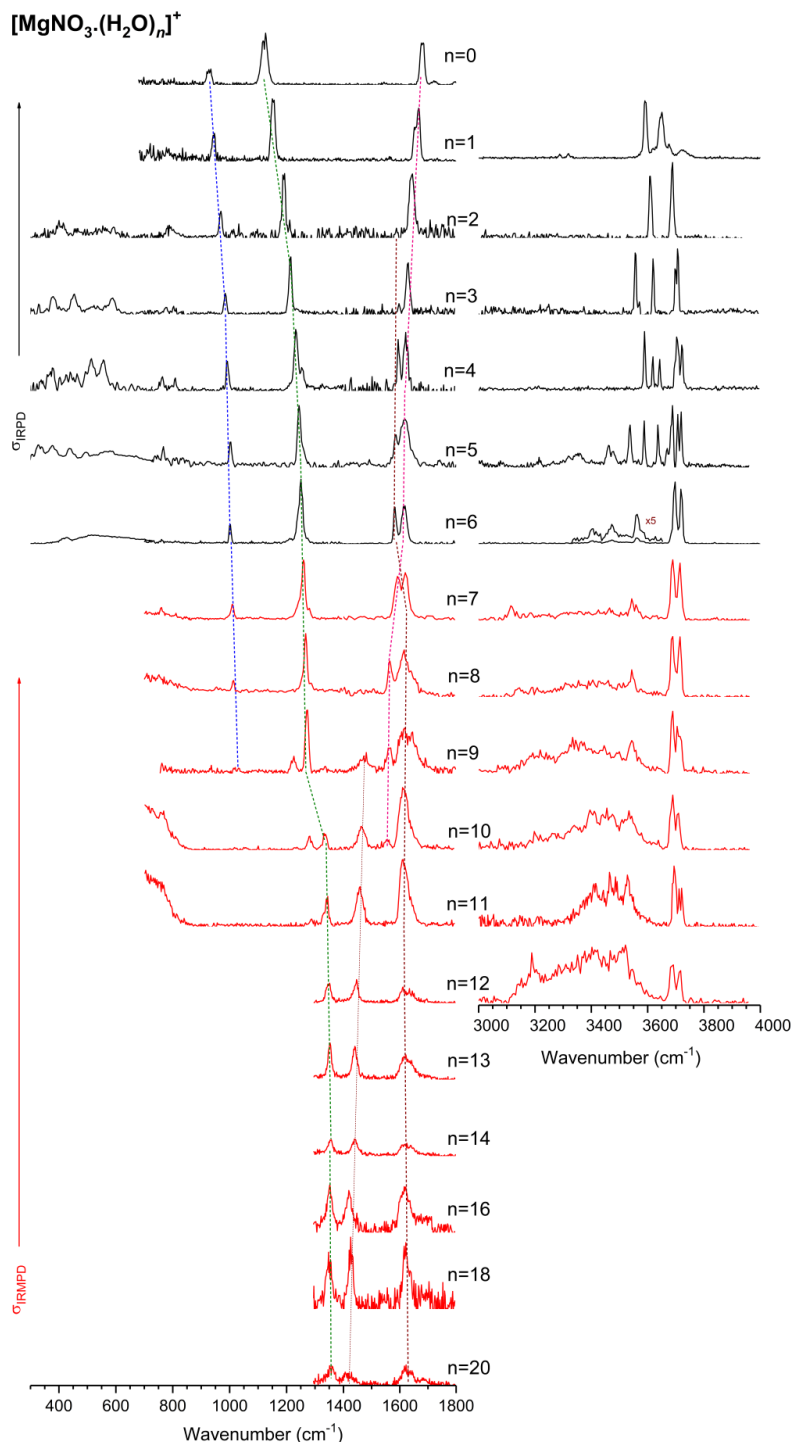


Figure C.1.01. Experimental IRPD spectra of $[(\text{MgNO}_3) \cdot (\text{H}_2\text{O})_n]^+$ clusters. For $n=0, 1$ He-tagging was possible, D_2 tagging could be achieved for $n=2-6$ clusters, rest of the others showed very tiny tagging efficiency. Accordingly, IRPD spectra (black) was measured for $n=0-6$ clusters looking at the depletion of the tag and for $n=7-20$ IRMPD spectra (red) was measured looking at the first H_2O depletion channel.

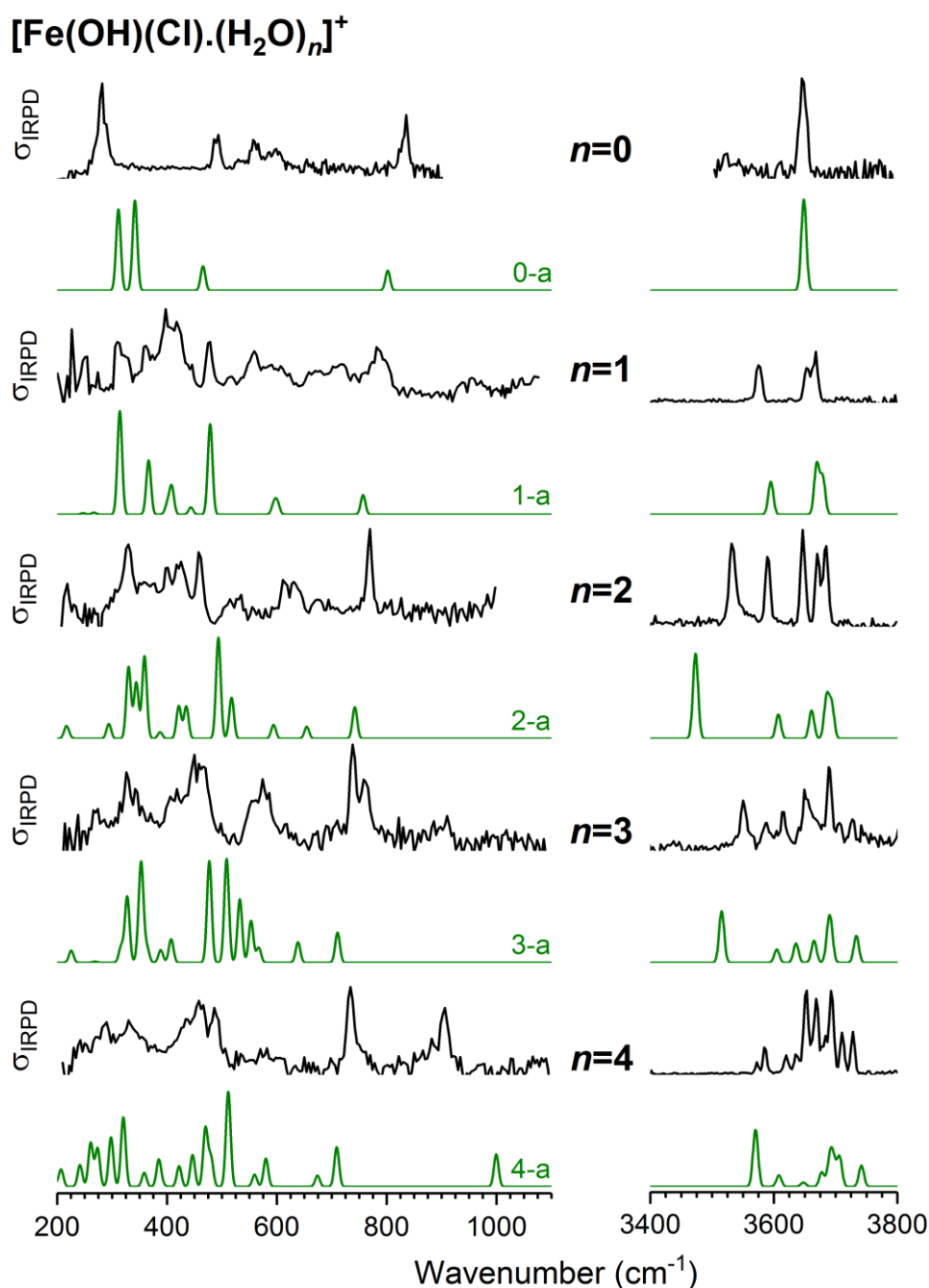
C.2. $[\text{Fe}(\text{OH})(\text{Cl})\cdot(\text{H}_2\text{O})_n]^+$ 

Figure C.2.01. Experimental IRPD spectra of He- ($n=0$) /D2- ($n=1-4$) tagged $[(\text{Fe})(\text{OH})(\text{Cl})(\text{H}_2\text{O})_n]^+$ ($n=0-4$) (black) compared with the simulated IR spectra (green) of the lowest-energy isomer. The calculated IR spectra, derived from TPSSh/aug-cc-pVTZ harmonic frequencies and intensities are plotted with 10 cm^{-1} fwhm Gaussian line shape convolution. Isomers are labelled with $n-x$, where n is the number of H_2O molecules and x indicates energetic ordering of the isomers. Presented calculated spectra are not scaled in the $200-1100 \text{ cm}^{-1}$ region, but $3400-3800 \text{ cm}^{-1}$ region is scaled with a factor of 0.971. See Figure E.02 for the structure of the isomers.

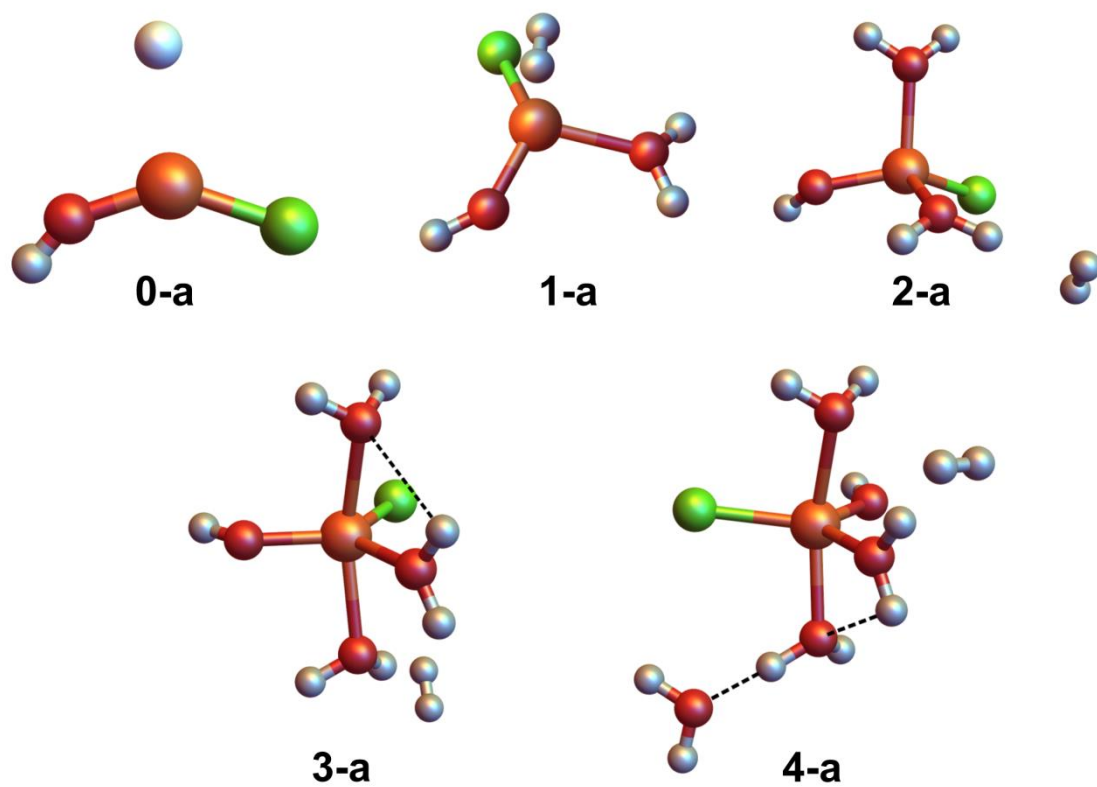


Figure C.2.02. TPSSh/aug-cc-pVTZ minimum-energy structures of all the calculated isomers of $[(\text{Fe})(\text{OH})(\text{Cl})(\text{H}_2\text{O})_n]^+$ ($n=0-4$). (Fe: Brown, O: Red, H: White, Cl: Green)

Acknowledgements

I would like to take this opportunity to thank all the people who have contributed to this thesis in one way or the other. Biggest thank goes to my supervisor Knut Asmis for his help, support, encouragement and fruitful discussions from the very first day. He had already moved as a professor at the University of Leipzig before I joined the group in Berlin. Despite having related responsibilities there, he always managed to come to Berlin at least once in a week. This helped me to discuss things in person and I never felt separated from the group. I also want to thank you Knut because you never failed to show the hope of ray with your patience and guidance whenever I needed during hard times with the experiments and related things in the lab. Moreover, thank you for believing in me that I can single-handedly manage to run the experiments after Matias and Xiaowei finished their tenure.

I also want to express my gratitude to Gerard Meijer, director of the MP department Fritz-Haber-Institute, for giving me the opportunity to work here. One of my batch mates from my master's studies was a summer intern at the theory department of the FHI. When he came to know that I got the chance to work here, I'm quoting what his words were: "I would dream to pursue my PhD at that institute". After spending five years at the department I can certainly say that the FHI is one of the best places in the world to pursue a scientific career. The friendly working atmosphere is a big plus for the excellent science and scientist the MP department is continuously producing.

When I joined the lab, my knowledge about gas phase experiments, mass spectrometry, vibrational spectroscopy and experience of handling vacuum systems and Lasers were rather limited. I wish to express my heartfelt gratitude and sincere thanks to Matias and Xiaowei, who introduced me to the experimental set-up, explained me how to operate it, supervised my first projects and more importantly patiently answered my stupid questions. I would like to mention this small anecdote here: before my arrival I was looking for accommodations in Berlin. That time, I had sent an email to Matias with the convenient flats (around 15-20 flats at different location) I found online, and asked him which one will be reasonable to rent. In a day or two, I got a reply from him with the details of the locations and approx. time it will take every day to commute to the lab from each place. Now, I feel embarrassed when I think how much of a pain I caused back then. I am extremely grateful to both of you for your supports in the lab. I rather enjoyed the insane amount of hours we spent together in the lab during beam-times than getting stressed. Thanks also to Yake. In this short overlap time, we worked together on many projects and finally managed to be productive despite of having some stressful time. I wish you good luck for your future jobs you are looking for. I would like to acknowledge the assistance from Harald and Marcel for the productive projects we worked on together. Special thanks to Harald for the codes you wrote, which helped me a lot to workup and analyse the data. Martin, thank you too for the productive discussions, in particular the ones regarding writing the thesis. Benjamin, Max, Sonja, Arghya, Alexandra and Manuela, although we did not spent much in the lab or at the coffee

room, still I was always happy to see you around whenever I was at the University, and thank you for the nice times we shared together. Max, my best wishes for you to win the next group table tennis championship. Jürgen, thank you too for the technical supports and I specially appreciate the Leipzig tour you gave. Tim and Harald you deserve a special mention for being more than just colleagues. I wish you all the very best for your future.

This thesis would not have been completed without the data I measured using the Fritz-Haber-Institute Free-electron laser. I want to express my gratitude to all the people of the FEL team: Sandy, Wieland, Heinz and the new member Marco. Special thanks to Sandy, for tuning the laser to our needs. Wieland, saying a thank you is not enough to your efforts for uncountable late night shifts and the help for translating the summary of this thesis in German. I have always enjoyed explaining you what system we are studying and why it is important, it's always nice to have a patient listener like you for a novice PhD student. Having the electronic and mechanical workshop with excellent engineers was a big bonus point and I want to express my sincere thanks to the colleagues from there. In particular, Thorsten Nemes, Patrick Jäckel, Harald Fischer and Nicolai Große, thanks for your kind behavior and understanding of the urgency of a repair or a new part to be made.

I'm also grateful to all the MPer's of the FHI. The BBQ parties, after-work beer parties and many other events which turned out to be great social evenings, gave a healthy and friendly atmosphere to the workplace. Sincere thanks to Inga, Andrea, Karin, Evelyn and Manuela for organising the department and supporting in every kind of administrative works. Stephan Schlichting, thank you for organising the gas bottles and ordering the required chemicals. Sebastian Kray, thanks for your helping hands during reorganising the lab after renovation of the basement. Heba, Nicole and Klaus Peter I will surely miss our lunch times seating at the terrace. You are and will be more than just colleagues to me.

I would like to convey my special thanks to Sandra Tamminga from the administration of FHI for her efforts to get me several appointments at the *ausländerbehörde*. Carmen, thank you in particular for giving values to my photographs and organising to hang them at the reception area. I want to express my sincere gratitude for Kerstin Schleinitz (secretary, Wilhelm-ostwald-institute), for the help in all kind of administrative works.

I consider myself fortunate to have many excellent theoretical and experimental collaborators, the group of Joachim Sauer (Humboldt University), the group of Daniel Neumark (University of California, Berkeley), the group of Helmut Schwarz (TU Berlin), the group of Andrey Lyalin (NIMS Japan) and the group of Ling Jiang (Chinese Academy of Sciences). My sincere thanks to all the people involved in producing the high quality works.

I'm also grateful to all my friends in India and here in Germany. Bedvit Da, Kuntal, Shubhadeep, Akash, Anubhab, Shalini, Pallavi thank you all for the nice time we

spent together in the weekends to get refreshed for a new start of the week. Achintya da special thanks to you for finding time to read the chapters of this thesis and giving helpful suggestions.

Next the person without whom this scientific journey would not have been possible: My chemistry teacher Naba Kumar Bera, whose magical teaching made the physical chemistry interesting to me, thanks for your support and encouragements. Thanks for everything. You always have been the friend-philosopher and guide for me.

And then, the very special person who was always there besides me for the last 10 years in every ups and downs, but was never tired of me. Ankita, you endured all my work related stress and complained only a little. I am happy to have you by me and would like to thank you for all the care, support and love.

Finally, I fail to put into words the enormous support I received from my family. My parents and my brother you have supported me throughout my whole life, I can always rely on you and thank you for giving me a wonderful family.

আজ থেকে প্রায় বছর ৪০ আগে, সদ্য বিভক্ত বাংলাদেশ থেকে ভারতবর্ষের পূর্ব প্রান্তে একটা ছোট গ্রামে নিজের দিদির বাড়ি বেড়াতে আসে একটি ছেলে। ১৮ বছর বয়সের সেই ছেলেটার ভালো লেগে যায় সেই গ্রামের ই স্কুল পড়ুয়া একটি মেয়েকে। অদ্ভুতের নিয়মে মেয়েটিও পছন্দ করে ফেলে ছেলেটিকে। ভাগ্যিস সেদিন সেই ছেলেটির বেড়াতে আসা সার্থক হয়েছিল, তাই আজ আমি বসে এই খিসিস লিখতে পাড়ছি। ছেলেটি আমার বাবা, আর বলা বাহুল্য, মেয়েটি আমার মা। গ্রামটার নাম বসিরহাট। ৪০ বছর আগের সেই দিনটার জন্য আমি তোমাদের কাছে কৃতজ্ঞ। এভাবেই পাশে থেকে সবসময়।

List of Publications

Papers Included in This Thesis

1. S. Debnath, X. Song, M. R. Fagiani, M. L. Weichman, M. Gao, S. Maeda, T. Taketsugu, W. Schöllkopf, A. Lyalin, D. M. Neumark, K. R. Asmis, *CO₂ Adsorption on Ti₃O₆⁻: A Novel Carbonate Binding Motif*, Article in *The Journal of Physical Chemistry C*, 2019, **123**, 8439–8446.
2. S. Debnath, H. Knorke, W. Schöllkopf, S. Zhou, K. R. Asmis, H. Schwarz, *Experimental Identification of the Active Site in the Heteronuclear [AlVO_x]⁺/CO/N₂O (x = 3, 4) Redox Couples by Gas-Phase IR Spectroscopy*, Communication in *Angewandte Chemie International Edition*, 2018, **57**, 7448–7452 (VIP paper).
3. Y. Li, S. Debnath, M. Schlangen, W. Schöllkopf, K. R. Asmis, H. Schwarz, *Direct Identification of Acetaldehyde Formation and Characterization of the Active Site in the [VPO₄]^{•+}/C₂H₄ Couple By Gas-Phase Vibrational Spectroscopy*, Communication in *Angewandte Chemie International Edition*, 2019, **58**, 18868–18872.

Papers Not Related to This Thesis

4. J. A. DeVine, S. Debnath, Y. Li, L. M. McCaslin, W. Schöllkopf, D. M. Neumark, K. R. Asmis, *Infrared photodissociation spectroscopy of D₂-tagged CH₃CO₂⁻·(H₂O)₀₋₂ anions*, Article in *Molecular Physics*, (in press).
5. M. L. Weichman, S. Debnath, J. T. Kelly, S. Gewinner, W. Schöllkopf, D. M. Neumark, K. R. Asmis, *Dissociative water adsorption on gas-phase titanium dioxide cluster anions probed with infrared photodissociation spectroscopy*, Article in *Topics in Catalysis*, 2018, **61**, 92-105.
6. X. Song, M. R. Fagiani, S. Debnath, M. Gao, S. Maeda, T. Taketsugu, S. Gewinner, W. Schöllkopf, K. R. Asmis, A. Lyalin, *Excess Charge Driven Dissociative Hydrogen Adsorption on Ti₂O₄⁻*, *Physical Chemistry Chemical Physics*, 2017, **19**, 23154-23161.
7. M. R. Fagiani, X. Song, S. Debnath, S. Gewinner, W. Schöllkopf, K. R. Asmis, F. A. Bischoff, F. Müller, J. Sauer, *Dissociative Water Adsorption by Al₃O₄⁺ in the Gas Phase*, Letter in *The Journal of Physical Chemistry Letters*, 2017, **8**, 1272-1277.

8. M. R. Fagiani, X. Song, P. Petkov, S. Debnath, S. Gewinner, W. Schöllkopf, T. Heine, A. Fielicke, K. R. Asmis, *Structure and Fluxionality of B_{13}^+ Probed by Infrared Photodissociation Spectroscopy*, Communication in *Angewandte Chemie International Edition*, 2017, **56**, 501-504 (Cover).
9. M. L. Weichman, X. Song, M. R. Fagiani, S. Debnath, D. M. Neumark, K. R. Asmis, *Gas Phase Vibrational Spectroscopy of Cold $(TiO_2)_n^-$ ($n=3-8$) Clusters*, Article in *The Journal of Chemical Physics*, 2016, **144**, 124308.

Submitted Papers

1. J. Warneke, M. Mayer, M. Rohdenburg, X. Ma, J. K. Y. Liu, M. Grellmann, S. Debnath, V. A. Azov, E. Apra, R. P. Young, C. Jenne, G. E. Johnson, H. I. Kenttämaa, K. R. Asmis, J. Laskin, *Direct functionalization of C-H bonds by electrophilic anions*, (under revision in **PNAS**).

Manuscripts under Preparation

1. S. Debnath, M. Jorewitz, F. Müller, F. Bischoff, J. B. Stückrath, J. Sauer, K. R. Asmis, *Infrared Photodissociation Spectroscopy of $[(Al_2O_3)_nFeO]^+$ with $n = 2-5$ Influence of Fe-Impurities on Structure and Other Properties*.
2. F. Müller, J. B. Stückrath, F. A. Bischoff, L. Gagliardi, J. Sauer, S. Debnath, M. Jorewitz, K. R. Asmis, *Valence and Structure Isomerism of $Al_2FeO_4^+$: Synergy of Spectroscopy and Quantum Chemistry*.
3. F. Müller, F. A. Bischoff, J. Sauer, S. Gewinner, W. Schöllkopf, M. R. Fagiani, X. Song, S. Debnath, Knut R. Asmis, *Water Adsorption on $Fe_3O_4^+$ Gas Phase Clusters*.

Talks and Conference Contributions

- **Frontiers in Size-Selected Cluster Research: Bridging the Gap**, Sept 29 - Oct 04, **2019**, Bad Honef, Germany.

Poster presentation: “Infrared Photodissociation Spectroscopy of $[(\text{Al}_2\text{O}_3)_n\text{FeO}]^+$ with $n = 2-5$: Influence of Fe-Impurities on Structure and Other Properties”.

- **Bunsentagung**, May 29-31st, **2019**, Jena, Germany.

Poster presentation: “Structural Properties of $[(\text{Al}_2\text{O}_3)_n(\text{FeO})]^+$ Clusters Studied by Infrared Photodissociation Spectroscopy”.

- **CRC-1109 final meeting**, October **2018**, Berlin, Germany.

Speaker: Structure and reactivity of bi-metallic metal oxide clusters.

- **Gordon Research Seminar and Conference on Molecular and Ionic Clusters**, Feb 24-25th, **2018**, Tuscany IL Ciocco in Lucca (Barga), Italy.

Speaker (GRS): “CO₂ Activation by Ti₃O₆ anion Studied by Infrared Photodissociation Spectroscopy”.

Poster presentation (GRC): “CO₂ Activation by Ti₃O₆ anion Studied by Infrared Photodissociation Spectroscopy”.

- **Bunsentagung**, May 10-12th, **2018**, Hannover, Germany.

Speaker: “CO₂ Adsorption by Ti₃O₆⁻: A Novel Carbonate Binding Motif”.

- **Workshop “Introduction to Gaussian: Theory and Practice”**, January 8-12th, **2018**, New Delhi, India.

- **Workshop “Horizons in Cold Cluster Spectroscopy”**, September 12-15th, **2017**, Großbothen, Germany.

Speaker: “Reactivity of Titanium Oxide Anions: A vibrational Spectroscopic Study”.

- **Bunsentagung**, May 25-27th, **2017**, Kaiserlautern, Germany.

Speaker: “Vibrational Spectroscopy of Microhydrated Magnesium Nitrate Cations $[\text{MgNO}_3]^+(\text{H}_2\text{O})_{0-12}$ Evolution of Characteristic Binding Motifs”.

- **CRC 1109 Symposium**, February 19-22nd, **2017**, Berlin, Germany.

Poster presentation: “Vibrational Spectroscopy of Water Adsorption on Metal Oxide Clusters”

- **Future of Chemical Physics Conference 2016**, Aug 31st-September 2nd, **2016**, Oxford, UK.

Poster presentation: “Vibrational Spectroscopy of D₂-Tagged Microhydrated Magnesium Nitrate Cations [MgNO₃]⁺(H₂O)_{n=2-12}”

- **Bunsentagung**, May 5-7th, **2016**, Rostock, Germany.

Speaker. “Gas Phase Vibrational Spectroscopy of Titanium Oxide Anions: Structure-Reactivity Relationship”

- **CRC-1109 Summer School**, August 22-25th, **2016**, Berlin, Germany.

Poster presentation: “Mass Spectrometry and Vibrational Spectroscopy of Silicate and Fe-Hydroxychloride Oligomers”

Curriculum Vitae

Personal Data

Name Sreekanta Debnath
Date of Birth 19th June 1991
Place of Birth Kolkata, India
Address Stephanstraße 49, Berlin
E-Mail debnathsreekanta50@gmail.com

Education:

2015 – present **Doctoral** researcher at the Wilhelm-Ostwald-Institut für Physikalische und Theoretische Chemie der Universität Leipzig, Leipzig.
(Supervisor: Prof. Dr. Knut. R. Asmis)

2012 – 2014 **M.Sc.** in Chemistry (Physical chemistry special), Indian Institute of Technology Bombay, India.
Master thesis: “Unconventional hydrogen bonding study of propargyl benzene complexes with different ligands in gas phase”.
(Supervisor: Prof. G. Naresh Patwari)

2013.05 – 2013.07 **Summer Project**, University of Calcutta, Kolkata, India.
Project title: “The structural and dynamical aspects of halide ion solvation in acetonitrile medium with special emphasis on Asymmetric solvation”.
(Supervisor: Dr. Pinaki Chaudhury)

2009 – 2012 **B.Sc.** in Chemistry, Barasat Government College, West Bengal State University, West Bengal, India

Ort, Datum

Sreekanta Debnath

